DIFFUSE RADIO SOURCES IN NON-MERGING GALAXY CLUSTERS

Dissertation

zur Erlangung des Doktorgrades
an der Fakultät für Mathematik, Informatik und
Naturwissenschaften
Fachereich Physik
der Universität Hamburg

vorgelegt von
FEDERICA SAVINI

Hamburg, Wintersemester 2018/19

Gutachter/innen der Dissertation:	Prof. Dr. Marcus Brüggen Prof. Dr. Annalisa Bonafede
Zusammensetzung der Prüfungskommission:	Prof. Dr. Marcus Brüggen Prof. Dr. Jochen Liske Prof. Dr. Robi Banerjee Prof. Dr. Francesco De Gasperin Prof. Dr. Annalisa Bonafede
Vorsitzende/r der Prüfungskommission:	Prof. Dr. Jochen Liske
Datum der Disputtation:	16.11.2018
Vorsitzender Fach-Promotionsausschusses PHYSIK:	Prof. Dr. Wolfgang Hansen
Leiter des Fachbereichs PHYSIK:	Prof. Dr. Michael Potthoff
Dekan der Fakultät MIN:	Prof. Dr. Heinrich Graener

Zusammenfassung

Galaxienhaufen (Cluster) sind großräumige Systeme, in denen hunderte bis tausende von Galaxien, sowie heißes, magnetisiertes Gas (bekannt als Intracluster Medium; ICM) und Dunkle Materie koexistieren. Sie bilden sich durch Kollaps von den größten gravitationsbedingten Überdichten im ursprünglichen Dichtefeld des Universums. Eine Reihe von Galaxienhaufen beherbergen diffuse Radioquellen, die nicht von aktiven Galaxien herrührt sondern mit dem ICM verbunden ist. Diese Synchrotronquellen deuten auf das Vorhandensein einer nicht-thermischen Komponente hin, die aus kosmischer Strahlung und magnetischen Feldern besteht.

Der Fokus dieser Arbeit liegt auf der Untersuchung der Entstehung und der Eigenschaften von Radiostrahlung im Zentrum von Galaxienhaufen. Abhängig von ihrer Größe, werden zentrale, diffuse Radioquellen üblicherweise als riesige Radio-Halos oder Mini-Halos klassifiziert. Nach aktuellen theoretischen Erkenntnissen bilden sich riesige Radio-Halos durch die Wiederbeschleunigung von Elektronen durch Turbulenz, die während der Verschmelzung von Galaxienhaufen entsteht. Mini-Halos hingegen befinden sich normalerweise im Zentrum von sogenannten cool-core Clustern, in denen nur geringfügige Verschmelzungen mit anderen Galaxienhaufen stattgefunden haben können. Die führende Theorie zu der Entstehung der relativistischen Elektronen, die die Mini-Halos verursachen, besagt, dass Elektronen durch Turbulenz angetrieben werden. Die Turbulenz entsteht wiederum durch Gasbewegungen (sloshing) der dichten Kerne der Galaxienhaufen. Laut einer konkurrierenden Theorie werden frische Elektronen durch Kollisionen zwischen Protonen der kosmischen Strahlung und thermischen Ionen des ICM erzeugt. Beobachtungen von niedrig-frequenten Radiowellen liefern neue Einblicke in dieses Phänomen. Von besonderem Interesse sind hier insbesondere Galaxienhaufen, die sich nicht in Kollision mit anderen Galaxienhaufen befinden. Im Zuge dieser Arbeit habe ich fünf erfolgreiche Beobachtungsanträge geschrieben. Die Ergebnisse sind in drei Erstautorveröffentlichungen dargestellt.

Ich habe eine Stichprobe von neun massenselektierten Galaxienhaufen untersucht, die keine Anzeichen für größere Kollisionen aufweisen. So habe ich neue diffuse Radioquellen in Form von Halos und Steilspektrums-Emission um Mini-Halos entdeckt. Letzteres deutet darauf hin, dass das Sloshing im kühlen Zentrum eines Galaxienhaufens die Teilchenbeschleunigung auf großen Skalen auslösen kann. Dieses Resultat ist besonders relevant für zukünftige Studien. Grenzwerte für die Intensität der Radiostrahlung können verwendet werden, um das Energiebudget der Protonen der kosmischen Strahlung im

ICM einzuschränken. Diese Ergebnisse konkurrieren mit den niedrigsten Grenzwerten, die mit dem Gammastrahlen Satelliten *Fermi* gewonnen worden sind. Schließlich habe ich eine Radiogalaxie entdeckt, die in steile, diffuse Radioemission eingebettet ist und die sich im Zentrum einer Galaxiengruppe befindet. Das Radiospektrum legt nahe, dass die Radioquelle in einem sehr entwickelten Zustand ist, und zeigt das Potential von niedrigfrequenten Radiobeobachtungen zur Untersuchung von altem Radioplasma.

Summary

Galaxy clusters are large-scale systems where hundreds to thousands of galaxies, hot magnetized gas (known as intracluster medium; ICM), and Dark Matter co-exist. Their formation corresponds to the collapse of the largest gravitationally-bound overdensities in the initial density field in the universe. A number of clusters host radio diffuse emission that is not associated with single active galaxies, but is instead connected to the ICM. These synchrotron sources indicate the presence of cosmic rays and magnetic fields.

The main focus of this thesis is to study the formation and properties of radio diffuse emission located at the center of galaxy clusters. Of particular interest are non-merging clusters where particle acceleration mechanisms can be studied in absence of a major merger. Depending on their size, centrally-located radio diffuse sources are commonly classified as giant radio halos or mini halos. According to the current theoretical picture, giant radio halos form via the re-acceleration of electrons in the ICM via turbulence injected during cluster mergers. Mini halos, instead, are usually found at the center of cool-core clusters where only minor or off-axis mergers may have taken place. The origin of mini halos is still debated: electrons can be re-accelerated by turbulence induced by gas sloshing of the dense cores powered by minor mergers, or fresh electrons can be produced by collisions between cosmic ray protons and thermal ions. Low-frequency radio observations provide new insights into the origin of known diffuse radio sources, and have the potential to discover new sources.

Using the LOw Frequency ARray (LOFAR), I have studied a sample of nine mass-selected clusters that show no signs of major mergers. Among the results, I have discovered new diffuse radio sources in the form of halos and steep-spectrum emission around mini halos in two cool-core clusters. The latter indicates that the sloshing of a dense cool core can trigger particle acceleration on large scales, and is particularly relevant for future studies. In case of non-detection of radio diffuse sources, I showed that limits on the radio power can be used to constrain the energy budget of cosmic ray protons in the ICM with results that are competitive with the deepest limits from the gamma-ray satellite *Fermi*. In addition, I have discovered a radio galaxy embedded in steep diffuse emission located at the center of a galaxy group. The radio spectrum suggests that the radio source is evolved and shows the potential of studying old radio plasma and fading sources with low-frequency radio observations.

Eidesstattliche Versicherung

Hiermit versichere ich an Eides statt, die vorliegende Dissertationsschrift selbst verfasst und keine anderen als die angegebenen Hilfsmittel und Quellen benutzt zu haben.

Die eingereichte schriftliche Fassung entspricht der auf dem elektronischen Speichermedium.

Die Dissertation wurde in der vorgelegten oder einer ähnlichen Form nicht schon einmal in einem früheren Promotionsverfahren angenommen oder als ungenügend beurteilt.

Federica Savini
Hamburg, den 16.11.2018

Contents

Chapter 1

Introduction

1.1 Context of the project

Clusters are the most massive, gravitationally-bound systems in the whole universe: hundreds to thousands galaxies are found in a region that is a few Mpc across. They form by accretion from the diffuse gas present in the universe, known as intergalactic medium (IGM), and through a sequence of mergers of smaller systems [Peebles & Yu, 1970]. As known from optical observations, hundreds, and even thousands of galaxies inhabit a single cluster. Compared to the age of the universe, clusters are latecomers, and their formation is still on-going at the nodes of the filamentary large-scale structure of the universe, known as cosmic web. These features make them ideal sources for studying the history of structure formation and the nucleosynthesis of heavy elements. Furthermore, clusters can be used for testing different cosmological models: the cluster mass function helps constraining the cosmological parameters (e.g. [Allen et al., 2008], [Vikhlinin et al., 2009]) completing the picture given by independent complementary methods, such as the cosmic microwave background and the supernovae type Ia tests.

By contrast with their name, the largest mass fraction of galaxy clusters is not provided by galaxies themselves, but instead by the Dark Matter (DM) and the intracluster medium (ICM), an extremely hot ($10^7 - 10^8$ K) and rarefied ($\sim 10^{-3}$ particle/cm^3) gas that pervades the volume in between the galaxies [Borgani & Kravtsov, 2011]. The presence of DM is inferred from dynamical analysis, by estimating the radial velocities of the member galaxies, or from gravitational analysis, by quantifying the distortion of background galaxies caused by strong/weak lensing. It was found that the sum of the masses of the single galaxies ($\sim 10^{13}$ M$_\odot$) is much smaller than the total cluster mass (10^{14} - 10^{15} M$_\odot$). This indicates that clusters host a large amount of non-baryonic matter: Dark Matter accounts for 70 - 80% of the total mass of the cluster. Moreover, galaxies do not even hold the record of containing the majority of the baryonic matter of a cluster that can actually be found in the ICM, which accounts for 15 - 20% of the total mass of the cluster. Due to its high temperature and low density, this gas emits in the soft X-ray regime, and important information on galaxy clusters has been obtained in the past decades through X-ray studies of this emission.

It is interesting to compare the ICM with the interstellar medium (ISM), which fills the space in between stars in our Galaxy. The ISM contains a mixture of at least three different types of matter: thermal gas, solid dust grains, and a relativistic component, which includes magnetic fields and high-energy particles (or cosmic rays; CR). The ICM content might be similar, however, due to its temperature, we do not expect to find dust grains and cool thermal gas phases to survive in the hot ICM. On the other hand, there is evidence for a large amount of magnetic fields and relativistic particles. Particles with energies less than few GeV have a diffusion time that is longer than the Hubble time [Berezinsky et al., 1997]. Thus, clusters are very effective traps for cosmic ray protons and ions.

The striking evidence for the presence of non-thermal components in the ICM comes from radio observations: a number of clusters is detected in the radio band, where diffuse, extended, synchrotron radio sources with no optical counterparts are associated with the ICM. This emission proves that the thermal plasma is mixed with non-thermal components, i.e. high-energy particles and large-scale magnetic fields. Their interplay gives origin to radio halos: low-surface brightness sources at the cluster center that can extend from few hundreds of kiloparsecs, the so-called mini halos, to 1 - 2 Megaparsecs, the so-called giant halos. Since halos are characterized by a steep spectrum[1], an increasing number of radio sources are being detected by low-frequency radio facilities, such as the LOw Frequency ARray (LOFAR), and will be detected with the advent of new-generation radio telescopes, such as the Square Kilometre Array (SKA).

Radio halo properties are connected to the cluster properties. A correlation between the radio power of halos and the cluster X-ray luminosity, mass, and temperature has been observed [Feretti et al., 2012]. The size of radio halos requires the action of mechanisms that inject fresh particles or re-accelerate pre-existing cosmic rays to energies that are millions of times larger than what the Large Hadron Collider, i.e. the world's largest particle accelerator, is capable of producing. The typical Lorentz factor of the relativistic particles in the ICM is $\gamma \gg 10^3$, which means that their velocities are close to the speed of light. Halos have been found mainly in merging systems, indicating a possible connection with mergers that are indeed the most energetic events in the universe after the Big Bang. In this scenario, shock waves and turbulence are introduced into the ICM, so that a fraction of the energy can be transferred to the cosmic rays that can then be re-accelerated up to energies of several GeV [Brunetti & Jones, 2014]. The hydrodynamic Reynolds number Re of the ICM is $\gg 10^3$, considering the velocities of large-scale motions and the effective particle mean-free-path, which suggests a turbulent regime that can operate through cascades [Brunetti & Jones, 2014]. Nevertheless, this value is small when compared to Re in the Earth's atmosphere that is in the range $10^7 - 10^8$, or in the oceans, where a large-scale current, such as the Gulf Stream, reaches $Re \sim 10^{11}$, indicating an extremely turbulent regime.

The ICM is a unique laboratory to collect information on the particle acceleration

[1]The radio spectrum follows a power law $S(\nu) \propto \nu^{\alpha}$, where S is the flux density, and ν the observing frequency. Steep-spectrum radio sources have spectral indices $\alpha < -1$.

mechanisms and the magnetic field properties in galaxy clusters. Cosmic rays undergo acceleration processes that can affect the ICM heating [Lau, 2010]. Moreover, cosmic rays and large-scale magnetic fields are closely connected to the cluster evolution and formation, and provide an additional contribution to the cluster's pressure budget that is used for precision cosmology. The typical magnetic field strength, which ranges between $1 - 10\,\mu$G [Brüggen et al., 2012], is small when compared to the Earth's magnetic field of $3 - 6 \times 10^2$ mG, or that of sunspots of ~ 1 kG, or that used in magnetic resonance imaging systems of 10^2 kG. Nevertheless, the ICM magnetic fields affect the heat conduction and the dynamics of the ICM. However, only few details are known about the topology and strength of the magnetic fields, and their origin, whether primordial or astrophysical. These aspects are still under debate.

A cluster of galaxies is a very peculiar region of the universe that offers a physical context beyond anything achievable in any laboratory on Earth. Here one can observe the interplay of cosmology, the formation of large-scale structure via Dark Matter, astroparticle physics due to the acceleration of cosmic rays, and plasma physics due to the presence of the ICM as an extremely dilute (collisionless), magnetized, turbulent, hot plasma.

1.1.1 Aim

The aim of my PhD project was to investigate the origin of diffuse radio emission, its evolution and its connections to the cluster dynamics. In particular, I addressed the following key questions:

- are radio halos common in non-merging clusters?
- are giant radio halos and mini halos connected?
- how are particles accelerated in mini halos?

Answering these question represents a considerable step forward in our understanding of particle acceleration mechanisms in galaxy clusters. To this end, I performed low-frequency high-resolution radio observations of a galaxy group and nine galaxy clusters. Observations were carried out mainly with the new generation radio interferometer LOFAR in the frequency range 120 - 168 MHz, and data were calibrated using innovative advanced techniques that have been recently developed. The sources studied in this work are examples of steep-spectrum radio sources that can be discovered and studied using low-frequency observations.

1.1.2 Thesis outline

In the following sections of *Chapter* 1, I will give an introduction on the sources and processes in galaxy clusters that can be studied at low radio frequencies, and on the methods used, such as radio interferometry and data calibration techniques. In the main chapters,

I present the three papers that I wrote as first author.

In *Chapter* 2 is presented my paper "*A LOFAR study of non-merging massive galaxy clusters*" that collects the results of the largest sample of galaxy clusters studied within the LOFAR Two-Metre Sky Survey (LoTSS) and reduced with a direction-dependent calibration. For a number of cases, archival VLA/GMRT observations have also been used. The campaign of observations targets massive galaxy clusters that have been classified as non-merging using *Chandra* X-ray data. This selection is motivated by the recent discoveries of radio halos in clusters that are not undergoing major mergers, and in clusters that were known to host mini halos. The aim is to investigate whether low-frequency steep-spectrum emission can be powered by minor mergers, and/or if there is a connection between halos and mini halos. For the first time, a large-scale ultra-steep-spectrum halo is found in a cool-core cluster which hosts a mini halo, and in *Chapter* 3 I analyze in detail such a source.

In *Chapter* 3 is presented my paper "*First evidence of diffuse ultra-steep-spectrum radio emission surrounding the cool core of a cluster*" where a cluster that belongs to the sample presented in the previous paper is studied in detail. The sloshing of the dense core after a minor merger is suggested as a mechanism for the formation not only of a central mini halo, but also of larger-scale emission that is visible at low radio frequencies. This conclusion is crucial for future low-frequency observations of cool-core clusters.

In *Chapter* 4 is presented my paper "*Studying the late evolution of a radio-loud AGN in a galaxy group with LOFAR*" where a 650 kpc-size central radio galaxy is observed in a galaxy group at LOFAR frequencies. A GMRT follow-up observation at 607 MHz was obtained to study the spectral properties of the sources. The low-frequency spectral index map reveals a steepening of the spectrum from the outer edge of the lobes toward the central source and a steep core, which is in disagreement with the usual spectrum of an active radio galaxy. Possible interpretations are discussed, concluding that the radio source is an evolved radio-loud active galaxy surrounded by diffuse emission that is likely related to old plasma left behind by the jets forming the lobes, or a continuation of the lobes that experienced a backflow at the edges. The two jets are interacting with the intragroup medium that shows asymmetrical features in the lobe regions. These observations probe the great potential of LOFAR to detect old plasma, and demonstrate that low-energy electrons are present in the intragroup medium (IGM), and could furnish a seed population for particle re-acceleration mechanisms.

Finally, in *Chapter* 5, I provide a summary of the work and lay out the relevance with respect to my overarching goals.

In the *Appendix*, a short primer on radiative processes is provided, with the description of the processes that play a role in the physics of galaxy clusters, and are relevant for this thesis, i.e. Bremsstrahlung emission, synchrotron emission, and Sunyaev Zel'dovich effect. Moreover, a technique used to estimate magnetic fields in galaxy clusters is briefly outlined.

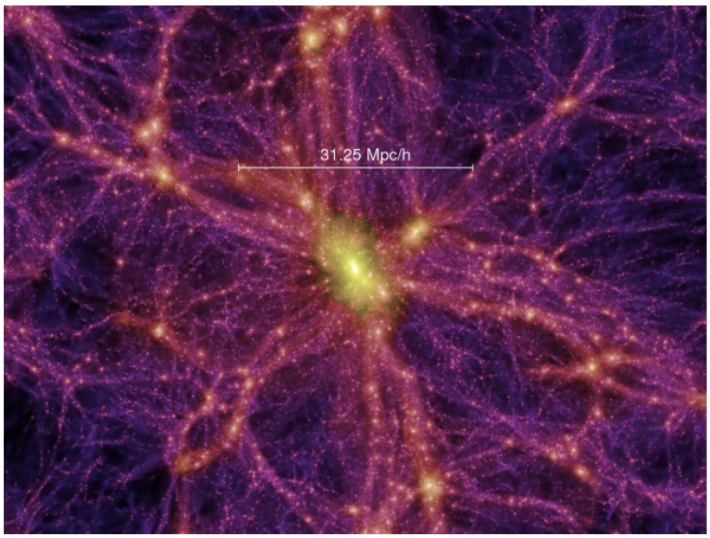

Figure 1.1: The millennium simulation [Springel et al., 2005]. The density field of the Dark Matter is shown at the present age of the Universe, i.e. 13.6 Gyr (z = 0). Yellow indicates high densities, while purple low densities. Clusters form at the nodes of this cosmic web, as shown at the center of the image, where the density is higher.

1.2 Galaxy clusters

Cosmological simulations (e.g. [Springel et al., 2005]) reveal that matter in the universe has evolved through initial density fluctuations under the action of gravity. Structures formed where the matter overdensity had overcome the expansion of the universe, and are now concentrated in filaments and sheets that form a large-scale network called the "cosmic web", as shown in Fig. 1.1. At the nodes of the cosmic web, the largest gravitationally-bound systems are found: galaxy clusters. Their abundance, structure, and mass ($10^{14} - 10^{15}$ $M_\odot$) provide powerful probes of the history of structure and galaxy formation, and of cosmology. According to the hierarchical model of structure formation, clusters form via the gravitational merger of smaller systems and accretion of gas from the warm-hot intergalactic medium (WHIM), driven by Dark Matter, dissipating energies up to $\sim 10^{64}$ erg on a few Gyr timescale. Clusters are dominated by elliptical and S0 galaxies, especially in the dense central regions, where we can also find the most luminous giant ellipticals. Smaller, less massive ($\ll 10^{14}$ $M_\odot$) bound systems of galaxies are termed as galaxy groups, and are usually dominated by spiral and irregular galaxies. The closest example is the Local Group with the three largest members being all spirals: Andromeda, the Milky Way, and the Triangulum Galaxy. In the present-day universe, clusters and groups are still accreting mass, and new systems are forming.

A galaxy cluster contains hundreds or thousands of galaxies, a dilute magnetized intracluster medium (ICM) that fills the space between the galaxies [Forman et al., 1972] and Dark Matter, whose presence is indirectly inferred from optical and X-ray observations.

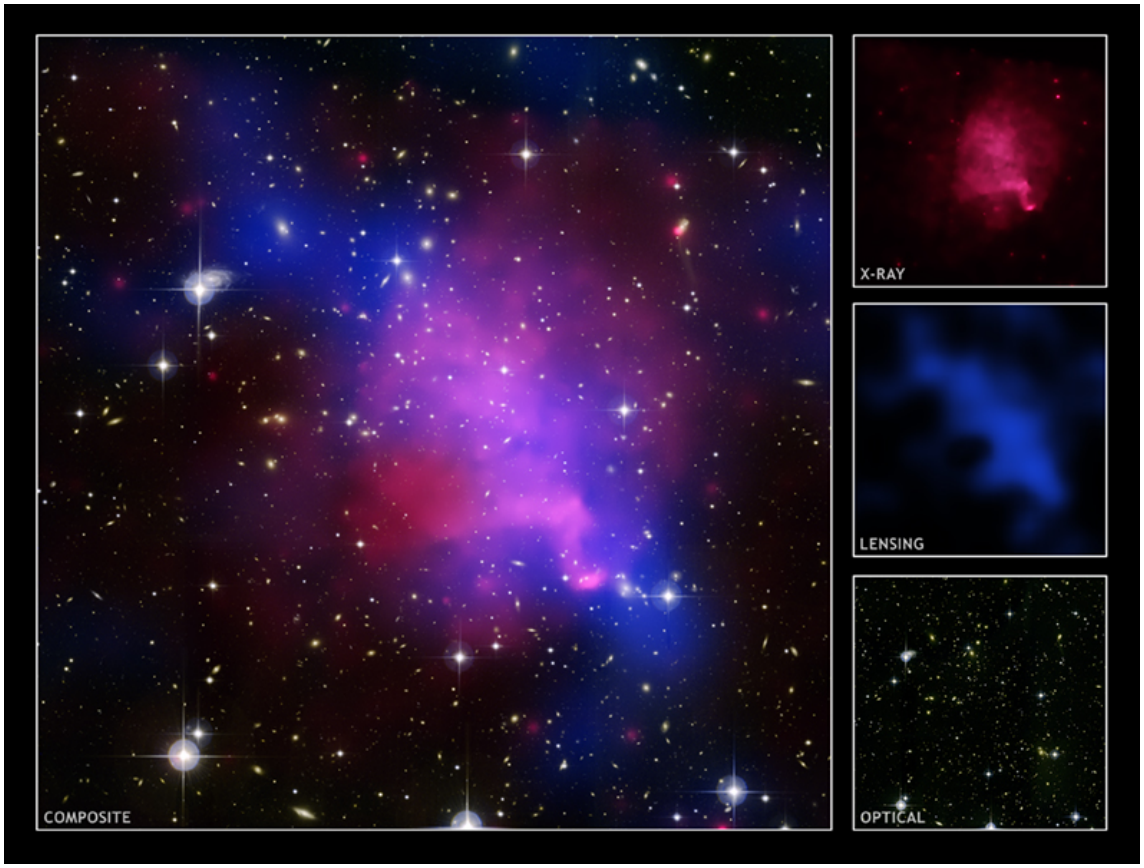

Figure 1.2: Composite image of the merging cluster Abell 520, also known as the "train wreck cluster". Galaxies are shown in the natural-color optical image taken with the *Hubble* Space Telescope and with the Canada-France-Hawaii Telescope. The ICM contribution from the X-ray image as detected by *Chandra* is overlaid in red, and a Dark Matter map derived from the *Hubble* observations via gravitational lensing is overlaid in blue. The distribution of the hot gas is a clear evidence that a collision (cluster merger event) took place. Credit: *Chandra* X-ray observatory site, Harvard University.

Galaxies, ICM and Dark Matter account respectively for 3 - 5 %, 15 - 20%, and 70 - 80% of the total mass of the cluster. This means that the majority of the observable mass, i.e. baryonic matter, is not contained in the galaxies, but in the hot gas in between. In Fig. 1.2, the spatial distribution of these three cluster components is shown in the case of the merging cluster Abell 520.

The ICM displays the following features:

- is hot with a temperature of $10^7 - 10^8$ K, which corresponds to an energy of $1 - 10$ keV;
- has a low density with an electron number density $10^{-2} - 10^{-3}$ cm^{-3} in the central regions that decrease to 10^{-4} cm^{-3} in the outskirts;

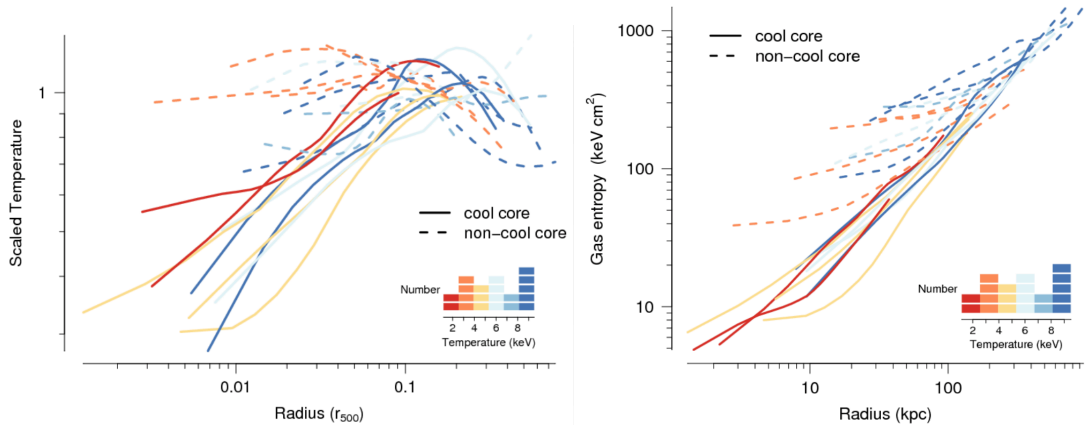

Figure 1.3: Gas temperature and entropy profiles as a function of radius for a sample of 20 galaxy clusters observed with *Chandra* [Sanderson et al., 2009]. The colors refer to the mean cluster temperature.

- is mainly composed of hydrogen and helium, with traces of heavier elements, such as iron and oxygen. Due to its high temperature, the gas is kept in an ionized state;
- is composed of magnetic fields [Clarke, 2004].

Note that a fraction of clusters also show the presence of relativistic particles, which reveal themselves through synchrotron radio emission, as will be explained in detail in Sec. 1.2.3.

1.2.1 X-ray properties

Clusters are extended, luminous X-ray sources due to thermal Bremsstrahlung emission from the ICM given its combination of high temperatures and low densities. The spectrum is dominated by continuum emission, plus emission lines from heavy element such as iron, oxygen, and calcium. Being the products of stellar processes, these metals must have been injected into the ICM through supernova-driven winds or outflows, providing evidence of a non-primordial origin of part of the gas. Moreover, obtaining the X-ray spectrum provides direct information on the gas temperature.

Obtaining the ICM density and temperature profiles from X-ray observations is fundamental for studying galaxy clusters. A bimodal gas distribution has been observed (see Fig. 1.3), and one distinguishes between cool-core clusters and non-cool-core clusters[2] (e.g. [De Grandi & Molendi, 2001], [Cavagnolo et al., 2009]). Examples of X-ray surface brightness map and temperature profile of a cool-core cluster and a non-cool-core cluster are shown in Fig. 1.4. A cool-core cluster shows, within the inner 100 kpc, a significant drop in temperature ($< 10^7 - 10^8$ K) and a strong X-ray surface brightness peak with the

[2]Note that X-ray-selected samples are known to be biased towards cool-core clusters due to the presence of their prominent surface brightness peak. Thus, in this work we made use of SZ-selected samples (see *Appendix*).

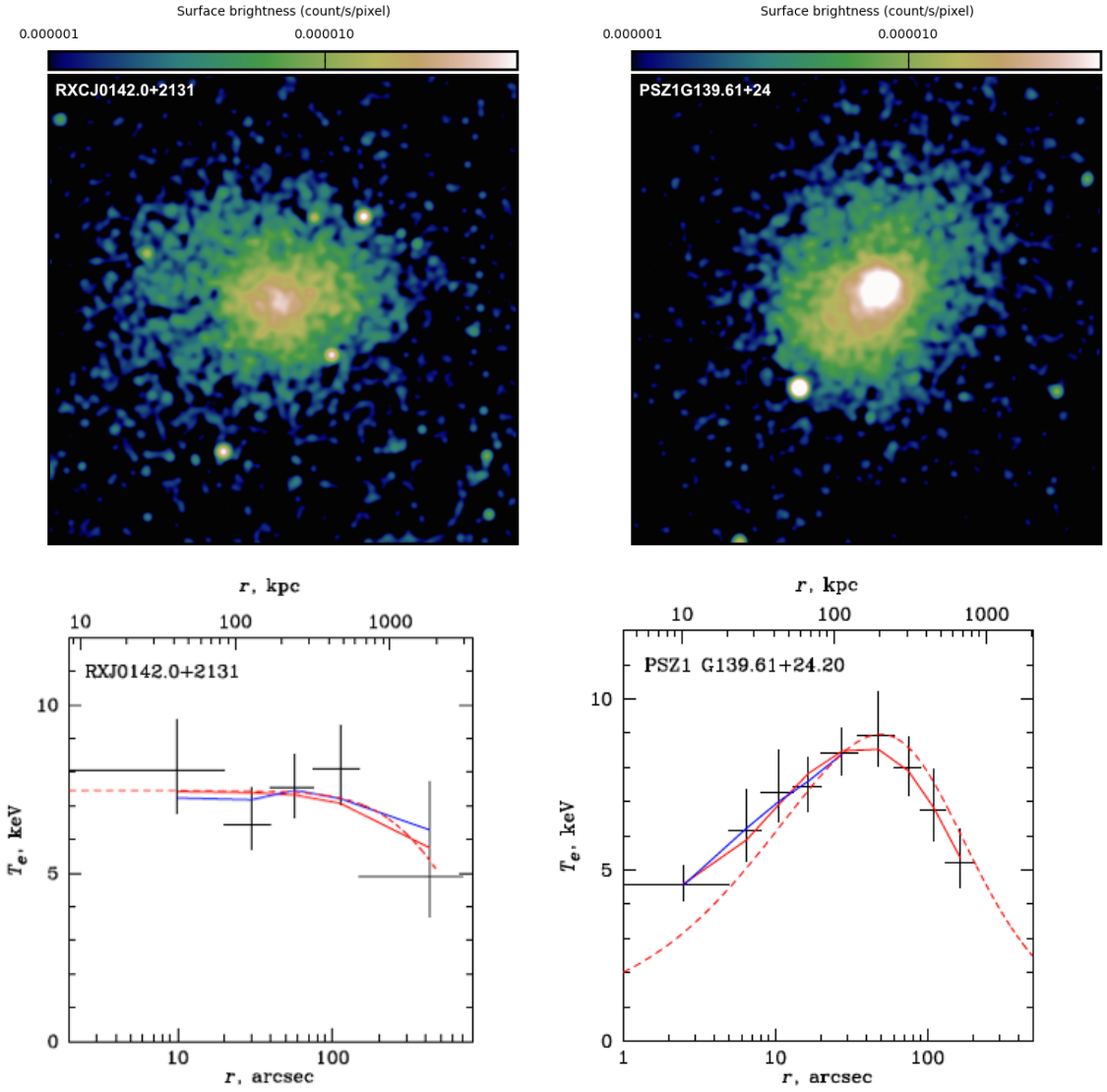

Figure 1.4: The clusters RXCJ0142.0+2131 and PSZ1G139.61+24.20 are taken as example of non-cool-core and cool-core cluster, respectively, being the subject of studies reported in a paper presented in this thesis. The *Chandra* X-ray images are adapted from Savini et al. [2018a]. The temperature profiles are taken from Giacintucci et al. [2017]. The observed projected temperatures indicated with crosses. The solid and dashed red lines show the best-fit 3D model and the corresponding projected profile, respectively. The solid blue lines show the best-fit entropy model.

gas density rising towards the cluster center, which implies a cooling time ($\ll 10^9$ yr) that is much shorter than the Hubble time. To balance the radiative losses and the consequent inwards gas flow, a source of heating is necessary, and is likely to be in the form of AGN feedback from the brightest cluster galaxy (BCG) that is usually located at the cluster center. Several X-ray cavities, i.e. regions where the radio plasma has displaced the X-ray emitting gas, are typically found coincident with the lobes of the radio-loud BCG.

The thermal gas distribution can be described through a model, called the β-model from the parameter that defines the ratio of the specific energy in galaxies to the specific energy in the hot gas, i.e. $\beta = \frac{\mu m_{\rm p} \sigma^2}{kT}$, where T is the gas temperature, σ is the line-of-sight velocity dispersion, μ is the mean molecular weight, and $m_{\rm p}$ the proton mass [Cavaliere & Fusco-Femiano, 1976]. The gas density profile is:

$$\rho_g(r) = \rho_{\rm g0} \cdot \left[1 + \left(\frac{r}{r_{\rm c}}\right)^2\right]^{-\frac{3}{2}\beta}, \tag{1.1}$$

where ρ_{g0} is the central gas density and r_c the core radius. This result is obtained considering the ICM being isothermal, spherically symmetric, and in hydrostatic equilibrium, hence:

$$\frac{1}{\rho_{\rm g}} \frac{dP}{dr} = -\frac{GM(r)}{r^2}, \tag{1.2}$$

where $P = \frac{\rho_{\rm g} kT}{\mu m_{\rm p}}$ is the pressure for an ideal gas.

The single β-model is a good approximation for non-cool-core clusters, while it does not describe well cool-core clusters (e.g. [Jones & Forman, 1984]), for which a double β-model can be used (e.g. [Giacintucci et al., 2017]).

A key parameter to measure the thermodynamic state of the ICM is the gas entropy, which is defined as $kT \cdot n_e$, and is derived from temperature and density profiles. The radial dependence can be written as:

$$K(r) = K_0 + K_{100} \left(\frac{r}{100\,\mathrm{kpc}}\right)^{\eta}, \tag{1.3}$$

where K_0 is the so-called core entropy, K_{100} is a normalization for entropy at 100 kpc, and η is the power law index. As shown by Cavagnolo et al. [2009], K_0 is a good estimator to distinguish cool-core from non-cool-core clusters. Giacintucci et al. [2017] consider clusters with low central entropies ($K_0 < 30-50$ keV cm^2) as cool-core clusters, and those with higher values as non-cool-core clusters.

Since cosmological structures are still forming and galaxy clusters still growing, clusters are dynamically-active objects. The motion of gas and the presence of entropy gradients lead to the formation of cold fronts (e.g. [Vikhlinin et al., 2001], [Ghirardini et al., 2018]). Most of the clusters analyzed in this thesis have a cool core and host cold fronts. Cold fronts are believed to form when the bulk of the central ICM in the cool core is perturbed by an event, such as a merger with a subcluster or a small group. The low-entropy

Figure 1.5: Optical image of the cool-core cluster Abell 2052 taken with the Very Large Telescope. Overlaid in blue is the *Chandra* X-ray image. A large-scale spiral structure of the gas, induced by a minor merger, can be seen. The collision caused the hot gas in the cluster to slosh. Credit: *Chandra* X-ray observatory site, Harvard University.

gas is displaced from the center of the Dark Matter potential well, and meets the outer higher-entropy ICM. The gas then slowly oscillates - "sloshes" - around its hydrostatic equilibrium configuration [Markevitch et al., 2000], and an arc-shaped discontinuity, known as cold front, forms. These very sharp discontinuities can be seen in their X-ray images where the surface brightness (and correspondingly the gas density) drops. A jump in the gas temperature is also found, with the denser region colder than the more rarefied region, unlike shock fronts. The density and the temperature discontinuities have similar amplitudes so that pressure is approximatively continuous across the front. The perturbation responsible for sloshing can be driven by the occurrence of a minor or off-center merger, i.e. the passage of a subcluster through the main cluster. Therefore, a cool-core cluster, which can experience a merger that does not disrupt the dense core, is the best candidate to look at for cold fronts. Sloshing lasts for several Gyr, such that the perturbed cluster can appear quite relaxed except for the presence of cold fronts. Examples of cool-core clusters with sloshing cold fronts are Abell 2052 [Blanton et al., 2011] in Fig. 1.5 and RXJ1720.1+2638 [Giacintucci et al., 2014b].

The study of the X-ray morphology of a cluster is also a powerful tool to classify the dynamical state [Rasia et al., 2013], and discriminate between merging and non-merging systems [Cassano et al., 2010]. In the following, I will outline the three morphological indicators I used in my work:

- the power ratio, which is the multipole decomposition of the projected two-dimensional mass distribution inside a given aperture of radius R, centered on the cluster X-ray centroid (e.g. [Böhringer et al., 2010]). The generic m-order power ratio (with $m > 0$) is defined as P_m/P_0 with

$$P_{\rm m} = \frac{1}{2m^2 R^{2m}} (a_m^2 + b_m^2),$$

  where a_0 is the total intensity within the aperture, $P_0 = a_0 \cdot \ln(R)$, and

$$a_m(r) = \int_{R' \leq R} S(x') R' \cos(m\phi') d^2x',$$

$$b_m(r) = \int_{R' \leq R} S(x') R' \sin(m\phi') d^2x',$$

  where S is the X-ray surface brightness. The ratio P_3/P_0 provides a good indication of substructure and asymmetries;

- the concentration parameter, c, which is defined as the ratio of the X-ray flux within 100 kpc over the X-ray flux within 500 kpc. It helps to select clusters with a compact core, i.e. clusters whose core has not been disrupted by a merger [Santos et al., 2008]

$$c = \frac{S(< 100\,\mathrm{kpc})}{S(< 500\,\mathrm{kpc})};$$

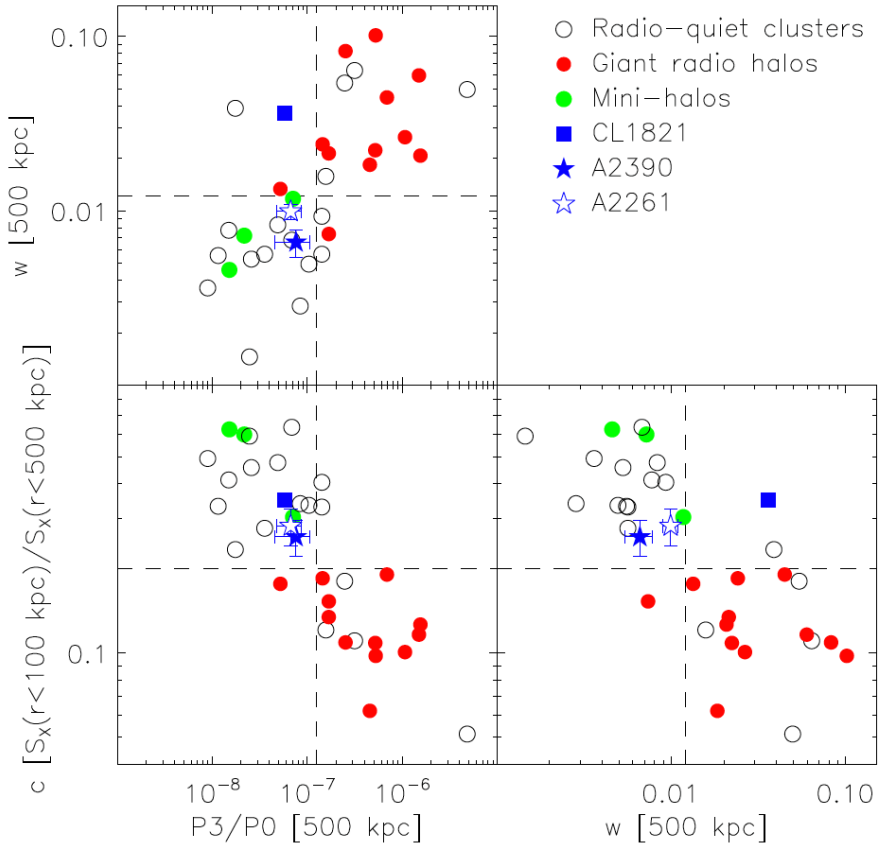

Figure 1.6: Morphological parameters for a sample of clusters from a study of [Sommer et al., 2017]. Symbols indicate the different type of diffuse radio emission (see Sec. 1.2.3) found in the clusters (clusters containing peculiar radio sources are indicated with different symbols). Clusters were considered as relaxed systems when: $P_3/P_0 \leq 1.2{\cdot}10^{-7}$, $w \leq 0.012$ and $c \geq 0.2$.

- the emission centroid shift, w, which is defined as the standard deviation of the projected separation Δ between the peak and the cluster X-ray centroid computed within N circles of increasing radius R (e.g. [Böhringer et al., 2010])

$$w = \frac{1}{R} \times \sqrt{\frac{\Sigma_{i=0}^{N}(\Delta_{\rm i} - \langle\Delta\rangle)^2}{N-1}}.$$

High values of P_3/P_0 and w indicate a dynamically disturbed system, while high values of c indicate a peaked core, typical of non-merging systems. Lovisari et al. [2017] show that w and c are the estimators most sensitive to the cluster dynamical state, hence I will not refer to P_3/P_0 throughout this work.

Fig. 1.6 shows an example of a plot containing these three parameters. As I will explain in Sec. 1.2.3, radio halos are found typically in merging systems, while mini halos in cool-core, regular clusters.

1.2.2 Mass estimates

The mass of a cluster is tightly connected to its history and dynamics. Estimating this parameter is fundamental not only for studying individual clusters or statistical samples of clusters, but also for testing different cosmological models [Sadat, 1997].

Masses can be determined via various methods. A simple (historically, the first used) approach involves the application of the virial theorem. Assuming a stable, self-gravitational, spherical distribution of the galaxies in a cluster, the virial mass is:

$$M_{\rm vir} \propto \frac{2\,R_G\,\sigma^2}{G}, \tag{1.4}$$

where σ is the velocity dispersion of the galaxies and R_G is the size of the system. Both parameters can be determined through optical observations of the galaxies. Furthermore, a scaling relation between the cluster mass and gas temperature can be derived from the virial equilibrium:

$$k\,T \propto M_{\rm vir}^{2/3}. \tag{1.5}$$

The bremsstrahlung X-ray luminosity scales with the temperature and the gas density, thus the luminosity can be directly related to the cluster mass, via:

$$L_X \propto M_{\rm vir}^{4/3}. \tag{1.6}$$

However, given the number of required approximations, these relations can not provide an accurate estimate of the cluster mass, but rather an indication of the order of magnitude.

Assuming hydrostatic equilibrium can be assumed, the equation that relates pressure and gravitational forces in case of spherical symmetry can be solved for the mass interior to a radius r, and results in:

$$M(r) = -\frac{k\,T}{G\,m_{\rm p}\,\mu}\left[\frac{d\,\log(\rho)}{d\,r} + \frac{d\,\log(T)}{d\,r}\right], \tag{1.7}$$

where the temperature and the gas density profiles can be determined through X-ray observations of the ICM. However, hydrostatic equilibrium is not a good approximation in most cases.

A more accurate method to derive the cluster masses is based on the gravitational lensing effect: when a massive cluster is located between a source and the observer, its mass deviates the path of the light coming from the source, acting as a lens. The geometry and the mass distribution can be used to estimate the lensing mass (e.g. [Hoekstra et al.,

2013], [von der Linden et al., 2014]).

Finally, in this work, I used mass estimates derived from a selection based on the Sunyaev-Zel'dovich (SZ) effect (see *Appendix* for details). The SZ effect is computed measuring the distortion of the Cosmic Microwave Background (CMB) spectrum, which depends on the temperature and density of the cluster. The SZ signal (typically indicated with a Y) is related to the cluster mass, via:

$$Y_{500}\, D_{\rm A}^2 \propto M_{\rm gas} T = f_{\rm gas}\, M_{\rm tot} T, \tag{1.8}$$

where Y_{500} is the Compton parameter integrated within R_{500}, i.e. the radius within which the average density is 500 times the critical density of the Universe at the cluster redshift, D_A is the angular diameter distance, $f_{\rm gas}$ is the fraction of mass in form of ICM, and $M_{\rm tot}$ is the cluster mass. Thus, using eq. 1.5:

$$Y_{500}\, D_{\rm A}^2 \propto f_{\rm gas}\, M_{\rm tot}^{5/3}\, E(z)^{2/3}, \tag{1.9}$$

where $E(z)$ is the Hubble function, defined as $\Omega_{\rm M}\,(1+z)^3+\Omega_{\rm r}\,(1+z)^4+\Omega_{\rm k}\,(1+z)^2+\Omega_{\Lambda}$. The SZ signal is a powerful proxy of the cluster mass for two reasons: it is almost not affected by the dynamical state of the cluster, and, being a scattering process, it is redshift-independent [Motl et al., 2005].

1.2.3 Radio properties

Galaxy clusters show a large variety of non-thermal radio sources that differ in size, morphology, and spectrum, and can be produced either by single member radio galaxies, or, more interestingly, by the ICM. Populations of cosmic ray electrons (CRe) spiraling around magnetic fields[3] present in the cluster volume cause synchrotron emission (see Fig. 1.7 for an example). These sources, unlike the thermal emission visible in the X-ray band, are not common. The first source of this kind was discovered in the Coma cluster [Large et al., 1959], and, in the last decades, diffuse radio sources have become the subject of studies and observations that substantially increased in line with the improvement of the capabilities of radio telescopes, in particular interferometers. Among these, the Very Large Array (VLA) and the Giant Metrewave Radio Telescope (GMRT) have obtained such great results that new array of antennas have been conceived and built to explore the radio sky to greater depths, such as the LOw Frequency ARray (LOFAR) and the up-coming Square Kilometre Array (SKA).

Based on their properties, diffuse radio sources have been divided into radio halos or smaller mini halos at the cluster centers, and radio relics[5] at the cluster peripheries (see Feretti et al. [2012] for a review). Their detection is difficult because of the low surface

[3]The strength of the magnetic fields in the ICM is $\sim 0.1-1\mu$G, and their presence is also demonstrated through Faraday Rotation[4] measures of polarized radio galaxies located inside or behind galaxy clusters (e.g. [Govoni & Feretti, 2004]).

[5]Radio relics are elongated, arc-like sources that reside at the cluster outskirts. In this thesis, these sources will not be discussed.

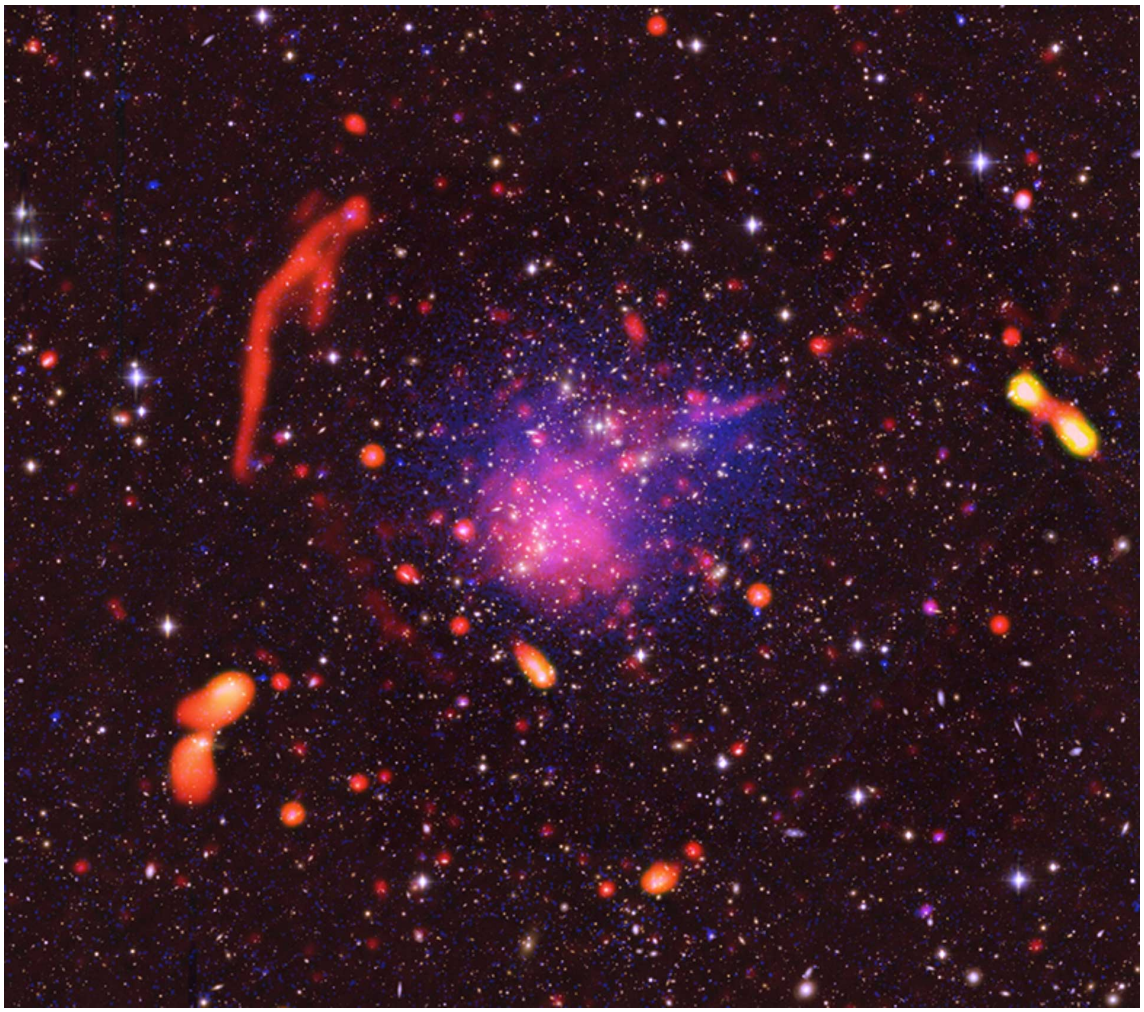

Figure 1.7: Composite image of the merging cluster Abell 2744, also known as "Pandora cluster", with a *Subaru* natural-color image of the galaxies, a *Chandra* image of the concentration of hot gas in blue, and a VLA image of the radio emission in red. Credit: Pearce et al.; Bill Saxton, NRAO/AUI/NSF; *Chandra*, Subaru; ESO.

brightness ($\sim 0.1 - 1\,\mu$Jy arcsec^{-2} at 1.4 GHz) and challenging considering the difficulties in the data reduction at low frequencies, where these sources are brighter due to the steepness of their spectra[6] ($\alpha < -1$; see Sec. 1.2.5 for details). Nevertheless, diffuse radio sources provide the evidence for relativistic electrons and for large-scale magnetic fields. Using radio observations, we have the unique chance to understand how energy is transported and dissipated in the ICM and investigate CR acceleration and magnetic field amplification processes on the largest scales in the universe (see Brunetti & Jones [2014] for a review).

In this thesis, I focus on the centrally-located sources, i.e. radio halos, which can be divided into:

- **giant halos** are non-polarized, extended sources with a typical size of 1 - 2 Mpc, a smooth morphology, and a radio power at 1.4 GHz of $10^{23} - 10^{25}$ W Hz^{-1}. Their brightness is usually nearly co-spatial with the X-ray emission from the cluster central regions, following the distribution of the thermal ICM. Halos are mainly found in clusters that have undergone a major merger, i.e. with a disturbed dynamical X-ray morphology (e.g. [Cassano et al., 2010], [Cuciti et al., 2015]). Indicators for a perturbed cluster are complex X-ray morphologies, a distinct distribution of velocities of the cluster member galaxies, the presence of multiple BCGs, and a non-spherical spatial galaxy distribution. The prototypical example of this class is the giant halo found in the Coma cluster [Large et al., 1959], shown in Fig. 1.8. Halos are rather common in massive clusters, and up to now, ~ 80 radio halos have been discovered (van Weeren et al., review in prep.). Cuciti et al. [2015] found that the fraction of halo-hosting clusters increases with the cluster mass, and reaches up to $60 - 80$ % for clusters with $M_{500} > 8 \times 10^{14}$ M$_\odot$. Studying a sample of giant radio halos has revealed that the radio power correlates with the X-ray luminosity, the ICM temperature and the cluster mass (e.g. [Liang et al., 2000], [Cassano et al., 2006]), indicating an interaction between thermal and non-thermal components;

- **mini halos** are also extended sources with a regular morphology, but on a size of few hundreds of kpc, from 100 kpc up to 500 kpc. A mini halo is typically found in a cool-core cluster, surrounding a central elliptical galaxy, usually the Brightest Cluster Galaxy (BCG), which is often radio-loud. In the latter case, the radio lobes may produce cavities visible as depletion of emission in the X-ray images. The separation of the mini halo from the central radio galaxy is difficult and needs a high-dynamic range. The typical radio power at 1.4 GHz is in the range $10^{23} - 10^{25}$ W Hz^{-1}, as for giant halos. However, compared to giant halos, mini halos show a larger synchrotron-volume emissivity [Murgia et al., 2009]. The prototypical source is the mini halo found in the Perseus cluster shown in Fig. 1.8. In general, the radio emission fills the cooling region within a radius of 300 kpc, and in some cases appears to be bound by sloshing cold fronts, suggesting a connection between mini

[6] Recently, halos with integrated spectral indices steeper than -1.5, up to -2 have been observed, and classified as ultra-steep-spectrum radio halos (USSRH). USSRH extend on a smaller scale than that of giant halos, and are believed to be connected to minor mergers, which dissipate less energy than a major merger event. The first USSRH has been found in A521 [Brunetti et al., 2008].

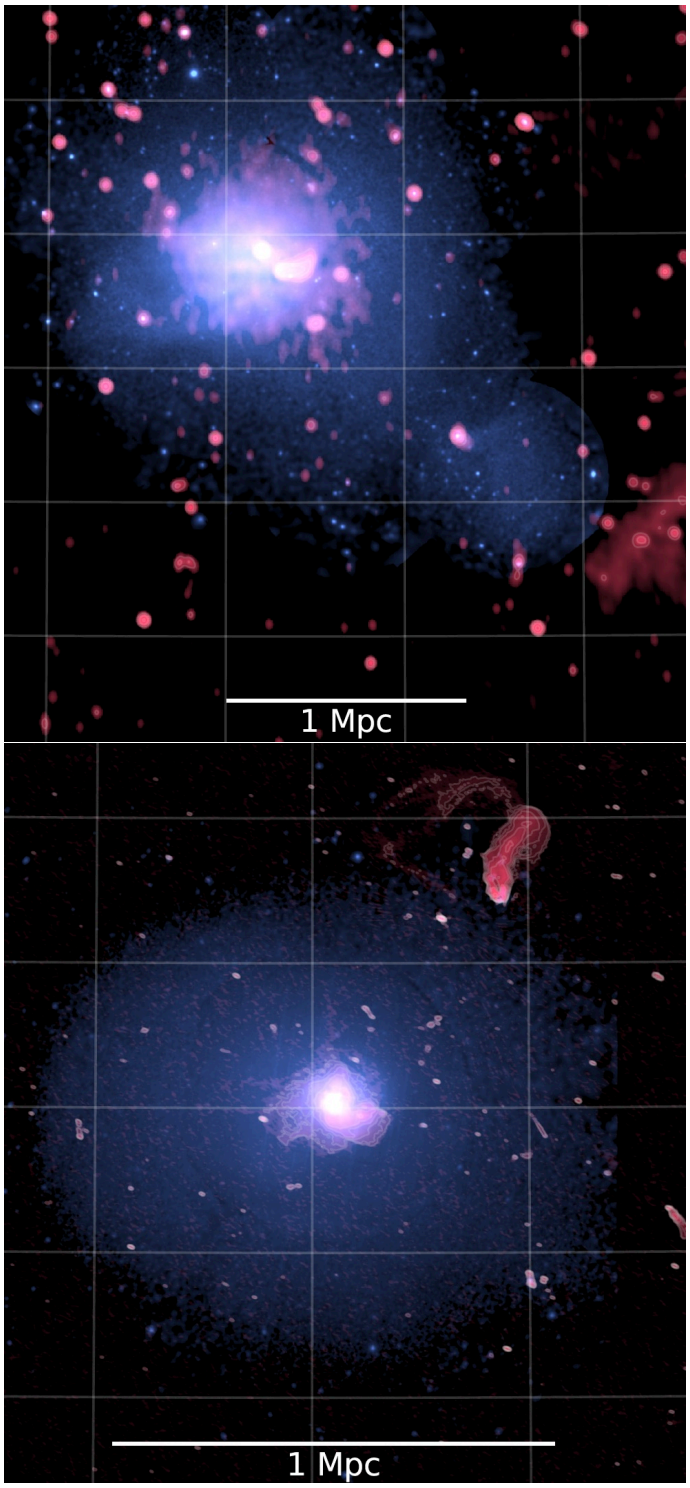

Figure 1.8: The prototypical giant halo in the Coma cluster in the top image and the prototypical mini halo in the Perseus cluster in the bottom image. The *Chandra* X-ray images are overlaid in blue. Credit: van Weeren et al., in prep.

halos and the motion of the gas in the core (e.g. [Mazzotta & Giacintucci, 2008], [Giacintucci et al., 2014b]). Giacintucci et al. [2017] studied a sample of 58 clusters with $M_{500} > 6 \times 10^{14}$ $M_{\odot}$ finding that 80% of the cool-core clusters host a mini halo, and no mini halos were found in non-cool-core systems. Turbulence generated by the gas sloshing in the dense cool core can re-accelerate aged electrons. The existence of a possible connection between gas sloshing and mini halos was first proposed by Mazzotta & Giacintucci [2008], who found that the mini halos in the clusters RXJ1720.1+2638 and MS1455.0+2232 appear to be confined to the region bounded by cold fronts. Numerical simulations (e.g. [ZuHone et al., 2013]) predicts that the diffuse radio emission connected to gas sloshing is mostly confined within the cold fronts.

The surface brightness of both giant and mini halos, when they show a regular morphology, can be fitted by an exponential law, $I(r) = I_0 \cdot e^{-r/r_e}$, where r_e is the e-folding radius. Murgia et al. [2009] found that r_e is smaller for mini halos compared to giant halos, as expected from their sizes. This modeling is particularly useful to estimate the size of a source that does not depend on the sensitivity of the observation as for the typical estimate of $D_{radio} = \sqrt{D_{min}\, D_{max}}$, where D_{min} and D_{max} are the minimum and maximum diameter of the 3σ surface brightness isocontours where σ is the image rms. An example of r_e application can be found in *Chapter* 3.

1.2.4 Particle acceleration mechanisms

CR acceleration and dynamics in the ICM significantly differ from those in other astrophysical environments: particles diffuse in a dilute, magnetized, hot plasma on very large volumes and for very long time. CR protons are confined and accumulated in the cluster volume for a time equal to the Hubble time. Instead, CR electrons undergo significant energy losses, which are dominated by ionization and Coulomb losses at low energies, and by synchrotron and inverse Compton losses at higher energies (see *Appendix*). The radiative lifetime of electrons with energies in the GeV range in a μG-magnetic field is 10^8 yr. The time necessary for particles to diffuse over a distance L is $\propto \frac{L^2}{4\,D}$, where D is the spatial diffusion coefficient [Berezinsky et al., 1997]. The diffusion of cosmic rays over Mpc-scales within a few Gyr would require a value of $D > 2 \times 10^{31}$ cm^2 s^{-1}, which is extremely large considering that it is several orders of magnitude larger than that in our Galaxy. The formation of Mpc-scale diffuse sources shows the need of a mechanism where pre-existing electrons are re-accelerated or fresh electrons are continuously produced throughout the cluster volume.

Two processes have been proposed to produce the synchrotron radiation observed in the radio band and explain the origin of radio halos:

- primary models, where electrons are continuously re-accelerated in-situ [Jaffe, 1977] to energies of few GeV by the magneto-hydrodynamical (MHD) turbulence [Roland, 1981]. Turbulence is assumed to be injected in the ICM during merger events, which induce large-scale motions that, dissipating part of their gravitational energy, generate random and turbulent velocity fields (e.g. [Sarazin, 1999], [Petrosian, 2001]).

In a major merger, hydrodynamical shocks can dissipate energies of the order of $\sim 10^{63}$ erg. This mechanism interests the whole cluster volume in a timescale of $\sim 10^9$ yr. The key point is the chain of processes that transport energy from large scales to collisionless small-scales in the ICM. In this scenario, once turbulence is developed, a Kolmogorov-like cascade can channel energy into electromagnetic fluctuations (magneto-sonic waves) at small scales where particles are scattered and accelerated[7] within a timescale that is inversely proportional to the efficiency of turbulent acceleration.

Turbulent re-acceleration is a second-order Fermi mechanism, i.e. a stochastic process where the mean fractional energy change is proportional to β^2. To derive this, we consider the elastic collision between a magnetic cloud with velocity $\vec{V}$ and a charged particle with initial energy E_i and momentum p_i that hits the cloud at an angle θ. In the reference system of the cloud (indicated by $'$), we write:

$$E_i^{'} = \gamma\,(E_\mathrm{i} + \beta\,c\,p_\mathrm{i}\,\cos\theta); \qquad\qquad c\,p_i^{'}\,\cos\theta = \gamma\,(c\,p_\mathrm{i}\,\cos\theta + \beta\,E_\mathrm{i}).$$

Since the collision is elastic, $E_\mathrm{f}^{'} = E_\mathrm{i}^{'}$ and $p_\mathrm{f}^{'} = -p_\mathrm{i}^{'}$. In the observer frame:

$$E_f = \gamma\,(E_\mathrm{f}^{'} - \beta\,c\,p_\mathrm{f}^{'}\,\cos\theta) = \gamma\,(E_\mathrm{i}^{'} + \beta\,c\,p_\mathrm{i}^{'}\,\cos\theta) = \gamma^2\,E_\mathrm{i}\,(1 + 2\,c\,\beta\,\frac{p_\mathrm{i}\,\cos\theta}{E_\mathrm{i}} + \beta^2).$$

Knowing that $\gamma^2 = (1-\beta^2)^{-1}$ can be approximated to second order as $(1+\beta^2)$, then:

$$E_f \sim (1+\beta^2)\,E_\mathrm{i}\,(1 + 2\,c\,\beta\,\frac{p_\mathrm{i}\,\cos\theta}{E_\mathrm{i}} + \beta^2),$$

that gives:

$$\frac{E_f - E_i}{E_\mathrm{i}} = \frac{\Delta E_\mathrm{i}}{E_\mathrm{i}} = 2\,c\,\beta\,\frac{p_\mathrm{i}\,\cos\theta}{E_\mathrm{i}} + 2\,\beta^2. \tag{1.10}$$

Hence, the energy variation ΔE_i is proportional to the initial energy and is independent of charge and magnetic field strength. Moreover, energy gain or loss depends on the relative direction of velocity of the particle and the cloud.

In reality, directions are isotropized in the cloud, so we can compute the probability of collision averaging over the angle θ. We assume that the regime is ultra-relativistic so that $E_\mathrm{i} = cp_\mathrm{i}$, and that the particles stream at a uniform velocity $\vec{v}$, hence θ is fixed with respect to the cloud velocity.

[7] The model assumes transit time damping with magnetosonic/fast turbulent modes as mechanisms of re-acceleration (see Brunetti et al. [2007] for details).

The interaction rate is given by:

$$R^{'} = \frac{1}{\Delta T'} = \frac{1}{\Delta T} + \frac{V}{v\,\Delta T'}\,\cos\theta \sim R\,(1 + \beta_{\rm v}\,\cos\theta),$$

since $\Delta T^{'} = \frac{\Delta T}{1+\frac{V}{v}\cos\theta}$ for Doppler's effect.

We can finally compute the energy variation for a single collision, as:

$$< 2\,\beta\,\cos\theta >= \frac{2\,\beta\,\int_{-1}^{1} R^{'}\,\cos\theta\,d\theta}{\int_{-1}^{1} R'\,d\theta} = \frac{2}{3}\,\beta^2.$$

Using eq. 1.10, we find:

$$< \frac{\Delta E}{E} >= \frac{2}{3}\,\beta^2 + 2\,\beta^2 = \frac{8}{3}\,\beta^2. \tag{1.11}$$

This implies a second order in $\frac{v}{c}$ and a positive energy gain.

In conclusion, in each particle-cloud scattering the energy of the particle can either increase or decrease, but on average particles gain energy since head-on collisions are more probable than the tail-on ones.

As shown above, the primary model is based on the re-acceleration of electrons, and this leads to the question about their origin, which is also known in literature as "injection problem". Liang et al. [2000] proposed that relativistic particles can be accelerated out of the thermal electron background in the ICM (often referred to as "thermal pool"), however Petrosian [2001] and Petrosian & East [2008] pointed out that the process would have to overcome the large Coulomb energy losses that the electrons suffer as they are accelerated from their initial low-energy to relativistic energies. This mechanism would lead to heating of the ICM plasma to above 10^8 K in less than 10^8 yr. The problem is solved if long-lived (10^9 yr) non-thermal electrons have already energies greater than a few hundred MeV. Hence, the primary model assumes the presence in the cluster volume of a pre-existing population of relativistic electrons, known as seed electrons (note that seed electrons with $\gamma_{\rm e} < 300$ have life times > 3.5 Gyr). It has been proposed that seed electrons are injected in the ICM by the AGN activity, or star formation in normal galaxies (e.g. supernovae and galactic winds), or shocks during the cluster dynamical history, and accumulated for a few Gyr at energies of a few hundred MeV (e.g. [Sarazin, 1999], [Brunetti et al., 2001], [Blasi et al., 2007]).

- secondary models, where electrons are bi-products of hadronic collisions between cosmic ray protons (CRp) and thermal protons/ions of the ICM [Dennison, 1980]. The decay chain involves the production of pions via:

$$p + p \rightarrow \pi^{+} + \pi^{-} + \pi^{0} + [...].$$

The charged pions decay in muons that in turn decay in positron/electron pairs, via:

$$\pi^{\pm} \rightarrow \mu^{\pm} + \nu_{\mu}(\bar{\nu_{\mu}}),$$

$$\mu^{\pm} \rightarrow e^{\pm} + \bar{\nu_{\mu}}(\nu_{\mu}) + \nu_{\mathrm{e}}(\bar{\nu_{\mathrm{e}}}).$$

In the chain, γ-ray emission from the decay of neutral pions is also expected:

$$\pi^{0} \rightarrow 2\gamma,$$

with an average energy of $\sim$ 67 MeV. This provides a measure of the low-energy γ-ray spectrum.

Protons can diffuse over larger scales compared to electrons due to their negligible energy losses. The expected accumulation of CRp generated during cluster formation motivate the quest for the presence of CRp in galaxy clusters. The most direct approach to constrain the energy content of CRp consists in the search for γ-ray emission. However, diffuse gamma-ray emission has not yet been detected from galaxy clusters. Hence, upper limits on the ratio between CRp energies and thermal energies $E_{\mathrm{CRp}}/E_{\mathrm{ICM}}$ have been derived. Early space-based observations provided limits of $E_{CRp}/E_{ICM} < 0.3$ in a number of nearby galaxy clusters [Reimer et al., 2003]. More stringent limits have been derived from deep, pointed observations at energies $>$ 100 GeV with ground-based Cherenkov telescopes. These results depend on the unknown spectral shape of the CRp-energy distribution and their spatial distribution. The most stringent limits are obtained assuming $\delta = 2.1$ where $N_{CRp} \propto p^{-\delta}$ and a linear scaling between CRp and thermal energy densities. A particularly deep limit of $E_{CRp}/E_{ICM} < 0.016$ was derived for the Perseus cluster [Aleksić et al., 2012]. Recently, the *Fermi*-LAT Gamma-ray Space Telescope greatly improved the sensitivity of observations at MeV/Gev energies and reported for a large sample of clusters gamma-ray upper limits of $E_{CRp}/E_{ICM} < 1\%$ [Ackermann et al., 2010]. These non-detections constrain the possible energy density in CRp and, therefore, the density of relativistic electrons that may be produced from these [Vazza et al., 2014].

The direct γ-ray observations of the Coma cluster clearly tell us that the radio halo in Coma can not be of hadronic origin. Furthermore, the existence of ultra-steep-spectrum radio halos also disfavor the hadronic model. Re-acceleration models would instead explain the existence of ultra-steep-spectrum radio halos, and the connection between halos and major mergers. The primary model however involves several poorly constrained parameters, such as the magnetic field intensity, the fraction of turbulent energy, the fraction of energy converted into magneto-sonic waves. In addition, open questions remain about the origin of seed electrons. Nevertheless, it allows to derive basic and unavoidable predictions on the statistical properties of radio halos that can be investigated with observational studies. Hence, although no direct observation of turbulence in connection with halos, in-situ electron re-acceleration is the most accredited model that theoretically explains the origin of giant radio halos.

In the case of mini halos, the γ-ray limit derived on the Perseus cluster do not allow to exclude the contribution of secondary process. Hence, the hadronic process could also provide a contribute, especially in the cool cores, where the rate of hadronic interactions should be the highest. Alternatively, it has been proposed that mini halos trace gas-sloshing turbulence induced by minor mergers. In this scenario, the seed electrons are likely provided by the AGN residing in the cluster core.

A correlation between mergers and radio halos was first found by Buote [2001], analyzing the dynamical state of clusters with radio halos. Venturi et al. [2008] extended the analysis thought a 610 MHz GMRT radio halo survey of clusters with masses $> 1.4 \times 10^{15}$ $M_{\odot}$, discovering a clear separation between relaxed and disturbed clusters, with radio halos in the disturbed region and clusters without diffuse emission in the relaxed one. For mini halos, Giacintucci et al. [2017] found a clear connection between mini halos and cool-core clusters. However, in the past years few outliers have been found. A giant radio halo was discovered in the cool-core cluster CL1821+643 [Bonafede et al., 2014]. A minor or early-stage merger that has not disrupt the cool core, was proposed as mechanism responsible for the formation of the Mpc-scale emission. However, Boschin & Girardi [2018] have recently carried out optical studies where no evidence of a merging process was found in the cluster CL1821+643. This radio halo raises many questions about our understanding of diffuse radio sources in clusters, and remain an open problem. Another interesting case is that of A2142 with a giant halo and flatter radio emission similar to a mini halo at the cluster center. The outer component might be of turbulent origin, while the inner component might be related to gas sloshing, both induced by a minor merger. Overall, it is not yet understood whether transition objects exist in clusters, such as sources formed by both hadronic and re-acceleration processes. Another interesting scenario is the possibility of giant halos evolving into mini halos or vice-versa.

1.2.5 Spectral studies

Since the spectrum of a synchrotron-emitting source is a power law of the frequency (see *Appendix*), the radio spectral index can be determined by measuring the surface brightness (S_1, S_2) at two arbitrary frequencies (ν_1, ν_2), via:

$$\alpha = \frac{\log(S_1/S_2)}{\log(\nu_1/\nu_2)}, \tag{1.12}$$

and a spectral index map can be obtained for an entire source, as shown in Fig. 1.9. This map is a powerful tool to study the source age and evolution, and the properties of the relativistic electrons. In general, regions of flat spectrum ($\alpha \sim -0.5$) indicate more energetic radiating particles, and/or a larger value of the local magnetic field strength, and they are usually associated to young particle populations. Regions with a spectrum flatter than -0.5 are nearly always very compact, such as AGN cores. Regions with a steep spectrum ($\alpha < -1$) are typically associated with (i) aged plasma, such as old lobes in a dying radio galaxy, or (ii) an inefficient particle acceleration mechanism that that generates an electron population with a steep energy distribution, such as turbulent re-acceleration. Steep-spectrum sources can be better studied at low frequencies.

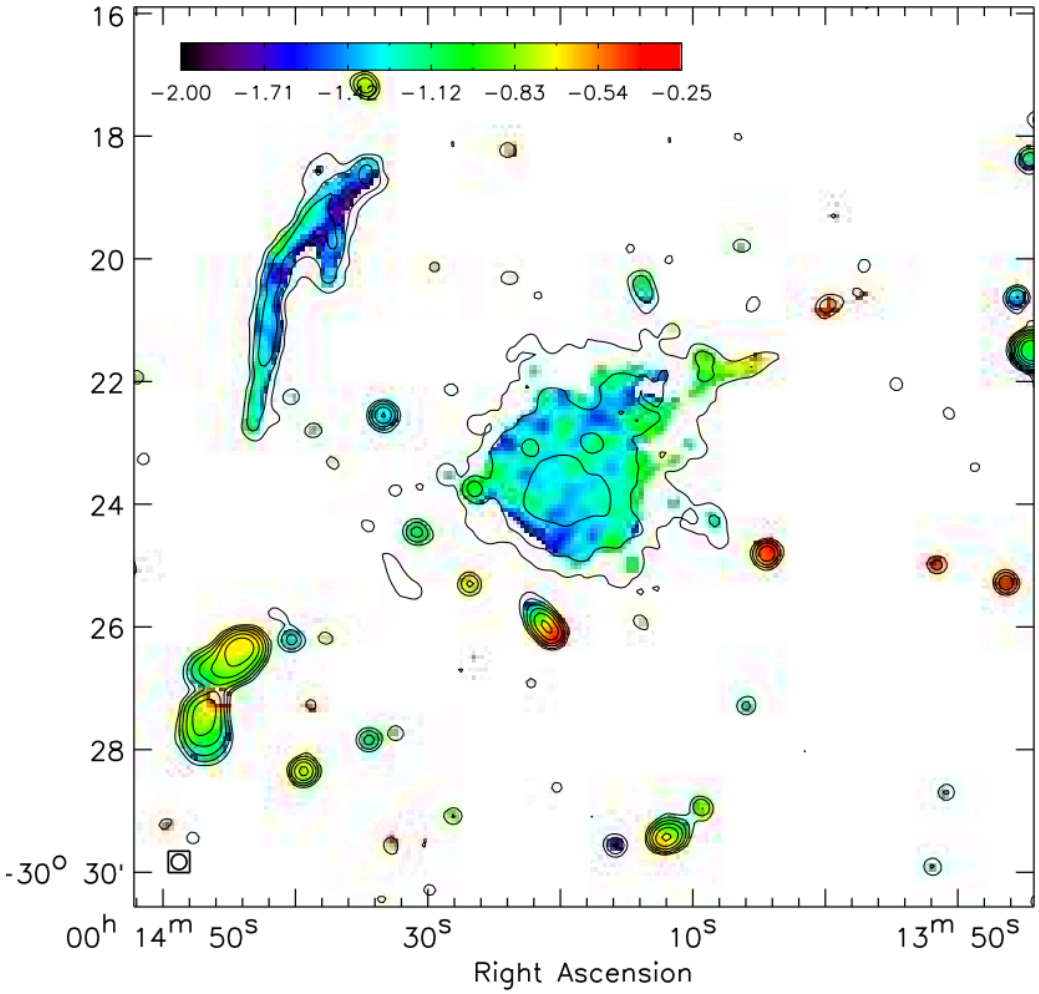

Figure 1.9: Spectral index map of the cluster A2744 (shown in Fig. 1.7) between 1.5 and 3.0 GHz, tapered to a resolution of $15'' \times 15''$. Contour levels are obtained from the 1.5 GHz image [Pearce et al., 2017].

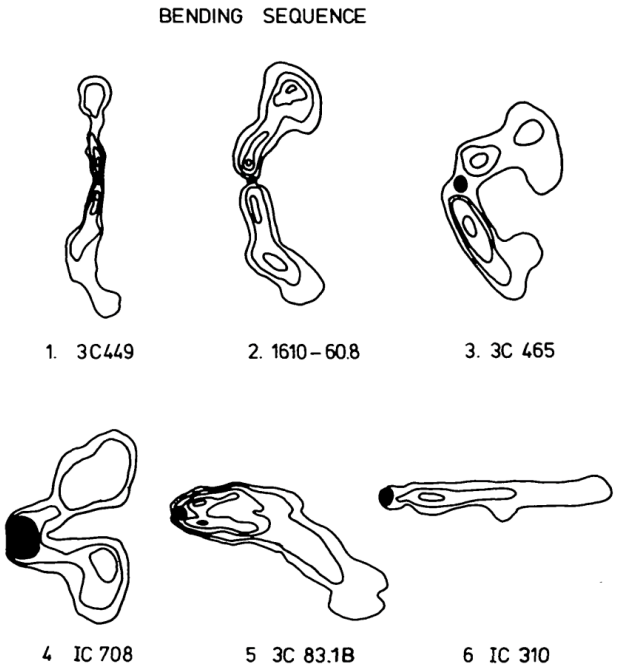

Figure 1.10: Bending sequence of radio galaxies from [Miley, 1980].

Performing the spectral analysis of a source is not straightforward. When using radio observations carried out with different instruments, one must take into account the differences in *uv*-coverage[8], sensitivity, resolution, and absolute flux calibration. Only images with the same resolution, same pixel size, and same baseline range can be compared.

1.2.6 Cluster radio galaxies

A general difference in the emission of an isolated (field) or a cluster radio galaxy has been first observed by De Young [1972]. A field radio galaxy emits without being influenced by the surrounding environment, while the emission of a cluster radio galaxy is strongly disturbed by the interaction of the lobes with the ICM and with other cluster galaxies. As a result of the cluster gravitational potential, the galaxies move through the ICM at a high velocity v, and the radio lobes experience a ram pressure $P_{\rm ram} = \rho_{\rm g} v^2$, where $\rho_{\rm g}$ is the intracluster gas density. This pressure decelerates the galaxies, and has a significant impact on their morphology and evolution. Hence, the lobes of cluster radio galaxies can be bent with a wide angle (wide-angle-tails; WAT), or with a small angle (narrow-angle-tail; NAT) up to the scenario where both lobes lie in one single tail on one side of the galaxy (head-tail; HT), as shown in the sequence in Fig. 1.10. Radio galaxies throughout

[8]During imaging, visibilities can be weighted in different ways, to alter the instrument's natural response function according to the imaging goals. A uniform weighting scheme is typically used to minimize the differences in the *uv*-coverage of two interferometers. See Sec. 1.3 for details on the *uv*-plane and imaging procedures.

the cluster volume can provide seed particles for the formation of halos, and an additional non-thermal pressure in the ICM.

1.3 A short primer on radio interferometry

The great advantage that interferometry offers to radio astronomy is the large improvement of resolution, obtained by synthesizing an equivalent aperture through the summations of separated pairs of antennas. The fundamental parameter is the distance between two antennas, the so-called baseline $\vec{b}$, which defines the direction and separation between two antennas. In an interferometer array of N antennas, the total number of baselines is $N \cdot (N-1)/2$ and the image resolution is related to the maximum baseline $b_{\rm max}$:

$$\theta(\rm rad) \sim \frac{\lambda}{\rm b_{max}}, \tag{1.13}$$

where λ is the observing wavelength. For instance, observing at the 1.5 GHz with the Effelsberg radio dish that has a diameter of 100 m would result in a resolution of $\sim 7'$, while with the VLA that has 27 antennas that can reach a maximum baseline of 36.4 km a resolution of $1''$.

Each pair of antennas, hence each baseline $\vec{b}$, measures the spatial coherence function, or visibility $V_\nu(\vec{b})$, of a source in the sky in the direction $\vec{s}$. The visibility is a Fourier component of the sky brightness[9] $I_\nu(\vec{s})$:

$$V_\nu(\vec{b}) = \int\int I_\nu(\vec{s})\, e^{\frac{-2\pi i\nu}{c}\vec{b}\cdot\vec{s}} d\Omega, \tag{1.14}$$

where $d\Omega$ is the source element. The baseline $\vec{b}$ is usually expressed as $(\lambda u, \lambda v, \lambda w)$ where (u, v, w) is the coordinate system show in Fig. 3.5, so the eq. 1.14 can be rewritten as:

$$V_\nu(u,v,w) = \int\int I_\nu(l,m)\, e^{-2\pi i[ul+vm+w(\sqrt{1-l^2-m2}-1)]} \frac{dl\, dm}{\sqrt{1-\, l^2-\, m2}}. \tag{1.15}$$

For more details on radio synthesis, we refer the reader to Taylor et al. [1999]. The general problem is to recover the sky brightness $I(l, m)$ from an ensemble of measurements of the visibility function $V(u, v, w)$. For one-dimensional (coplanar) interferometer arrays, this equation can be reduced to the form of a two-dimensional Fourier transform assuming that the w-axis is in the direction of the celestial pole, so that $w = 0$. However, for two-dimensional arrays, such as the VLA and LOFAR, this assumption can not be applied, and a more general inversion technique must be developed in order to account for non-coplanar baselines and large fields of view. Two methods, namely w-projection and w-stacking, are typically used to correct the additional phase shift in the Fourier space or in the image space, respectively.

[9] The sky brightness is defined as energy per unit time, area, frequency, and solid angle.

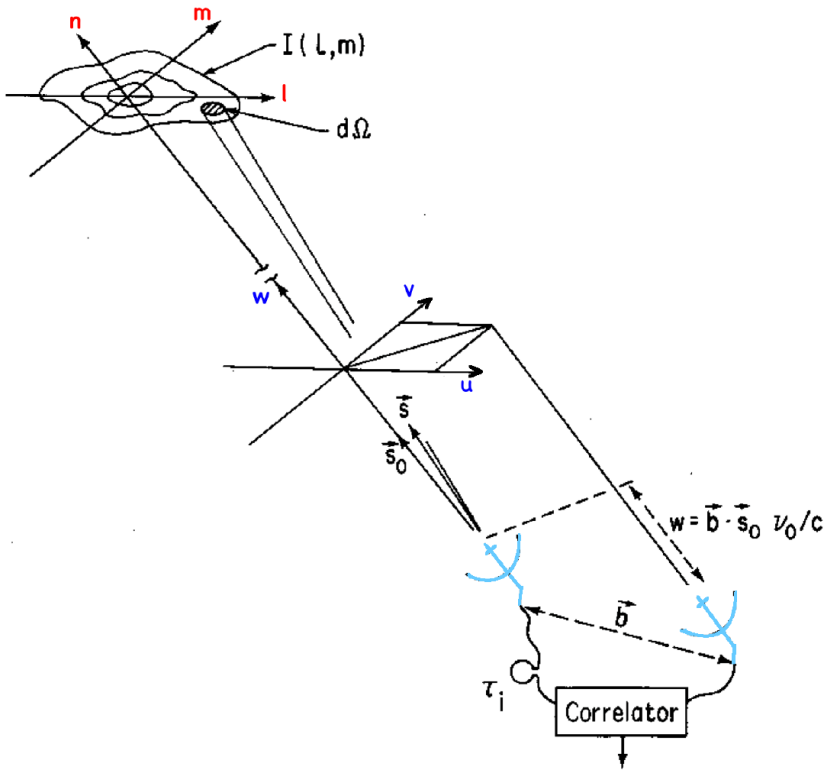

Figure 1.11: The (u, v, w) coordinate system of the Fourier plane and the (l, m, n) coordinate system on the plane of the sky [Taylor et al., 1999]. A pair of antennas, separated by the baseline $\vec{b}$, is pointing in the direction $\vec{s}$ toward a source of brightness $I(l, m)$.

The spatial sampling of the brightness distribution of a source is referred to as uv-coverage. The larger the number of baselines, the more spatial information on a variety of scales is collected. In practice, visibilities are complex numbers that contain information on both amplitude and phase of a signal. A real array only samples the visibility function at discrete locations in the uv-plane. Hence, the initial image of the sky, also called dirty image I^D, is the result of a inverse Fourier transform of the sampled visibility:

$$I^D = F^{-1}\{S(u,v) * V(u,v)\} = F^{-1}\{S(u,v)\} * F^{-1}\{V(u,v)\} = I * B, \tag{1.16}$$

where $S(u, v)$ is the sampling function, whose inverse Fourier function gives the dirty beam B. Basically, the dirty image is the convolution of the true image with a dirty beam, as shown in Fig. 1.12. Deconvolution algorithms have been developed to counteract the sparse sampling of an observation, and obtain high-quality images that estimate the true sky brightness. The most widely used deconvolution method is the CLEAN algorithm [Hoegbom, 1974], which performs many iterations of a process where the brightest pixel of the image is found and a certain amount (usually 10%) of its flux is convolved with

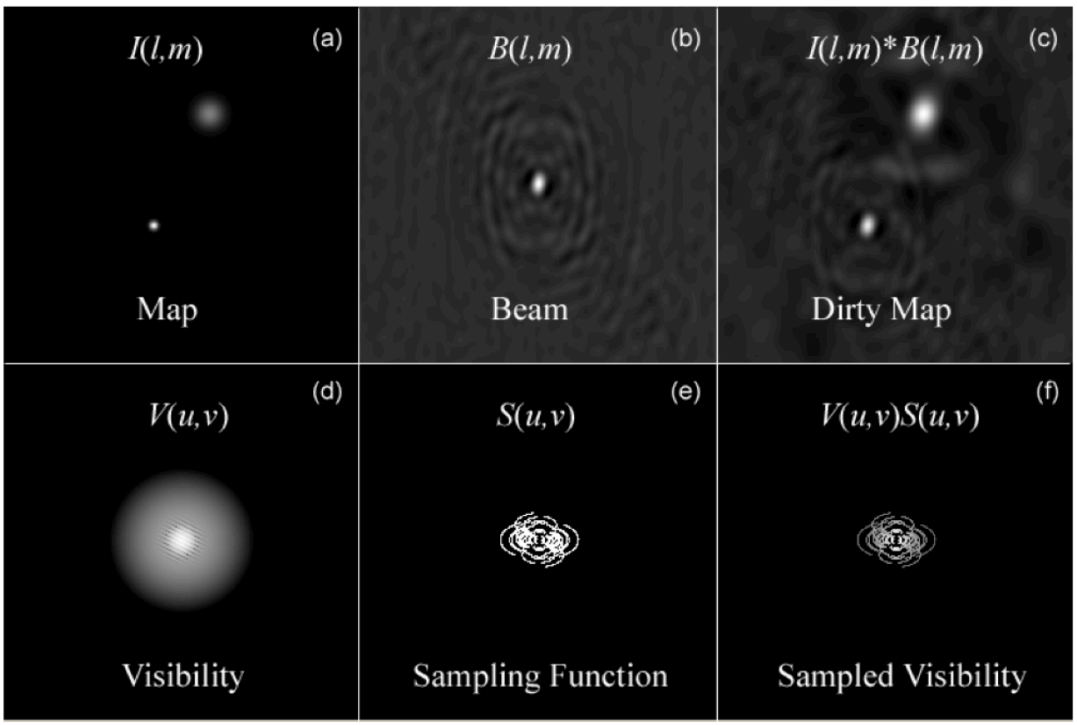

Figure 1.12: The images in the upper row are related to the sky plane: (a) a model map; (b) the synthesized beam, or point-spread-function, of an antenna array; (c) the convolution between (a) and (b) that is the actual image made by an array. The images in the lower row are the corresponding *uv*-plane representations: (d) the visibilities of the map in (a); (e) the sampling function of the array; (f) the convolution between (d) and (e) that is the actual measurement made by an array. The image reconstruction techniques try to predict the visibilities missing in (d), to arrive at the true map in (a). Credit: Radio astronomy lectures, Prof. D. E. Gary's website.

the dirty beam and subtracted from the image. Different softwares that implement the CLEAN process (with the w-stacking algorithm, as in WSClean [Offringa et al., 2014], or the w-projection algorithm, as in CASA [McMullin et al., 2007]) can be used. For extended sources, the performance can be improved by adopting a multi-scale approach that considers simultaneously components of emission having different size scales [Cornwell, 2008]. A multi-frequency synthesis is also adopted in case of wide-band observations, so that visibility data can be used to form a continuum image over a large range of frequencies.

1.3.1 The Low Frequency Array

The LOw Frequency ARray (LOFAR) is a radio interferometer designed with the aim of imaging the radio sky with large fields of view and high sensitivity at frequencies $<$ 170 MHz. LOFAR consists of a number of simple dipole receivers that take advantage of the aperture synthesis technique and multi-beaming capabilities [Harwood et al., 2013].

Figure 1.13: Top panel: aerial photograph of the Superterp: the circular island encompasses 6 core stations (CS). Additional CS are visible in the upper right and lower left of the image. Each of them includes 96 LBA and 2 sub-stations of 24 HBA tiles each. Bottom left panel: a single LBA dipole including the ground plane. The inset images show the electronics in the cap and the wire attachment points. Bottom right panel: a single HBA tile, showing underneath the protective covering where the dipoles are located. Credit: images adapted from van Haarlem et al. [2013a].

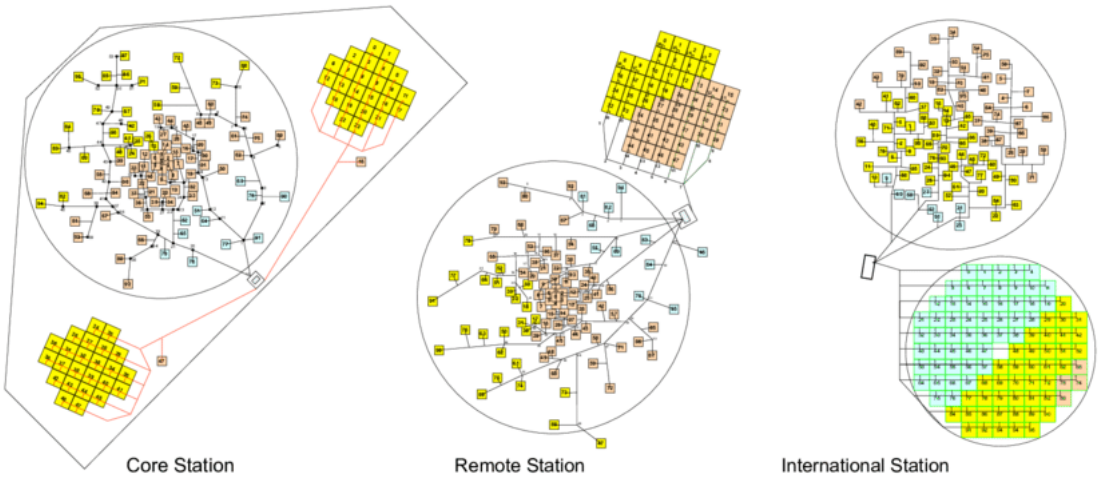

Figure 1.14: The layout of the different LOFAR stations: CS, RS, and IS. The large circles represent the LBA, while the arrays of small squares indicate the HBA tiles. Note that the station layouts are not shown on the same spatial scale [van Haarlem et al., 2013a].

The dipoles are grouped in stations, and the signals from each station are sent through a high-speed-fibers network to a processing facility in Gröningen in the Netherlands, where the data are correlated. Two frequency bands can be observed with LOFAR using dipole antennas with different designs (bottom images in Fig. 1.13): 15 - 80 MHz with the Low Band Antennas (LBA) and 110 - 240 MHz with the High Band Antennas (HBA). The LBA cover a circular area of $\sim$ 90 m across, while the HBA are arranged in tiles. The station beams have a Full Width Half Maximum (FWHM) of $\sim 8^\circ$ and $\sim 5^\circ$ for LBA and HBA, respectively. The LOFAR core, the so-called Superterp, is in the Netherlands, and consists of 6 stations within a 300-m diameter, and additional stations further out, for a total of 24 core stations (CS) within a 2-km diameter. Other 14 stations are located to larger distances, the so-called remote stations (RS), and have a different configuration. Outside of the Netherlands, international stations (IS) in several European countries (UK, Germany, France, Sweden, Poland) have been built to reach even better resolutions, emulating a small VLBI network. CS, RS, and IS, shown in Fig. 1.14, can reach baselines 150 m - 3 km, 5 km - 100 km, 300 km - 1000 km, respectively. In this thesis, I made use of the Dutch part of the array (CS and RS) only.

Classical radio dishes can be moved to point in the desired direction in the sky. LOFAR antennas instead are steered electronically, and multiple directions can be observed at the same time. This is obtained through the so-called digital beam forming. Hence, LOFAR is a really versatile instrument, and can be used to study different science cases, such as the formation and evolution of galaxies, AGN, clusters, and pulsars. Moreover, it is one of the precursor for the Square Kilometre Array (SKA) telescope, which is under construction in Australia and South Africa.

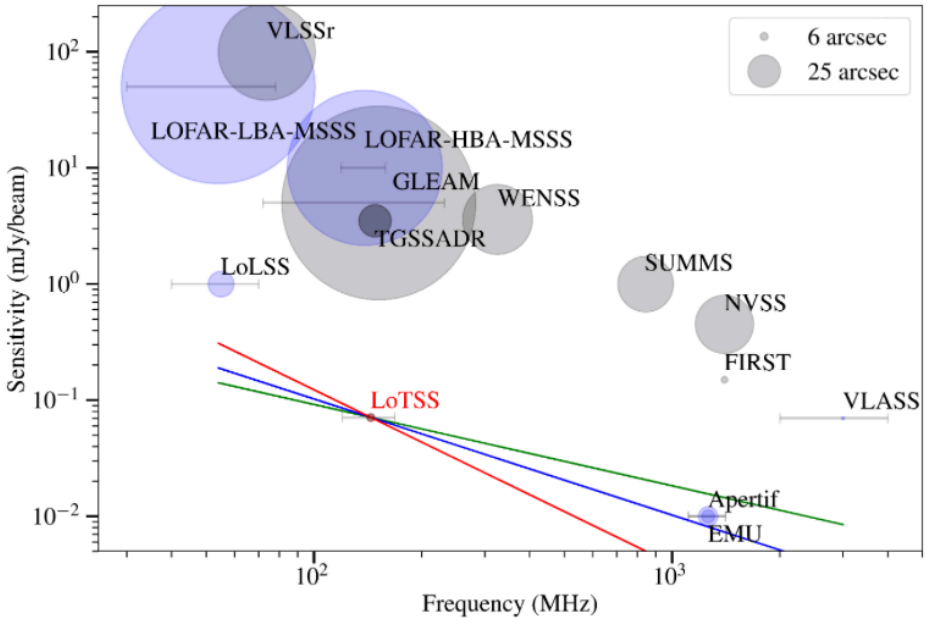

Figure 1.15: Sensitivity (image rms) vs. frequency. The angular resolution is shown with circles of linearly-proportional radii. A selection of completed (grey) and upcoming (blue) radio surveys is shown for comparison with LoTSS. The horizontal lines show the frequency coverage for surveys with large fractional bandwidths. The green, blue, and red lines show an equivalent sensitivity to LoTSS for compact radio sources with spectral indices of -0.7, -1.0, and -1.5, respectively [Shimwell et al., 2017].

1.3.2 Surveys

Low-frequency surveys allow radio astronomers to observe a vast area of the poorly-explored MHz sky improving our knowledge of the properties, occurrence, and statistics of radio sources. Thanks to its large primary beam, LOFAR can look at large area of the sky at once, which makes it an excellent telescope for surveys. Thus, deep radio images of the low-frequency sky can be obtained in a very efficient way. In particular, the ongoing LOFAR Surveys Key Science Project is conducting the LOFAR Two-metre Sky Survey (LoTSS; [Shimwell et al., 2017]) with the aim of observing the entire northern hemisphere in the range 120-168 MHz. This survey is deeper than the first, the Multifrequency Snapshot Sky Survey (MSSS; [Heald et al., 2015]), reaching sensitivities that are two orders of magnitude smaller. In general, LoTSS achieves better results than any survey carried out with different telescopes in the low-frequency regime, as shown in Fig. 1.15. The entire northern sky will be covered with 3168 pointings, and each observation lasts 8 hrs, bookended by 10-min calibrator observations (primarily 3C196 and 3C295), for a total of $\sim$ 13000 hrs of observing time. As of May 2018, $\sim$ 20% of the data have now been gathered, and the first full-quality public data release (LoTSS-DR1) has been published [Shimwell et al., 2018]. LoTSS-DR1 covers 424 square degrees (2% of the total coverage) with a resolution of $6''$, and has detected a total of 325,694 sources. Among the many

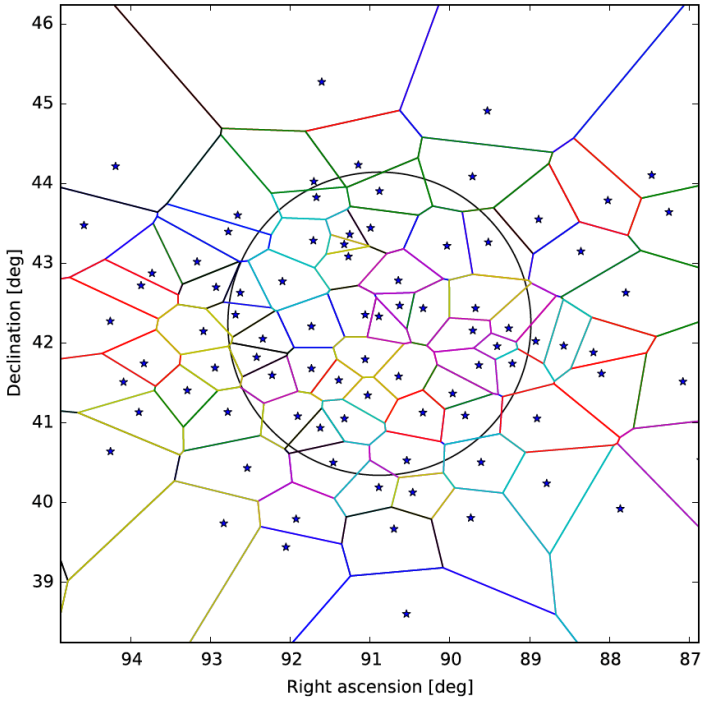

Figure 1.16: An example of Voronoi tessellation used for a LOFAR field [van Weeren et al., 2016a]. The black circle indicates the Half Power Beamwidth (HPBW) of the station beam at 150 MHz. Stars indicate the bright sources or groups that are used as facet calibrators.

goals of the survey, the most relevant for this thesis are: increasing the samples of AGN, including giant, dying and relic sources, up to the highest redshifts, which permits statistical studies of the evolution of the properties of different classes of AGN over cosmic time, and the sensitive images of the steep-spectrum radio sources from galaxy clusters that help investigating magnetic fields and particle acceleration mechanisms.

1.3.3 Data calibration

Data calibration at low radio frequencies has always been considered a challenge, due to the ionosphere that affects the quality of the observations. The ionosphere is a magneto-active plasma in the region between 60 km and 200 km above the Earth's surface. This medium is partially ionized mostly by the solar radiation, and the amount of free electrons varies in space and time[10]. Radio waves are refracted by the ionosphere with a refraction index that varies on small scales. Hence, a time- and space-dependent correction is required, since phase solutions in one direction in the sky cannot be applied to another. Another problematic aspect of the low-frequency data reduction is wide-field imaging. In the last years, many efforts have been made to obtain low-noise high-quality wide-field images for instruments that observe below 1 GHz. To correct for the beam effects, cal-

[10]In detail, the amount of phase change caused by the ionosphere is related to the amount of the electron column density along a line of sight, known as total electron content (TEC).

ibrate the observations, and image the full bandwidth over a large field of view, new advanced processing techniques are required. In addition to the phase distortion effects, which become more important at low frequencies, one has to account for the curvature of the celestial coordinate system. A 3D inversion from the *uvw*-plane to the image plane must be performed while deconvolving, taking into account the variable station beams.

In this Section, I will outline the calibration scheme that was developed specifically for LOFAR HBA datasets, and that I used to reduce all the observations presented in this thesis. The calibration consists of a non-directional part (Pre-Facet Calibration, done through the Prefactor pipeline) and a directional part (Facet Calibration, done through the Factor pipeline [van Weeren et al., 2016a]).

The first step of the Pre-Facet Calibration is removing any possible radio frequency interference (RFI) and off-axis sources[11]. A flux calibrator, i.e. a bright and well-known source with a constant flux, is needed as a reference to measure amplitude and phase gains. A clock offset is present between the RS and the CS, since the RS have their own clocks that are not perfectly synchronized with the single clock that is used for all the CS. This cause a phase delay in the RS that needs to be considered when transferring the calibrator solutions to the target data. The clock offsets, the amplitude gains, and the instrumental phase offsets between stations are transferred to the target data. The resulting target field is then free of clock delays and the amplitudes are in units of Janskys (Jy)[12]. An initial phase calibration on the target data is also performed.

High-resolution and low-resolution direction-independent-calibrated images are obtained through a step called Initial Subtraction. First, the high-resolution compact sources are masked and imaged. Their clean components are then subtracted from the *uv*-data and listed into a sky model. Low-surface brightness emission that was not visible in the high-resolution images can now be detected, masked, and imaged. The low-resolution components are also subtracted from the *uv*-data and then added to the sky model. The resulting sky models and the empty datasets are the required inputs for the Factor pipeline.

The Facet Calibration is based on dividing the sky into a discrete number of directions (facets) covering the observed field of view and calibrating each of these directions separately, assuming that the solutions computed for each facet calibrator apply to the facet as a whole. The aim is to reduce the direction-dependent effects (DDE) to obtain near-thermal-noise-limited images using the full resolution offered by LOFAR. A single (group of) bright compact source(s) is selected for each facet, and then the field of view is divided using a Voronoi tessellation scheme (e.g. [Okabe, 2000]), as shown in Fig. 1.16, where each point on the sky is assigned to the closest calibrator source. After performing self-calibration cycles on a calibrator (see an example in Fig. 1.17), all the fainter sources

[11]The low-frequency radio sky is dominated by a few bright sources that form the so called A-team: the supernova remnants Cassiopeia A and Taurus A (also known as Crab Nebula), and the radio galaxies Cygnus A, Virgo A, Hydra A, and Hercules A. The removal of these sources from the target visibilities is crucial to obtain high-dynamic range images.

[12]A Jansky is the unit of spectral flux density: 1 Jy = 10^{26} W Hz^{-1} m^{-2}.

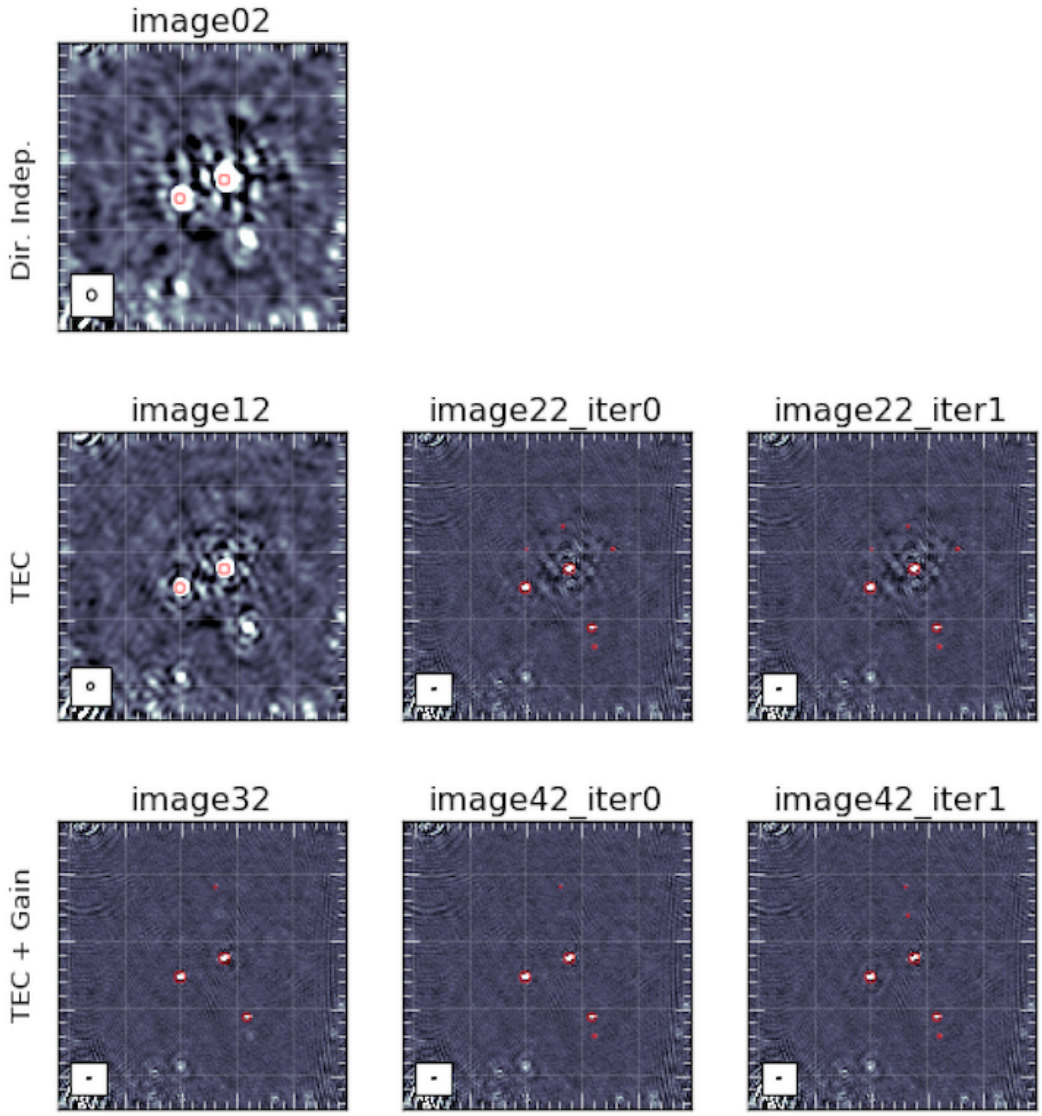

Figure 1.17: An example of self-calibration cycles from one of the LOFAR datasets presented in the paper "A LOFAR study of massive non-merging clusters" [Savini et al., 2018a]. The process starts with "image02" that is the image obtained after applying only the direction-independent solutions from Prefactor, and proceeds to "image12", "image22", and so on. In some cases, Factor will iterate a step until no more improvement is seen. These steps are indicated by the "iter" suffix.

in that facet are added back and calibrated using the calculated solutions. An updated sky model for the region of the sky covering the facet is obtained and then subtracted from the *uv*-data, and the whole process is repeated to obtain a direction-dependent-calibrated image for each facet. A mosaic image of the whole field is obtained by stitching together all the facets' images and correcting for the primary beam.

All the LOFAR images presented in the following Chapters have been reduced following the Facet Calibration scheme. This allowed me to obtain low-noise high-quality images of galaxy clusters in the low-frequency band 120 - 168 MHz.

Chapter 2

A LOFAR study of non-merging massive clusters

Federica Savini, Annalisa Bonafede, Marcus Brüggen, David Rafferty, Timothy Shimwell, Andrea Botteon, Gianfranco Brunetti, Huib Intema, Amanda Wilber, Rossella Cassano, Franco Vazza, Reinout van Weeren, Virginia Cuciti, Francesco de Gasperin, Huub Röttgering, Martin Sommer, Laura Bîrzan, Alexander Drabent

A & A, accepted on 2018, September 18

Abstract

Centrally located diffuse radio emission has been observed in both merging and non-merging galaxy clusters. Depending on their morphology and size, we distinguish between giant radio halos, which occur predominantly in merging clusters, and mini halos, which are found in non-merging, cool-core clusters. In recent years, cluster-scale radio emission has also been observed in clusters with no sign of major mergers, showing that our knowledge of the mechanisms that lead to particle acceleration in the intra-cluster medium (ICM) is still incomplete. Low-frequency sensitive observations are required to assess whether the emission discovered in these few cases is common in galaxy clusters or not. With this aim, we carried out a campaign of observations with the LOw Frequency ARay (LOFAR) in the frequency range 120 - 168 MHz of nine massive clusters selected from the *Planck* SZ catalogue, which had no sign of major mergers. In this paper, we discuss the results of the observations that have led to the largest cluster sample studied within the LOFAR Two-metre Sky Survey, and we present *Chandra* X-ray data used to investigate the dynamical state of the clusters, verifying that the clusters are currently not undergoing major mergers, and to search for traces of minor or off-axis mergers. We discover large-scale steep-spectrum emission around mini halos in the cool-core clusters PSZ1G139.61+24 and RXJ1720.1+2638, which is not observed around the mini halo in the non-cool-core cluster A1413. We also discover a new 570 kpc-halo in the non-cool-core cluster RXCJ0142.0+2131. We derived new upper limits to the radio power for clusters in which no diffuse radio emission was found, and we discuss the implication of our results

to constrain the cosmic ray energy budget in the ICM. We conclude that radio emission in non-merging massive clusters is not common at the sensitivity level reached by our observations and that no clear connection with the cluster dynamical state is observed. Our results might indicate that the sloshing of a dense cool core could trigger particle acceleration on larger scales and generate steep-spectrum radio emission.

2.1 Introduction

Diffuse radio emission in galaxy clusters is caused by relativistic electrons that emit synchrotron radiation in the intra-cluster magnetic field (see Feretti et al. [2012] and references therein). This emission has a low surface brightness ($\sim$ 0.1 - 1 μJy arcsec^{-2} at $\nu \sim 1.4$ GHz) and, depending on its morphology, location, and size (hundreds of kpc up to few Mpc), it is classified as radio relic, radio halo, or mini halo. In this paper, we are only concerned with radio halos and mini halos, which are sources that are located at the centres of galaxy clusters. Both type of sources are commonly characterised by a steep radio spectrum with a spectral index of [1] $\alpha < -1$.

Giant radio halos ($\sim$ Mpc-scale) have predominantly been found in merging clusters (e.g. [Buote, 2001], [Cassano et al., 2010], [Cuciti et al., 2015]) that typically do not have a cool core, i.e. a core characterised by a peaked X-ray surface brightness, high gas density, and significant drop in temperature within the inner $\sim$ 100 kpc. halos indicate the presence of a cluster-wide particle acceleration mechanism, such as in situ re-acceleration (see Brunetti & Jones [2014] for a review).

Mini halos ($<$ 500 kpc-scale) are detected in cool-core clusters that have not been disrupted or disturbed by major mergers. Often, the brightest cluster galaxy (BCG) resides at the centre of the mini halo and, when the BCG is radio loud, its radio lobes are embedded in the mini halo. The origin of the relativistic cosmic ray electrons (CRe) of mini halos is still unclear. The main contending theories are either leptonic (re-acceleration) models and hadronic models. Leptonic models involve the re-acceleration of a lower energy population of CRe by turbulent motions in the intra-cluster medium (ICM; [Gitti et al., 2002]). The turbulence can be caused by the sloshing of the low-entropy gas falling inside the Dark Matter potential well of the cluster. The sloshing can be instigated, for example, by a minor merger with a lower mass galaxy cluster or group. When the gas meets the higher entropy ICM, a cold front, i.e. a discontinuity in the X-ray emissivity, is formed [ZuHone et al., 2013]. Hadronic models involve the injection of secondary electrons produced continuously by inelastic collisions of relativistic cosmic ray protons (CRp) with the cluster thermal proton population [Pfrommer & Enßlin, 2004]. The CRp are expected to be present in the ICM, therefore some level of synchrotron emission from secondary electrons is expected in galaxy clusters, especially in non-merging clusters with a dense cool core, where the rate of hadronic interactions should be the highest.

Recent observations with the Giant Metrewave Radio Telescope (GMRT) and the Very

[1] The spectrum is defined by $S(\nu) \propto \nu^{\alpha}$.

Table 2.1: Observation details of the targets. The letter P indicates the clusters observed as part of dedicated proposals.

Name	RA (h m s, J2000)	DEC (° ′ ″, J2000)	LoTSS obs. ID	LoTSS obs. date	Radio flux calibrator	*Chandra* obs. ID	*Chandra* clean exp. time (ks)
RXCJ0142.0+2131	01 42 02.6	+21 31 19.0	LC9_011 (P)	21-02-18	3C196	10440	19.9
A478	04 13 20.7	+10 28 35.0	LC8_006 (P)	7/21-11-17	3C196	1669, 602, 6928 6929, 7217, 7128 7222, 7231, 7232 7233, 7234, 7235	139.3
PSZ1G139.61+24	06 22 04.6	+74 40 51.6	LC8_022	27-07-17	3C295	15139, 15297	23.1
A1413	11 55 18.9	+23 24 31.0	LC9_020 (P)	25-01-18	3C295	537, 1661, 5002 5003, 7696	127.8
A1423	11 57 22.5	+33 39 18.0	LC8_022	21-09-17	3C196	528, 11724	33.3
A1576	12 37 59.0	+63 11 26.0	LT5_007	04-04-16	3C196	7938, 15127	28.5
RXJ1720.1+2638	17 20 10.1	+26 37 29.5	LC7_004 (P)	25-01-17	3C295	1453, 3224, 4361	42.3
A2261	17 22 27.1	+32 08 02.0	LC6_015	27-07-17	3C295	550, 5007	30.6
A2390	21 53 34.6	+17 40 11.0	LC9_030	18-12-17	3C196	500, 501, 4193	99.1

Table 2.2: Properties and literature information of the selected sample of non-merging massive clusters. Col. 1: Name of the cluster; Col. 2: redshift; Col. 3: angular to physical scale conversion at the cluster redshift; Col. 4: mass within the radius enclosing a mean density of 500 times the critical density [Planck Collaboration et al., 2014]; Col. 5: core entropy from X-ray data [Giacintucci et al., 2017]; Col. 6: presence of a cool core (CC) from X-ray data [Giacintucci et al., 2017]; Col. 7: presence of radio diffuse emission as present in the literature (UL = upper limit; MH = mini halo; cMH = candidate mini halo; H = halo); Col. 8: observations present in the literature; Col. 9: radio references: (1)[Kale et al., 2013]; (2)[Giacintucci et al., 2014a]; (3)[Giacintucci et al., 2017]; (4)[Govoni et al., 2009] (5)[Venturi et al., 2008]; (6)[Giacintucci et al., 2014b]; (7)[Sommer et al., 2017].

Name	z	Scale (kpc/″)	M_{500} (10^{14} $M_\odot$)	K_0 (keV cm^2)	X-ray	Radio	Telescope & frequency	Ref.
RXCJ0142.0+2131	0.280	4.28	6.07	131	nCC	UL	GMRT: 235/610 MHz	1
A478	0.088	1.66	7.06	8	CC	MH	VLA: 1.4 GHz	2
PSZ1G139.61+24	0.270	4.17	7.09	10	CC	cMH	GMRT: 610 MHz	3
A1413	0.143	2.53	5.98	64	nCC	cMH	VLA: 1.4 GHz	4
A1423	0.214	3.50	6.09	27	CC	UL	GMRT: 610 MHz	5
A1576	0.302	4.51	5.98	186	nCC	UL	GMRT: 610 MHz	1
RXJ1720.1+2638	0.164	2.84	6.34	21	CC	MH	GMRT: 317/617 MHz, 1.28 GHz	6
							VLA: 1.5, 4.9, 8.4 GHz	6
A2261	0.224	3.63	7.39	61	nCC	H	VLA: 1.4 GHz	7
A2390	0.234	3.75	9.48	15	CC	H	VLA: 1.4 GHz	7

Large Array (VLA) have revealed the presence of radio halos in a few clusters that are not undergoing major mergers, and that - in some cases - host a cool core (i.e. CL1821+643, [Bonafede et al., 2014]; A2261, A2390, [Sommer et al., 2017]; A2142, [Venturi et al., 2017]), challenging the notion that radio halos only form in major mergers. It has been proposed that these sources might be connected to the occurrence of minor/off-axis mergers, although it remains unclear how minor mergers could initiate continuum emission on megaparsec scales. Models (e.g. [Cassano et al., 2006]) predict that minor mergers can generate ultra-steep spectrum (USS) emission ($\alpha < -1.5$) due to the smaller amount of energy available compared to major mergers. However, flatter spectrum sources such as that in CL1821+643, where $\alpha_{323}^{1665} \sim$ -1.1, are difficult to explain in this scenario. Finally, we note that signatures of minor-merging activities and gas-sloshing mechanisms have been detected in clusters containing mini halos (e.g. [Gitti et al., 2007], [Giacintucci et al., 2014b], [Savini et al., 2018b]). To assess whether the emission discovered in these few cases is common in galaxy clusters or not if looking at low radio frequencies, we selected and studied a sample of nine non-merging galaxy clusters. The observations were carried out with the LOw Frequency ARray (LOFAR; [van Haarlem et al., 2013b]) with the aim of studying large-scale radio emission to shed light on the non-thermal phenomena in galaxy clusters and the connection with cluster dynamics. Sensitive low-frequency observations allow us to detect steep-spectrum emission that cannot be observed at higher frequencies and are fundamental in the case of slightly disturbed clusters.

In case of the non-detection of large-scale diffuse sources, we provide new upper limits on the radio power of halos. These constraints demonstrate the importance of low-frequency observations to determine the cosmic ray pressure and energy budget in clusters.

In this paper, we assume a flat, ΛCDM cosmology with matter density $\Omega_M = 0.3$ and Hubble constant $H_0 = 67.8$ km s^{-1} Mpc^{-1} [Planck Collaboration et al., 2016]. All our images are in the J2000 coordinate system.

2.2 The sample

In order to investigate the presence of diffuse emission in non-merging systems at low radio frequencies, we selected a sample of galaxy clusters (listed in Tab. 4.3.1) on the basis of their cluster-scale X-ray morphology and lack of evidence of a recent major merger. Cuciti et al. [2015] and Cassano et al. [2016] studied a sample of clusters selected from the *Planck* Sunyaev Zel'dovich catalogue (PSZ; [Planck Collaboration et al., 2014]) with a mass of $M_{500} \geq 6 \times 10^{14}$ M$_\odot$ in the redshift range[2] $0.08 < z < 0.33$ and $0.2 < z < 0.33$, respectively. For this study, we selected the clusters whose dynamical status has been classified as non-merging from *Chandra* X-ray observations. In particular, we focus on two morphological indicators: the concentration parameter and centroid shift, which have been shown to be the most sensitive to the cluster dynamical state [Lovisari et al., 2017], We briefly describe these two parameters, as follows:

[2]The sample in Cuciti et al. [2015] consists of clusters with available radio and X-ray data. The sample in Cassano et al. [2016], although covering a smaller range in redshift, also includes clusters with available X-ray data but without radio observations. In total, a completeness in mass greater than 80% is achieved.

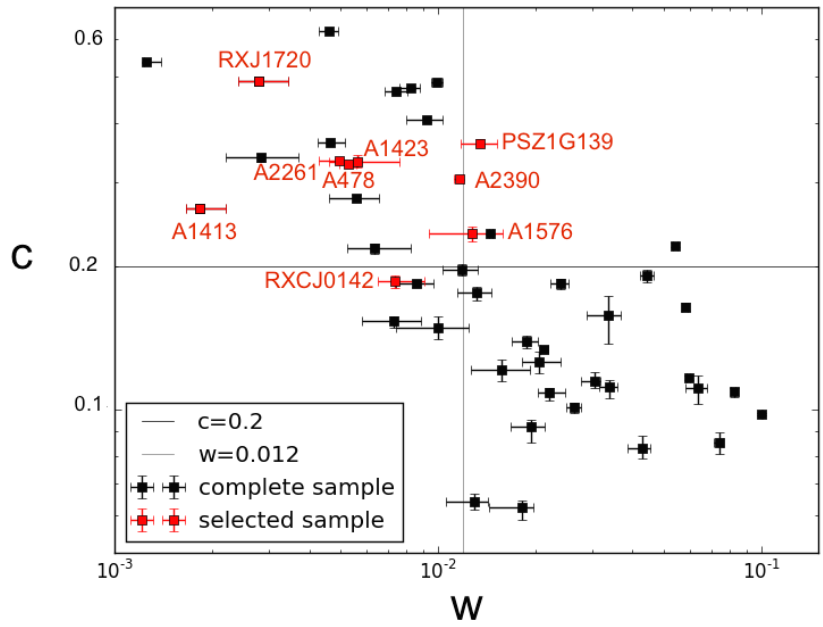

Figure 2.1: Diagram of the X-ray morphological indicators based on *Chandra* observations for the galaxy clusters, the emission centroid shift, w, and the concentration parameter, c, of the mass-selected cluster sample in Cuciti et al. [2015] and Cassano et al. [2016]. Red squares indicate the sources of our sample. Following Cassano et al. [2010], we adopted the values $w \leq 0.012$ and $c \geq 0.2$ as an indication of the distinction between merging/non-merging clusters. Merging clusters lie in the bottom right region of the plot, whilst non-merging clusters in the top left region.

- the concentration parameter, c, is defined as the ratio of the X-ray flux density within 100 kpc over the X-ray flux density within 500 kpc. It helps to select clusters with a compact core, i.e. clusters whose core has not been disrupted by a merger [Santos et al., 2008]

$$c = \frac{S(< 100\text{kpc})}{S(< 500\text{kpc})}; \tag{2.1}$$

- and the emission centroid shift, w, defined as the standard deviation of the projected separation Δ between the peak and the cluster X-ray centroid computed within N circles of increasing radius R (e.g. [Böhringer et al., 2010])

$$w = \frac{1}{R} \times \sqrt{\frac{\Sigma_{i=0}^{N}(\Delta_{\rm i} - \langle\Delta\rangle)^2}{N-1}}. \tag{2.2}$$

High values of w indicate a dynamically disturbed system, while high values of c indicate a peaked core that is typical of non-merging systems. We selected the clusters

labelled as "relaxed" in Cassano et al. [2016] and Cuciti et al. [2015]. In addition, we added the constraint that clusters must be easily observed with LOFAR, i.e. with declination greater than 10°. The selected clusters, which are shown as red symbols in Fig. 2.1 (together with the clusters belonging to the complete sample), lie in the top left region of the $c - w$ plot (non-merging clusters). We note that many of these clusters lie near the merging/non-merging boundary (defined with the values $w \sim 0.012$ and $c \sim 0.2$ in Cassano et al. [2010], where w is derived at 500 kpc.). These clusters are more likely to be slightly disturbed systems, thus through their observations we can search for low-frequency steep-spectrum emission powered by minor/off-axis mergers.

2.3 Data reduction

2.3.1 Radio: LOFAR observations

Five of the targets were observed as part of the deep imaging survey LoTSS (LOFAR Two-metre Sky Survey; [Shimwell et al., 2017]). The remaining four were observed as part of dedicated proposals (LC7_004, LC8_006, LC9_011, LC9_020), adopting the LoTSS observing set-up [3]. The observations were carried out at 120 - 168 MHz using the high band antenna (HBA) with a total on-source time of 8 h preceded and followed by a flux density calibrator observation for 10 minutes. More details can be found in Tab. 4.3.1. The calibration and imaging procedure is based on the Facet Calibration scheme presented in van Weeren et al. [2016a]. A complete outline of the procedure can be found in Savini et al. [2018c]. The main steps are as follows:

- Preliminary pre-processing, which was performed by the Radio Observatory (ASTRON) and has been applied to the data
- Direction-independent calibration, which was obtained by executing the Prefactor pipeline[4], following the strategy outlined in De Gasperin et al. (2018)
- Direction-dependent calibration using the FACTOR pipeline[5]

Each field of view was divided into a discrete number of facets that are separately calibrated. The calibrator for each facet was selected with a minimum flux density specified by the user in a range between 0.3 Jy and 0.6 Jy. The facets are usually processed in order of calibrator flux density, before processing those bordering the cluster facet. The cluster facet is the last to be processed, so that it could benefit from the calibration of the preceding facets. The facet images are stitched together to form a mosaic and the mosaicked final image is corrected for the primary beam. In line with other LOFAR HBA studies, we adopted a systematic calibration error of 15% on all the measured flux densities (e.g. [Shimwell et al., 2016], [van Weeren et al., 2016b], [Savini et al., 2018c]). Radio

[3] We note that the clusters observed for the proposals lie at the centre of the pointings and the clusters observed within LoTSS lie at a maximum distance from the phase centre of the pointing of 1°, where the primary beam response is > 0.8. This allows us to reach a consistent sensitivity to diffuse emission for the whole sample.

[4] https://github.com/lofar-astron/prefactor

[5] https://github.com/lofar-astron/factor

imaging was performed through the `WSClean` package [Offringa et al., 2014] implemented in FACTOR, varying the robust values of the Briggs weighting [Briggs, 1995] and uv-taper to obtain different resolutions and increase the sensitivity to diffuse emission. To obtain specific images, such as spectral index maps, compact-source-subtracted images, and halo-injected images, we used the Common Astronomy Software Applications (CASA, version 4.5.2; [McMullin et al., 2007]) with the multi-scale option of the `clean` task and took the w-projection parameter into account.

2.3.2 Radio: GMRT observation

We processed archival GMRT observations at 610 MHz of the clusters RXJ1720.1+2638 and A478 using the Source Peeling and Atmospheric Modeling (SPAM) pipeline (see Intema et al. [2017] for details) to perform a detailed spectral analysis with the LOFAR observations. A478 and RXJ1720.1+2638 were observed, respectively, on October 10, 2011 (under project code 21_017) and July 24, 2011 (under project code 11MOA01). Visibilities at 610 MHz were recorded in one polarisation (RR) over a bandwidth of 32 MHz, as part of a dual-frequency observation. The on-source time was 3.4 h for A478 and 5.2 h for RXJ1720.1+2638. The primary calibrator used for flux and bandpass calibrations in both observations was 3C 48. We adopted the same flux standard as for LOFAR [Scaife & Heald, 2012]. A $T_{\rm sys}$ gain correction of 0.963 for A478 and 0.981 for RXJ1720.1+2638 was derived using the all-sky map at 408 MHz by Haslam et al. [1995]; this $T_{\rm sys}$ gain correction was subsequently applied. The pipeline removed 56% of the data of A478 due to Radio Frequency Interferences (RFI) and various telescope issues and the pipline removed 48% for RXJ1720.1+2638. The pipeline output visibilities were imported into CASA for final imaging, using the multi-scale option of the `clean` task. Our highest fidelity images reach a sensitivity of $65\,\mu$Jy beam^{-1} with a $4.8'' \times 3.9''$ beam and $45\,\mu$Jy beam^{-1} with a $5.0'' \times 4.8''$ beam, for A478 and RXJ1720.1+2638 respectively. We adopted a 10% scale error on all flux density measurements [Chandra et al., 2004].

2.3.3 X-ray: *Chandra* observation

To investigate the connection between the thermal and non-thermal components in the ICM, we reprocessed *Chandra* X-ray observations for each cluster in the sample. The ID and clean exposure time of each observation can be found in Tab. 4.3.1. We carried out a standard data reduction using CIAO v4.9 and *Chandra* CALDB v4.7.3 to produce the exposure-corrected images in the $0.5-2.0$ keV band shown in the paper (see Botteon et al. [2017] for the procedure outline).

The *Chandra* X-ray density and temperature profiles of the clusters we selected were already obtained and combined by Giacintucci et al. [2017] to derive the specific entropy at the cluster centre, K_0. We used the values of K_0 for the clusters in our sample to distinguish between cool-core or non-cool-core clusters following Giacintucci et al. [2017]: clusters with low central entropies ($K_0 < 30-50$ keV cm^2) are expected to host a cool core. The values relevant for our sample are reported in Tab. 2.2, where we specify whether the clusters host a cool core or not, according to the above classification.

2.4 Results

In the following, each cluster is described in a separate subsection. The information from the literature is summarised in Tab. 2.2, while the LOFAR results are summarised in Tab. 2.3. In Fig. 2.2 - 2.12, we present the images obtained at low frequencies in our campaign of LOFAR observations: a high- and a low-resolution image at the central frequency of 144 MHz for each cluster and overlays with the X-ray images taken by *Chandra* and optical images taken within the Sloan Digital Sky Survey (SDSS) or the Panoramic Survey Telescope and Rapid Response System (Pan-STARRS). Our high-resolution LOFAR images with a larger field of view, which show the quality of the Facet Calibration and the presence of additional sources in the cluster periphery, can be found in the Appendix. The size of the diffuse emission is given by $D_{\rm radio} = \sqrt{D_{\rm min} \times D_{\rm max}}$, where $D_{\rm min}$ and $D_{\rm max}$ are the minimum and maximum diameter of the 3σ surface brightness isocontours (e.g. [Cassano et al., 2008a], [Giacintucci et al., 2017]), as measured from the low-resolution LOFAR images.

In some cases, to reveal diffuse emission, it is necessary to subtract the contribution of compact sources in the cluster centre. Therefore, we image the sources at high resolution applying a cut in the *uv*-range, subtract them from the *uv*-data, and re-image the data sets at lower resolution (see Wilber et al. [2018] for details on the subtraction procedure). The value of the *uv*-cut varies from target to target, depending on the extension of the sources that we attempt to subtract. The error on the total flux density is computed as $\sqrt{\sigma^2_{\rm cal} + \sigma^2_{\rm sub}}$, where $\sigma_{\rm cal}$ is equal to 15% of the measured flux density and $\sigma_{\rm sub}$ is the subtraction error. The latter is derived by varying the range of the *uv*-cut that is used for modelling the compact sources. We can then quantify the error on the total flux density of the diffuse emission after subtracting different models.

When no hint of cluster-scale radio emission is detected, we provide upper limits on the radio power through the mock halo injection procedure (e.g. [Venturi et al., 2008], [Bonafede et al., 2017]). We created a mock radio halo with a central brightness I_0 and an e-folding radius $r_{\rm e}$ derived from the total radio power at 1.4 GHz ($P_{1.4}$) and halo size ($R_{\rm H}$) following the known power-mass correlation found by Cassano et al. [2013] for halos. We used the relation $R_{\rm H}/r_{\rm e} = 2.6$ found by Bonafede et al. [2017], who compared the values of $R_{\rm H}$ and $r_{\rm e}$ of the clusters; these values are both in the samples of Cassano et al. [2007] and Murgia et al. [2009]. We then carried out a Fourier transform of the mock source into the *uv*-data of the LOFAR observation, which is then imaged taking into account the w-projection parameter. We chose a relatively empty region near the cluster centre, void of bright sources or artefacts, to host the injected flux density. We decreased the total flux density of the mock halo until it could not be detected in the LOFAR image, i.e. when the surface brightness above 2σ has a maximum linear size $< 3r_{\rm e}$ following Bonafede et al. [2017] and Wilber et al. [2018]. Assuming the typical spectral index value for the halos ($\alpha = -1.3$), we then rescaled the total flux density of the mock halo to 1.4 GHz and computed the limit to the total radio power at 1.4 GHz, which can be compared with values present in the literature.

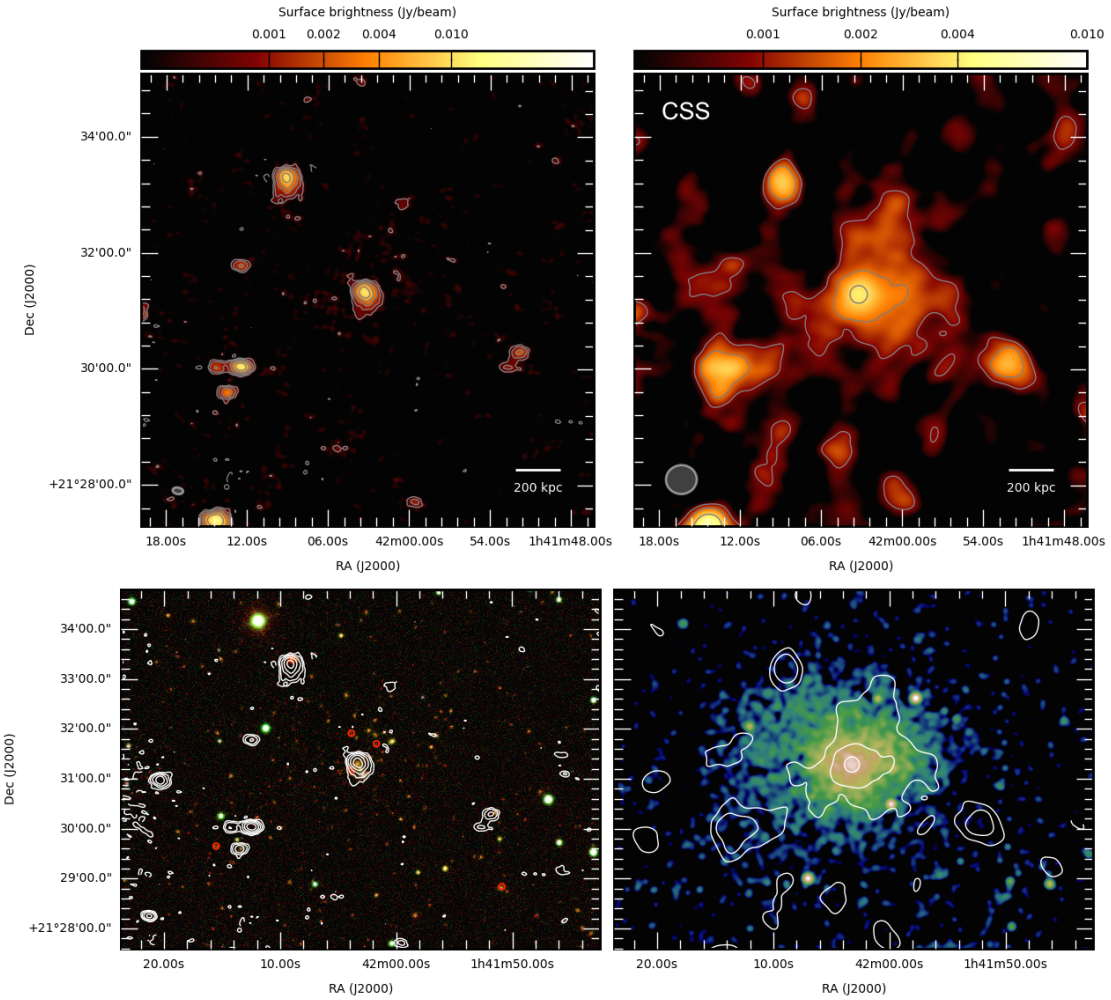

Figure 2.2: *RXCJ0142.0+2131* **Top left panel:** High-resolution 144 MHz LOFAR image of RXCJ0142.0+2131. The contour levels start at 3σ where $\sigma = 150$ μJy beam^{-1}, and are spaced by a factor of two. The negative contour level at -3σ is overlaid with a dashed line. The beam is $11'' \times 7''$ and is shown in grey in the bottom left corner of the image. **Top right panel:** Low-resolution 144 MHz LOFAR image of RXCJ0142.0+2131. The contour levels start at 3σ where $\sigma = 300$ μJy beam^{-1}, and are spaced by a factor of two. The negative contour level at -3σ is overlaid with a dashed line. The beam is $26'' \times 24''$ and is shown in grey in the bottom left corner of the image. This image was obtained after central source subtraction (CSS) with a taper of $15''$ and Briggs weighting (robust = 0). **Bottom left panel:** Optical Pan-STARRS image of RXCJ0142.0+2131 with the high-resolution ($11'' \times 7''$) 144 MHz LOFAR contours overlaid. The red circles indicate the cluster-member galaxies with available spectroscopic redshift. **Bottom right panel:** *Chandra* X-ray image of RXCJ0142.0+2131 smoothed on a scale of $5''$ with the low-resolution ($26'' \times 24''$) 144 MHz LOFAR contours overlaid.

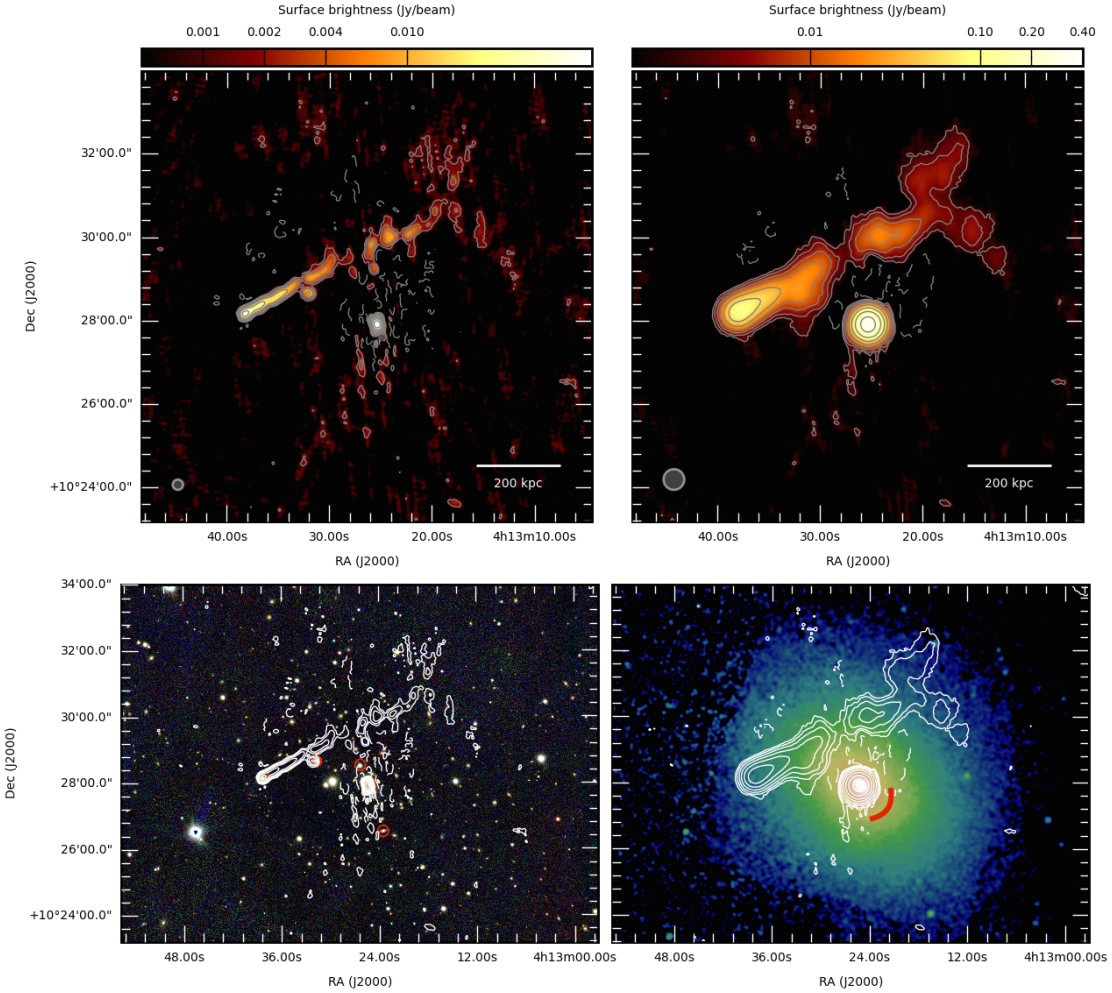

Figure 2.3: *A478* **Top left panel:** High-resolution 144 MHz LOFAR image of A478. The contour levels start at 3σ where $\sigma = 460$ μJy beam^{-1} and are spaced by a factor of two. The negative contour level at -3σ is overlaid with a dashed line. The beam is $10'' \times 10''$ and is shown in grey in the bottom left corner of the image. **Top right panel:** Low-resolution 144 MHz LOFAR image of A478. The contour levels start at 3σ, where $\sigma = 620$ μJy beam^{-1}, and are spaced by a factor of two. The negative contour level at -3σ is overlaid with a dashed line. The beam is $30'' \times 30''$ and is shown in grey in the bottom left corner of the image. **Bottom left panel:** Optical Pan-STARRS image of A478 with the high-resolution ($10'' \times 10''$) 144 MHz LOFAR contours overlaid. The red circles indicate the cluster-member galaxies with available spectroscopic redshift. **Bottom right panel:** *Chandra* X-ray image of A478 smoothed on a scale of $5''$ with the low-resolution ($30'' \times 30''$) 144 MHz LOFAR contours overlaid. The red arc indicates the position of the cold front found by Markevitch et al. [2003].

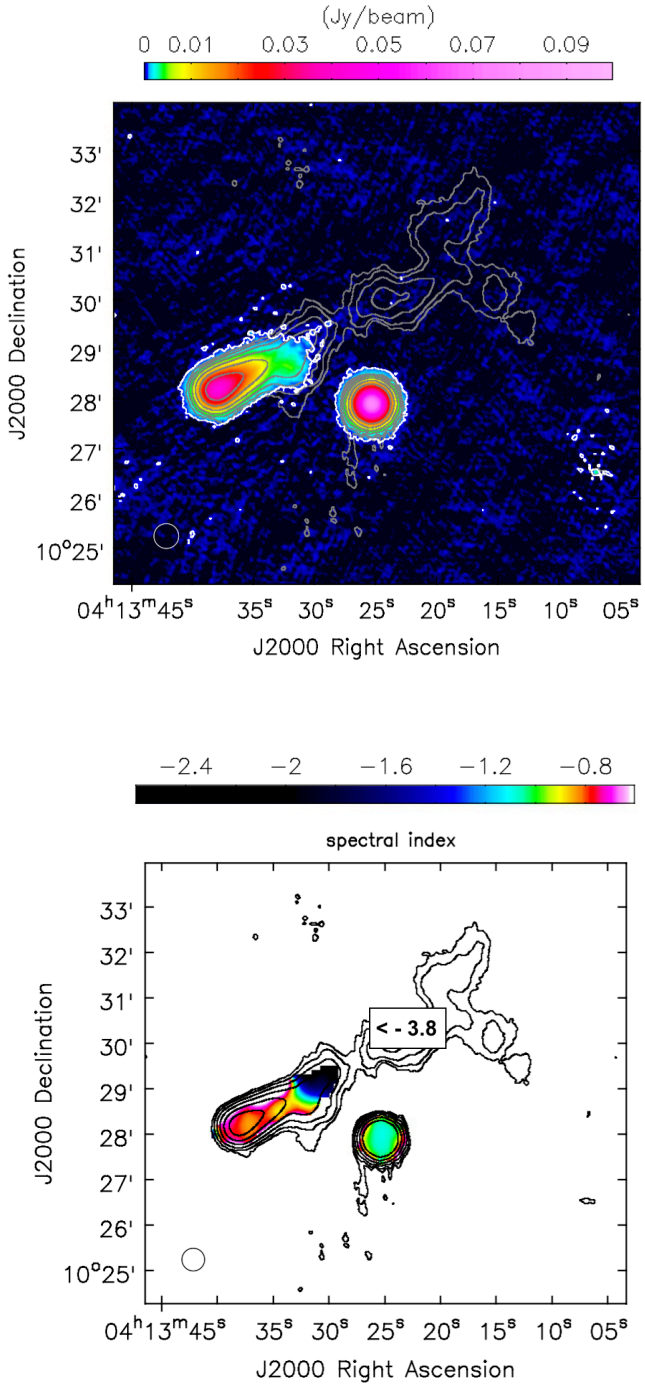

Figure 2.4: Contour levels from the low-resolution LOFAR image of A478 in Fig. 2.3 are overlaid in grey and black. **Left panel:** 610 MHz GMRT image of A478 with its 3σ contour level in white where $\sigma = 90\ \mu\mathrm{Jy\,beam^{-1}}$. The beam is $30'' \times 30''$ for both GMRT and LOFAR, and is shown in the bottom left corner of the image. **Right panel:** Spectral index map between the 610 MHz GMRT and 144 MHz LOFAR images of A478. Pixels below 3σ are blanked. The error map is shown in Fig. 2.17.

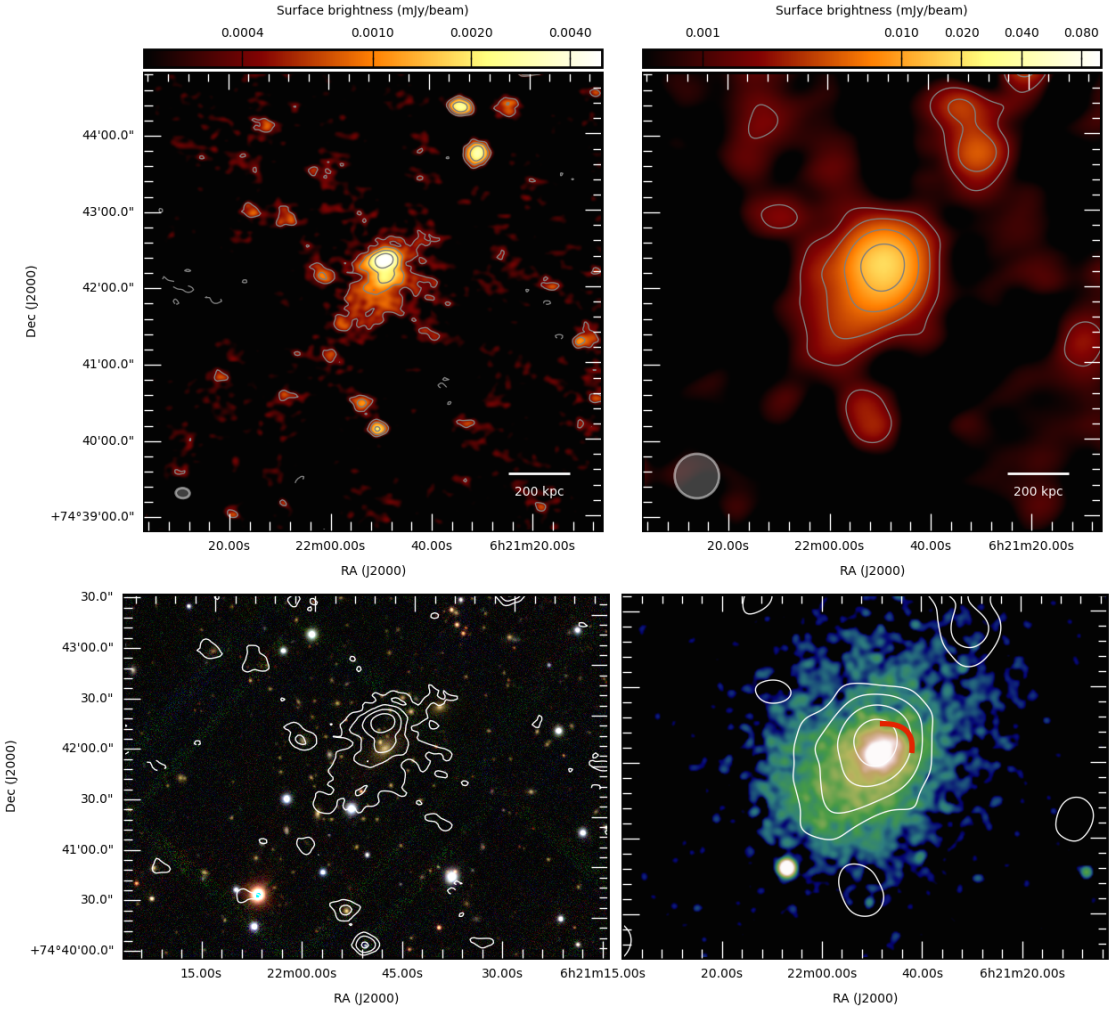

Figure 2.5: *PSZ1G139.61+24* **Top left panel:** High-resolution 144 MHz LOFAR image of PSZ1G139.61+24. The contour levels start at 3σ, where $\sigma = 150$ μJy beam^{-1}, and are spaced by a factor of two. The negative contour level at -3σ is overlaid with a dashed line. The beam is $11'' \times 8''$ and is shown in grey in the bottom left corner of the image. **Top right panel:** Low-resolution 144 MHz LOFAR image of PSZ1G139.61+24. The contour levels start at 3σ, where $\sigma = 500$ μJy beam^{-1}, and are spaced by a factor of two. The negative contour level at -3σ is overlaid with a dashed line. The beam is $35'' \times 35''$ and is shown in grey in the bottom left corner of the image. **Bottom left panel:** Optical Pan-STARRS image of PSZ1G139.61+24 with the high-resolution ($11'' \times 8''$) 144 MHz LOFAR contours overlaid. **Bottom right panel:** *Chandra* X-ray image of PSZ1G139.61+24 smoothed on a scale of $6''$ with the low-resolution ($35'' \times 35''$) 144 MHz LOFAR contours overlaid. The red arc indicates the position of the cold front found by Savini et al. [2018b].

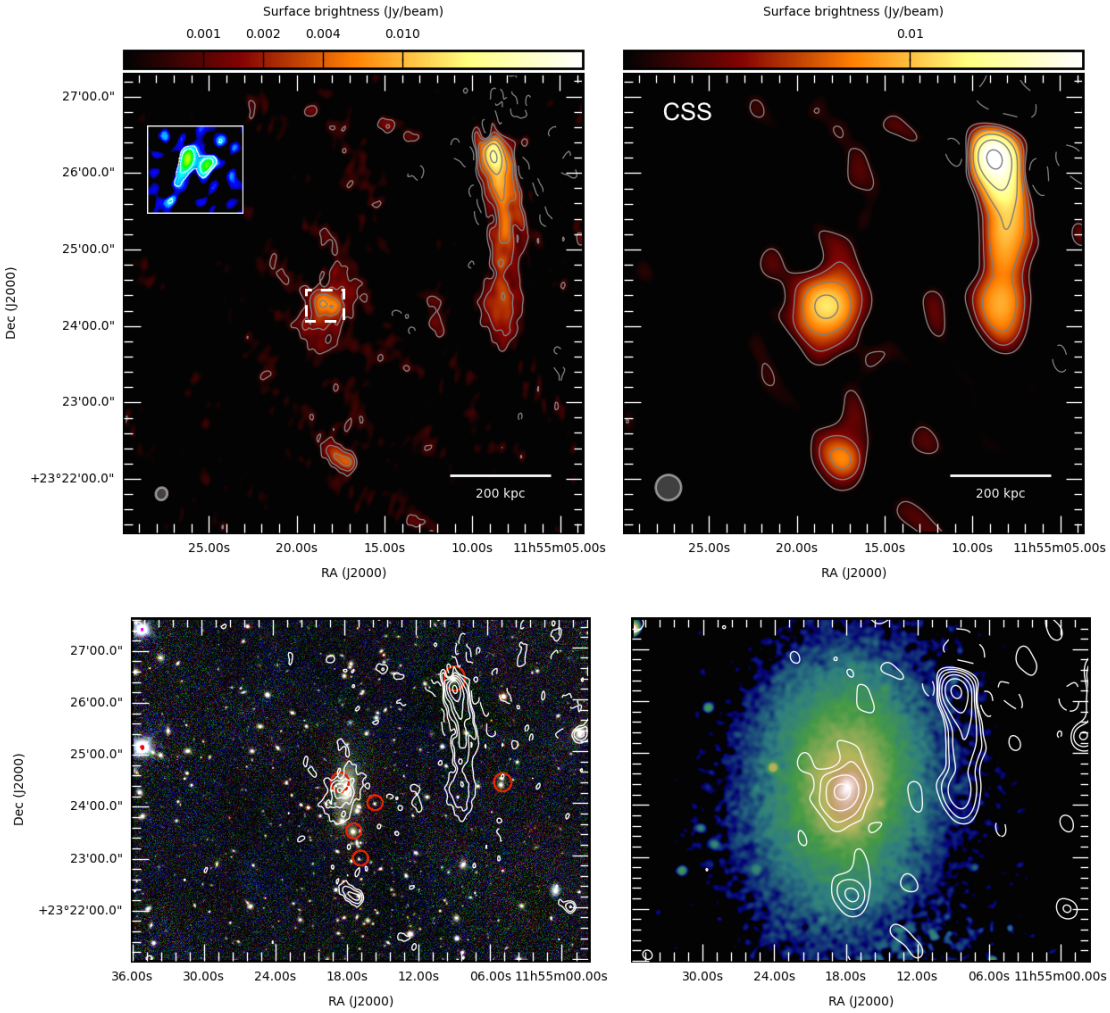

Figure 2.6: *A1413* **Top left panel:** High-resolution 144 MHz LOFAR image of A1413.The contour levels start at 3σ, where $\sigma = 270$ μJy beam^{-1}, and are spaced by a factor of two. The negative contour level at -3σ is overlaid with a dashed line. The beam is $10'' \times 9''$ and is shown in grey in the bottom left corner of the image. The insert box shows the *uv*-cut high-resolution image of the central sources that are subtracted to obtained the image in top right panel. **Top right panel:** Low-resolution 144 MHz LOFAR image of A1413. The contour levels start at 3σ, where $\sigma = 450$ μJy beam^{-1}, and are spaced by a factor of two. The negative contour level at -3σ is overlaid with a dashed line. The beam is $20'' \times 20''$ and is shown in grey in the bottom left corner of the image. This image was obtained after the CSS with a taper of $20''$ and Briggs weighting (robust = 0). **Bottom left panel:** Optical SDSS image of A1413 with the high-resolution ($10'' \times 9''$) 144 MHz LOFAR contours overlaid. The red circles indicate the cluster-member galaxies with available spectroscopic redshift. **Bottom right panel:** *Chandra* X-ray image of A1413 smoothed on a scale of $5''$ with the low-resolution ($20'' \times 20''$) 144 MHz LOFAR contours overlaid.

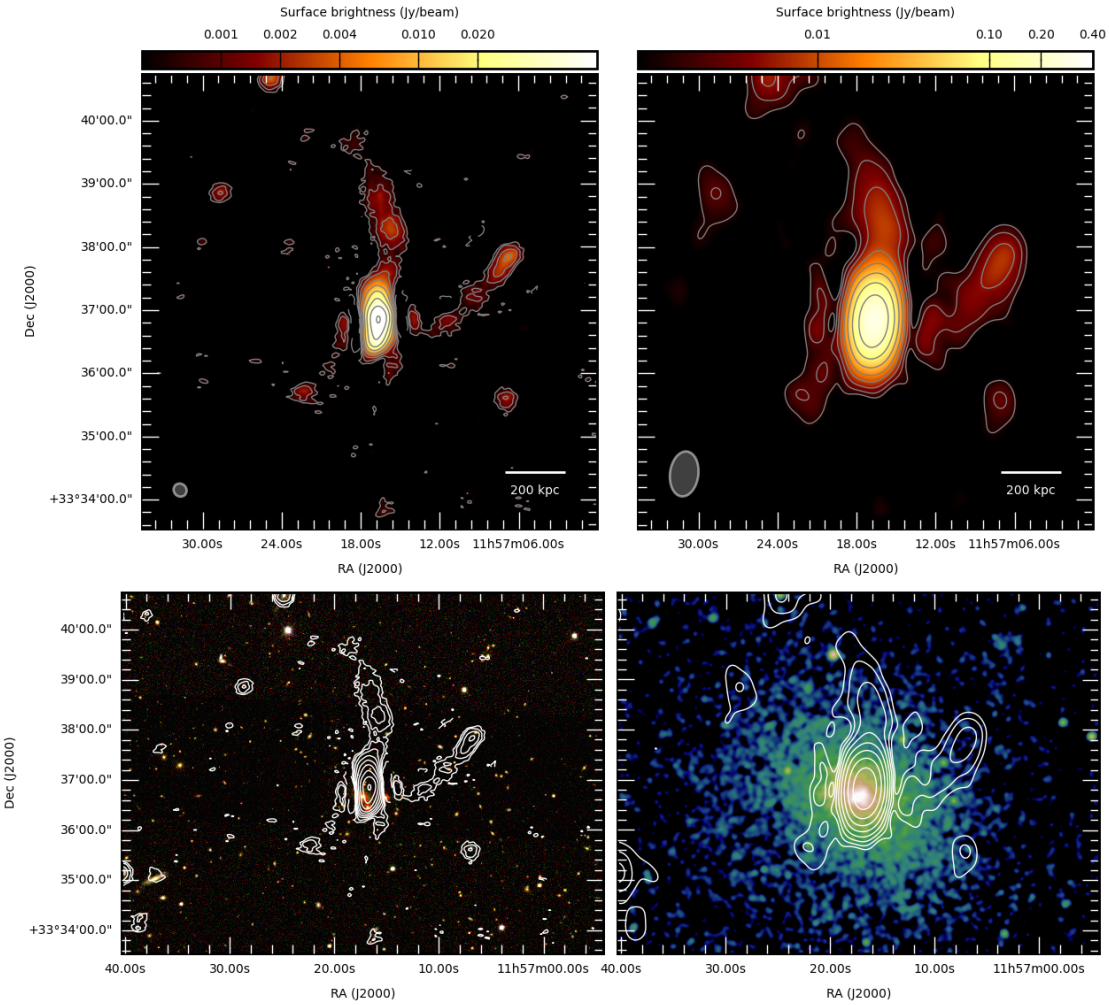

Figure 2.7: *A1423* **Top left panel:** High-resolution 144 MHz LOFAR image of A1423. The contour levels start at 3σ, where $\sigma = 170\ \mu\mathrm{Jy\,beam^{-1}}$, and are spaced by a factor of two. The negative contour level at -3σ is overlaid with a dashed line. The beam is $13'' \times 12''$ and is shown in grey in the bottom left corner of the image. **Top right panel:** Low-resolution 144 MHz LOFAR image of A1423. The contour levels start at 3σ, where $\sigma = 420\ \mu\mathrm{Jy\,beam^{-1}}$, and are spaced by a factor of two. The negative contour level at -3σ is overlaid with a dashed line. The beam is $43'' \times 27''$ and is shown in grey in the bottom left corner of the image. **Bottom left panel:** Optical Pan-STARRS image of A1423 with the high-resolution ($43'' \times 27''$) 144 MHz LOFAR contours overlaid. The red circles indicate the cluster-member galaxies with available spectroscopic redshift. **Bottom right panel:** *Chandra* X-ray image of A1423 smoothed on a scale of $5''$ with the low-resolution ($43'' \times 27''$) 144 MHz LOFAR contours overlaid.

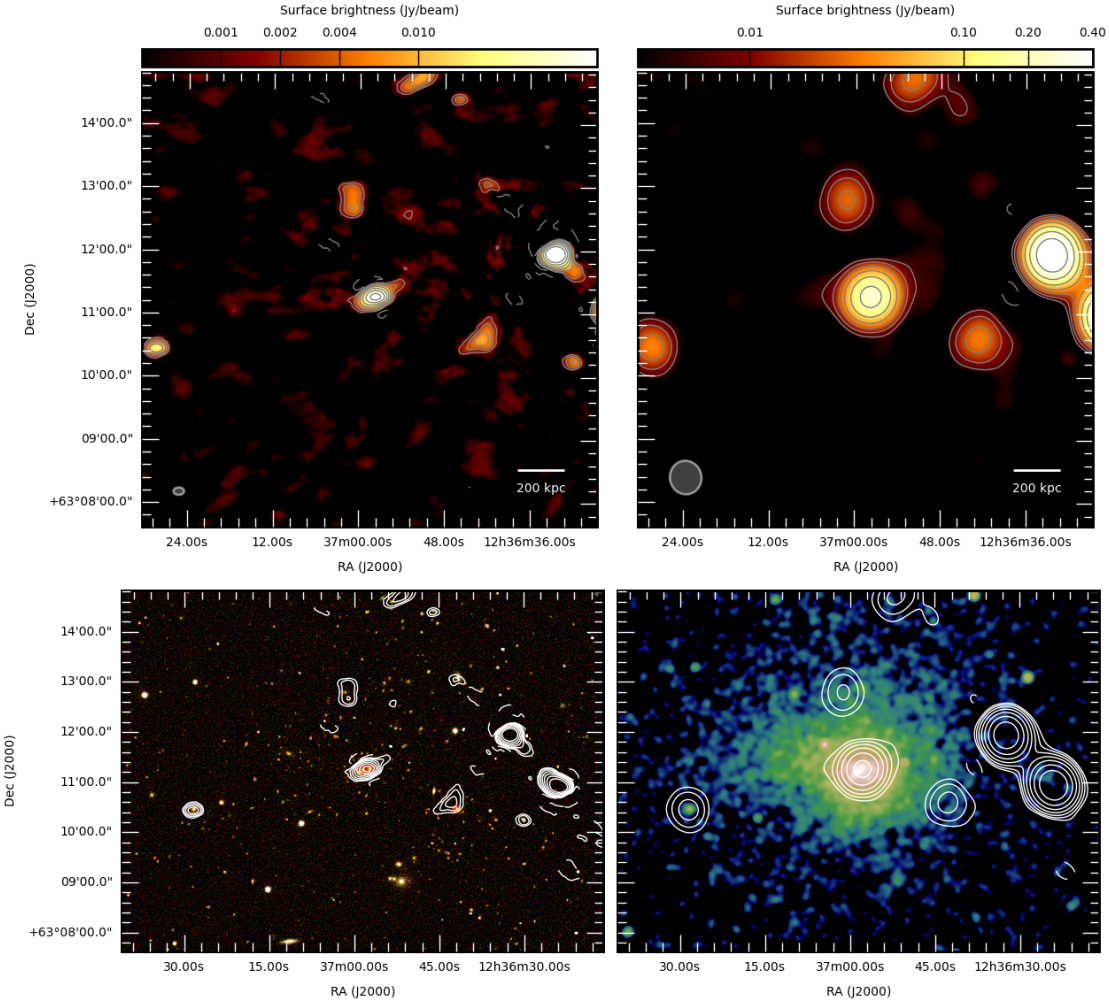

Figure 2.8: *A1576* **Top left panel:** High-resolution 144 MHz LOFAR image of A1576. The contour levels start at 3σ, where $\sigma = 500$ μJy beam^{-1}, and are spaced by a factor of two. The negative contour level at -3σ is overlaid with a dashed line. The beam is $10'' \times 7''$ and is shown in grey in the bottom left corner of the image. **Top right panel:** Low-resolution 144 MHz LOFAR image of A1576. The contour levels start at 3σ, where $\sigma = 150$ $\sigma = 2$ mJy beam^{-1}, and are spaced by a factor of two. The negative contour level at -3σ is overlaid with a dashed line. The beam is $32'' \times 30''$ and is shown in grey in the bottom left corner of the image. **Bottom left panel:** Optical Pan-STARRS image of A1576 with the high-resolution ($10'' \times 7''$) 144 MHz LOFAR contours overlaid. The red circles indicate the cluster-member galaxies with available spectroscopic redshift. **Bottom right panel:** *Chandra* X-ray image of A1576 smoothed on a scale of $5''$ with the low-resolution ($32'' \times 30''$) 144 MHz LOFAR contours overlaid.

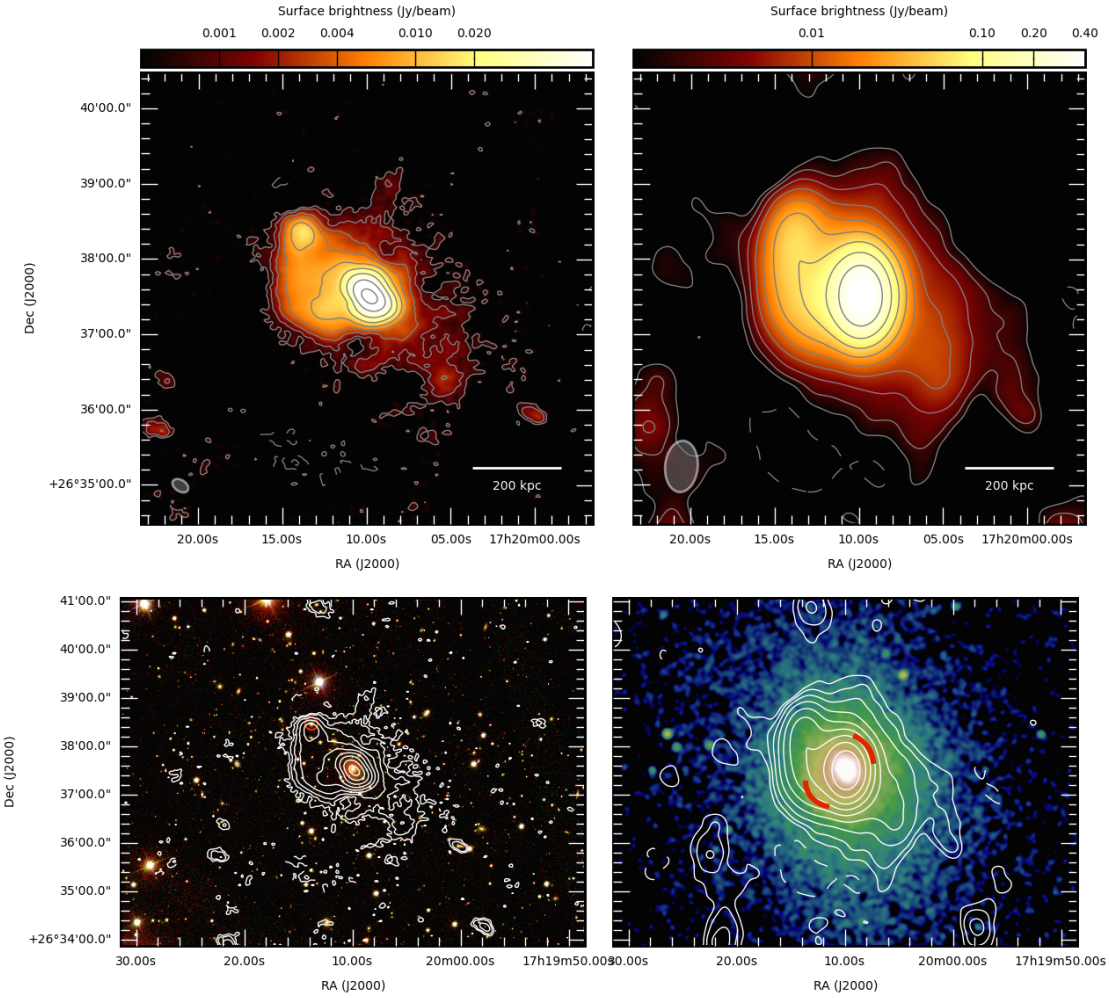

Figure 2.9: *RXJ1720.1+2638* **Top left panel:** High-resolution 144 MHz LOFAR image of RXJ1720.1+2638. The contour levels start at 3σ, where $\sigma = 200\ \mu\mathrm{Jy\,beam^{-1}}$, and are spaced by a factor of two. The negative contour level at -3σ is overlaid with a dashed line. The beam is $14'' \times 9''$ and is shown in grey in the bottom left corner of the image. **Top right panel:** Low-resolution 144 MHz LOFAR image of RXJ1720.1+2638. The contour levels start at 3σ, where $\sigma = 330\ \mu\mathrm{Jy\,beam^{-1}}$, and are spaced by a factor of two. The negative contour level at -3σ is overlaid with a dashed line. The beam is $41'' \times 26''$ and is shown in grey in the bottom left corner of the image. **Bottom left panel:** Optical Pan-STARRS image of RXJ1720.1+2638 with the high-resolution ($14'' \times 9''$) 144 MHz LOFAR contours overlaid. The red circles indicate the cluster-member galaxies with available spectroscopic redshift. **Bottom right panel:** *Chandra* X-ray image of RXJ1720.1+2638 smoothed on a scale of $5''$ with the low-resolution ($41'' \times 26''$) 144 MHz LOFAR contours overlaid. The red arcs indicate the position of the two cold fronts found by Giacintucci et al. [2014b].

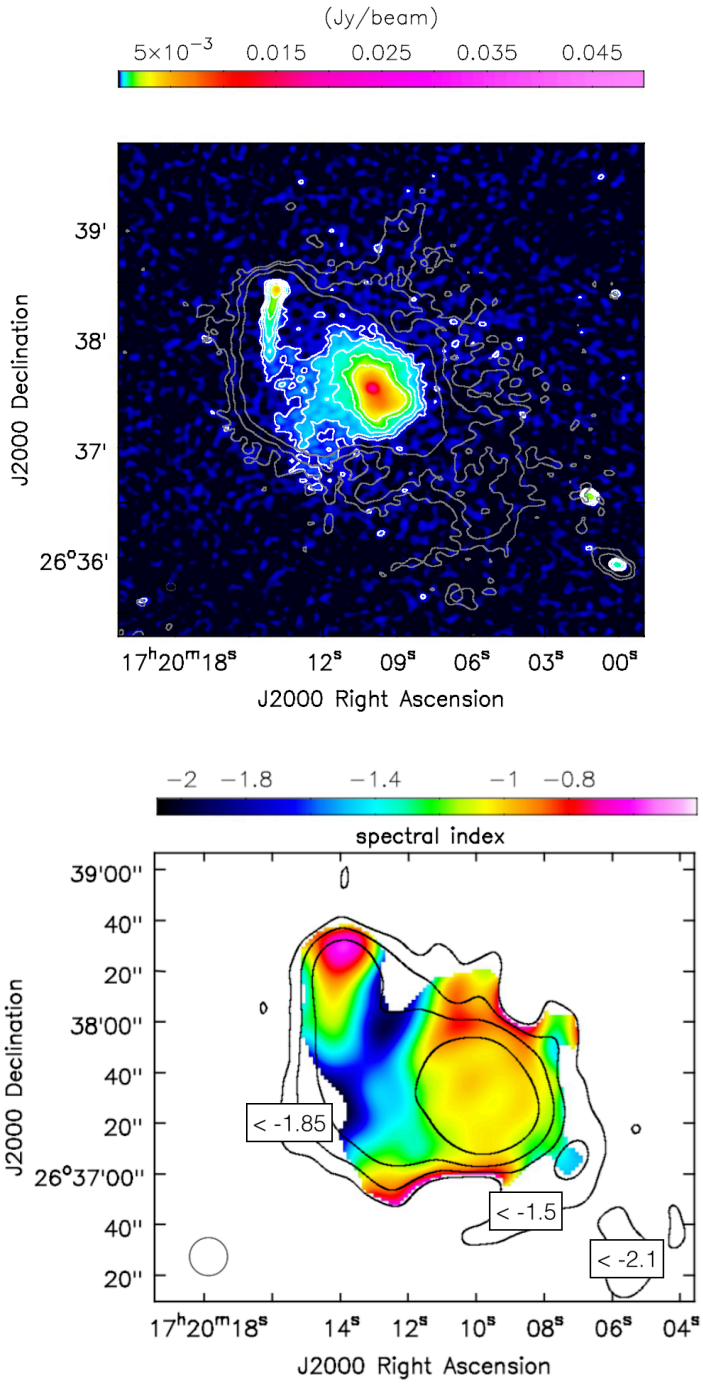

Figure 2.10: **Left panel:** 610 MHz GMRT image of RXJ1720.1+2638 with its contour levels in white starting at 3σ, where $\sigma = 45$ μJy beam^{-1} spaced by a factor of two. The first three contour levels from the high-resolution LOFAR image of Fig. 2.9 are overlaid in grey. The beam are $5'' \times 5''$ and $14'' \times 9''$ for GMRT and LOFAR, respectively, and are shown in the bottom left corner of the image. **Right panel:** Spectral index map between the 610 MHz GMRT and 144 MHz LOFAR images of RXJ1720.1+2638. The contour levels, overlaid in black, are from the LOFAR image obtained for the spectral analysis (uniform weighting, *uv*-cut, see main text), not shown in the paper. Pixels below 3σ are blanked. The error map is shown in Fig. 2.18.

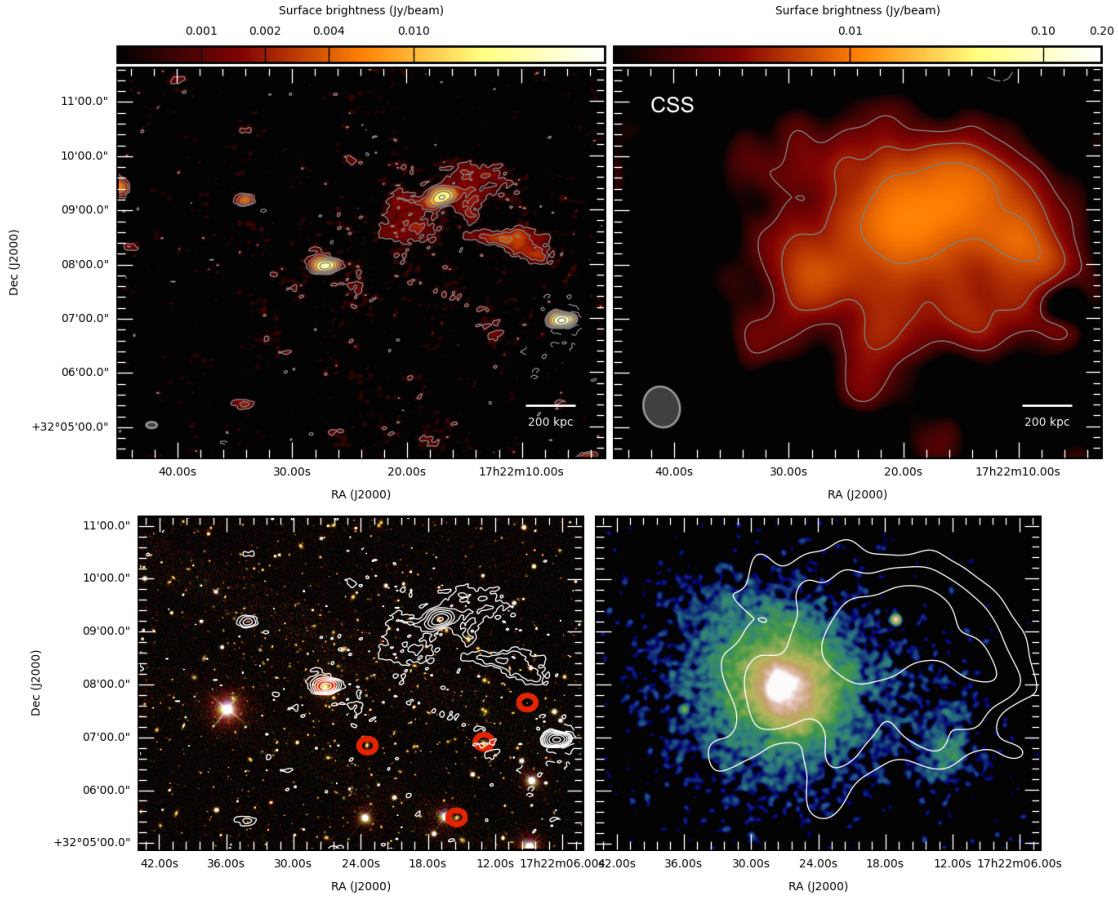

Figure 2.11: *A2261* **Top left panel:** High-resolution 144 MHz LOFAR image of A2261. The contour levels start at 3σ, where $\sigma = 280\ \mu\mathrm{Jy\,beam^{-1}}$, and are spaced by a factor of two. The negative contour level at -3σ is overlaid with a dashed line. The beam is $12'' \times 7''$ and is shown in grey in the bottom left corner of the image. **Top right panel:** Low-resolution 144 MHz LOFAR image of A2261. The contour levels start at 3σ, where $\sigma = 600\ \mu\mathrm{Jy\,beam^{-1}}$, and are spaced by a factor of two. The negative contour level at -3σ is overlaid with a dashed line. The beam is $46'' \times 40''$ and is shown in grey in the bottom left corner of the image. This image was obtained after CSS with a taper of $35''$ and Briggs weighting (robust = 0). **Bottom left panel:** Optical SDSS image of A2261 with the high-resolution ($12'' \times 7''$) 144 MHz LOFAR contours overlaid. The red circles indicate the cluster-member galaxies with available spectroscopic redshift. **Bottom right panel:** *Chandra* X-ray image of A2261 smoothed on a scale of $5''$ with the low-resolution ($46'' \times 40''$) 144 MHz LOFAR contours overlaid.

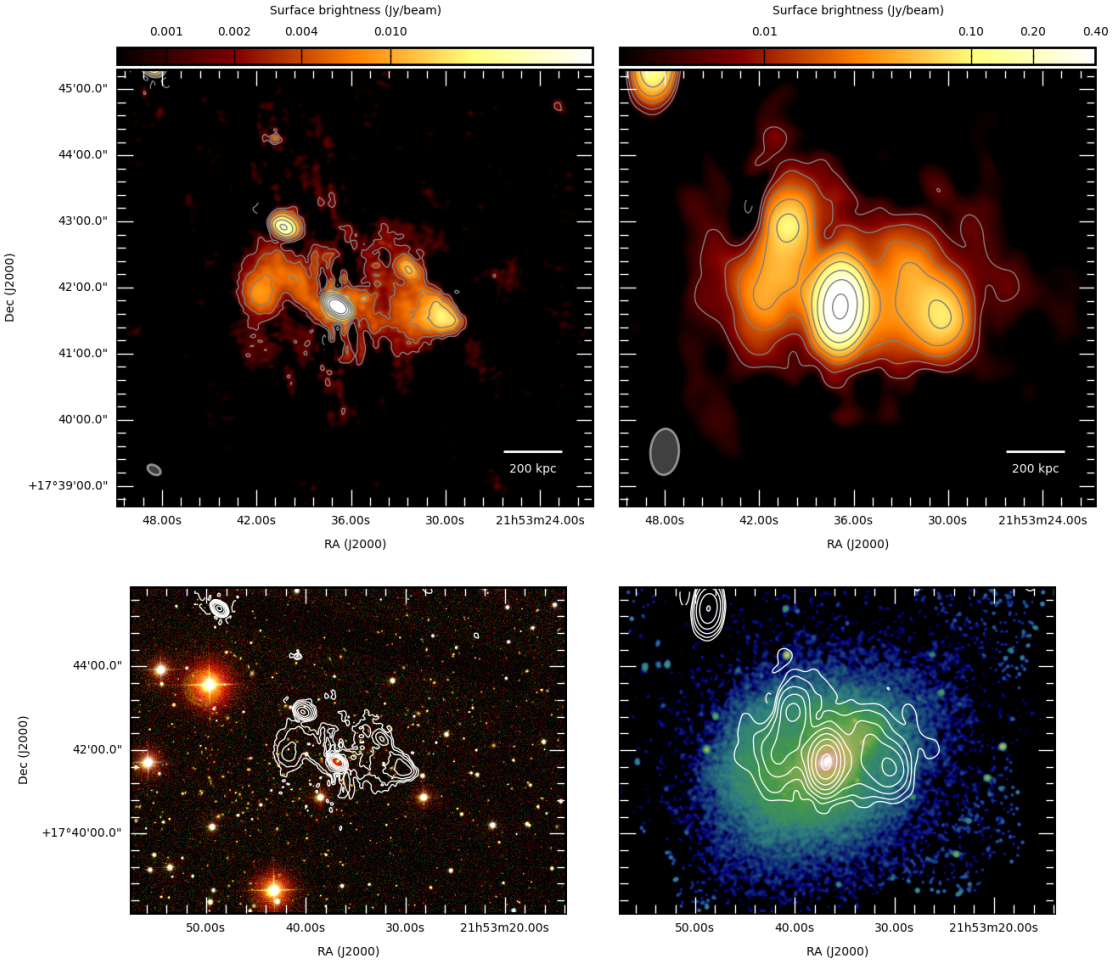

Figure 2.12: *A2390* **Top left panel:** High-resolution 144 MHz LOFAR image of A2390. The contour levels start at 3σ, where $\sigma = 400$ μJy beam^{-1}, and are spaced by a factor of two. The negative contour level at -3σ is overlaid with a dashed line. The beam is $13'' \times 8''$ and is shown in grey in the bottom left corner of the image. **Top right panel:** Low-resolution 144 MHz LOFAR image of A2390. The contour levels start at 3σ, where σ = 1.2 mJy beam^{-1}, and are spaced by a factor of two. The negative contour level at -3σ is overlaid with a dashed line. The beam is $42'' \times 26''$ and is shown in grey in the bottom left corner of the image. **Bottom left panel:** Optical Pan-STARRS image of A2390 with the high-resolution ($13'' \times 8''$) 144 MHz LOFAR contours overlaid. **Bottom right panel:** *Chandra* X-ray image of A2390 smoothed on a scale of $5''$ with the low-resolution ($42'' \times 26''$) 144 MHz LOFAR contours overlaid.

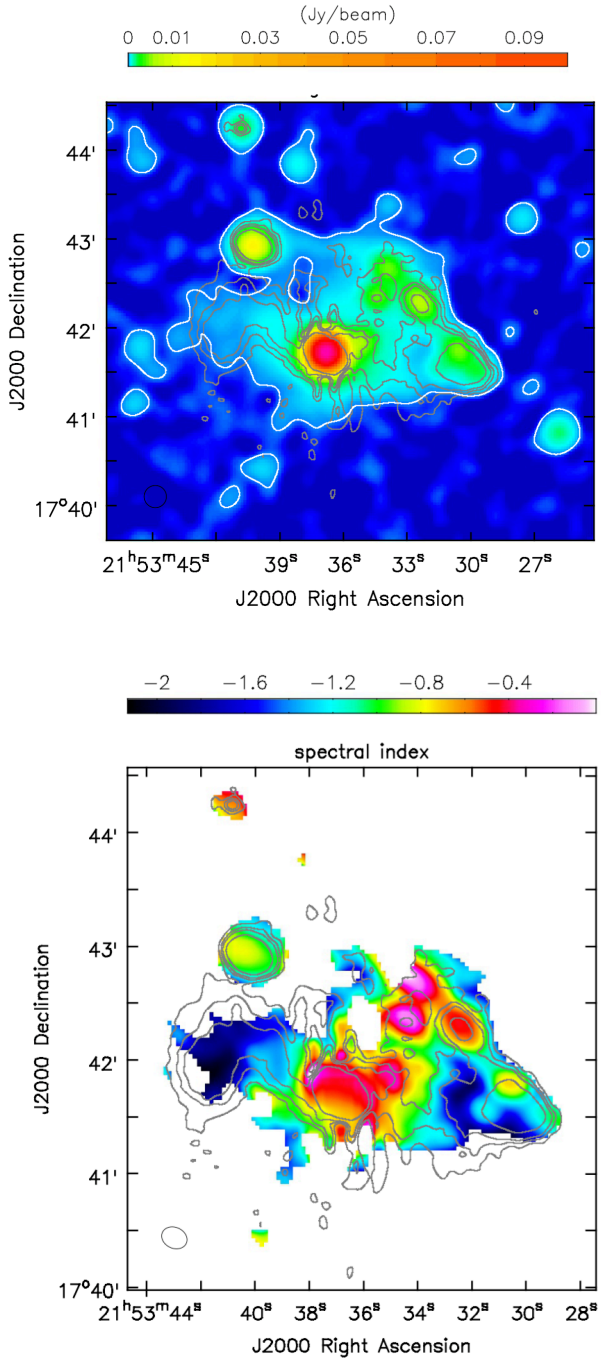

Figure 2.13: The contour levels, overlaid in grey, are from the LOFAR high-resolution image in Fig. 2.12 with $(4, 8, 12, 24) \times \sigma$ where $\sigma = 400\ \mu\mathrm{Jy\,beam^{-1}}$. **Left panel:** 1.5 GHz VLA image of A2390 with a beam of $15'' \times 15''$ and an rms noise of 26 $\mu\mathrm{Jy\,beam^{-1}}$. The first 3σ contour is shown in white. **Right panel:** Spectral index map between the 1.5 GHz VLA and 144 MHz LOFAR images of A2390. Pixels below 3σ are blanked. The error map is shown in Fig. 2.19.

2.4.1 RXCJ0142.0+2131

The non-cool-core cluster RXCJ0142.0+2131 is known to host a radio source at the cluster centre, that is coincident with the peak of the X-ray emission. Several bright radio sources in the field are visible in the image of the cluster [Kale et al., 2013]. The X-ray distribution has a relatively disturbed morphology with no strong features. We note that this cluster exhibits the smallest value of c in the sample.

Based on optical data, the occurrence of a possible merger event was inferred Barr et al. [2006], considering the presence of the second BCG (to the north-east) at z=0.283 located at ~ 650 kpc from the cluster centre and the X-ray morphology elongated in the same direction [von der Linden et al., 2014].

Since no diffuse radio emission has been detected in this cluster, an upper limit on the radio power was derived by Kale et al. [2013] using GMRT observations at 610 MHz and 235 MHz. The upper limit rescaled at 1.4 GHz is $P_{1.4} \leq 0.45 \times 10^{24}$ W Hz^{-1} [Cassano et al., 2013].

The high-resolution LOFAR image we obtained (left panel of Fig. 2.2) is consistent with the 610 MHz GMRT image in Kale et al. [2015] with a central radio source and few other radio sources to the north-east and south-west. We subtracted the contribution of the sources detected at high resolution using only the longer baselines with a uv-cut of $> 1750\lambda$ (that corresponds to 500 kpc) and re-imaged the data at lower resolution to search for diffuse emission. We were then able to see the presence of centrally located diffuse emission with $D_{\rm radio} \sim 570$ kpc, as shown in the right panel of Fig. 2.2. The total flux density is 32 ± 6 mJy corresponding to a total radio power at 144 MHz of $(8.6 \pm 1.6) \times 10^{24}$ W Hz^{-1}. Using the upper limit at 1.4 GHz placed by Kale et al. [2013], we can estimate the spectral index to be $\alpha_{144}^{1400} < -1.3$. We note that this is a conservative estimate, since the upper limit is computed considering a 1 Mpc halo, while the halo we detect is on a scale of less than 600 kpc. We can use the power-luminosity plot in Fig. 3 in Brunetti et al. [2007], where upper limits for 500 kpc-halos are also derived for the typical GMRT observations of the radio halo survey. At the redshift of this cluster, a limit evaluated on a size of 500 kpc would be 1.6 - 1.8 times deeper than that on a size of 1 Mpc. Hence, we derive a more stringent limit on the spectrum of $\alpha_{144}^{1400} < -1.6$, which would lead to an USS halo classification.

The size, although smaller than that of giant halos, and the estimated spectral index value are consistent with the properties of a radio halo, likely an USS halo. We note that the power measured with LOFAR and extrapolated at 1.4 GHz lies below the known power-mass correlation of Cassano et al. [2013] (see Fig. 2.14).

2.4.2 A478

A478 is a cool-core cluster with a relaxed X-ray morphology and a spherically symmetric temperature distribution on large scales. A number of X-ray substructures at the cluster centre, such as small cavities with sizes of few kpc, are found by Sun et al. [2003]. Gi-

acintucci et al. [2014a] presented VLA radio images at 1.4 GHz and reveal the presence of a central double-lobe radio galaxy with a size of $\sim$ 13 kpc. The hosting galaxy is the BCG, as can be seen in the optical overlay. Diffuse, low-brightness radio emission encompassing the central active galactic nucleus (AGN) and extending on a scale of $\sim$ 300 kpc is also detected and classified as a mini halo. The low-resolution image at 1.4 GHz (Fig. 1c in Giacintucci et al. [2014a]) shows that the mini halo blends with the tail of a cluster-member head-tail radio galaxy located to the north-east of the cluster centre. The tail extends for $\sim$ 200 kpc and encompasses an unresolved source, which is also a cluster member. A second unresolved source to the north with no optical identification is thought to be a background galaxy.

Markevitch et al. [2003] reported the presence of a cold front in the *Chandra* image at $\sim$ 60 kpc to the south-west of the cluster, which we show in the X-ray image of Fig. 2.3. Its position seems to indicate that the radio emission is confined by the front, as expected in simulations of mini halos [ZuHone et al., 2013].

The calibration of the LOFAR data set was difficult owing to the presence of a 3C source (3C109; 04h13m40.37s, $+11°12'13.8''$) with a flux density of $\sim$ 21 Jy located at 0.7° from the target. We created a sky model of this double-lobe radio galaxy using a high-resolution VLA image at 4.8 GHz to improve its calibration. However, the image sensitivity is limited by the dynamic range, therefore we consider the caveats relative to the presence of negative holes around the central source, and the higher noise of the target facet (460 μJy beam^{-1}) compared to that obtained for the other clusters. Nevertheless, the final image of A478 at 144 MHz (Fig. 2.3) confirms the presence of the central AGN; the head-tail radio galaxy to the north-east with a tail is overall much longer than previously seen, extending for more than 650 kpc. Interestingly, the tail appears to be divided into two regions. This is seen in the case of A1033 de Gasperin et al. [2017], in which the authors have proposed the gentle re-energisation of electrons as the mechanism that justifies the brightness of the second part of the radio tail, which is only visible at low frequencies.

With LOFAR, we do not see hints of centrally located diffuse emission. As a further argument, we injected mock mini halos with different sizes and flux densities in the data set, both at the cluster centre and in a void close-by region, to rule out the possibility that the calibration artefacts are responsible for the absence of the mini halo (see Fig. 2.16 in the Appendix section). We used the minimum and maximum values for r_e , i.e. 25 and 100 kpc, and for I_0 at 1.4 GHz, i.e. 13 and 1 μJy beam^{-1}, respectively, found by Murgia et al. [2009] for a sample of mini halos. Considering the flux density reported in Giacintucci et al. [2017] for the mini halo in A478, the recovered flux density of the mock mini halo indicates that the limit on the spectral index of the source would be $\alpha > -1$, which is unusually flat for a mini halo.

We processed an archival GMRT observation at 610 MHz and obtain the low-resolution image shown in the left panel of Fig. 2.4. Neither diffuse emission nor the second portion of the tail is visible. We re-imaged the LOFAR and GMRT data sets with a Gaussian taper of $30''$ and with the same pixel size, baseline range (200 - 40000λ), and uniform weighting scheme to minimise the differences in the *uv*-coverage of the two observations, and we obtain the spectral index map that is shown in the right panel of Fig. 2.4. The

central emission has a spectral index of ~ -1.1 and the head-tail radio galaxy has the typical trend of an active radio galaxy with a flat core ($\alpha_{610}^{144} \sim -0.6$) and a steepening along the tail up to $\alpha_{610}^{144} \sim -3$. We can provide an upper limit on the spectrum of the second portion of the tail, using the mean flux density from the LOFAR image and the rms noise from the GMRT image. This results in a spectral index < -3.8.

2.4.3 PSZ1G139.61+24

The cool-core cluster PSZ1G139.61+24 has been studied in detail in a dedicated paper by Savini et al. [2018b]. Giacintucci et al. [2017] have reported the detection of a tentative mini halo with an overall source size of $\sim$ 100 kpc located at the cluster centre, and the LOFAR image presented in Savini et al. [2018b] reveals new diffuse emission extending for more than 500 kpc. The radio source associated with the cluster consists of a central bright component surrounded by halo-like emission extending beyond the cool core. The two components become apparent in a spectral analysis performed between 144 MHz LOFAR and 610 MHz GMRT images that reveals a central component with $\alpha_{144}^{610} \sim$ -1.3, whilst the large-scale faint emission exhibits an USS with an upper limit of $\alpha_{144}^{610} <$ -1.7. Although the cluster core has a low entropy, typical of non-merging cool-core systems, the X-ray analysis shows that the cluster is slightly disturbed and hosts a cold front (shown in the bottom panel of Fig. 2.5) suggesting the presence of gas sloshing. Savini et al. [2018b] have argued that the large-scale radio emission outside the core is produced by a minor merger that powers electron re-acceleration without disrupting the cool core.

2.4.4 A1413

The 1.4 GHz VLA image in Govoni et al. [2009] reveals the presence of diffuse emission at the centre of the cool-core cluster A1413, extending on a scale of $\sim$ 220 kpc with a total flux density of 1.9 ± 0.7 mJy. At the sensitivity limit of the FIRST survey [Becker et al., 1995a], the central optical galaxy does not contain a compact radio source (Fig. 2 in Govoni et al. [2009]), and the authors suggested that the source might be a candidate mini halo, speculating about a scenario in which the central galaxy has switched off while the mini halo continues to emit. Govoni et al. [2009] also reported an offset between the emission peak of this radio source and both the central galaxy and the X-ray emission peak.
The X-ray morphology is slightly elongated in the north-south direction and shows a bright core with a moderate entropy value ($K_0 = 64 \pm 8$, [Giacintucci et al., 2017]) that indicates the absence of a cool core. We note that this cluster is the only (candidate) mini halo found in a non-cool-core cluster in the sample studied in Giacintucci et al. [2017].

With the LOFAR image in Fig. 2.6, we confirm the presence of centrally located diffuse emission. A head-tail radio galaxy, not mentioned or shown in Govoni et al. [2009], can be seen at the west of the cluster. The optical counter part is a galaxy member at $z = 0.144$. We obtain a high-resolution image using only the longer baselines with a uv-cut of $> 2580\lambda$ (corresponding to $\sim$ 200 kpc) to model the central compact sources (shown in the box within the top left panel of Fig. 2.6). We note that two sources are actually visible in the central region, one of which is co-located with the X-ray centre, hence no

offset is present. We then subtract the compact sources, imaging the central radio diffuse emission that is shown in the low-resolution image of Fig. 2.6; we classify this source as a mini halo. The size of the diffuse emission is $\sim$ 210 kpc with a total flux density of 40 ± 7 mJy at 144 MHz. The implied spectral index value is $\alpha_{144}^{1400} \sim$ -1.3. We note that the spectral index might be steeper, considering that the flux reported by Govoni et al. [2009] is likely overestimated, since the authors subtracted only the contribution of one of the central sources, i.e. that visible at 1.4 GHz with FIRST.

2.4.5 A1423

No hint of diffuse radio emission has ever been observed in the cool-core cluster A1423 and no radio images are available in the literature. An upper limit on the radio power was derived by Venturi et al. [2008] using a GMRT observation at 610 MHz. The upper limit rescaled at 1.4 GHz is $P_{1.4} \leq 0.38 \times 10^{24}$ W Hz^{-1} [Cassano et al., 2013].

Our high-resolution LOFAR image of A1423 (Fig. 2.7) shows a bright central radio source ($\sim$ 0.38 Jy) that is likely connected to the BCG visible in the optical image. This radio source is elongated in the north-south direction with a tail extending to the north for $\sim$ 400 kpc, which might be remnant emission connected to the central source. A second tailed source is found to the north-west of the cluster centre and might be connected to an optical galaxy of unknown redshift. Subtracting the bright and extended central source was not possible since it would leave residuals that cannot be distinguished from diffuse emission. The low-resolution LOFAR observation does not show additional emission. Moreover, no spatial correlation between radio and X-ray emission is found since the X-ray morphology appears disturbed along the east-west axis, whilst the radio emission is elongated along the north-south axis.

We computed a new upper limit on the radio power by injecting a mock halo in the data set (see Sec. 3.3). The integrated flux density of the mock halo computed within a region centred on the injected halo with a radius equal to $R_{\rm H} = 436$ kpc is 28 mJy at 144 MHz, which corresponds to a total radio power at 144 MHz of $P_{144} = 4.1 \times 10^{24}$ W Hz^{-1}. Assuming the typical spectral index value used in the power-mass correlation for halos ($\alpha = -1.3$), we derive a new upper limit to the radio power at 1.4 GHz, which we plot in Fig. 2.14. The new upper limit is $P_{1.4} < 0.20 \times 10^{24}$ W Hz^{-1}, i.e. almost a factor of 2 deeper than that derived in literature.

2.4.6 A1576

As in the case of A1423, no hint of diffuse radio emission has so far been observed in non-cool-core cluster A1576. A central radio galaxy with indications of a jet and three optical counterparts, which create a multiple core system, is reported by Kale et al. [2013]. Two other radio sources are visible in the field to the north (co-located with an optical source with unknown redshift) and to the south-west (likely connected to a cluster-member galaxy). The X-ray morphology is elongated in the east-west direction and does not show

a strong central peak. Moreover, based on weak lensing analysis, Dahle et al. [2002] inferred significant dynamical activity. An upper limit on the radio power was derived by Venturi et al. [2008] using a GMRT observation at 610 MHz. The upper limit rescaled at 1.4 GHz is $P_{1.4} \leq 0.64 \times 10^{24}$ W Hz^{-1} [Cassano et al., 2013].

During the LOFAR observation of this cluster, the ionosphere was very active and we reached a noise of 500 μJy beam^{-1} (Fig. 2.8). At this sensitivity level, no radio diffuse emission is detected at 144 MHz either after subtracting the contribution of the compact sources. Hence, we compute a new upper limit on the radio power by injecting a mock halo in the data set (see Sec. 3.3). The integrated flux density of the mock halo computed within a region centred on the injected halo with a radius of $R_{\rm H} = 429$ kpc is 37 mJy at 144 MHz, which corresponds to a total radio power at 144 MHz of $P_{144} = 11.9 \times 10^{24}$ W Hz^{-1}. Assuming the typical spectral index value used in the power-mass correlation for halos ($\alpha = -1.3$), we derived the radio power that we plot in Fig. 2.14. The new upper limit on the radio power at 1.4 GHz is $P_{1.4} < 0.62 \times 10^{24}$ W Hz^{-1}, i.e. comparable with that derived in literature.

2.4.7 RXJ1720.1+2638

The cool-core cluster RXJ1720.1+2638 has been studied in detail by Giacintucci et al. [2014b] using VLA and GMRT observations. The central source is classified as a mini halo consisting of a bright central component with a size of $\sim$ 160 kpc, and a fainter spiral-shaped tail of emission extending towards the south for more than 200 kpc. Two cold fronts detected in the *Chandra* X-ray image of the cluster appear to confine the mini halo.

The LOFAR images, shown in Fig. 2.9, reveal a new diffuse component extending beyond the cold fronts, not visible at higher frequencies. The emission extends towards the south-west with an overall size of $\sim$ 600 kpc. We reprocessed the GMRT observation at 610 MHz and obtained the high-resolution image shown in the left panel of Fig. 2.10. The head-tail radio galaxy to the north-east of the cluster is clearly visible and a connection between the central diffuse emission and the tail is already seen at this frequency. We re-imaged the LOFAR and GMRT data sets with a Gaussian taper of 20$''$ and with the same pixel size, baseline range (200 - 40000λ), and uniform weighting scheme to minimise the differences in the *uv*-coverage of the two observations and obtained a spectral index map that is shown in the right panel of Fig. 2.10. The mini halo appears to have a constant spectrum with a spectral index of $\alpha_{144}^{610} \sim -1$, whilst the head-tail radio galaxy has the typical trend of an active radio galaxy with a flat core and a steepening along the tail. The emission connecting the tail and the mini halo is steep, ranging between $\alpha_{144}^{610} \sim$ -1.4 and $\alpha_{144}^{610} \sim$ -1.8. The cluster-scale diffuse emission, which cannot be seen at 610 MHz, is ultra steep, and we can only provide upper limits, as shown in Fig. 2.10, using the mean flux density from the LOFAR image and the rms noise from the GMRT image. The radio emission in RXJ1720.1+2638 resembles that of PSZ1G139.61+24 [Savini et al., 2018b] with an inner, flatter component in the form of the already-known mini halo, and an outer part with a steeper-spectrum halo-like emission on larger scales, with $\alpha_{144}^{610} <$ -1.5. The

two inner cold fronts (reported in the X-ray image of Fig. 2.9) appear to separate the two components. Interestingly, the cluster A2142 [Venturi et al., 2017] also shows a two-component emission, and the presence of cold fronts both in the inner and outer region. However, because of the scarcity of X-ray counts in the outer cluster regions, we are not able to search for cold fronts on a larger scale.

2.4.8 A2261

A2261 is a non-cool-core cluster with a central radio source coincident with the BCG. The cluster has a relaxed morphology in X-rays in the central 500 kpc-radius region, while showing a diffuse patch of X-ray emission towards the west of the cluster; this is likely an infalling group, which suggests a possible minor merger [von der Linden et al., 2014]. Sommer et al. [2017] found a centrally located diffuse component on a scale of $\sim$ 1 Mpc using VLA observations at 1.4 GHz and classified the large-scale source as a radio halo.

The high-resolution LOFAR image (left panel of Fig. 2.11) shows the presence of a central compact radio source and a radio galaxy located at $\sim$ 540 kpc towards the north-west of the cluster centre; this radio galaxy has a faint, diffuse emission, symmetric with respect to its core, which could be the two remnant radio lobes. The core is identified with an X-ray source and an optical galaxy whose redshift is unknown. At the cluster redshift, the radio galaxy would extend up to $\sim$ 590 kpc. A patch of diffuse radio emission with no clear origin, which might be a relic or a dying AGN, is seen to the west of the cluster centre. After modelling these compact sources using only the longer baselines with a *uv*-cut of $> 750\lambda$ (that corresponds to 1 Mpc), we subtracted their contribution, revealing the presence of diffuse emission extending up to 1.2 Mpc. In general, the *uv*-subtraction method is not indicated for extended sources and in this case the remaining contribution of the diffuse lobes of the radio galaxy can be clearly seen. This affects the morphology of the diffuse emission that shows the brightness peak and an extension at the location of the radio galaxy and the unknown patch of diffuse emission. We note that the image obtained by Sommer et al. [2017] (Fig. 2) shows a different morphology of the large-scale diffuse source, which is likely due to the result of the *uv*-subtraction at a different frequency. For instance, the fact that the radio galaxy lobes are better subtracted might be related to their probable steep spectrum that contributes at high frequencies to a much smaller extent compared to what is observed at low frequencies. However, the radio source as seen at 144 MHz extends on a larger scale than the single radio sources, around the cluster centre, and also towards west and south-west, where the patch of X-ray emission is located, which might indicate a minor merger. This could also explain the offset between radio and X-ray emission peaks, also visible in the 1.4 GHz image. We obtained images using different *uv*-cut for subtraction corresponding to 800 kpc, 1 Mpc, and 1.2 Mpc. We show in Fig. 2.20 in the Appendix, models, and resulting images. Although the *uv*-subtraction is not entirely reliable as for the case of a compact point source, we can state that diffuse emission that is not related to the radio galaxy is clearly visible. Hence, the LOFAR image at 144 MHz confirms the presence of a radio halo, as suggested by the VLA observation at 1.4 GHz, although its morphology and radio power are hard to determine. We estimate the contribution of the flux densities of the radio galaxy and

unknown patch of emission, re-imaging the LOFAR *uv*-subtracted data set with the same taper and weighting scheme used for the halo (Fig.11 in the paper), keeping, in addition, the *uv*-cut of 750λ used for modelling the single sources. Subtracting this value of 20 mJy from the total flux density of the large-scale diffuse emission that is ~ 185 mJy; the radio halo has ~ 165 mJy corresponding to a total radio power at 144 MHz of $\sim 26 \times 10^{24}$ W Hz^{-1}.

Considering the total flux density at 240 MHz, 610 MHz, and 1.4 GHz reported in Tab. 3 in Sommer et al. [2017], we can provide an approximate estimate of the spectral index of the halo including LOFAR measurements to be $\alpha = -1.7 \pm 0.3$, which makes the radio halo in A2261 a candidate USS halo.

2.4.9 A2390

The cool-core cluster A2390 is particularly interesting for its large mass ($\sim 10^{15}$ M$_\odot$), which sets it apart from the other clusters in the sample (see top left panel of Fig. 2.15). A2390 has been observed at 1.4 GHz with the VLA. The data were analysed by Bacchi et al. [2003], who classified the detected emission as a mini halo with an integrated flux density of 63 ± 3 mJy and an extension of ~ 550 kpc. Using deeper Jansky VLA observations in the 1-2 GHz frequency band and re-analysing the VLA observation in Bacchi et al. [2003], Sommer et al. [2017] discovered diffuse radio emission on a larger scale extending for ~ 800 kpc in the form of a radio halo, after subtracting the compact source contribution. A spectral in-band analysis was also performed, finding a steep spectrum of $\alpha^{1\mathrm{GHz}}_{2\mathrm{GHz}} = -1.60 \pm 0.17$.

Our high-resolution LOFAR image shows that the central radio source is a double radio galaxy with the lobes extending in the east-west axis for ~ 600 kpc. The morphology indicates the presence of a bright core and fading lobes. Radio galaxies of such a size are not common at the centre of clusters, where the ICM usually prevents the expansion of the lobes to such large scales. The absence of emission in the north-south axis around the galaxy core had already been pointed out in previous works by Bacchi et al. [2003] and Sommer et al. [2017]. We note that there are some imaging artefacts due to the imperfect calibration of the galactic core that is brighter than the diffuse lobes and causes the image sensitivity to be limited by the dynamic range. The low-resolution LOFAR image shows the presence of diffuse emission on a larger scale with a total extension of 1.2 Mpc. The lowest contour of the low-resolution image might still be interpreted as cluster-scale diffuse emission or old lobes emission. It is not possible to disentangle this emission from that of the fading lobes of the radio galaxy, neither it is possible to accurately subtract its core to search for the presence of an underlying radio halo. Hence, we can only conclude that the radio emission is mostly dominated by the contribution of the radio galaxy whose morphology is clearly visible with LOFAR.

In the left panel of Fig. 2.13, we show the image of the VLA data set that was calibrated in Sommer et al. [2017]. We re-imaged this data set to match[6] the LOFAR imaging

[6]In this case we did not apply a *uv*-cut and the uniform weighting parameter (as we did for the spectral

Table 2.3: Derived physical parameters of the radio diffuse emission of our target clusters as seen by LOFAR. Col.1: Name of the cluster; Col. 2: classification of the diffuse emission as based on observations at 144 MHz (UL = upper limit; MH = mini halo; cMH = candidate mini halo; H = halo; USSH = USS halo; Col.3: size of the diffuse emission as measured from the low-resolution LOFAR images; Col.4: Total flux density at 144 MHz; Col.5: Total radio power at 144 MHz; Col. 6: Notes on the final image.

Name	LOFAR class.	$D_{\rm radio}$ (kpc)	$S_{144}^{\rm diff}$ (mJy)	$P_{144}^{\rm diff}$ ($\times 10^{24}$ W Hz^{-1})	Notes
RXCJ0142.0+2131	H	570	32 ± 6	8.6 ± 1.6	new H discovered
A478	uncertain	-	-	-	no diffuse emission
PSZ1G139.61+24	MH+USSH	550	30 ± 4	7 ± 1	MH: 3×10^{24} W Hz^{-1}, USSH: 4×10^{24} W Hz^{-1}
A1413	MH	210	40 ± 7	2.3 ± 0.4	MH confirmed
A1423	UL	-	23	3.3	mock H injection; $P_{1.4} < 0.17 \times 10^{24}$ W Hz^{-1} ($\alpha = -1.3$)
A1576	UL	-	37	11.9	mock H injection; $P_{1.4} < 0.62 \times 10^{24}$ W Hz^{-1} ($\alpha = -1.3$)
RXJ1720.1+2638	MH+USSH	600	820 ± 123	72 ± 11	MH: 64×10^{24} W Hz^{-1}, USSH: 8×10^{24} W Hz^{-1}
A2261	H	1200	~ 165	~ 26	H confirmed
A2390	uncertain	1100	-	-	600 kpc-central double radio galaxy

parameters, such as cell size and resolution, and obtain the spectral index map shown in the right panel of Fig. 2.13. The core appears to have a flat spectrum with $\alpha_{144}^{1400} \sim$ -0.5, which is a typical value for the core of an active radio galaxy, whilst the lobes are much steeper with α_{144}^{1400} ranging between $\sim$ -1.3 and $\sim$ -2. We can speculate on the type and evolutionary phase of the radio galaxy. It could be an FR-II radio galaxy that has recently restarted (which would explain the flat core), still showing old lobes and relic hotspots from a previous activity cycle (e.g. [Shulevski et al., 2015], [Brienza et al., 2016b]). Interestingly, Augusto et al. [2006] classified the radio galaxy of A2390 as an FR-II with a flat-spectrum core and a compact twin-jet structure in a northsouth direction on a sub-arcsec scale, as seen in the 1.7 - 43 GHz frequency range with very long baseline interferometry (VLBI) observations. They also note that the orientation of the jets is misaligned with respect to the ionisation cones and dust disc of the host galaxy on larger scales. They suggest that the misalignment might be due to a precession of the central super massive black hole, and that the radio source might be an example of a bubble being blown into the ICM at its early stage ($10^3 - 10^4$ yr duration). This is in line with our interpretation that the east-west jets are originated by a previous AGN active phase. The AGN might then be experiencing a second episode of activity with the jets growing in the north-south direction after a precession. With this scenario we expect the presence of X-ray cavities and bubbles. Four inner cavities are found by Sonkamble et al. [2015] and coincide with the location of the inner jets (east-west and north-south). Further cavities on large scales at the location of the old lobes are also expected and could be searched in future studies.

2.5 Discussion

On the basis of the X-ray morphology, the nine clusters presented in this work are not currently undergoing a major merger. As shown in the top panels of Fig. 2.15, five of these clusters host a cool core, whilst the remaining host a warm core, according to the classification based on the central gas entropy value [Giacintucci et al., 2017]. The overall picture as seen in the low-frequency radio band by LOFAR is very diverse with the presence of radio diffuse emission in the form of two radio halos, three mini halos, and two uncertain cases, while two clusters do not host diffuse emission at all. Even though the sample we studied is not large enough to derive statistical results, we note that this is the largest sample of galaxy clusters studied within LoTSS, and we can draw a number of conclusions that can also be indicative for future low-frequency observations. In our sample, the diffuse radio emission appears to be uncorrelated with the dynamical state as indicated by the centroid shifts, w, of the X-ray emission computed at 500 kpc. Even looking at w on smaller scales, from 200 to 500 kpc, as shown in the bottom left panel of Fig. 2.15, no correlation between the radio emission and w is found. Clusters that possess similar dynamical properties do not show the same radio properties, for example the non-cool-core clusters RXC0142.0+2131 and A1576, which have similar X-ray properties (relaxed morphology, comparable c and K_0) and also comparable cluster masses, host a radio halo and

analysis of A2261) because this would prevent us from recovering the morphology of the diffuse lobes. However, we note that the shortest baselines of the VLA and LOFAR observations are able to detect large-scale emission up to few arcminutes, larger than the emission in A2390.

no diffuse emission, respectively. Also plotting the power at 144 MHz versus the ratio of the X-ray concentration parameter, c, to w (see bottom right panel of Fig. 2.15) does not reveal a clear connection between the radio emission and the dynamical state of the cluster. halos are not necessary found in clusters with low c and high w; see for example A2261.

In the top right panel of Fig. 2.15, we plot c versus K_0 for each cluster. Two-component radio halos (MH+USSH) are found in clusters with high c and low K_0, while giant halos are detected in clusters with low c and higher K_0. Clusters for which no radio emission is found at the sensitivity level of these observations are found in both sides of the plot. Finally, a mini halo, which is the only mini halo found in a non-cool-core cluster that is also in the sample studied in Giacintucci et al. [2017], is found in a cluster with low c and high K_0.

Our observations show that the two clusters, PSZ1G139.61+24 and RXJ1720.1+2638, that host a mini halo and have the largest value of c, also show larger-scale ultra-steep diffuse emission that extends beyond the cold fronts. In our sample, the only mini halo that is confined to the central region of a cluster is hosted by A1413, which is not a cool-core cluster. This might indicate that the presence of a dense cool core is required to initiate the re-acceleration of CRe in the regions surrounding the core through gas sloshing triggered by a minor merger, as suggested for PSZ1G139.61+24 by Savini et al. [2018b]. The observation that mini halos can have a flatter core that is surrounded by a faint, steep corona is helpful in resolving their origin. A contribution from hadronic collisions cannot be excluded for the central region of cool-core clusters, but this contribution cannot explain the large-scale ultra-steep emission (e.g. [Brunetti et al., 2008], [Macario et al., 2010]). Hence, different scenarios for the cosmic ray origin might co-exist in these clusters that show hints of gas sloshing, with a distinction between the region within and outside the core.

In our sample, no giant radio halos in cool-core clusters are found. A2261 and RXC0142.0+2131, where halos are found, do not host a cool core and the extended emission in A2390 is likely to merely originate from the central radio galaxy, whose very diffuse lobes could have accidentally been classified as a halo at 1.4 GHz in Sommer et al. [2017]. We also note that both A2261 and RXC0142.0+2131 show traces of the occurrence of minor mergers. However, the non-cool-core cluster A1576, which presents hints of a minor merger, does not host diffuse emission.

Many head-tail radio galaxies have been observed in the cluster environment, however a clear connection with the central diffuse emission is only seen in the case of RXJ1720.1+2638, where the tail might provide seed electrons for re-acceleration.

2.5.1 Limits on cosmic ray protons

In this section, we aim to use some of our results to constrain the energy density of relativistic protons in the ICM by computing the maximum possible radio emission that can originate from hadronic collisions (e.g. [Blasi & Colafrancesco, 1999], [Dolag & Enßlin, 2000]). We use a similar albeit more complicated procedure as in Brunetti et al. [2007],

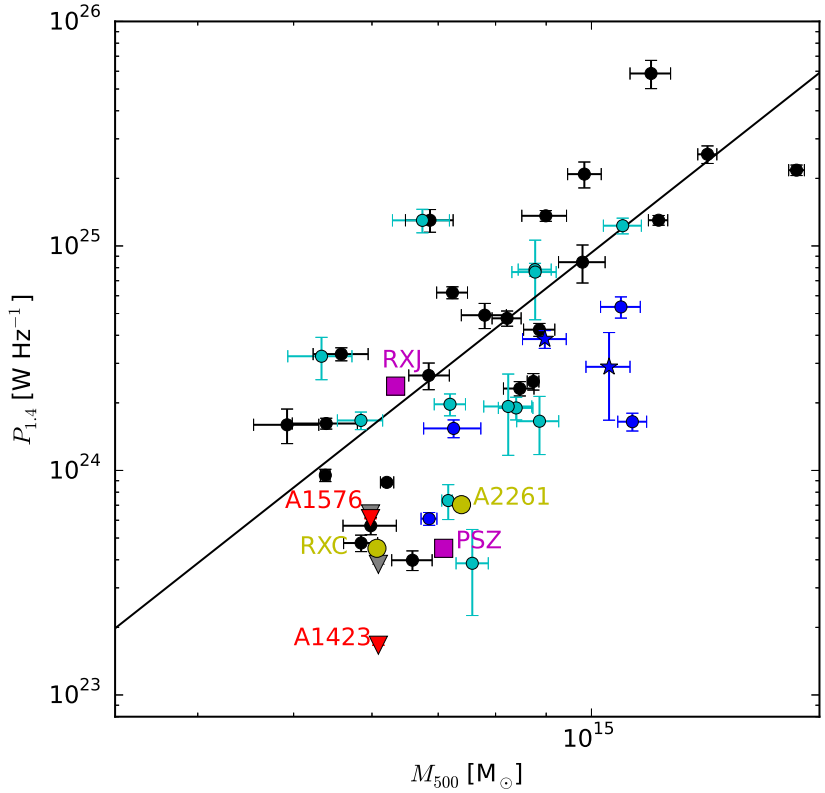

Figure 2.14: Radio power at 1.4 GHz vs. cluster mass M_{500} for a sample of clusters with radio halo. The plot is reproduced from Martinez Aviles et al. [2016]. halos with flux density measured at 1.4 GHz are indicated by black circles and their related fit is shown as a black line. halos with flux density measured at frequencies other than 1.4 GHz are indicated by cyan circles, ultra-steep halos by blue circles, and ultra-steep halos with flux density measured at frequencies other than 1.4 GHz by blue stars. The upper limit of radio halo power at 1.4 GHz in A1423 and A1576 are indicated by triangles, as derived in the literature in grey and the new limits obtained with LOFAR in red. The limit derived for A1576 is almost coincident with the value in literature, while that for A1423 is almost a factor of 2 smaller. We also indicate the power of the halos in A2261 and RXCJ0142.0+2131 with yellow circles, and the steep-spectrum sources in PSZ1G139.6+24 and RXJ1720.1+2638 with magenta squares.

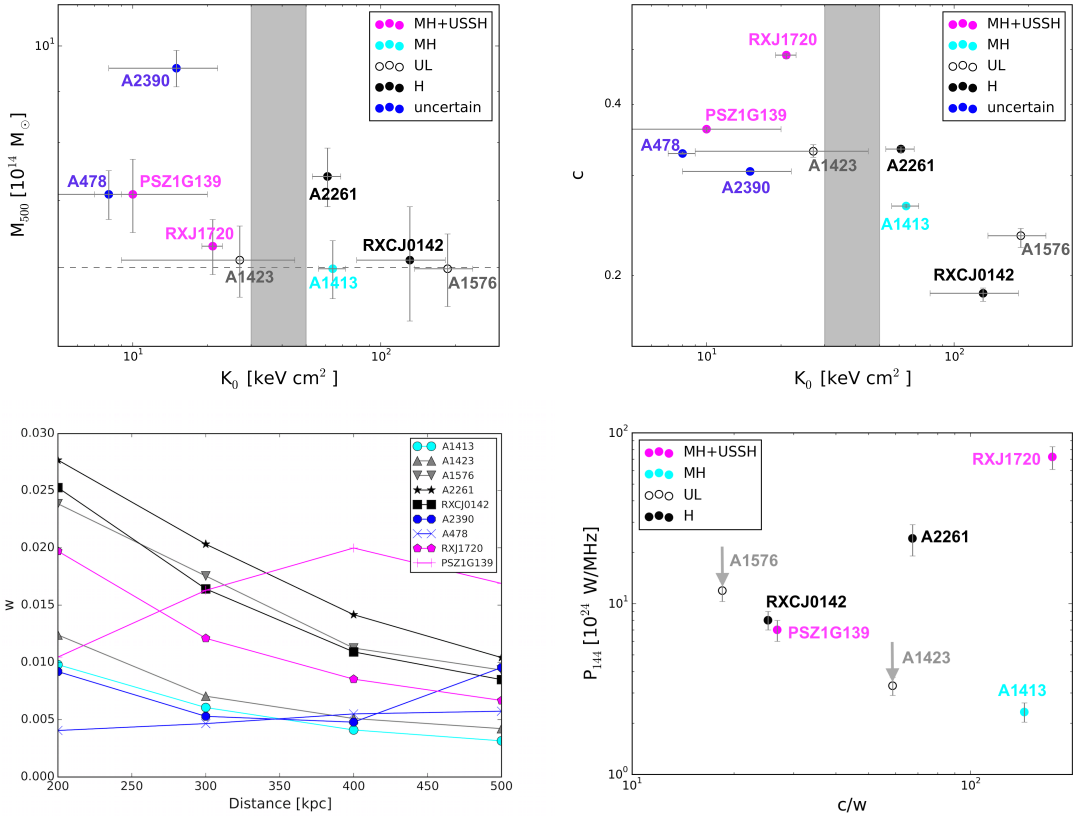

Figure 2.15: **Top left panel:** Central entropy K_0 vs. cluster mass M_{500} of our selected sample of clusters. The selection in mass ($M_{500} \geq 6 \times 10^{14}$ M$_\odot$) is indicated by a dashed line. Clusters with low central entropies ($K_0 < 30 - 50$ keV cm^2) are expected to host a cool core, whilst high central entropy ($K_0 > 50$ keV cm^2) indicates a non-cool-core cluster [Giacintucci et al., 2017]. The sources are coloured according to the new LOFAR findings: clusters with mini halos and USS halos (MH+USSH) are indicated by magenta circles, with candidate mini halos (cMH) by cyan circles and radio halos (H) by black circles. Clusters with no detected central diffuse radio emission, for which new upper limits (UL) were derived, are denoted by empty circles. **Top right panel:** Central entropy K_0 vs. concentration parameter c. High values of c and low values of K_0 indicate that the cluster host a cool core. In particular, clusters with low central entropies ($K_0 < 30 - 50$ keV cm^2) host a cool core, whilst high central entropy ($K_0 > 50$ keV cm^2) indicates a non-cool-core cluster [Giacintucci et al., 2017]. The only warm-core cluster hosting a mini halo is A1413. **Bottom left panel:** Emission centroid shift w vs. distance from the cluster centre at which w is computed. The value w was computed at a scale of 200, 300, 400 and 500 kpc. We note that the value of w gets smaller going to outer distances for all the clusters but PSZ1G139.61+24. **Bottom right panel:** Total radio power at 144 MHz of the diffuse emission vs. the ratio between the concentration parameter and emission centroid shift derived at 500 kpc.

which we describe in the following.

The total admissible energy density of cosmic rays is given by requiring that this radio emission does not exceed our upper limit, given a model for the thermal gas pressure and the magnetic fields.

In this work, we place new upper limits on the radio power for the clusters A1576 and A1423. While the new upper limit for A1576 is comparable to the value previously derived in literature, for A1423 we were able to obtain a limit that is almost a factor of two deeper. Hence, we created a model for the gas density and temperature of A1423 following Ghirardini et al. [2018], who presented best-fit formulas for the thermodynamical properties of cool-core and non-cool-core clusters based on the analysis of a sample of clusters observed with XMM-Newton. We rescaled the values to the cluster mass and temperature[7] of A1423, $M_{500} = 6.04 \times 10^{14}$ $M_{\odot}$ and $T_{500} = 6.4$ keV.

We assumed that the magnetic field in A1423 is similar to the best-fit 3D model of the magnetic field in the Coma cluster presented in Bonafede et al. [2010] owing to the similarity in the cluster total mass. We generated a power-law distribution of the magnetic vector potential A in Fourier space for a $(256)^3$ grid with a fixed resolution of $\Delta x = 10$ kpc that is randomly drawn from the Rayleigh distribution. The magnetic field in real space follows $B = \nabla \times A$, which ensures that $\nabla \cdot B = 0$ by construction. As in Coma, we assumed that the maximum coherence scale of the field is ~ 40 kpc, the power law of fluctuations exhibits a Kolmogorov spectrum and the average magnetic field strength in the centre is $B_0 \sim 4\,\mu$G. The volume-averaged magnetic field within a radius equal to $R_{\rm H}$ (i.e. the radius used for the upper limit, 436 kpc for A1423) is $\langle B \rangle = 1.2\,\mu$G.

To be self-consistent with the profile of the mock halo that we injected, we assumed that the ratio of the spatial distribution of the cosmic ray energy density, $E_{\rm CR}$, over the gas energy density profile, $E_{\rm gas}$, is

$$\frac{E_{\rm CR}}{E_{\rm gas}} = \left(\frac{E_{\rm CR}}{E_{\rm gas}}\right)_0 \left(\frac{r}{\Delta x}\right)^{\alpha_{\rm CR}},$$

where the index 0 indicates the ratio computed at the cluster centre, and $\alpha_{\rm CR}$ is a shape parameter that allows for the non-linear scaling between cosmic rays and gas matter, as in Donnert et al. [2010] and Brunetti et al. [2012]. We fixed $\alpha_{\rm CR} = 1$ based on the requirement that the profile of the simulated radio emission within 1σ (see below) matches the input halo model used in Sec. 2.4.5. We also imposed that the ratio E_{CR}/E_{gas} is no larger than 0.1.

The radio emission from hadronic collisions was derived following Pfrommer & Enßlin [2004], i.e. assuming a Dermer model to compute the cross section of the proton-proton interaction, and integrating the CRp population from $E_{\rm min} = 0.1$ GeV to $E_{\rm max} = 100$ GeV for a particle spectrum of $\alpha_p = 2.6$, corresponding to a radio spectral index of $\alpha \sim$ -1.3. Finally, we projected the emission and measured the flux density within a radius $R_{\rm H}$ from the cluster centre, and compared it to the upper limit we derived from the LOFAR

[7] We used the core-excised temperature given by Giacintucci et al. [2017].

observation of A1423.

Through this procedure, we find that $\left(\frac{E_{\rm CR}}{E_{\rm gas}}\right)_0 \sim 0.1\%$ yields $\left(\frac{E_{\rm CR}}{E_{\rm gas}}\right) \sim 3\%$, averaged on the volume of a sphere of radius $R_{\rm H}$.

A comparison with the limit derived from the lack of hadronic γ-ray emission reported by the *Fermi* satellite for a sample of galaxy clusters (e.g. [Ackermann et al., 2014]) is not straightforward, and would require, for instance, a more detailed treatment of the cosmic ray energy density distribution. However, we note that the limit we derived is of the same order of magnitude. Our constrain demonstrates the great potential of future, deeper LOFAR observations to constrain the energy budget of CRp in the ICM.

2.6 Summary

In this paper, we have presented the results of the largest campaign of LOFAR observations targeting galaxy clusters so far. The mass-selected sample consists of clusters with no sign of major mergers observed in the frequency range between 120 MHz and 168 MHz. Data reduction was performed following the Facet Calibration scheme. Below we summarise our main results:

1. We find central, diffuse emission in the form of mini halos surrounded by USS halos in the cool-core clusters RXJ1720.1+2638 and PSZ1G139.6+24. Hence, we argue that the sloshing of the dense core after a minor merger can be responsible for the formation, not only of a central mini halo, but also of larger-scale emission that is visible at low radio frequencies. Moreover, the presence of a cool core, indicated by high values of the concentration parameter, c, and low values of the central entropy, K_0, might be significant for the formation of radio diffuse emission on scales larger than the cluster core that hosts a mini halo.

2. We confirm the presence of a mini halo in the non-cool-core cluster A1413 as proposed by Govoni et al. [2009].

3. We discover a radio halo in the non-cool-core cluster RXCJ0142.0+2131 with a scale of 570 kpc and a spectral index of $\alpha_{144}^{610} < -1.3$.

4. We confirm the presence of a radio halo in the non-cool-core cluster A2261 as proposed by Sommer et al. [2017].

5. The central radio galaxy discovered in the massive cool-core cluster A2390 might account for most or even all the radio flux that was attributed to the giant radio halo proposed by Sommer et al. [2017]; high-resolution observations in the frequency range between 144 GHz and 1.4 GHz are needed to confirm the morphology of the two radio jets and lobes and exclude the presence of the giant radio halo.

6. At LOFAR frequencies no centrally-located diffuse emission is observed in the cool-core cluster A478. We injected a mock mini halo, and placed a limit on the spectrum, i.e. $\alpha > -1$.

7. No cluster-scale diffuse radio emission is found in the cluster A1576 and in the cool-core cluster A1423 at the sensitivity of the observations, hence we derive new upper limits on the total radio power.

8. We use the limit on the radio power of A1423 to constrain the energy budget of CRp in the ICM and compare the result with the constraints derived from the lack of hadronic γ-ray emission reported by the FERMI satellite. We find that our LOFAR observations are competitive with the deepest limits derived by FERMI for the Coma cluster.

9. We discover head-tail radio galaxies in the clusters A1423 and A1413. We note also the presence of head-tail radio galaxies in A478, and in RXJ1720.1+2638, where the tail appears to be connected to the central source, and it might be a possible source of seed particles that can be re-accelerated.

10. No giant radio halos in the cool-core clusters of our sample are found.

Low-frequency radio observations are ideal for discovering diffuse emission, in particular steep-spectrum emission from low-energy CRe in galaxy clusters. Future studies performed on a larger sample of clusters will provide statistical information and help to further investigate the connection between the formation of radio emission from the ICM and its dynamical state.

Acknowledgements

This paper is based (in part) on data obtained with the International LOFAR Telescope (ILT) under the project codes listed in Tab. 2.2. LOFAR (van Haarlem et al. 2013) is the LOw Frequency ARray designed and constructed by ASTRON. It has observing, data processing, and data storage facilities in several countries, which are owned by various parties (each with their own funding sources) and are collectively operated by the ILT foundation under a joint scientific policy. The ILT resources have benefitted from the following recent major funding sources: CNRS-INSU, Observatoire de Paris and Universite d'Orleans, France; BMBF, MIWF-NRW, MPG, Germany; Science Foundation Ireland (SFI), Department of Business, Enterprise and Innovation (DBEI), Ireland; NWO, The Netherlands; The Science and Technology Facilities Council, UK; Ministry of Science and Higher Education, Poland.

Part of this work was carried out on the Dutch national e-infrastructure with the support of the SURF Cooperative through grant e-infra 160022 & 160152. The LOFAR software and dedicated reduction packages on https://github.com/apmechev/GRID_LRT were deployed on the e-infrastructure by the LOFAR e-infragroup, consisting of J. B. R. Oonk (ASTRON & Leiden Observatory), A. P. Mechev (Leiden Observatory) and T. Shimwell (Leiden Observatory) with support from N. Danezi (SURFsara) and C. Schrijvers (SURFsara).

This research made use of the NASA/IPAC Extragalactic Database (NED), which is operated by the Jet Propulsion Laboratory, California Institute of Technology, under contract with the National Aeronautics and Space Administration.

A. Bonafede acknowledges support from the ERC-StG grant DRANOEL, n. 714245. F. Vazza acknowledges financial support from the ERC Starting Grant MAGCOW, no.714196. H. Röttgering and R. van Weeren acknowledge support from the ERC Advanced Investigator programme NewClusters 321271 and the VIDI research programme with project number 639.042.729, which is financed by the Netherlands Organisation for Scientific Research (NWO). F. de Gasperin is supported by the VENI research programme with project number 1808, which is financed by the Netherlands Organisation for Scientific Research (NWO). A. Drabent acknowledges support by the BMBF Verbundforschung under the grant 05A17STA.

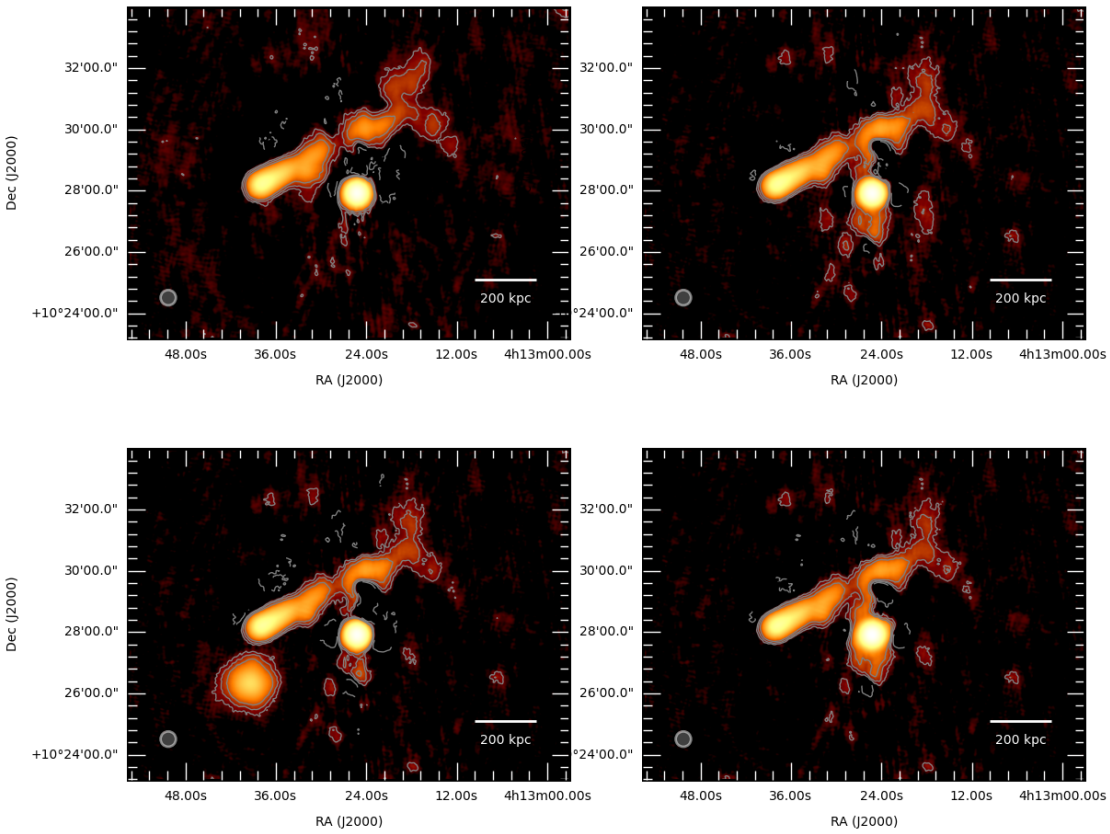

Figure 2.16: Low-resolution ($30'' \times 30''$) LOFAR image of the cluster A478 at 144 MHz. The contour levels are $(1, 2, 4) \times 3\sigma$, where $\sigma = 620\ \mu\mathrm{Jy\,beam}^{-1}$. No mock mini halo is injected in the data set in the top left panel. A mock mini halo with $I_0 = 1\ \mu\mathrm{Jy\,arcsec}^{-2}$ is injected at the cluster centre with $r_e = 100$ kpc in the top right panel. A mock mini halo with $I_0 = 13\ \mu\mathrm{Jy\,arcsec}^{-2}$ is injected at the cluster centre with $r_e = 25$ kpc at the cluster centre in the bottom right panel, and in a close-by void region in the bottom left panel. The values for r_e and I_0 are chosen accordingly to the top panel of Fig. 5 in Murgia et al. [2009] and are referred to measurements at 1.4 GHz.

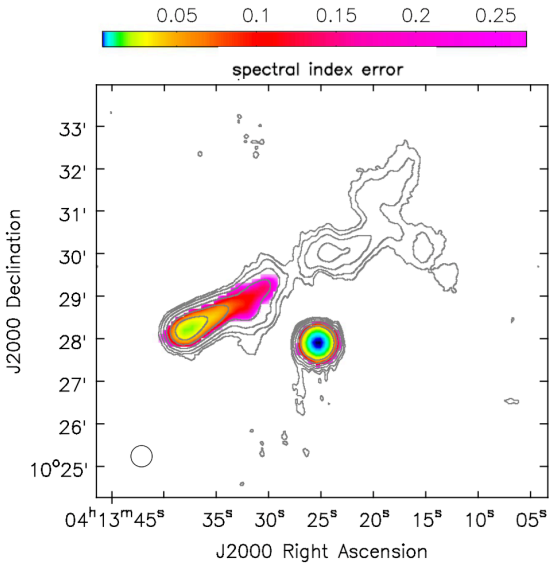

Figure 2.17: Spectral index error map of A478 (α_{144}^{610}) related to Fig. 2.4. Pixels below 3σ are blanked.

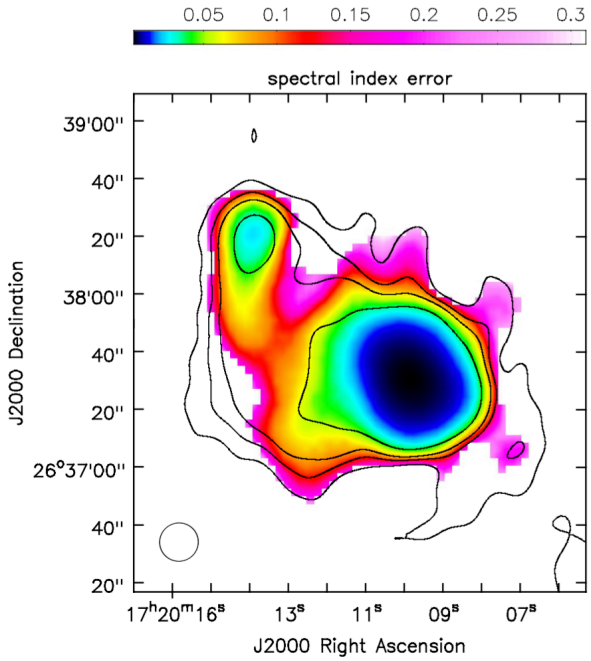

Figure 2.18: Spectral index error map of RXJ1720.1+2638 (α_{144}^{610}) related to Fig. 2.10. Pixels below 3σ are blanked.

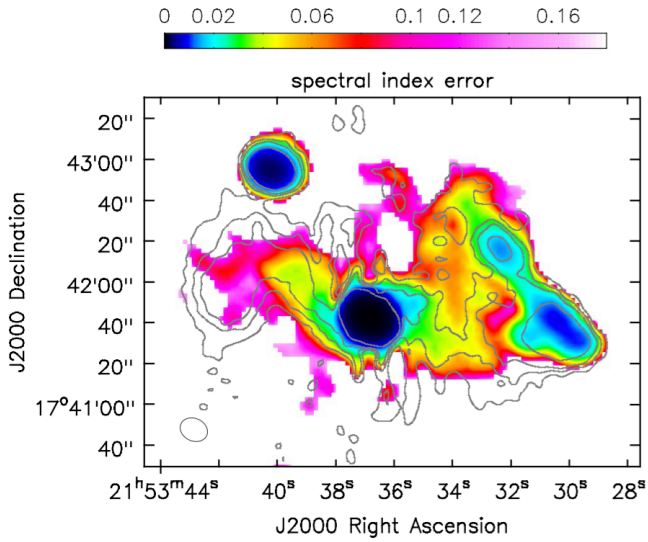

Figure 2.19: Spectral index error map of A2390 (α_{144}^{1500}) related to Fig. 2.13. Pixels below 3σ are blanked.

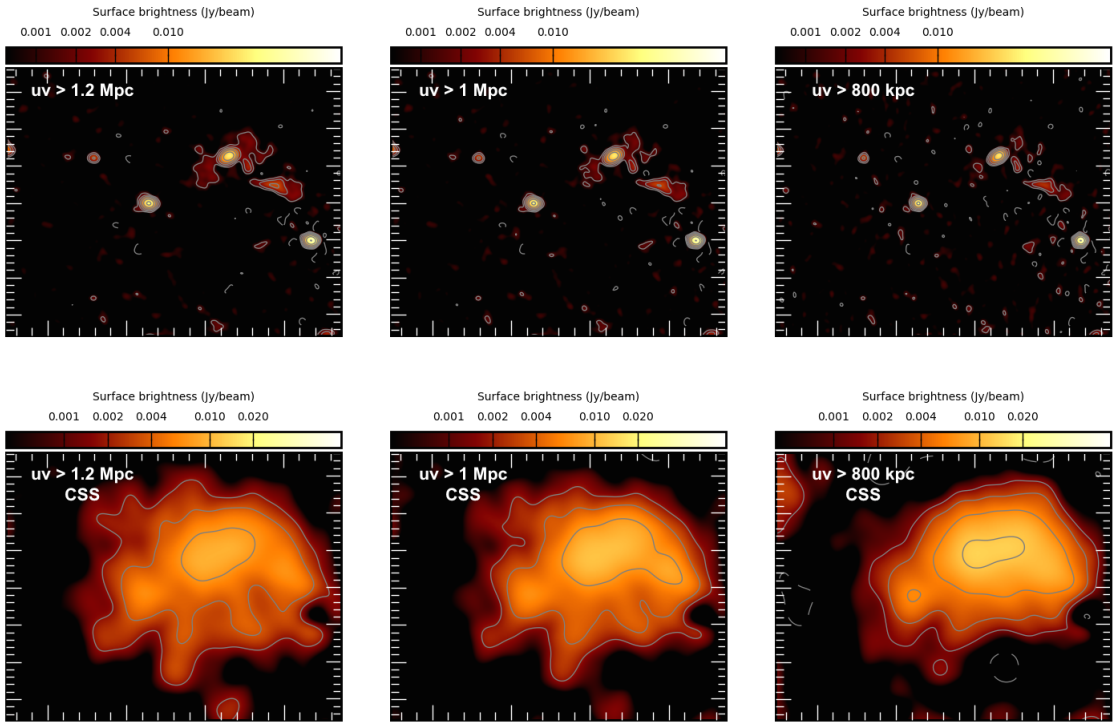

Figure 2.20: **Top row**: Images obtained by changing the *uv*-range of the LOFAR observation of A2261 with different cuts. Contours start at 3σ, where $\sigma = 450$ μJy beam^{-1}, and are spaced by a factor of 2. **Bottom row**: Corresponding *uv*-subtracted images. Different models of the discrete sources do not affect the detection of large-scale diffuse emission. Contours start at 3σ, where $\sigma = 600$ μJy beam^{-1}, and are spaced by a factor of 2.

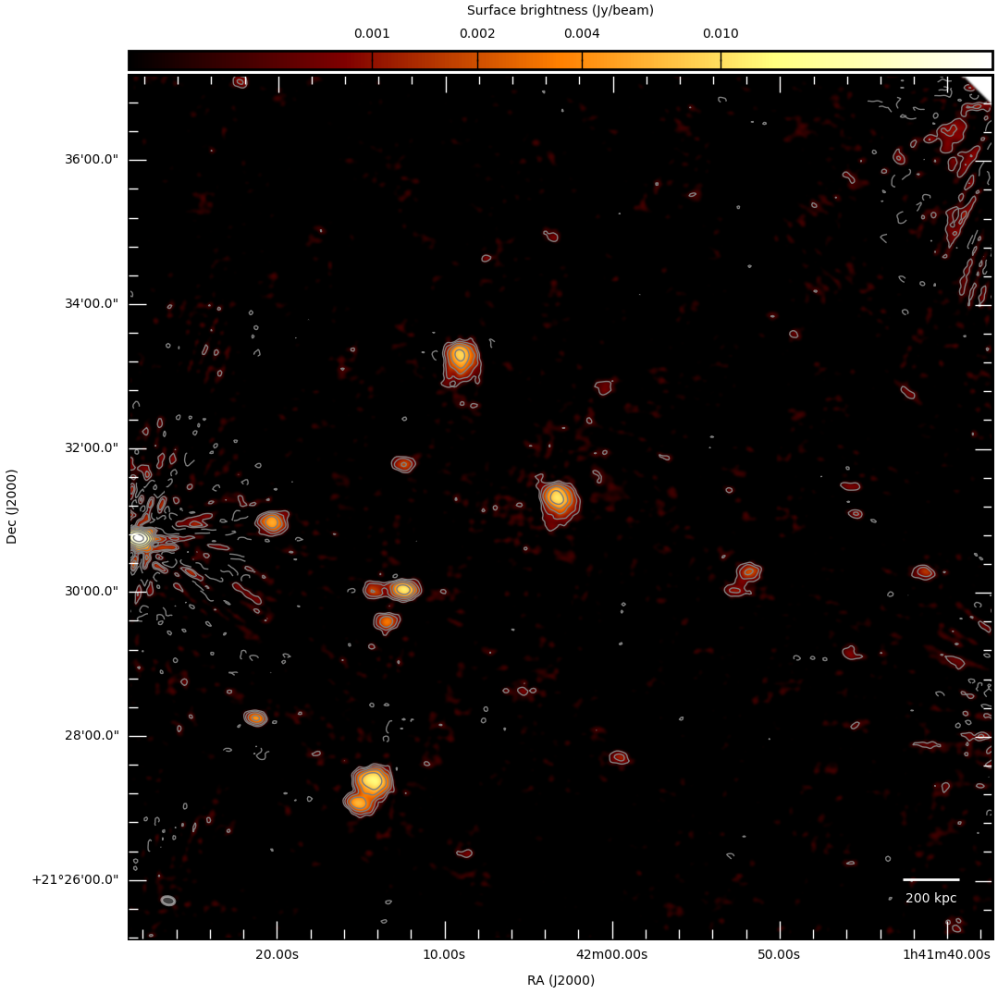

Figure 2.21: High-resolution 144 MHz LOFAR image of RXCJ0142.0+2131. The contour levels start at 3σ, where $\sigma = 150\ \mu\mathrm{Jy\,beam^{-1}}$, and are spaced by a factor of two. The negative contour level at -3σ is overlaid with a dashed line. The beam is $11'' \times 7''$ and is shown in grey in the bottom left corner of the image.

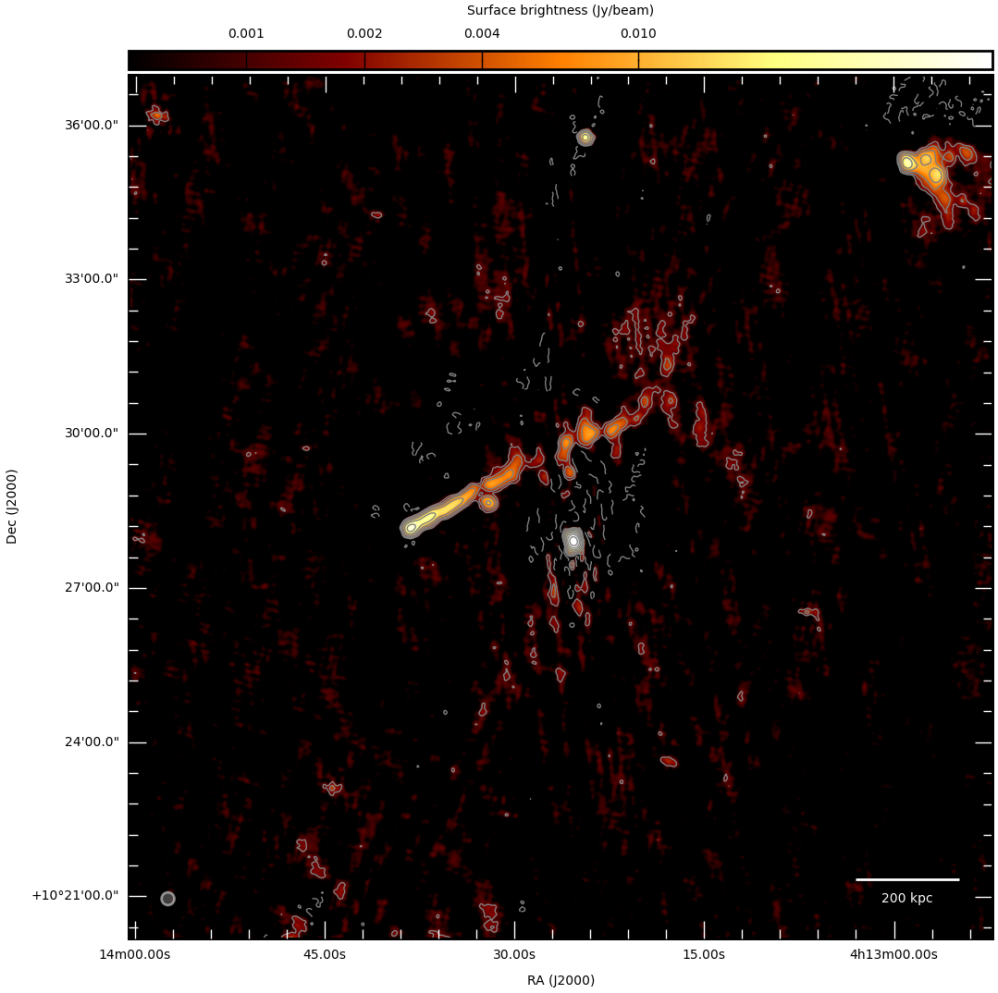

Figure 2.22: High-resolution 144 MHz LOFAR image of A478. The contour levels start at 3σ, where $\sigma = 450$ μJy beam^{-1}, and are spaced by a factor of two. The negative contour level at -3σ is overlaid with a dashed line. The beam is $15'' \times 15''$ and is shown in grey in the bottom left corner of the image. We note the presence in the field of an head-tail radio galaxy located to the north-west of the cluster centre, which has an optical counterpart but no redshift information.

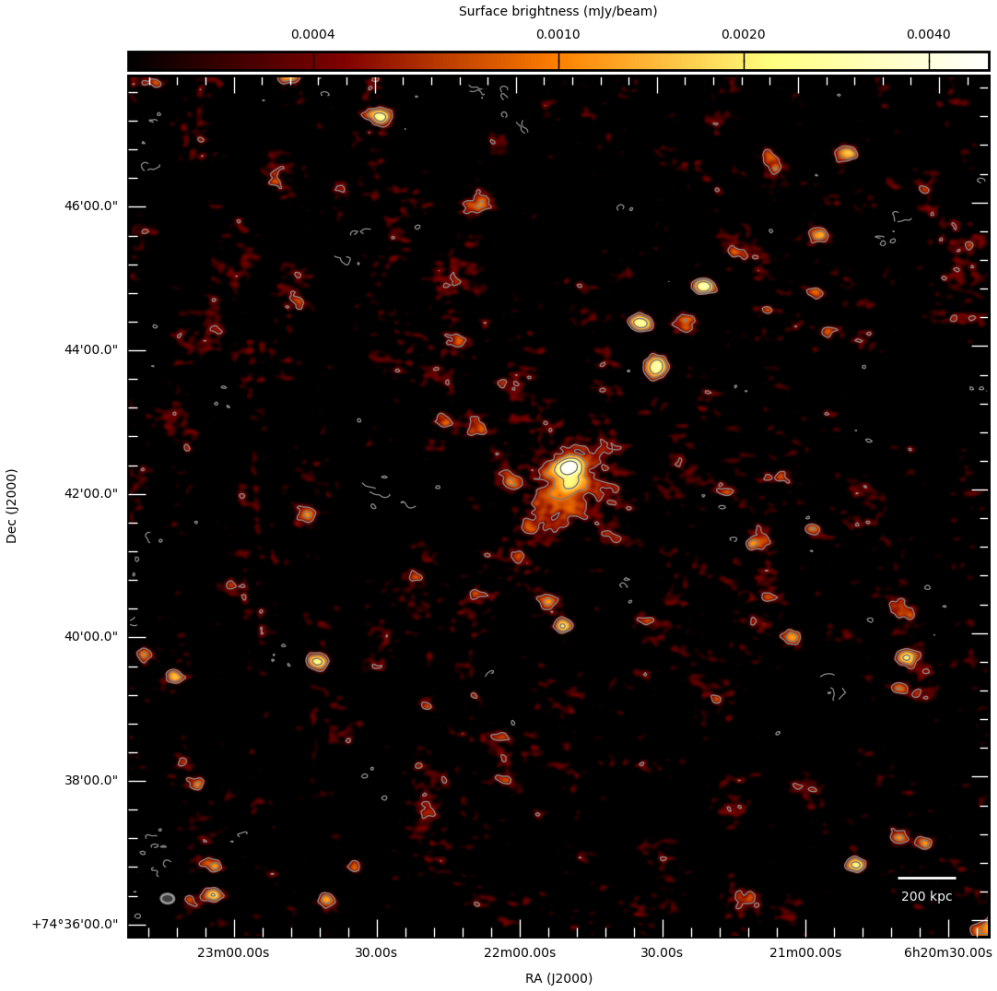

Figure 2.23: High-resolution 144 MHz LOFAR image of PSZ1G139.61+24. The contour levels start at 3σ, where $\sigma = 150\ \mu\mathrm{Jy\,beam^{-1}}$, and are spaced by a factor of two. The negative contour level at -3σ is overlaid with a dashed line. The beam is $11'' \times 8''$ and is shown in grey in the bottom left corner of the image.

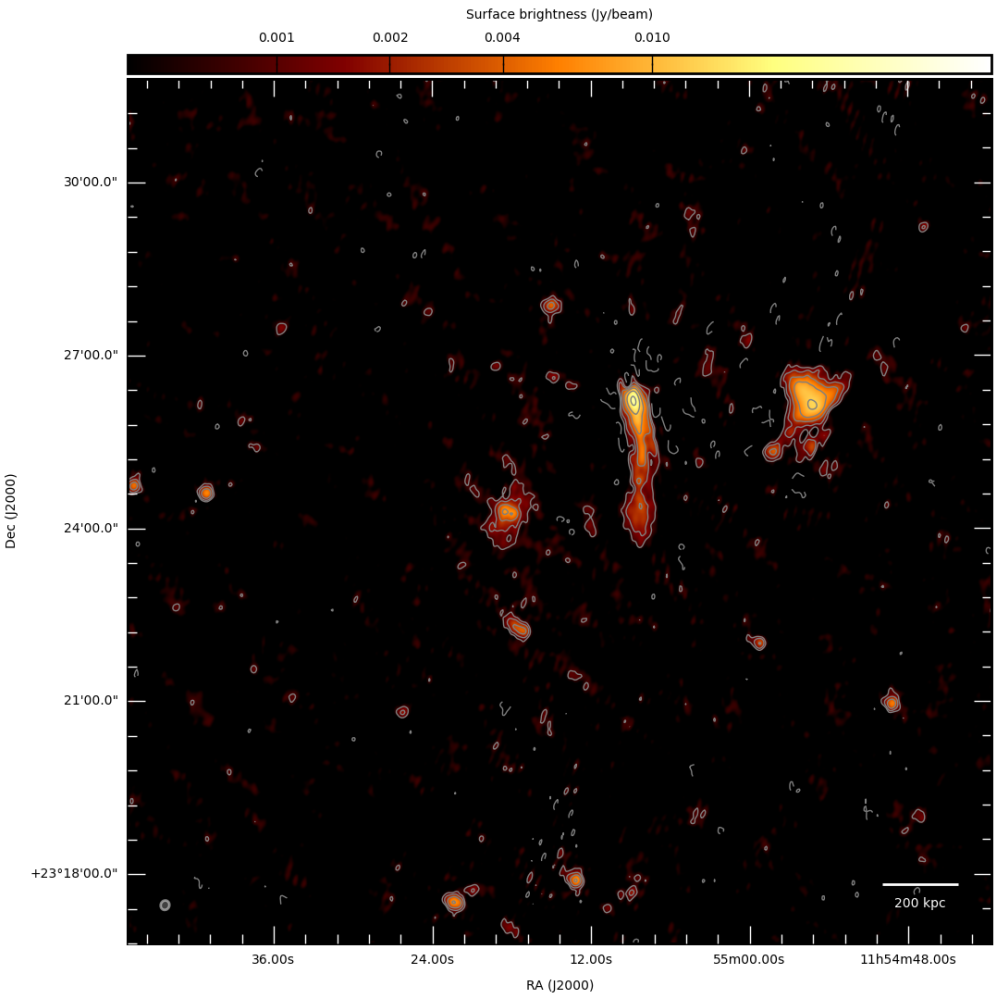

Figure 2.24: High-resolution 144 MHz LOFAR image of A1413. The contour levels start at 3σ, where $\sigma = 270\ \mu\mathrm{Jy\,beam}^{-1}$, and are spaced by a factor of two. The negative contour level at -3σ is overlaid with a dashed line. The beam is $10'' \times 9''$ and is shown in grey in the bottom left corner of the image. We note the presence in the field of a patch of diffuse emission located to the north-west of the cluster centre, which has no optical counter part.

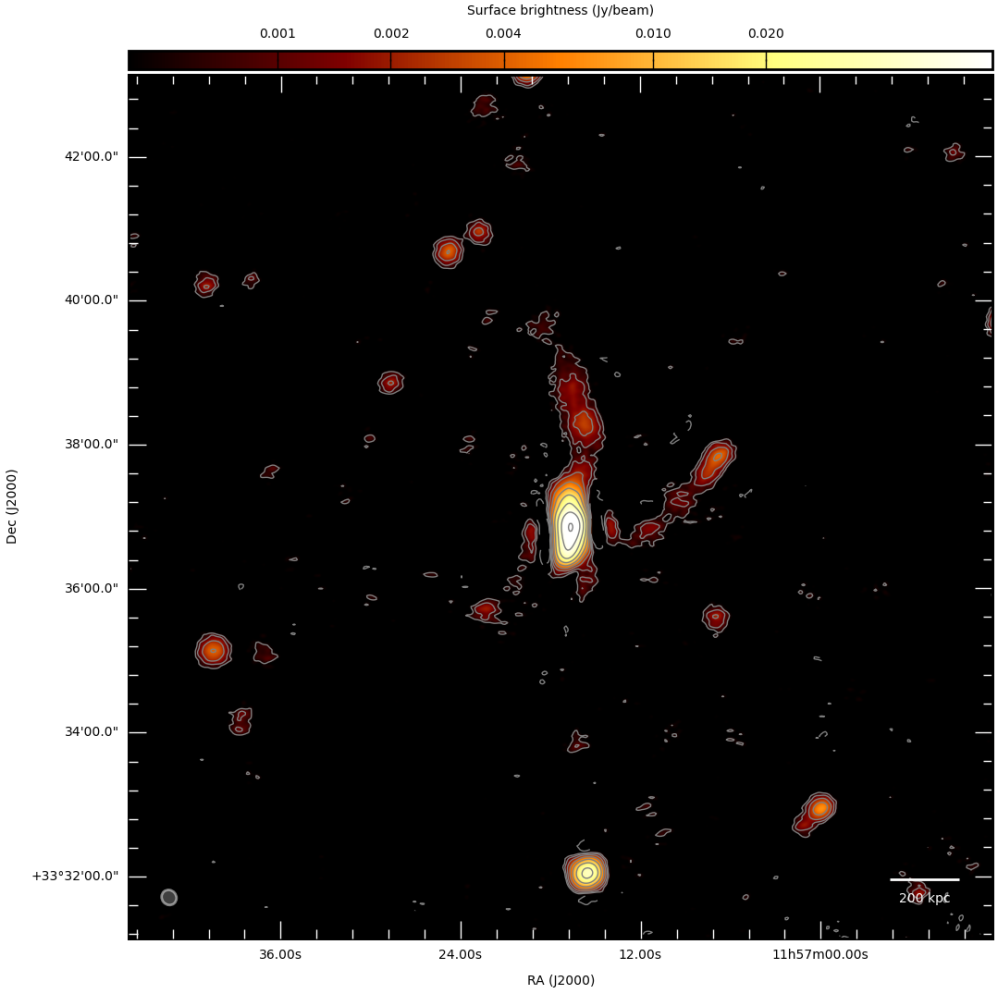

Figure 2.25: High-resolution 144 MHz LOFAR image of A1423. The contour levels start at 3σ, where $\sigma = 170\ \mu\mathrm{Jy\,beam}^{-1}$, and are spaced by a factor of two. The negative contour level at -3σ is overlaid with a dashed line. The beam is $13'' \times 12''$ and is shown in grey in the bottom left corner of the image.

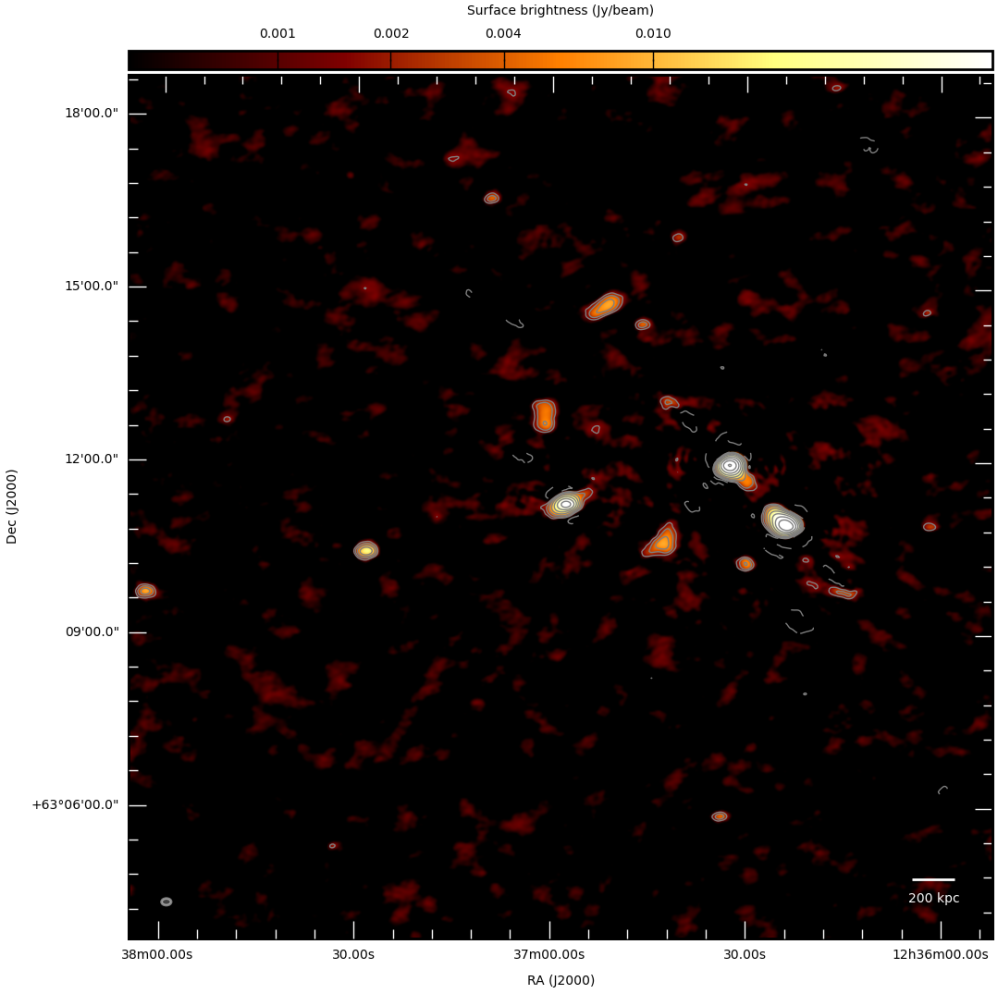

Figure 2.26: High-resolution 144 MHz LOFAR image of A1576. The contour levels start at 3σ, where $\sigma = 500\ \mu\mathrm{Jy\,beam}^{-1}$, and are spaced by a factor of two. The negative contour level at -3σ is overlaid with a dashed line. The beam is $10'' \times 7''$ and is shown in grey in the bottom left corner of the image.

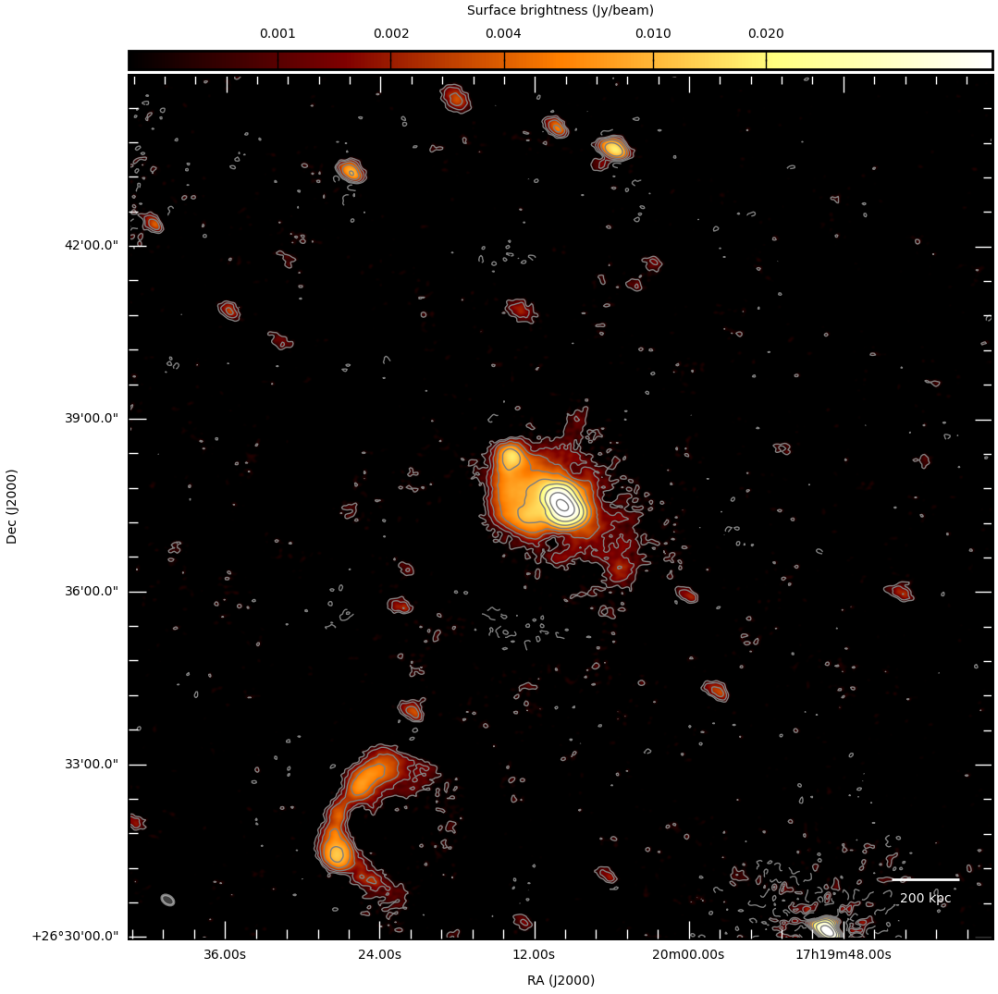

Figure 2.27: High-resolution 144 MHz LOFAR image of RXJ1720.1+2638. The contour levels start at 3σ, where $\sigma = 200\ \mu\mathrm{Jy\,beam^{-1}}$, and are spaced by a factor of two. The negative contour level at -3σ is overlaid with a dashed line. The beam is $14'' \times 9''$ and is shown in grey in the bottom left corner of the image. We note the presence in the field of a wide-angle tail radio galaxy located to the south-east of the cluster centre, which is associated with a cluster member galaxy at $z = 0.159$.

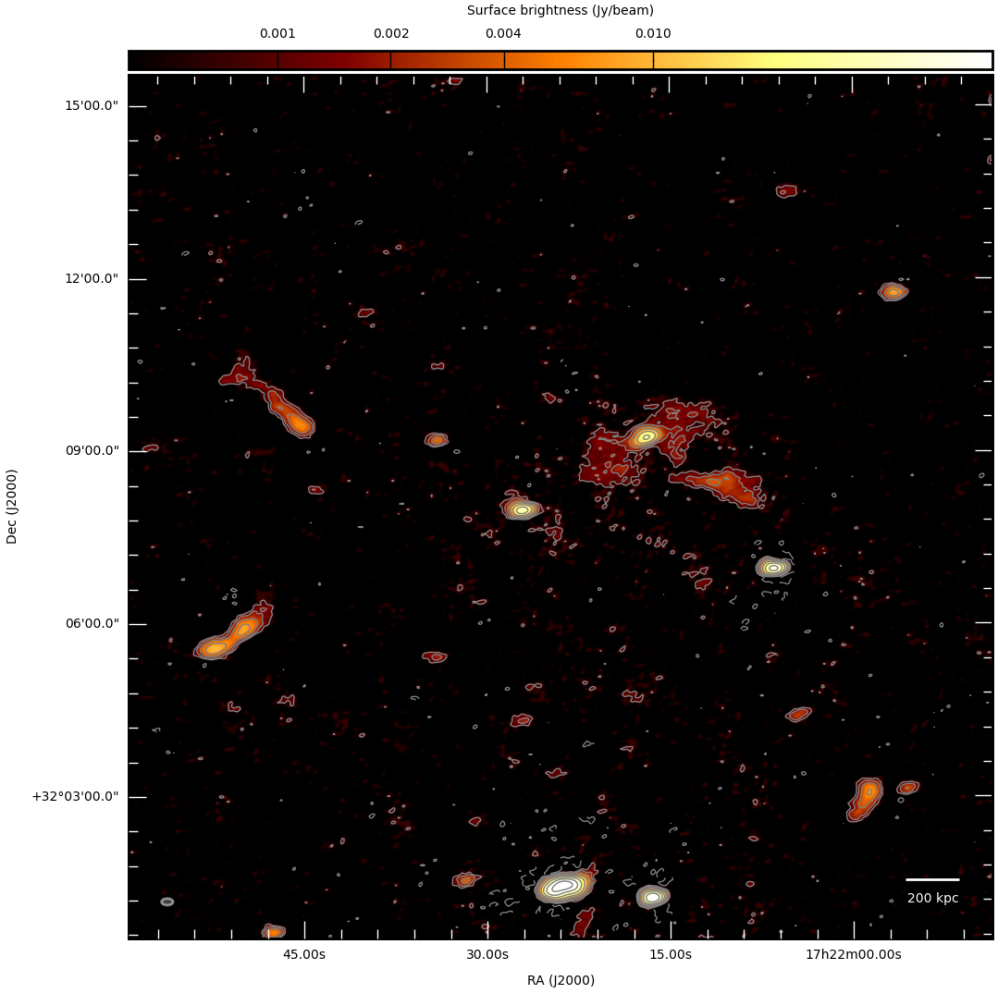

Figure 2.28: High-resolution 144 MHz LOFAR image of A2261. The contour levels start at 3σ, where $\sigma = 270\ \mu\mathrm{Jy\,beam}^{-1}$, and are spaced by a factor of two. The negative contour level at -3σ is overlaid with a dashed line. The beam is $12'' \times 7''$ and is shown in grey in the bottom left corner of the image. We note the presence in the field of a tail located to the north-east of the cluster centre, which has an optical counterpart but no redshift information.

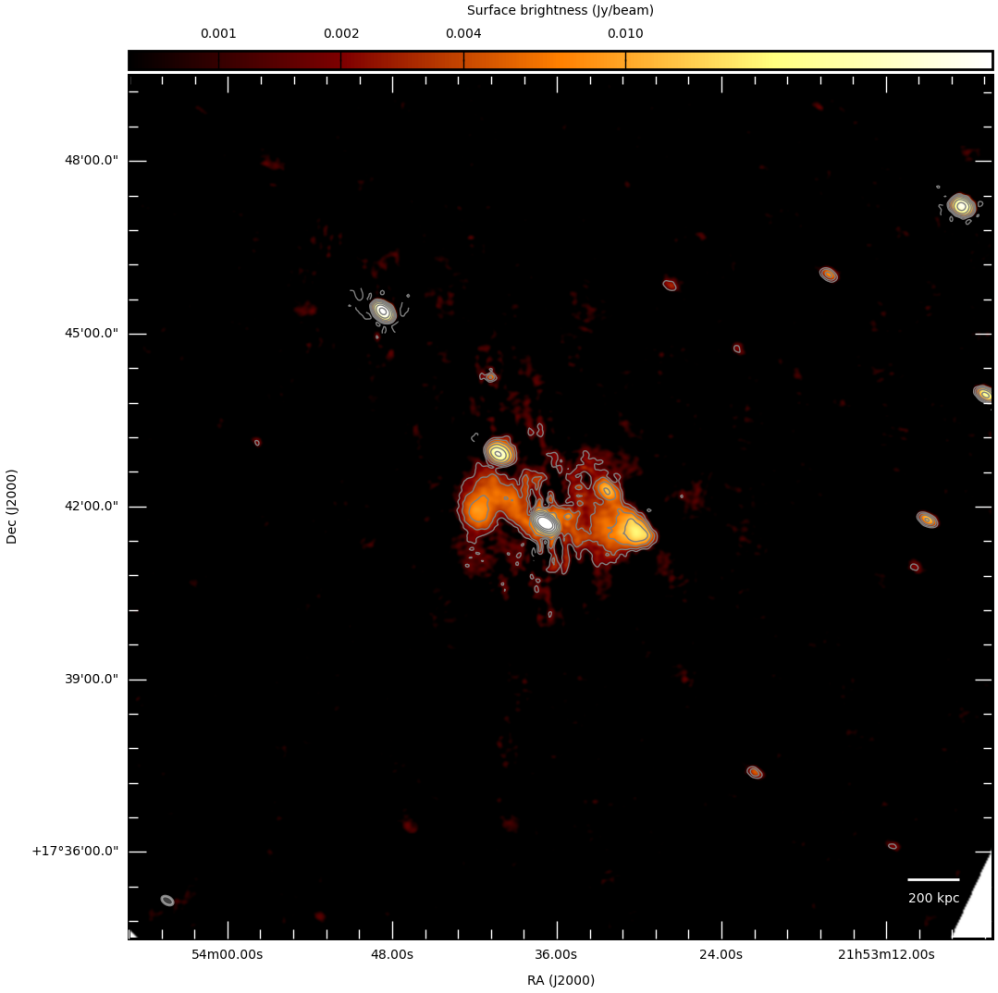

Figure 2.29: High-resolution 144 MHz LOFAR image of A2390. The contour levels start at 3σ, where $\sigma = 400\ \mu\mathrm{Jy\,beam^{-1}}$, and are spaced by a factor of two. The negative contour level at -3σ is overlaid with a dashed line. The beam is $13'' \times 8''$ and is shown in grey in the bottom left corner of the image.

Chapter 3

First evidence of diffuse ultra-steep-spectrum radio emission surrounding the cool core of a cluster

Federica Savini, Annalisa Bonafede, Marcus Brüggen, Reinout van Weeren, Gianfranco Brunetti, Huib Intema, Andrea Botteon, Timothy Shimwell, Amanda Wilber, David Rafferty, Simona Giacintucci, Rossella Cassano, Virginia Cuciti, Francesco de Gasperin, Huub Röttgering Matthias Hoeft, Glenn White

MNRAS, accepted on 2018, April 27

Abstract

Diffuse synchrotron radio emission from cosmic ray electrons is observed at the center of a number of galaxy clusters. These sources can be classified either as giant radio halos, which occur in merging clusters, or as mini halos, which are found only in cool-core clusters. In this paper, we present the first discovery of a cool-core cluster with an associated mini halo that also shows ultra-steep-spectrum emission extending well beyond the core that resembles radio halo emission. The large-scale component is discovered thanks to LOFAR observations at 144 MHz. We also analyze GMRT observations at 610 MHz to characterize the spectrum of the radio emission. An X-ray analysis reveals that the cluster is slightly disturbed, and we suggest that the steep-spectrum radio emission outside the core could be produced by a minor merger that powers electron re-acceleration without disrupting the cool core. This discovery suggests that, under particular circumstances, both a mini and giant halo could co-exist in a single cluster, opening new perspectives for particle acceleration mechanisms in galaxy clusters.

3.1 Introduction

An increasing number of diffuse radio sources associated with galaxy clusters are being detected with the advent of new facilities and techniques at low radio frequencies. Not only has the number of sources increased, but the quality of imaging in terms of resolution and noise has also improved, revealing various source morphologies and properties that might require a broadening of the taxonomy of radio emission in galaxy clusters (e.g. [de Gasperin et al., 2017]). Diffuse emission in the form of giant radio halos or mini halos is found in the central regions of some galaxy clusters. These sources have low surface brightnesses and steep radio spectra[1] that make them much brighter at lower frequencies. The Low Frequency Array (LOFAR; [van Haarlem et al., 2013b]) operating between 30 and 240 MHz can discover steep-spectrum sources that are impossible to detect with other radio telescopes.

Giant radio halos have typical sizes of 1 to 2 Mpc, and are predominantly found in massive, merging clusters (e.g. [Buote, 2001], [Cassano et al., 2010], [Cuciti et al., 2015]), suggesting that merger-driven turbulence re-accelerates primary or secondary electrons in the ICM (e.g. [Brunetti et al., 2007], [Brunetti & Lazarian, 2011], [Pinzke et al., 2017]). Mini halos have typical sizes of a few hundred kpc and a higher emissivity than giant halos (e.g. [Cassano et al., 2008b], [Murgia et al., 2009]). Mini halos are found exclusively in cool-core clusters, and are confined within the inner regions of the cluster (e.g. [Govoni et al., 2009], [Kale et al., 2015], [Giacintucci et al., 2017]). Cool-core clusters display a peaked X-ray surface brightness and a significant drop in temperature ($< 10^7 - 10^8$ K) at the centre. Signatures of minor mergers have been detected in some cool-core clusters which host mini halos [Mazzotta & Giacintucci, 2008]. When the low-entropy central gas at the bottom of the Dark Matter potential well is perturbed by a minor merger and meets the higher-entropy ICM, a discontinuity in the X-ray emissivity, called a cold front, is formed. The gas then falls back into the Dark Matter potential well and "sloshes", possibly generating the turbulence that re-accelerates weakly relativistic electrons within the core [ZuHone et al., 2013]. Particle acceleration by turbulence is an inefficient mechanism and according to theoretical models only major mergers between massive clusters can dissipate enough energy to power radio emission on Mpc scales up to GHz frequencies. So far, it is unknown what happens when a cool-core cluster hosting a mini halo undergoes a minor merger that does not disrupt the core. This scenario is particularly interesting when observed at low radio frequencies, as it may provide new insights on the connections between mini halos, giant radio halos, and the cluster dynamics.

In this paper we report on the results of a LOFAR radio observation of the galaxy cluster PSZ139139.61+24.20. We assume a flat, ΛCDM cosmology with matter density $\Omega_M = 0.3$ and Hubble constant $H_0 = 67.8$ km s^{-1} Mpc^{-1} [Planck Collaboration et al., 2016]. The angular to physical scale conversion at z = 0.267 is 4.137 kpc/″. All our images are in the J2000 coordinate system.

[1]The radio spectrum follows a power law $S(\nu) \propto \nu^{\alpha}$, where S is the flux density, and ν the observing frequency. Steep spectrum radio sources spectra have spectral indices $\alpha < -1$.

Table 3.1: Properties of the galaxy cluster PSZ1G139.61+24.20 [Giacintucci et al., 2017]. (1),(2),(3),(4): Target coordinates; (5): Redshift; (6): Global temperature computed within the radius enclosing a mean density of 2500 times the critical density at the cluster redshift. Note that the central region with a radius of 70 kpc was excised; (7): Core entropy; (8): Mass within the radius enclosing a mean density of 500 times the critical density [Planck Collaboration et al., 2014]; (9): Radius that encloses a mean overdensity of 500 with respect to the critical density at the cluster redshift.

1: RA (h:m:s)	06:22:13.9
2: DEC (°:′:″)	+74:41:39.0
3: l (°)	95.57
4: b (°)	74.69
5: z	0.267
6: kT (keV)	7.5 ± 0.4
7: K_0 (keV cm^2)	< 20
8: M_{500} ($\times 10^{14}$ $M_\odot$)	7.1 ± 0.6
9: R_{500} (Mpc)	1.24

3.1.1 The cluster

PSZ1G139.61+24 (z = 0.267, RA = 06:22:13.9, DEC = +74:41:39.0; hereafter PSZ139) has been classified as a galaxy cluster through detection of the Sunyaev-Zel'dovoch effect with the Planck satellite [Planck Collaboration et al., 2014]. Using GMRT observations at 610 MHz, Giacintucci et al. [2017] report the detection of a tentative mini halo with an overall source size of $\sim$ 100 kpc located at the cluster centre. They also present density and temperature profiles derived from a Chandra X-ray observation of PSZ139. Details can be found in Tab. 4.1. The cluster core is characterized by low values of temperature, and the temperature profile inverts and starts decreasing approaching the cluster centre within a radius of $\sim$ 100 kpc (see Fig.2 in Giacintucci et al. [2017]). The specific entropy [Cavagnolo et al., 2009] at the cluster centre, K_0, is used to distinguish between cool-core or non cool-core clusters [Giacintucci et al., 2017]: clusters with low central entropies ($K_0 < 30 - 50$ keV cm^2) are expected to host a cool core. The specific entropy of PSZ139 is $K_0 < 20$ keV cm^2 [Giacintucci et al., 2017], indicating that this cluster has a cool core.

3.2 Data reduction

3.2.1 LOFAR radio observation

The cluster PSZ139 was observed as part of the LOFAR Two-Metre Sky Survey (LoTSS; [Shimwell et al., 2017]) at High Band Antenna (HBA) frequencies (120 - 168 MHz). The observation was carried out on July 27, 2017 (ID LC8_022) with a total on-source time of 8 h preceded and followed by a flux calibrator (3C295) observation of 10 min. The calibration and imaging procedure is based on the Facet Calibration scheme presented in van Weeren et al. [2016a]. A complete outline of the procedure can be found in Savini et al. [2018c]; here we will only briefly summarize the main steps:

Table 3.2: Col. 1: Telescope/Survey; Col. 2: Central frequency; Col. 3: Minimum baseline; Col. 4: Largest angular scale; Col. 5: Resolution; Col. 6: rms noise level; Col. 7: Parameters used for LOFAR and GMRT imaging, such as gaussian taper (T) and weighting scheme; when Briggs weighting scheme is used, the robust value is specified [Briggs, 1995].

1: Telescope	2: Freq. (MHz)	3: B_{min} (λ)	4: LAS ($'$)	5: Res.	6: rms (μJy/beam)	7: Imaging
LOFAR	144	80	43	$5''\times 5''$	140	Briggs -0.25
		80	43	$11''\times 8''$	150	Briggs -0.25
		80	43	$35''\times 35''$	500	Briggs 0, $20''$ T
		200	17	$18''\times 18''$	240	uniform, $20''$ T
GMRT	610	150	23	$8.0''\times 4.7''$	27	Briggs -0.1
		150	23	$32''\times 32''$	180	Briggs 0, $20''$ T
		200	17	$20''\times 20''$	130	uniform, $20''$ T

- Preliminary pre-processing was performed by the Radio Observatory (ASTRON) and has been applied to the data;
- Initial calibration was performed using the standard LOFAR direction independent calibration pipeline[2];
- Flagging was performed after inspecting the dataset; bad data were found and flagged for a total of 30 min;
- To refine the calibration, a pipelined version of the direction dependent Facet Calibration procedure was used[3].

In Facet Calibration the field of view is divided up into a discrete number of directions (facets) that are separately calibrated through the selection of a calibrator (with a minimum flux of 0.5 Jy) for each facet. The coordinates of PSZ139 and a $15'$ radius around it were also specified to include the source in one single facet. We processed 13 facets, i.e. the brightest sources in the field and those bordering the facet containing PSZ139, which was then processed at last, so that it could benefit from the calibration of the preceding facets. All the images were corrected for the station primary beam.

Due to inaccuracies in the LOFAR beam model the images can require rescaling (e.g. [Harwood et al., 2016]). In line with other LOFAR studies [van Weeren et al., 2014], we have cross-checked the 144 MHz LOFAR flux scale against the 150 MHz TIFR GMRT Sky Survey (TGSS; [Intema et al., 2017]) using 50 compact sources. We found and applied a scaling factor of 0.75 with a scatter that we take into account by assigning a 15% uncertainty in our flux scale.

Radio imaging was performed using the Common Astronomy Software Applications (CASA, version 4.5.2; [McMullin et al., 2007]) tools with different parameters to obtain

[2]https://github.com/lofar-astron/prefactor
[3]https://github.com/lofar-astron/factor

different resolutions and increase the sensitivity to diffuse emission. The imaging details are summarized in Table 4.3.1.

3.2.2 GMRT radio observation

GMRT observations at 610 MHz were collected during two distinct observations on October 25, 2014, and September 4, 2015, under project codes 27_025 and 28_077, respectively. Visibilities were recorded in two polarizations (RR and LL) over a bandwidth of 33.3 MHz. The total combined on-source time was 9.4 h. The GMRT data were pre-calibrated, combined and processed using the SPAM pipeline (see Intema et al. [2017] for details). The primary calibrators used for flux and bandpass calibrations were 3C147 and 3C48, respectively. We adopted the same flux standard as for LOFAR [Scaife & Heald, 2012]. A $T_{\rm sys}$ correction of 0.92 was derived using the all-sky map at 408 MHz by Haslam et al. [1995], and applied. Both observations had 4 of the 30 antennas not working properly. Removing them during pre-calibration resulted in a 25% data loss. Furthermore, the pipeline removed another 15% of the data due to RFI and various telescope issues. The pipeline output visibilities were imported into CASA for final imaging, using the multi-scale option of the `clean` task. Our highest-fidelity images reach a sensitivity of 27 μJy/beam with a $8.0'' \times 4.7''$ beam. We adopted a 10% scale error on all flux density measurements [Chandra et al., 2004].

3.2.3 Chandra X-ray observation

We reprocessed Chandra X-ray observations merging two Chandra ACIS-I observations of PSZ139 in `VFAINT` mode with a total exposure time of 28 ks (ObsID: 15139, 15297). Data were reprocessed with CIAO v4.9 and Chandra CALDB v4.7.3 using the `level=1` event file, following the standard Chandra reduction threads. Soft proton flares were removed by inspecting the light curves extracted in the S2 chip using the `deflare` script. The resulting exposure time after this procedure is 23.1 ks. A single point spread function map at 1.5 keV was obtained combining the corresponding exposure maps for each ObsID, then point sources were detected with `wavdetect`, confirmed by eye and removed in the further analysis. Spectra were fitted in the 0.5-11.0 keV band with XSPEC v12.9.0o adopting an absorbed thermal model with metallicity fixed at 0.3 $Z_{\odot}$ for the ICM emission and with a fixed column density [Kalberla et al., 2005] $N_{\rm H} = 8.1 \times 10^{20}$ cm^{-2} accounting for the Galactic absorption in the direction of the cluster. The background was treated as follows: the astrophysical background was assumed to be composed of a Galactic component, modeled with a two temperature-plasma (with $kT_1 = 0.14$ keV and $kT_2 = 0.25$ keV), and a cosmic X-ray background component, modeled with an absorbed power-law (with $\Gamma = 1.4$); the instrumental background was modeled following the analytical approach proposed in Bartalucci et al. [2014]. The X-ray analysis follows the procedure described in Botteon et al. [2018], to which we refer the reader for more details.

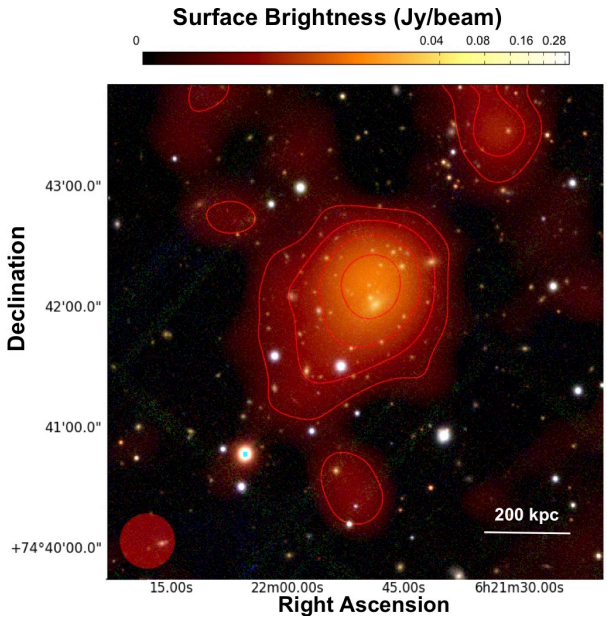

Figure 3.1: Optical Pan-STARRS g, r, i mosaic image with the 144 MHz LOFAR smoothed image overlaid. The contour levels are at $(-1, 1, 2, 4, 8) \times 3\sigma$ where $\sigma = 500$ μJy/beam. The beam is $35'' \times 35''$, and is shown at the bottom left of the image.

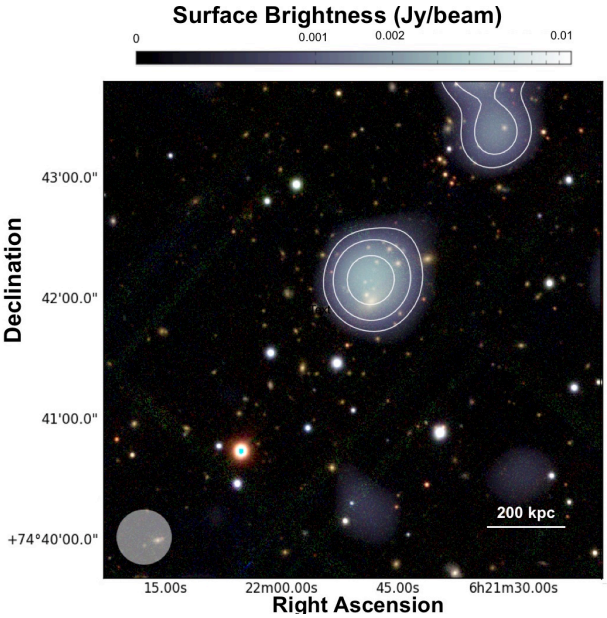

Figure 3.2: Optical Pan-STARRS g, r, i mosaic image with the 610 MHz GMRT smoothed image overlaid. The contour levels are at $(-1, 1, 2, 4) \times 3\sigma$ where $\sigma = 180$ μJy/beam. The beam is $35'' \times 35''$, and is shown at the bottom left of the image.

3.3 Results

3.3.1 Radio analysis

Using LOFAR observations at 144 MHz, we have discovered previously undetected cluster-scale diffuse emission in PSZ139, as visible in Fig. 3.1. We have re-analysed two archival 610 MHz GMRT observations, and combined their visibilities to achieve better sensitivity and *uv*-coverage. In Fig. 3.1 and 3.2, we present the low-resolution LOFAR and GMRT radio images. The images were smoothed to enhance the diffuse emission, and are overlaid onto Pan-STARRS g, r, i optical images [Chambers et al., 2016]. In Fig. 3.3, we present the high-resolution radio contours in the core region of the cluster. This consists of two radio components: one at the cluster centre where also the X-ray peak is, and one towards the N. The central source is likely to be related to the Brightest Central Galaxy (BCG) that is visible in the optical image, whilst there is no obvious optical counterpart for the northern radio brightness source that might be a foreground radio galaxy. For our analysis, we have considered the X-ray centre as the cluster centre.
Although both GMRT and LOFAR detect emission in the inner 200 kpc, i.e. within the core, LOFAR reveals a more extended component which is not detected in the GMRT image. To confirm the detection of radio diffuse emission from PSZ139, we re-imaged the GMRT residual visibilities (after subtracting the full-resolution model image) with a gaussian taper of 25″ while enhancing the contribution of the short baselines with a Briggs weighting scheme (robust=0). We detected emission above 3σ on a scale marginally larger than the cluster core ($\sim$ 350 kpc, having a beam size equivalent to 75 kpc). Since we do not detect emission that corresponds to the halo observed with LOFAR, and since instrumental differences of the two observations must be taken into account, we did not use this image to derive spectral index information, but proceeded with a more conservative approach, as explained in Section 4.4.

From the LOFAR image, we measure an overall source size of $D_{\rm radio} \sim 550$ kpc. This value has been estimated as $D_{\rm radio} = \sqrt{D_{\rm min} \times D_{\rm max}}$, where $D_{\rm min}$ and $D_{\rm max}$ are the minimum and maximum diameter of the 3σ surface brightness isocontours. Since this value may depend on the sensitivity of the observation, we have also estimated the e-folding radius, $r_{\rm e}$, which is defined as the radius at which the brightness drops to I_0/e, where I_0 is the central brightness of the source. Following Murgia et al. [2009], we have obtained the radio brightness average in concentric circular annuli centred on the X-ray centre with widths of 12″ ($\sim$ 50 kpc) that is 1/2 FWHM of the synthesized beam, and assumed a profile that follows the simple exponential law $I(r) = I_0\, e^{-r/r_e}$. We convolved the exponential profile with a gaussian with FWHM equal to the beam, obtaining the convolved profile that we used to fit the data points shown in Fig. 3.4. The error of each annulus is equal to $\sqrt{\sigma^2_{\rm flux} + \sigma^2 \times N}$ where the first contribution is the calibration error on the surface brightness and the second one is the noise level of the radio image weighted by the number of beam in the annulus. The best-fit values are $r_e = 94 \pm 10$ kpc and $I_0 = 48 \pm 2\,\mu$Jy/arcsec^2. The fit shows a relatively compact ($r_{\rm e} \sim 94$ kpc) emission in the core region. Larger-scale emission, although faint, can be seen beyond the core region, especially extending towards the SE.

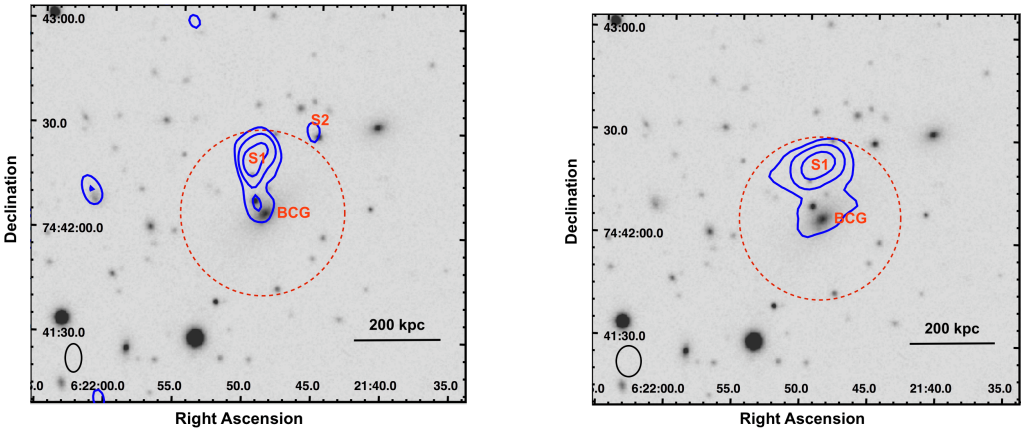

Figure 3.3: Optical Pan-STARRS image in gray scale with the high-resolution 610 MHz GMRT (top) and 144 MHz LOFAR (bottom) blue contours overlaid. The GMRT and LOFAR beam is $8.0'' \times 4.7''$ and $8.0'' \times 6.5''$ respectively, and the GMRT and LOFAR levels are $(2, 4, 8) \times 3\sigma$ where $\sigma = 27$ μJy/beam and $\sigma = 140$ μJy/beam respectively. The central radio components are indicated with labels: BCG is the brightest central galaxy that corresponds also to the X-ray centre; S1 is a source that has no obvious optical counterpart, and is likely to be a background galaxy; S2 is a faint source that is not detected in the LOFAR image. The dashed red region indicated the core region of the cluster, which has a size of ~ 200 kpc.

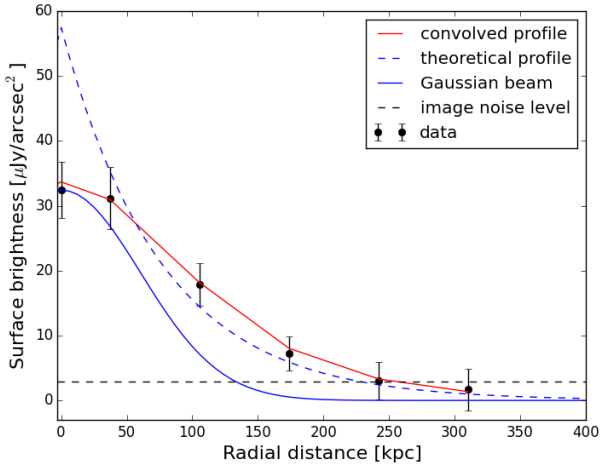

Figure 3.4: The azimuthally-averaged brightness profiles of the radio emission in PSZ139. The best-fit line is indicated in red, and the 3σ noise level of the radio image is indicated with a horizontal dashed-dotted black line. The best-fit values are $r_e = 94 \pm 10$ kpc and $I_0 = 48 \pm 2\,\mu$Jy/arcsec^2.

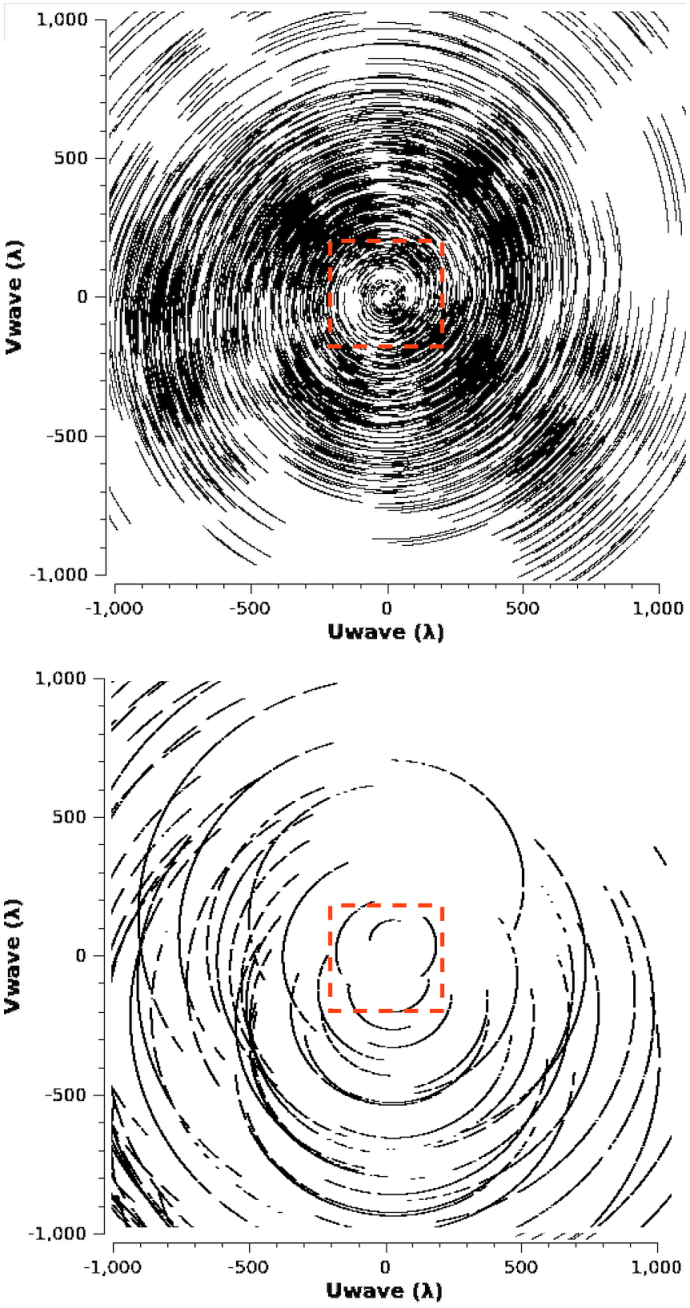

Figure 3.5: Plots of the inner *uv*-plane coverage of the LOFAR observation (three time chunks are plotted; top panel) and GMRT observation (bottom panel). The red box indicates the region within 200λ that was excluded in the imaging process for the spectral analysis. To minimise the difference between the two observations we have also used a uniform weighting parameter.

Spectral analysis

We have re-imaged the LOFAR and GMRT datasets with a guassian taper of $20''$, same pixel size, baseline range (200 - 40000 λ) and uniform weighting scheme to minimize the differences in the *uv*-coverage of the two interferometers.

Since only the central region of the cluster can be seen both at 610 MHz and 144 MHz, we have measured the value of the average spectral index of the inner $D_{\rm radio} \sim 200$ kpc. To ensure that no contamination from AGN or background sources was included in our estimate of the spectral index of the core region, we measured the integrated surface brightness of the compact sources detected in the high resolution image within the 6σ GMRT and LOFAR contours, as shown in Fig. 3.3; we then measured the integrated surface brightness of the entire core region (inner $\sim$200 kpc, indicated by a dashed red circle), and finally we subtracted the contribution of the compact sources[4]. We obtained $\alpha_{144}^{610} = -1.3 \pm 0.1$. The error takes into account the flux calibration error. To confirm this value, we also calculated the spectral index, completely masking the sources at 6σ, obtaining a consistent value.

To constrain the spectral properties of the diffuse emission (i.e. emission outside the inner $\sim$ 200 kpc) that was detected in the LOFAR image only, we have also used the LOFAR and GMRT dataset re-imaged with uniform weighting and same *uv*-range mentioned above. We first considered the LOFAR mean surface brightness of the diffuse emission (3.5 mJy/beam) and the GMRT rms noise (0.17 mJy/beam), deriving $\alpha_{144}^{610} \leq -1.9$. The inner *uv*-coverage of the GMRT and LOFAR datasets are different (see Fig. 3.5). Although the radio emission extends on a scale of $2'$, that is well sampled by both observations, we have injected a mock radio halo in the GMRT visibilities. Using this procedure, we can image the diffuse emission and place an upper limit on the spectral index given the specific *uv*-coverage of that observation. The mock source was modeled with the exponential law and the parameters obtained from the best-fit of the radio surface brightness profile. The model was Fourier transformed into the visibilities of the GMRT dataset taking into account the w-projection effect, which is necessary due to the large field of view and low frequency. We added the mock sources to the original visibilities in a region close to the cluster but without bright sources and clear noise structures, such as negative holes, and then re-imaged the dataset with uniform weighting and measured the properties of the recovered simulated emission. We created a set of mock sources assuming different spectral indices, i.e. with different integrated flux densities. We started with $\alpha_{144}^{610} = -1$ and then we lowered the value, until the recovered flux of the mock source could not be considered detected anymore, i.e. when the emission was $< 2\sigma$ and the extension $< 3r_e$. Using this procedure, we put an upper limit of $\alpha < -1.7$.

On the basis of the spectral information and surface brightness we derived in our radio analysis, we can distinguish two components of the radio emission:

[4]The best strategy would be subtracting the compact sources from the visibilities of the LOFAR and GMRT observations. However, in this case this procedure is uncertain, since these compact sources may have extended components (e.g. lobes) that are not easily separable from the surrounding emission.

- a flatter-spectrum ($\alpha_{144}^{610} = -1.3 \pm 0.1$), higher-brightness ($\sim$ 8 - 9 mJy/beam at 144 MHz) component within the cluster core with a size of $D_{\rm radio} \sim 200$ kpc, classified as mini halo by Giacintucci et al. [2017];
- a steeper-spectrum ($\alpha_{144}^{610} < -1.7$), lower-brightness ($\sim$ 1 - 2 mJy/beam at 144 MHz) component visible on larger scales at low frequencies.

3.3.2 X-ray analysis

Merger activity in clusters leaves a clear imprint on the X-ray brightness distribution, hence the morphology of the ICM provides a way to discriminate between merging and non-merging clusters. Here, we focus on two morphological indicators that can be derived from the X-ray surface brightness distribution [Cuciti et al., 2015]: the emission centroid shift w and the concentration parameter c. The former is defined as the standard deviation of the projected separation between the peak and centroid of the X-ray surface brightness distribution when the aperture used to compute it decreases from a maximum radius of 500 kpc to smaller radii. The latter is defined as the ratio of the X-ray surface brightness within a radius of 100 kpc over X-ray surface brightness within a radius of 500 kpc. High values of w indicate a dynamically disturbed system, whilst high values of c indicate a peaked core, typical of non-merging systems. The position of PSZ139 in the $w - c$ diagram, based on Chandra X-ray observations, is reported in Fig. 3.6, where we see that despite the high value of the concentration parameter ($c = 0.362^{+0.007}_{-0.004}$), the value of the emission centroid shift ($w = 1.35^{+0.18}_{-0.17} \times 10^{-2}$) is intermediate between merging and non-merging systems [Cassano et al., 2016]. These values strengthen the argument that the cluster hosts a cool core (as also suggested by the low central entropy of the ICM) but is not fully virialised (relaxed).

We reprocessed Chandra observations of the cluster in the 0.5-2.0 keV band to search for possible surface brightness and temperature jumps. We obtained a projected temperature map of the ICM using CONTBIN v1.4 [Sanders, 2006] shown in the bottom panel of Fig. 3.7. Given the short exposure of the Chandra observations, we required 900 background-subtracted counts per bin. This resulted in 8 spectral regions that were then extracted and fitted. The temperature map clearly shows the presence of the cool core, and indicates a temperature jump from the central regions outwards in the NW direction. We then obtained the surface brightness profile and found a discontinuity towards the NW direction. The profile extraction and fitting were performed with PROFFIT [Eckert et al., 2011] on the exposure-corrected image of the cluster. The spectral profile was extracted in the sector indicated in grey in the top left panel of Fig. 3.7 and fitted with three models: broken-power law, power-law, and beta-model. The profile is best described by a broken power-law with compression factor $C = 1.7 \pm 0.1$. The spectral analysis provides temperatures of $6.8^{+1.0}_{-0.8}$ keV and $10.2^{+4.0}_{-2.2}$ keV in the upstream and downstream regions, respectively. In general, both shocks and cold fronts are sharp surface brightness discontinuities [Markevitch & Vikhlinin, 2007], however shocks mark pressure discontinuities where the gas is heated in the downstream region, with higher temperature values with respect to the upstream region, whilst cold fronts do not show a pressure jump and the downstream temperature is lower than the upstream temperature. We have combined the

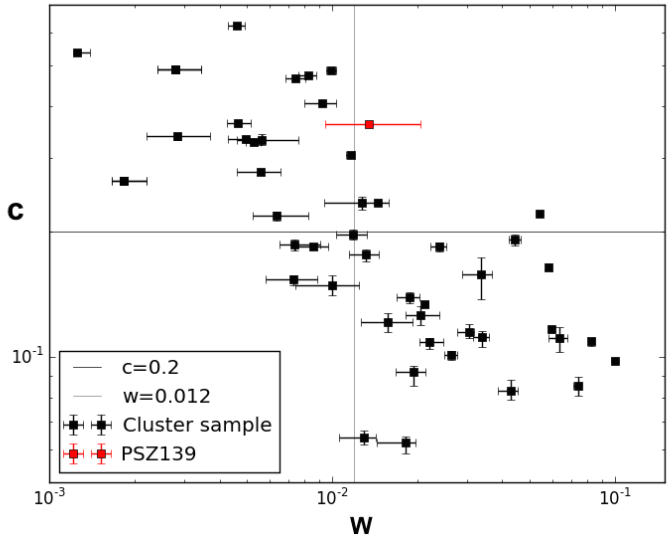

Figure 3.6: Diagram of the X-ray morphological indicators based on Chandra observations for the galaxy clusters, w and c, of the mass-selected cluster sample in Cuciti et al. [2015] and Cassano et al. [2016]. The red square represents PSZ139. Following Cassano et al. [2010], we have adopted the values $w \leq 0.012$ and $c \geq 0.2$ to separate merging from non-merging clusters. Merging clusters lie in the lower right region of the plot, whilst non-merging clusters in the upper left region.

temperature jump and compression ratio to estimate the pressure ratio across the edge and checked that the pressure is continuous across the front, as expected in the case of a cold front.

Given the discontinuity found both in the emissivity and temperature profiles, the morphology of the X-ray emission (elongated in the NW-SE direction) and the presence of a cool core, we argue that the cold front scenario is the most likely interpretation of the discontinuity.

3.4 Discussion and summary

The information from the literature and the X-ray analysis that we have performed indicate that PSZ139 shows typical features of a non-merging cluster, i.e. a cool core with low central entropy. The X-ray morphology of the cluster on larger scales, though, is not spherically symmetric, suggesting the occurrence of a merger that has left a clear imprint on the gas distribution towards the SE of the cluster core. The morphological indicators w and c also suggest a cluster with a dense core and an elongated shape. Moreover, the radio mini halo discovered by Giacintucci et al. [2017] suggests that the core has not been disrupted. These features suggest a scenario where the cluster is undergoing a merger that is not powerful enough to disrupt the cool core. In fact, simulations have shown that it is

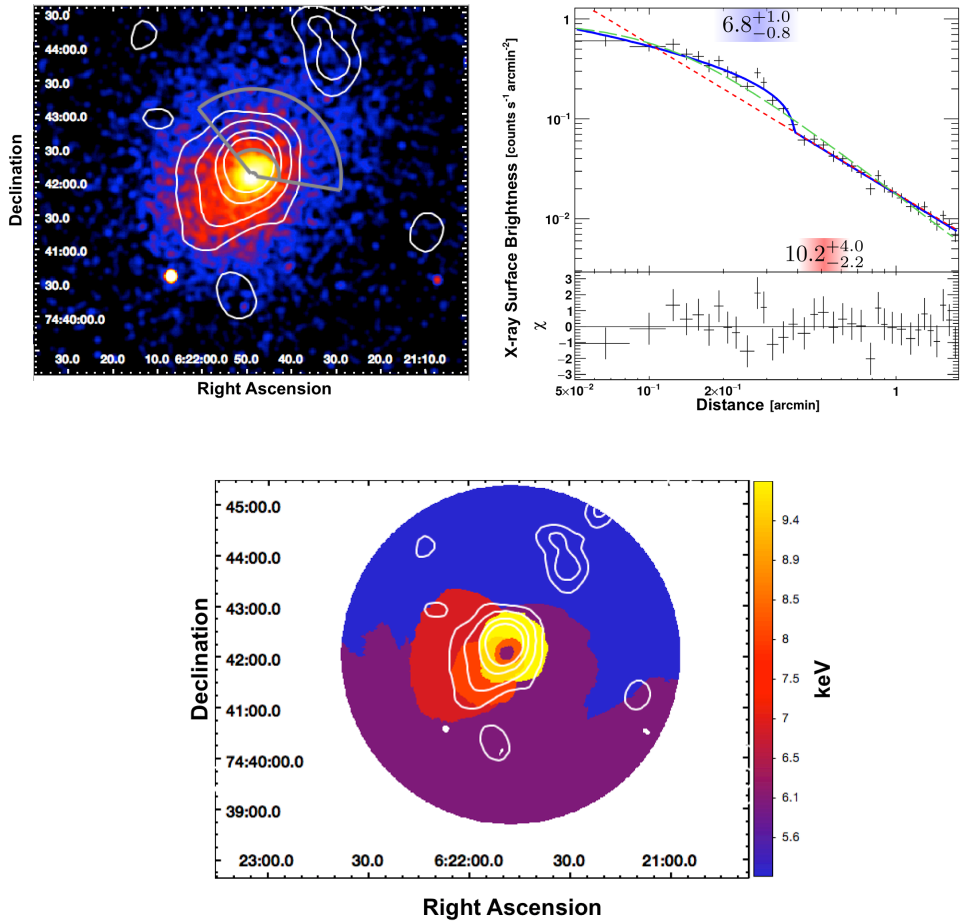

Figure 3.7: **Top left panel:** Chandra X-ray image smoothed on a scale of 6″ with the overlay of the LOFAR contours and the sector used for the profile extraction. The inner grey arc indicates the position ($\sim$ 100 kpc from the centre) of the cold front that we have discovered. Radio emission extends far beyond the cold front. **Top right panel:** X-ray surface brightness profile of the discontinuity detected in the Chandra image. The data were rebinned to reach a minimum signal-to-noise ratio of 7, and fitted with three models: broken-power law in solid blue (χ^2/dof = 26.5/29), power-law in dashed red (χ^2/dof = 152.1/31), and beta-model in dashed green (χ^2/dof = 67.8/31). The residuals at the bottom of the plot refer to the broken-power law model. The two colored boxes indicate the temperature in keV in the upstream and downstream regions, and their sizes indicate the radial extension of the spectral region. **Bottom panel:** Projected temperature map of the cluster with the contour levels at $(1, 2, 4, 8) \times 3\sigma$ where σ = 500 μJy/beam of the 144 MHz LOFAR image with a beam of 35″$\times$ 35″ overlaid. The removed background sources (in white) are indicated. The presence of a cool core can be clearly seen.

quite hard for mergers to destroy cool cores in galaxy clusters [Burns et al., 2008].

Based on the correlation in Cassano et al. [2013] for giant halos, which compares cluster mass, halo radio power, and halo size, a cluster with the mass of PSZ139 is expected to host a giant halo with a power of $P_{\rm tot,1.4} \sim 2 \times 10^{24}$ W Hz^{-1} and a total size of $D_{\rm radio} \sim 950$ kpc. The total estimated radio power at 144 MHz is $P_{\rm tot,144} = (7.2 \pm 1.1) \times 10^{24}$ W/Hz, which corresponds to $P_{\rm tot,1.4} = (3.7 \pm 0.5) \times 10^{23}$ W/Hz at 1.4 GHz, assuming a conservative spectral index of $\alpha = -1.3$ for the whole source (see Table 4.4.). Even considering a large scatter around this correlation, the diffuse emission of PSZ139 is more than an order of magnitude underluminous and almost a factor of 2 smaller in size.

We argue that PSZ139 is the first example of a cluster that hosts ultra-steep-spectrum radio halo emission outside of its cool core. This radio emission is detected only at low frequencies and extends out to smaller radii than in typical giant radio halos. The radio analysis suggests that the more compact emission, which is coincident with the cool core and has a spectrum typical of mini halos ($\alpha_{144}^{610} \sim -1.3$), is surrounded by ultra-steep diffuse emission ($\alpha_{144}^{610} < -1.7$) that is correlated with the X-ray morphology on larger scales[5]. The X-ray analysis indicates the presence of a cool core with traces of dynamical activity, especially towards the SE, in line with the direction where most of the larger-scale diffuse emission is detected. The presence of a cold front suggests that the core is likely to be sloshing. This observational evidence motivates us to identify a new scenario that links cool-core clusters and particle re-acceleration on cluster scales. We argue that the radio emission found in PSZ139 is caused by a minor merger that has dissipated enough energy in the ICM to accelerate particles, but leaves the core intact, as indicated by the low central entropy and temperature. Through the same mechanism that generates giant radio halos in merging clusters, less energetic mergers are predicted to form halos with a steeper spectrum and lower power than more energetic (major) mergers (e.g. [Cassano et al., 2006], [Brunetti et al., 2008]). Up until now, this population of minor-merger, cool-core clusters remains largely undetected, and PSZ139 may in fact be the first example. The radio emission of PSZ139 suggests that the energy dissipated during a minor merger can drive turbulent motions outside the cluster core, but on scales smaller than that of giant halos, whilst still preserving the mini halo emission. We exclude the scenario where the source in PSZ139 is a transition object: either that it is a giant halo decaying into a mini halo, or a mini halo growing into a giant halo. For a giant radio halo to fade from the edges and shrink to its present size, the radiative losses, and hence the magnetic field strength, would have to be stronger at the edges than in the core of the cluster. This is considered unlikely. In the other case, we can exclude that the relativistic plasma has been transported from the core out to larger scales since this would require unrealistically high transport coefficients.

The presence of diffuse emission on scales larger than the core has rarely been seen

[5]We note that ultra-steep spectrum emission can also originate from the old lobes of a radio galaxy but we consider such a scenario unlikely, since we observe a strong spatial correlation between the radio and X-ray emission, as is typically seen in radio halos.

Table 3.3: Integrated surface brightness and estimated radio power of the radio emission of PSZ139. The first two columns refer to values measured from the LOFAR and GMRT datasets. The last two columns refer to the value estimated for the surface brightness rescaled to 1.4 GHz, and the spectral index value used for rescaling. The core component is defined as the emission from the inner region with a size of $\sim$ 200 kpc; the diffuse component corresponds to the emission on larger scales. The total value refers to the emission as a whole.

	LOFAR	GMRT	1.4 GHz	α
$S_{\rm core}$ (mJy)	12	2.3	-	
$P_{\rm core}$ (W/Hz)	3×10^{24}	-	1.5×10^{23}	-1.3
$S_{\rm diff}$ (mJy)	18	-		
$P_{\rm diff}$ (W/Hz)	4×10^{24}	-	2.2×10^{23}	-1.7 (UL)
$S_{\rm tot}$ (mJy)	30	-		
$P_{\rm tot}$ (W/Hz)	7×10^{24}	-	3.7×10^{23}	-1.3

in non-merging clusters. Among the few known cases[6], A2142 is the cluster that shares some similarities with PSZ139: it shows a two-component radio halo with flatter-spectrum emission in the core and a slightly steeper spectrum emission on Mpc scales [Venturi et al., 2017]. However, A2142 does not host a cool core, its halo has a size typical of giant radio halos, and the difference in the spectral index of the radio emission in the two components is only marginally significant. A case of a cool-core cluster hosting Mpc-scale emission is A2390 [Sommer et al., 2017], however the dynamic of the cluster is not clear, and the large errors on the spectral indices do not permit an assessment whether the emission on cluster scales has a steep spectrum.

PSZG139 is the first cool-core cluster to host steep-spectrum emission on larger scales. This example indicates that the connection between the evolution of radio emission on different scales and the dynamical status of the cluster is more complex than previously thought, and that particle acceleration mechanisms at different scales can be observed simultaneously in the same cluster. As the energy dissipated by minor mergers is primarily observed at low radio frequencies, we expect that radio halos with steep spectra will be found in these types of clusters by forthcoming high-sensitivity, low-frequency radio observations.

Acknowledgements

LOFAR, the Low Frequency Array designed and constructed by ASTRON, has facilities owned by various parties (each with their own funding sources), and that are collectively operated by the International LOFAR Telescope (ILT) foundation under a joint

[6]Few cases of Mpc-scale halos have been found in massive clusters with no evidence of major mergers (CL1821+643, [Bonafede et al., 2014]; A2261, A2390, [Sommer et al., 2017]; A2142, [Venturi et al., 2017]). The former two sources substantially differ from PSZ139: CL1821+643 for being a flat-spectrum giant halo, and A2261 for not hosting a cool core. The latter two sources also differ from PSZ139, but deserve a more accurate comparison, and are therefore discussed in the main text.

scientific policy. The LOFAR software and dedicated reduction packages on Github were deployed on the e-infrastructure by the LOFAR e-infragroup, consisting of J.B.R.O. (ASTRON & Leiden Observatory), A.P.M. (Leiden Observatory) and T.S. (Leiden Observatory) with support from N. Danezi (SURFsara) and C. Schrijvers (SURFsara). This research had made use of the LOFAR Solution Tool (LoSoTo), developed by F.dG., and of the NASA/IPAC Extragalactic Database (NED), which is operated by the Jet Propulsion Laboratory, California Institute of Technology, under contract with the National Aeronautics and Space Administration. We thank the staff of the GMRT that made the observation possible. GMRT is run by the National center for Radio Tata Institute of Fundamental Research.
A.B. acknowledges support from the ERC-Stg 714245 DRANOEL. H.R. and R.vW. acknowledge support from the ERC Advanced Investigator programme NewClusters321271. R.vW. acknowledges support of the VIDI research programme with project number 639. 042. 729, which is financed by the Netherlands Organisation for Scientific Research (NWO). Basic research in radio astronomy at the Naval Research Laboratory is supported by 6.1 Base funding. G.W. gratefully thanks the Leverhulme Trust for funding.

Chapter 4

Studying the late evolution of a radio-loud AGN in a galaxy group with LOFAR

Federica Savini, Annalisa Bonafede, Marcus Brüggen, Amanda Wilber, Jeremy J. Harwood, Matteo Murgia, Timothy Shimwell, David Rafferty, Aleksandar Shulevski, Marisa Brienza, Martin J. Hardcastle, Raffaella Morganti, Huub Röttgering, Alex O. Clarke, Francesco de Gasperin, Reinout van Weeren, Philip N. Best, Andrea Botteon, Gianfranco Brunetti, Rossella Cassano

MNRAS, accepted on 2017, November 2

Abstract

Feedback by radio-loud active galactic nuclei (AGN) in galaxy groups is not fully understood. Open questions include the duty cycle of the AGN, the spatial extent of the radio lobes, the effect they have on the intragroup medium, and the fate of the cosmic rays. We present the discovery of a 650 kpc-radio galaxy embedded in steep diffuse emission at $z = 0.18793 \pm 5 \times 10^{-5}$ located at the center of the galaxy group MaxBCG J199.31832+51.72503 using an observation from the LOFAR Two-meter Sky Survey (LoTSS) at the central frequency of 144 MHz. Subsequently, we performed a GMRT observation at the central frequency of 607 MHz to study the spectral properties of the source. The observations reveal a radio galaxy with a total radio power $P_{\rm tot,1.4} \sim 2.1 \times 10^{24}$ W Hz^{-1}, exhibiting two asymmetrical jets and lobes. The derived spectral index map shows a steepening toward the inner regions and a steep-spectrum core region. We model the integrated radio spectrum, providing two possible interpretations: the radio source is evolved but still active or it is just at the end of its active phase. Finally, in the same field of view we have discovered Mpc-sized emission surrounding a close pair of AGN located at a redshift $z = 0.0587 \pm 2 \times 10^{-4}$ (SDSS J131544.56+521213.2 and SDSS J131543.99+521055.7) which could be a radio remnant source.

4.1 Introduction

The majority of galaxies in the local Universe are grouped in dynamically bound systems, such as galaxy groups and clusters. Groups differ from clusters in terms of scaling relations, luminosity functions and halo masses, which are in the range 10^{12} - 10^{14} $M_{\odot}$ for groups and $\sim 10^{15}$ $M_{\odot}$ for clusters (e.g. [Kravtsov & Borgani, 2012]). Low-power radio galaxies are commonly found in the centers of rich galaxy groups and clusters, and contribute to the heating of the intra-cluster/-group medium (ICM/IGM) through the on-going activity in their nuclei (e.g. [Croston et al., 2005], [Croston & Hardcastle, 2014]). Radio-loud active galactic nuclei (AGN) play a crucial role in the thermal evolution of galaxy clusters, providing energy that can offset the radiative losses suffered by the medium and hence averting catastrophic cooling (e.g. [Fabian et al., 1991], [O'Sullivan et al., 2011]).

The details of this feedback mechanism are still not fully understood, particularly in small galaxy groups, since X-ray measurements are inherently limited to high-temperature groups. Among the many uncertainties about the features of radio galaxies in groups, it is not clear how the AGN affects the thermal state of the intragroup gas and hence the accretion in the nucleus, and how the cosmic rays in the lobes of the radio-loud AGN diffuse, mix, and cool in the IGM (e.g. [Giacintucci et al., 2011]). The AGN emission can reach hundreds of kpc and in the case of galaxy groups, the low-density environment allows the lobes to expand to scales of up to Mpc (e.g. [Kaiser & Alexander, 1999], [Clarke et al., 2017]), which has implications for the hydrodynamics of a possible feedback process. Furthermore, the electrons injected into the intragroup medium provide a seed population that could be re-accelerated by shocks and turbulence during group mergers, as occurs in cluster mergers (e.g. [van Weeren et al., 2017]).

In addition, little is known about what sets the duty cycle of the AGN, i.e. the activity/quiescence phases that radio-loud galaxies undergo. Once the jets of a radio galaxy stop supplying fresh cosmic ray electrons (CRe) to the lobes, the radio sources start to fade on a timescale of $\sim 10^7$ Myr due to losses through synchrotron radiation, inverse Compton, and plasma adiabatic expansion (e.g. [Kardashev, 1962], [Murgia et al., 1999]). Due to particle energy losses, the high-frequency spectrum steepens with spectral indices[1] of $\alpha < -1$, and a spectral break develops depending on the magnitude of the energy loss and the age of the particle population.

Low-frequency observations are ideal for discovering steep-spectrum diffuse radio emission since they trace the low-energy, old CRe less affected by the energy losses.
The Low Frequency ARray (LOFAR; [van Haarlem et al., 2013c]) probes the right frequency range and offers the good sensitivity to diffuse, low-surface brightness emission regions due to its *uv* plane sampling properties. With its high imaging angular resolution, LOFAR can identify the presence of evolved radio galaxies, explore their morphology, and model their spectrum. With LOFAR, so far, only few remnants have been detected and studied in detail (e.g. [Hardcastle et al., 2016], [Brienza et al., 2016c], [Shulevski et al., 2017]). However, the first systematic searches of these sources in the LOFAR fields have already provided an indication of their fraction (between 10 and 30 %) relative to the entire radio source population (e.g. [Brienza et al., 2016a], [Hardcastle et al., 2016]).

[1] The spectrum is defined by $S(\nu) \propto \nu^{\alpha}$.

Table 4.1: MaxBCG J199 in the Sloan Digital Sky Survey [Koester et al., 2007]. Col. 1, Col. 2, Col. 3, Col. 4: Target position, right ascension and declination, longitude and latitude; Col. 5: Photometric redshift; Col 6: Luminosity in i band; Col. 7: Number of red-sequence galaxies in the cluster; Col. 8: Radius within which the density of galaxies is 200 times the mean density of such galaxies; Col. 9: $N_{\rm gal}$ within R_{200} from the cluster center. Note that R_{200} and $N_{\rm gal,200}$ are related through a power law (e.g. [Hansen et al., 2005], [Rykoff et al., 2012]).

1: RA	2: DEC	3: l	4: b	5: z	6: L_i	7: $N_{\rm gal}$	8: R_{200}	9: $N_{\rm gal,200}$
(h:m:s, J2000)	(°:′:″, J2000)	(°)	(°)		($\times 10^{10} L_\odot$)		(kpc)	
13:17:16.4	+51:43:30.0	199.318	51.725	0.18 ± 0.01	17.658	13	530	10

In this paper, we study the peculiar radio source discovered at the center of the galaxy group MaxBCG J199.31832+51.72503 (hereinafter MaxBCG J199) using multi-frequency radio observations to constrain the properties and the origin of the emission discovered by LOFAR. The target was selected from a pointing within the LOFAR Two-meter Sky Survey (LoTSS; [Shimwell et al., 2017]) after a preliminary inspection of the dataset with the aim of finding radio diffuse emission associated with galaxy groups/clusters. LoTSS is a deep imaging survey carried out as part of the LOFAR Surveys Key Science Project [Röttgering et al., 2006] to obtain deep (~ 100 μJy/beam) high-resolution ($\sim 5''$) images at 120 - 168 MHz using the Dutch part of the array in order to map the entire Northern sky.

The structure of the paper is the following: we present the source in Sec. 4.1.1; we outline the radio observations and data reduction in Sec. 4.2; our main results are presented in Sec. 4.3, and we discuss our findings and conclusions in Sec. 4.4, 4.5, and 4.6. Throughout the paper, we assume a flat, ΛCDM cosmology with matter density $\Omega_M = 0.3$ and Hubble constant $H_0 = 67.8$ km s^{-1} Mpc^{-1} [Planck Collaboration et al., 2016]. The angular to physical scale conversion at z = 0.188 is 3.167 kpc/$''$.

4.1.1 The galaxy group MaxBCG J199

The source MaxBCG J199 was classified as a galaxy cluster by Koester et al. [2007] after being identified in the Sloan Digital Sky Survey (SDSS I/II; [York et al., 2000]). The SDSS photometric data were searched for clusters in the redshift range $0.1 \leq z \leq 0.3$ containing 10 or more red-sequence[2] galaxies [Bower et al., 1992]. The number of galaxies, $N_{\rm gal}$, gives a first estimate of the cluster richness, which is then used to estimate the cluster size $R_{200} \propto N_{\rm gal}^{0.6}$ Mpc, where R_{200} is the radius within which the mean density of red-sequence galaxies is $200\,\Omega_M$ times the mean galaxy density [Hansen et al., 2005]. Considering the scaled richness estimate $N_{\rm gal,200}$, i.e. the number of galaxies within R_{200} from the cluster center, we can use the scaling relation between M_{500} and $N_{\rm gal,200}$ in Rozo et al. [2009] to get an estimate of the cluster mass (contained within an overdensity of 500 relative to critical at the group redshift): $M_{500} = e^B (N_{\rm gal,200}/40)^A \times 10^{14}$ M$_\odot$, where $A = 1.06 \pm 0.17$ and $B = 0.95 \pm 0.16$. Based on the SDSS selection, the number of galaxies in MaxBCG J199 within R_{200} is 10, and $M_{500} = (0.6 \pm 0.2) \times 10^{14}$ M$_\odot$. The richness and the estimated

[2]Galaxies with $-24 < M_r < -16$ where M_r is the magnitude in the r band.

Table 4.2: Details of the radio observations.

Telescope	LOFAR	GMRT
Observation ID	LC2_038	31_071
Pointing center (RA,DEC)	13:12:03.2, +52:07:19.4	13:17:16.4, +51:43:30.0
Observation date	2014 Aug 24	2016 Dec 25
Total on-source time	8 h	8 h
Flux calibrator	3C295	3C147 & 3C286
Central frequency	144 MHz	607 MHz
Bandwidth	48 MHz	32 MHz
Channels	64	256
Integration time	1 sec	8 sec
Field of view	5°	1°
Baselines	Dutch (80 - 40000)λ	(150 - 49000)λ

mass for MaxBCG J199 are much lower than the typical values for galaxy clusters, hence we will refer to it as a galaxy group.
Details of the group are summarized in Table 4.1.

4.2 Radio observations and data reduction

Summaries of the observations can be found in Table 4.2.
The calibration and imaging procedure performed on the Low Frequency Array (LOFAR) and Giant Meter Radio Telescope (GMRT) observations are outlined below. We consider a calibration error of 15% on all the measured flux densities (e.g. [Shimwell et al., 2016], [van Weeren et al., 2016b]).

4.2.1 LOFAR

LOFAR is an array of antenna dipoles grouped into so-called stations (see van Haarlem et al. [2013c] for details). The Low Band Antennas (LBA) operate in the range 10 - 90 MHz and the High Band Antennas (HBA) in the range 110 - 240 MHz.
In this paper, we present a HBA LOFAR observation at the central frequency of 144 MHz within LoTSS. A preliminary pre-processing step has been performed through a pipeline offered by the Radio Observatory (ASTRON) to flag bad data and average in time and frequency (down to 0.1 MHz/ch and 8 s). Data reduction was performed following the calibration scheme described in van Weeren et al. [2016a], which has been developed to correct for direction-dependent effects within the observed field of view at HBA frequencies. The calibration scheme consists of two main components: a non-directional part and a directional part, briefly summarized below. For more details we refer the reader to van Weeren et al. [2016a].

Table 4.3: Col. 1: Telescope/Survey; Col. 2: Central frequency; Col. 3: Minimum baseline; Col. 4: Largest angular scale; Col. 5: Resolution; Col 6: rms noise; Col. 7: Parameters used for LOFAR and GMRT imaging, such as taper (T) and weighting scheme; when Briggs weighting scheme is used, the robust value is specified [Briggs, 1995].

1: Telescope	2: Freq. (MHz)	3: B_{min} (λ)	4: LAS	5: Res.	6: rms (mJy/beam)	7: Imaging
LOFAR	144	80	2578″	10.6″ × 6.0″	135	Briggs -0.25
		150	1375″	19″ × 19″	350	uniform, 15″ T
		80		27″ × 26″	350	Briggs 0, 20″ T
GMRT	607	150	1375″	6.0″ × 4.8″	60	Briggs -0.25
		150		18″ × 17″	250	Briggs 0, 20″ T
		150		19″ × 19″	290	uniform, 20″ T
VLSSr	74	94	1100″	80″ × 80″	50000	-
WENSS	325	150	1375″	54″ × 68″	300	-
NVSS	1400	210	970″	45″ × 45″	500	-
FIRST	1400	1720	60″	5.4″ × 5.4″	200	-

Pre-Facet Calibration

The direction-independent part, so-called Pre-Facet Calibration (Prefactor pipeline[3]), is a preparatory step for the directional calibration processing. Amplitudes and phase gains, station phase correlation offsets, and clock-TEC[4] solutions are calculated for the flux calibrator, adopting the flux scale of Scaife & Heald [2012]. The flux calibrator for our dataset is 3C295 and was observed for 10 minutes.
After these steps we transferred the amplitude gains, station phase correlation offsets, and clock offset to the target data. An initial phase calibration was performed using a low-resolution sky model (Global Sky Model for LOFAR[5]) from the VLA Low-Frequency Sky Survey Redux (VLSSr ; [Lane et al., 2012]), the Westerbork Northern Sky Survey (WENSS; [Rengelink et al., 1997]), and the NRAO VLA Sky Survey (NVSS; [Condon et al., 1998]).
High-resolution (39″× 31″) and low-resolution (126″× 108″) direction-independent calibrated images were obtained through a step called Initial Subtraction.

In this step, high-resolution compact sources are masked and imaged. Their clean components are then subtracted from the *uv* data and listed into a sky model (one for each subband). Diffuse emission that was not visible in the high-resolution images can now be detected and low-resolution sources are then masked and imaged. The low-resolution components are also subtracted from the *uv* data and then added to the sky model. The calibrator 3C295, which appears as a bright source far outside the FWHM of the primary beam ($\sim 8^\circ$ far away from the science target) causing some artifacts in the field of view, was peeled off from the first half of the bandwidth where the effects are more relevant.

[3]https://github.com/lofar-astron/prefactor
[4]TEC refers to the station differential Total Electron Content.
[5]https://www.astron.nl/radio-observatory/lofar/lofar-imaging-cookbook

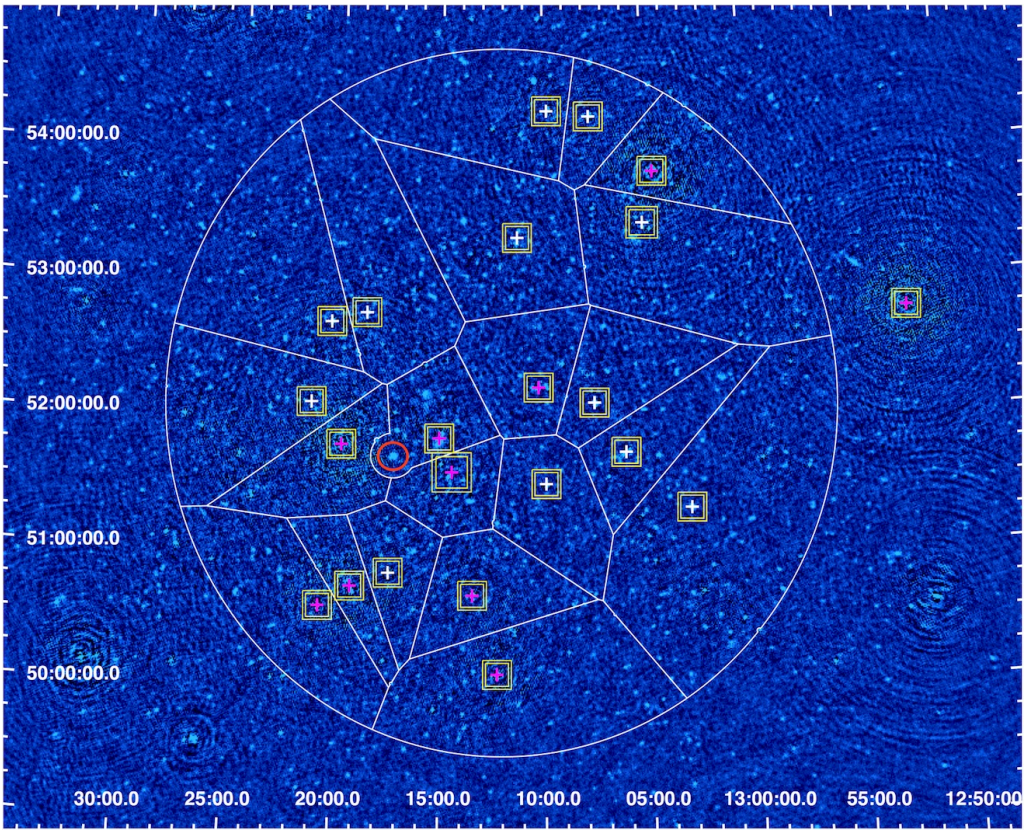

Figure 4.1: Wide-field high-resolution image with the overlay of the facet layout generated by the Factor pipeline. White regions show the facets and the elliptical region that encompasses the faceted area with a 2.5° radius adjusted for the primary beam shape. Outside this radius, only small patches, which are faster to process, are used. The coordinates of the target were specified in the parameter settings to include the source in one single facet that therefore shows a curved boundary. Each calibrator is indicated with a cross (magenta for the facets that were processed with Factor and white for the non-processed facets) and the region used in the self-calibration step is indicated with a yellow square. The target is indicated with a red circle.

Facet Calibration

The direction-dependent step, so-called Facet Calibration (Factor pipeline[6]), is based on dividing the sky into a discrete number of directions (facets) covering the observed field of view and calibrating each of these directions separately. The aim is to calculate the direction-dependent corrections needed to obtain near-thermal-noise-limited images using the full resolution offered by LOFAR. The input needed for the pipeline are the sky models obtained through Initial Subtraction and empty datasets that will be filled with the calibrated sources. A default calibrator, typically a bright compact source, is selected for each facet with restrictions, such as minimum flux density in the highest-frequency band and maximum size. The user may modify the calibration region, and multiple sources within the region can be used. We use settings in the Factor pipeline to restrict the facet calibrator sources to have a reasonable total number of facets with reasonable sizes. The aim is to compute solutions on small portions of the sky and reduce the processing time. We choose a minimum flux density of 0.6 Jy for the calibrators, and we also choose to calibrate and image using baselines above 80 λ to prevent residual diffuse emission seen by the shortest baselines from affecting the results. The coordinates of MaxBCG J199 and a $10'$ radius around it are also specified to include the source in one single facet. After performing self-calibration cycles on the calibrator, all the fainter sources in the facet are added back and calibrated using the calculated solutions which are assumed to apply to the whole facet. An updated sky model for the region of the sky covering the facet is obtained and then subtracted from the *uv* data and the whole process is repeated to finally obtain a direction-dependent corrected image for each facet. Finally, a mosaic field image containing all the facets' images is corrected for the primary beam. Re-imaging was performed with different parameters on the target facet to obtain different resolutions and weights to increase sensitivity to diffuse, extended emission. As we were focusing on one single science target, we chose to process only 9 facets, i.e. the brightest sources in the field and those bordering the target facet. In addition, the last and 10th facet we processed was the target facet itself, so that it could benefit from the improved subtraction obtained by calibrating the preceding facets. The calibration regions of the processed facets are indicated with yellow boxes in Fig. 4.1.

4.2.2 GMRT

We used a follow-up GMRT observation in the range 591 - 623 MHz to enable a study of the spectral properties of the sources.
In the GMRT calibration the sources 3C147 and 3C286 were used as absolute flux and bandpass calibrators respectively and were observed for 10-15 minutes, at the beginning and at the end of the target observation. The source 1400+621 was used as a phase calibrator and was observed every 10-15 minutes. Data reduction was performed using the CASA tools (Common Astronomy Software Applications, version 4.5.2; [McMullin et al., 2007]). After inspecting the dataset, bad data were flagged through both manual flagging and using the AOFlagger software [Offringa et al., 2012]. Flux and bandpass calibration were performed against 3C147 and 3C286, adopting the flux scale in Perley &

[6]https://github.com/lofar-astron/factor

Butler [2013][7]. Gain phases and amplitudes were calibrated every 10-15 minutes against 1400+621. One compact source (13:09:46, +51:48:10) residing in the primary lobes of the primary beam was peeled off. To speed up the imaging process, the dataset has been averaged in frequency and time (down to 3.2 MHz/ch and 16 s). Imaging was carried out in CASA, using the multi-frequency synthesis (MFS) CLEAN algorithm [Rau & Cornwell, 2011] and the wide-field imaging technique to compensate for the non-coplanarity of the array.

Only one cycle of phase self-calibration cycle was needed to reach convergence and obtain an image of the target field, which was finally corrected for the primary beam.

4.3 Results

To study the emission and its spectral properties, we have made several images at high- and low- resolution, summarized in Tab. 4.3 and shown in Fig. 4.2. The images obtained for spectral analysis (see Sec. 4.3.1) are not shown.
The LOFAR images show that the radio emission associated with MaxBCG J199 is coming from a radio galaxy with a pair of jets and lobes extending from a compact core, and diffuse emission likely connected to the AGN. The core of the radio galaxy is coincident with the optical source SDSS J131716.39+514330.1, which corresponds to the brightest galaxy of the group and is identified as a broad-line galaxy with a redshift of $z = 0.18793 \pm 5 \times 10^{-5}$ (Data Release 13; [SDSS Collaboration et al., 2016]). However, the structure of the core region appears to be more complex, since SDSS images show three galaxies which create a multiple core system, as visible in the bottom right panel of Fig. 4.3. Moreover, there is an offset (smaller than beam in the full-resolution LOFAR image,) between the peak of the radio emission and the central galaxy seen in the optical image.
The radio diffuse emission has a mean surface brightness of 4.5 μJy/$''^2$ at 144 MHz and an extent of 3.4$'$, which corresponds to a projected linear size of 650 kpc at the spectroscopic redshift of the BCG[8]. Only the brightest and more compact emission is visible in the GMRT images at the achieved sensitivity level.
We note an asymmetry in the jet intensity and morphology: the NW lobe is brighter and it extends across the direction of the jet axis with a wing in the south-west direction, whereas the SE lobe is fainter, fading away towards the edge, but with a larger projected linear size.

Radio emission at the group coordinates is observed in the following surveys: NVSS at 1.4 GHz, WENSS at 325 MHz, and the VLA survey at 1.4 GHz, Faint Images of the Radio Sky at Twenty Centimeters (FIRST, [Becker et al., 1995b]). NVSS and WENSS are sensitive to emission from sources extended on scales of arcminutes, but their resolution ($45'' \times 45''$ and $54'' \times 68''$ at the group declination, respectively) and sensitivity (500 μJy/beam and 300 μJy/beam, respectively) are too low to identify features, such as a

[7]We used the most updated flux scale, although different from the scale used for LOFAR observations, since the flux difference between the Perley-Butler 2013 and Scaife-Heald models is within the calibration error of 15%.

[8]The photometric redshift of the galaxy group ($z = 0.18 \pm 0.01$) given in Koester et al. [2007] is not used throughout the paper, instead we use the spectroscopic redshift of the BCG ($z = 0.18793 \pm 5 \times 10^{-5}$) given by SDSS Collaboration et al. [2016] since the radio emission observed is related to that galaxy.

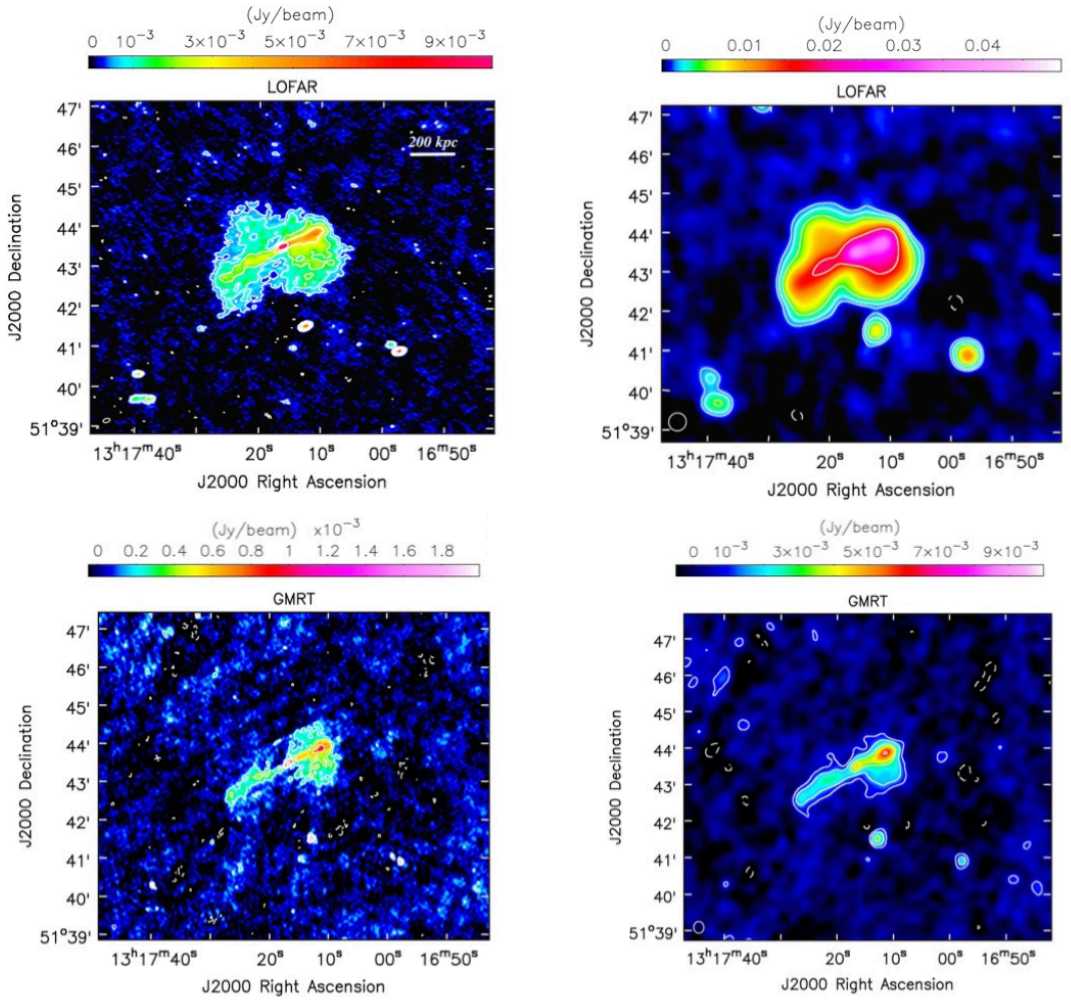

Figure 4.2: **Top left:** LOFAR image of MaxBCG J199 at the central frequency 144 MHz obtained with the Briggs scheme [Briggs, 1995], robust=-0.25, and no taper. The contour levels are at $(-1, 1, 2, 4, 8, 16) \times 3\sigma$ where $\sigma = 135$ μJy/beam. The beam shown at the bottom left of the image is $10.6'' \times 6.0''$. The image shows the presence of a radio galaxy embedded in radio diffuse emission with maximum angular size of $3.4'$ which corresponds to projected linear size of 650 kpc. **Top right:** LOFAR image of MaxBCG J199 at the central frequency 144 MHz obtained with the Briggs scheme [Briggs, 1995], robust=0, and taper of $15''$. The contour levels are at $(-1, 1, 2, 4, 8, 16) \times 3\sigma$ where $\sigma = 350$ μJy/beam. The beam shown at the bottom left of the image is $27'' \times 26''$. No additional diffuse emission can be observed in this image. **Bottom left:** GMRT image of MaxBCG J199 at the central frequency 607 MHz obtained with the Briggs scheme [Briggs, 1995], robust=0, and no taper. The contour levels are at $(-1, 1, 2, 4, 8, 16) \times 3\sigma$ where $\sigma = 60$ μJy/beam. The beam shown at the bottom left of the image is $6.0'' \times 4.8''$. The image shows the presence of the jets of the radio galaxy. **Bottom left:** GMRT image of MaxBCG J199 at the central frequency 607 MHz obtained with the Briggs scheme [Briggs, 1995], robust=-0.25, and taper of $20''$. The contour levels are at $(-1, 1, 2, 4, 8, 16) \times 3\sigma$ where $\sigma = 250$ μJy/beam. The beam shown at the bottom left of the image is $19'' \times 17''$. No diffuse emission can be observed in this image.

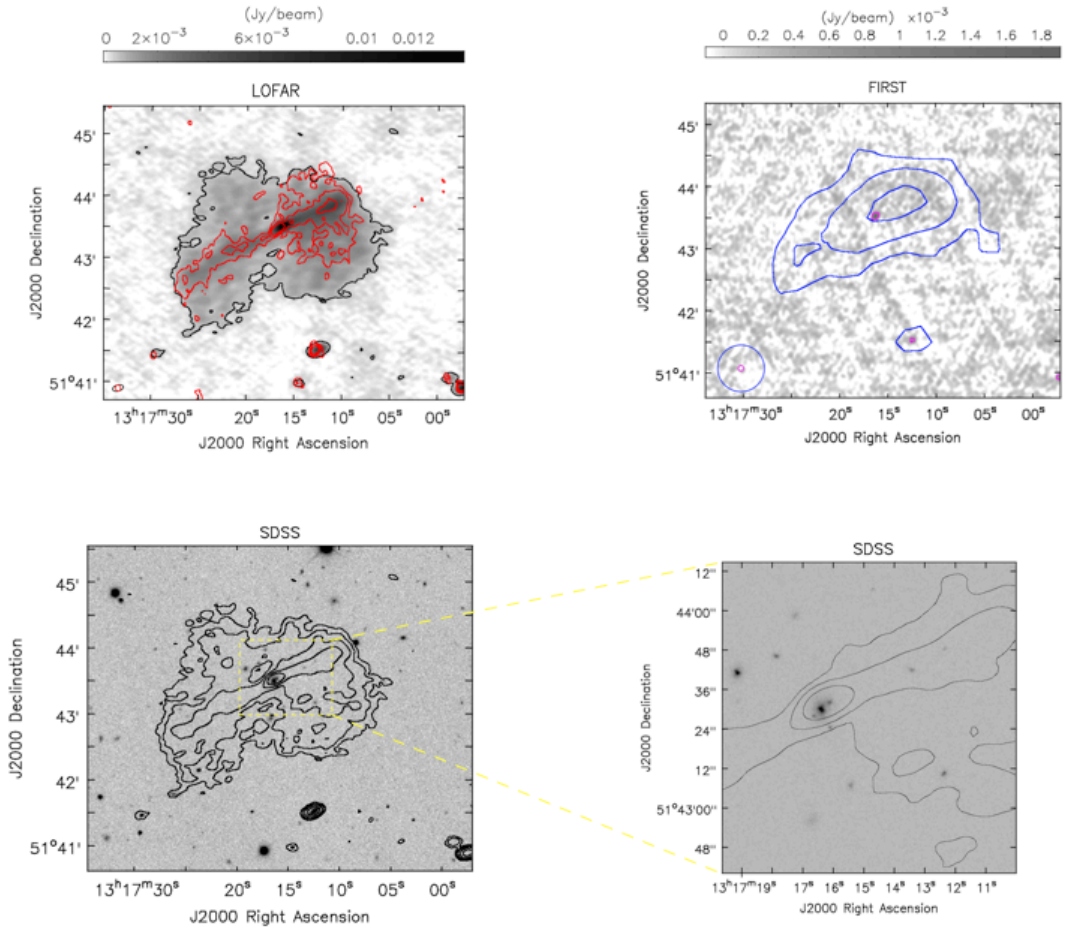

Figure 4.3: **Top left:** LOFAR image of MaxBCG J199 at the central frequency 144 MHz in greyscale with its contour level at 3σ where $\sigma = 135$ μJy/beam in black. GMRT 607 MHz contours levels at $(1, 2, 4, 8, 16) \times 3\sigma$ where $\sigma = 60$ μJy/beam are overlaid in red. The beams shown at the bottom left of the image are $10.6'' \times 6.0''$ and $6.0'' \times 4.8''$ for LOFAR and GMRT respectively. **Top right:** FIRST image of MaxBCG J199 at 1.4 GHz in greyscale with its contour level at 3σ where $\sigma = 200$ μJy/beam in magenta. NVSS contours levels at $(1, 2, 4) \times 3\sigma$ where $\sigma = 500$ μJy/beam are overlaid in blue. The beams shown at the bottom left of the image are $5.4'' \times 5.4''$ and $45'' \times 45''$ for FIRST and NVSS respectively. With the FIRST snapshot observation only the core region of the radio galaxy is visible, whereas NVSS observation could detect radio emission but without the resolution required to distinguish internal features. **Bottom left:** SDSS g, r, i mosaic image in greyscale with LOFAR 144 MHz contour levels at 3σ where $\sigma = 135$ μJy/beam in black and GMRT 607 MHz contour levels at 3σ where $\sigma = 60$ μJy/beam in red. The radio diffuse emission surroundings the two jets can be seen only with LOFAR. **Bottom right:** zoom of the SDSS g, r, i mosaic image in the core region. LOFAR 144 MHz contour levels at $(4, 8, 16) \times 3\sigma$ where $\sigma = 135$ μJy/beam in black. Three galaxies can be seen corresponding to the inner region of the radio emission.

core or jet emission, in the radio emission. With FIRST, which is a 3-min snapshot with resolution of 5″, only the region closest to the core is visible. The FIRST image with an overlay of NVSS contours is shown in the top right panel of Fig. 4.3. In addition, the source is detected in the Green Bank 6 cm survey at 4.85 GHz (GB6; [Gregory et al., 1996]), and in the VLSSr at 74 MHz. The flux densities from these survey observations can be combined to obtain an integrated radio spectrum (see Sec. 4.3.1).
No information about the X-ray emission of the group is available in the literature. The group is not detected in the ROSAT All Sky Survey (RASS; [Voges et al., 1999]) and no pointed observations exist.

From the NVSS image we measured the integrated flux density at 1.4 GHz to be $S_{\rm tot,1.4} = 21 \pm 3$ mJy, corresponding to a total radio power of $P_{\rm tot,1.4} \sim 2.1 \times 10^{24}$ W Hz^{-1}. The core is resolved at 1.4 GHz by FIRST and we measure the integrated flux density of the core region to be $S_{\rm core,1.4} = 1.3 \pm 0.2$ mJy.

4.3.1 Spectral analysis

In order to study the spectral properties of MaxBCG J199, we have reimaged LOFAR and GMRT data with a resolution of 19″, and same pixel size, baseline range (150 - 49000 λ) and uniform weighting scheme to minimize the effects of differences in the *uv* coverage of the two interferometers. We have produced a low-frequency spectral index map using CASA tasks, shown in Fig. 4.4. The spectral index values are calculated in the region where both LOFAR and GMRT images are above 3σ, where σ is 290 μJy/beam and 350 μJy/beam for GMRT and LOFAR respectively. Pixels below 3σ are blanked out. The spectral index error map is obtained using the following equation:

$$\Delta\alpha = \frac{1}{\log \frac{\nu_1}{\nu_2}} \sqrt{\left(\frac{\Delta S_1}{S_1}\right)^2 + \left(\frac{\Delta S_2}{S_2}\right)^2}, \tag{4.1}$$

where S_1 and S_2 are the flux densities at frequencies ν_1 and ν_2 and ΔS_1 and ΔS_2 are the respective errors which include the measured map noises and flux calibration errors.
The spectral index values range from -1.3 to -1.1 in the core region and inner edges, and from -0.7 to -0.5 at the outer edges. The lobes have spectral index values that flatten towards the outermost lobe edges; this is especially prominent in the NW lobe. We note that the regions that show the flattest spectral indices, which are also regions with large errors, do not match the highest surface brightness regions in the LOFAR and GMRT maps.

The global spectral index value of the source calculated using the integrated flux densities from the area where the GMRT detection is above 3σ is relatively steep: $\alpha_{144}^{607} = -1.14 \pm 0.13$.
The observed LOFAR emission extends well beyond the GMRT emission and the diffuse emission detected at 144 MHz that can not be seen at 607 MHz must be much steeper. This emission is detected by LOFAR even when only the same baselines as the GMRT are imaged. This enables us to derive a spectral index upper limit to the value of $\alpha_{144}^{607} < -1.8 \pm 0.2$, considering the LOFAR integrated flux density of the lobe and a 3σ GMRT flux density upper limit where σ was determined from a set of flux density

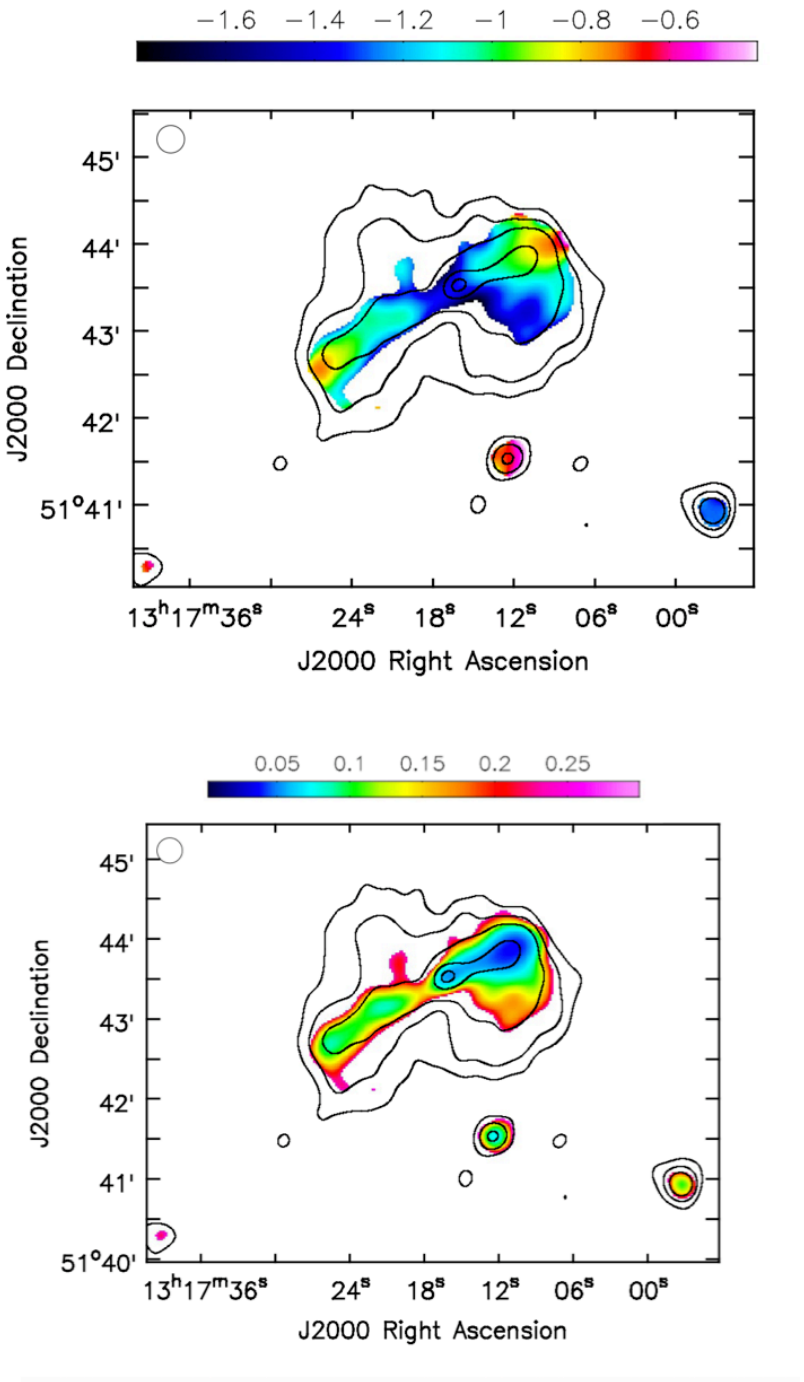

Figure 4.4: Spectral index map (top) and relative error map (bottom) between the 144 MHz LOFAR image and the 607 MHz GMRT image with an overlay of LOFAR contour levels at $(3, 10, 20, 50, 70) \times \sigma$ where $\sigma = 350$ μJy/beam. The beam shown at the top left of the image is $19'' \times 19''$.

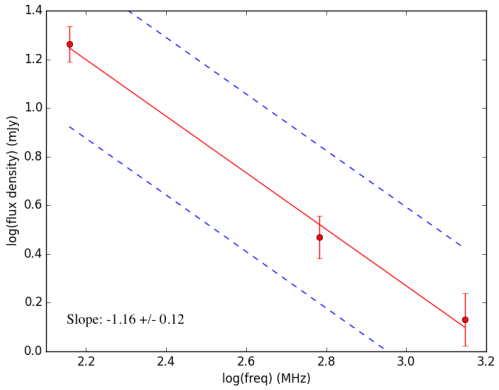

Figure 4.5: Plot of flux density against frequency with linear fit overlaid for LOFAR, GMRT and FIRST measurements of the core region of MaxBCG J199.

Table 4.4: Flux densities from VLSSr, LOFAR, WENSS, GMRT, NVSS, and GB6 in the region of MaxBCG J199. All the measurements onto the absolute flux density of Baars et al. [1977].

Central frequency (MHz)	Flux density (mJy)	Error (mJy)
74	823.0	214.0
144	388.0	38.8
325	115.5	14.0
607	93.7	9.4
1400	25.7	2.6
4850	2.9	0.3

measurements in the radio galaxy region.

The spectral index map reveals that the emission closest to the radio galaxy core is steep with $\alpha_{144}^{607} < -1$. The core can be seen in the intensity images also at 1.4 GHz (FIRST). Therefore, we can obtain a three-point spectrum of the core region, using LOFAR, GMRT, and FIRST images readjusted to have the same *uv* range, and same beam ($6''$) [9]. We measured the flux density from a region corresponding to the brightest central emission in each map and respective errors that include the measured map noises and flux calibration errors and estimated the spectral index of the core to be $\alpha_{144,607,1400} = -1.16 \pm 0.12$ performing a linear fit, as shown in Fig. 4.5.

In addition to the spectral information derived from our observations with LOFAR and GMRT, we measured the flux densities from **VLSSr**, WENSS, NVSS, and GB6 in

[9]We used a uniform weighting scheme to image GMRT and LOFAR datasets, whereas we note that the FIRST image could have been obtained with a different scheme. However, the effects of different weighting schemes should not be relevant since only the core region is visible in the FIRST image and it is unresolved.

the region of MaxBCG J199 constrained by the 3σ LOFAR contours to obtain the integrated radio spectrum of the source shown in Fig. 4.6. In Tab. 4.4 we report all the measurements. They were placed onto the absolute flux density of Baars et al. [1977] by scaling for the multiplicative factor listed in Helmboldt et al. [2008].

We computed the best-fit synchrotron model of the spectrum using the Broadband Radio Astronomy ToolS (BRATS[10], [Harwood et al., 2013], [Harwood et al., 2015]) software package, comparing two models:

- the continuous injection (CI; [Jaffe & Perola, 1973]) model for active sources, which assumes that fresh electrons are injected at a constant rate for a duration $t_{\rm CI}$ [Pacholczyk, 1970]. When the source is active, its radio spectrum changes as a function of time t, and the break frequency $\nu_{\rm b}$ shifts to lower values, via

$$\nu_{\rm b} \propto \frac{B}{t^2\,(B^2 + B_{\rm IC}^2)}, \tag{4.2}$$

  where B is the magnetic field, and $B_{\rm IC}$ is the equivalent magnetic field due to inverse Compton scattering of cosmic microwave background photons.

- the $\rm CI_{off}$ model (e.g. [Komissarov & Gubanov, 1994], [Murgia et al., 2011]), which extends the Jaffe & Perola model [Jaffe & Perola, 1973] to inactive sources. When the electron supply stops, the source enters the quiescence phase of duration $t_{\rm off}$ and the synchrotron age is $t_s = t_{\rm CI} + t_{\rm off}$. The break frequency $\nu_{\rm b,off}$ evolves via

$$\nu_{\rm b,off} = \frac{\nu_{\rm b}\,(t_{\rm off} + t_{\rm CI})^2}{t_{\rm off}^2}. \tag{4.3}$$

To estimate the magnetic field, we made the simple assumption of equipartition between relativistic particles and a uniform magnetic field and we calculated the minimum energy density $u_{\rm min}$ and the equipartition magnetic field $B_{\rm eq}$ for MaxBCG J199 using the revised formula in Beck & Krause [2005]. We adopted the source flux density at 144 MHz, where the energy losses of the synchrotron electrons ($\propto E^2$) should be negligible, the global spectral index value computed in the previous section ($\alpha \sim -1.1$), an electron/proton ratio of 100, and a volume filling factor of 1. Moreover, we assumed ellipsoidal geometry, hence a value of 200 kpc for the source depth. The resulting value is $B_{\rm eq}[\mu{\rm G}] \sim 15$.

The fit to the models and the best-fit parameters are shown in Fig. 4.6.
For both models, we assumed that the injected particles have a power-law energy spectrum $N(E) \propto E^{\delta}$ which results in a power-law radiation spectrum with spectral index $\alpha_{\rm inj} = (\delta + 1)/2$ over a wide range of frequencies. For the injection spectral index, we assumed $\alpha_{\rm inj}$ = -0.7, which is the value measured in the flattest regions of the source. Fixing $\alpha_{\rm inj}$ helps us to limit the number of free parameters for the model. We also neglect adiabatic losses and assume that the pitch angles of the radiating electrons are continually

[10] http://www.askanastronomer.co.uk/brats

isotropized in a time much shorter than the radiative timescale, which implies that the synchrotron energy losses are the same for all electrons.

Using an estimate of the magnetic field strength $B[\mu\mathrm{G}]$ and the break frequency $\nu_\mathrm{b}[\mathrm{GHz}]$ obtained from the spectral fitting of CI and $\mathrm{CI_{off}}$ models, it is possible to derive the spectral age of the source [Murgia et al., 2011], via

$$t_\mathrm{s}[\mathrm{Myr}] = 1590\,\frac{B^{0.5}}{(B^2 + B_\mathrm{IC}^2)\,[(1+z)\,\nu_\mathrm{b}]^{0.5}}. \tag{4.4}$$

Assuming the source magnetic field B constant and equal to the value computed using the above equipartition approach, the characteristic spectral age can be calculated for both models.
The best fit for the CI model is found for the break frequency value 0.6 MHz. However, the age that can be derived is very poorly fitted ($t_\mathrm{CI} \sim 830$ Myr), since the fit is forced to be as steep as possible before being limited by the low-energy cut off.
The best fit for the $\mathrm{CI_{off}}$ model is found for the break frequency value 439 MHz with an off component break at 12 GHz. The time during which the source has been on and off are estimated to $t_\mathrm{CI} \sim 25$ and $t_\mathrm{off} \sim 6$ Myr respectively, which give a total age of $t_\mathrm{s} \sim 31$ Myr.
As recently demonstrated by Harwood [2017], though, the CI and $\mathrm{CI_{off}}$ models are unable to provide a robust measure of the source's spectral age. Therefore, the break frequencies derived by modeling the integrated spectrum are to be considered only an indication of the break frequencies of the source, whereas they can provide a potentially useful tool for discerning between active and remnant radio galaxies. Possible interpretations of the origin of this source will be investigated in Sec. 4.4.

4.4 Discussion

At LOFAR frequencies it was possible to resolve the inner structure of the radio emission of the galaxy group MaxBCG J199, hosting a central radio galaxy which shows opposing radio jets, and lobes extending from the core out to hundreds of kpc. The spectrum of the brightest galaxy of the group indicates a broad-line galaxy (Data Release 13; [SDSS Collaboration et al., 2016]), therefore we expect an inclination of the AGN with respect to the line of sight, i.e. the jets are not in the plane of the sky. Moreover, the structure of the jets clearly shows an asymmetry in brightness that is a further indication that the source is inclined. The jet pointing towards NW is likely to be directed towards the observer, since the intensity of the approaching jet is enhanced as a consequence of bulk relativistic motion (Doppler boosting effect; [Rybicki & Lightman, 1979]). Analyzing the statistical distribution of the broad-line AGN orientations, Marin [2016] placed the inclination angle between the jets and the line of sight in the range 0° - 70°, with a mean expected value of 33°.

Luminous jets are typical of FR-I sources since the energy transport from the core to the edges is inefficient due to radiative losses and interaction with the surrounding environment. On the other hand, the spectral index map for this source suggests that

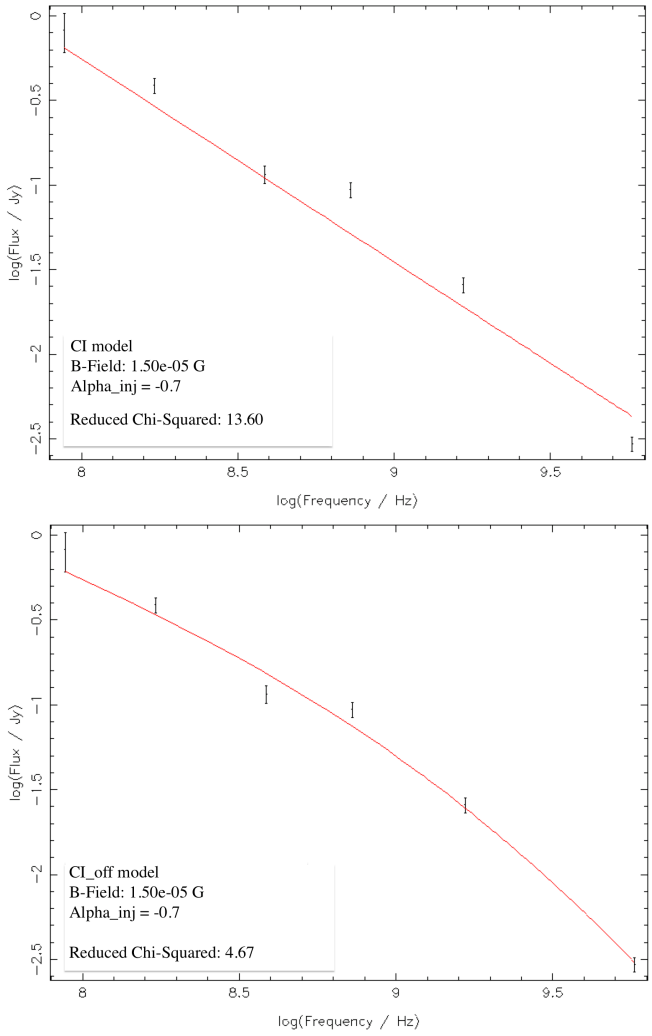

Figure 4.6: Fit and best-fit parameters of the CI model and CI_{off} model of the integrated radio spectrum.

there might be electron acceleration at the lobe edges in regions known as hotspots, and a consequential backflow typical of FR-II sources: the two jets are bent by interaction with the intragroup medium and the plasma is aging while traveling back toward the core region. However, clear hotspots are not visible in the intensity maps. As the classification scheme is purely morphological, other observed features, such as the power of the radio galaxy, cannot provide a definitive test of the source's FR type. The asymmetry in the jets' brightness suggests Doppler boosting that requires relativistic electrons, and usually the most powerful jets are observed in FR-II sources.

We suggest that the source is a radio galaxy with asymmetric jets and lobes, probably caused by Doppler boosting and interaction with the ambient medium, and with a morphology indicating a FR-I galaxy. However, the morphological classification of this source is challenging due to the variety of characteristics observed. There are no conclusive morphological elements to clearly classify the source as a FR-I or FR-II, therefore we can not exclude the FR-II scenario.

The global spectral index distribution is steeper ($\alpha \sim -1.1$) than that observed in most active radio galaxies. The steep diffuse emission that is fairly bright at LOFAR frequencies has not been detected at higher frequency, which allows us to limit the spectral index to $\alpha < -1.8 \pm 0.2$. We interpret this emission as lobe emission seen in projection, i.e old plasma from the two jets that were forced to bend (or old plasma left behind) by interacting with the ambient medium. The steep spectrum of the inner regions indicates that the particle energy content there is dominated by the low-energy electron population emitting below the sensitivity limit of the GMRT. In this scenario, the oldest plasma is located in the inner regions of the radio galaxy.

The spectral analysis shows that the inner regions have steeper spectral indices compared to the outer lobe regions (we refer to it as spectral type 2). This trend of spectral index steepening in the direction of the core region has already been found in both FR-I and FR-II radio galaxies (e.g. [Parma et al., 1999]). When the steepening occurs from the core outward, we refer to it as spectral type 1. We compared the linear size LS and synchrotron age of MaxBCG J199 computed via the $\mathrm{CI_{off}}$ model with those of low-luminosity radio galaxies (both FR-I and FR-II) in the sample selected by Parma et al. [1999]. As shown in Fig. 4.7, MaxBCG J199 (indicated by a green circle) lays within the correlation $LS \propto t_s^{0.97\pm0.17}$. We note that the linear size of MaxBCG J199 is larger than most of the galaxies in the sample, placing it in the upper region of the correlation plot.

The overall integrated flux density (3σ NVSS) at 1.4 GHz is $S_{\mathrm{tot},1.4} = 21 \pm 3$ mJy, corresponding to a total radio power of $P_{\mathrm{tot},1.4} \sim 2.1 \times 10^{24}$ W Hz^{-1} and the integrated flux density of the core region (3σ FIRST) is $S_{\mathrm{core},1.4} = 1.3 \pm 0.2$ mJy, corresponding to a total radio power of $P_{\mathrm{core},1.4} \sim 1.3 \times 10^{23}$ W Hz^{-1}.
The ratio R of core radio power at 1.4 GHz to total flux density at 150 MHz is defined as core prominence, and is used by a few authors as a criterion to search for remnant sources (e.g. [Hardcastle et al., 2016]). When $R < 10^{-4} - 5 \times 10^{-3}$, it might indicate a remnant source. However, this method alone is not enough to select remnant sources efficiently.

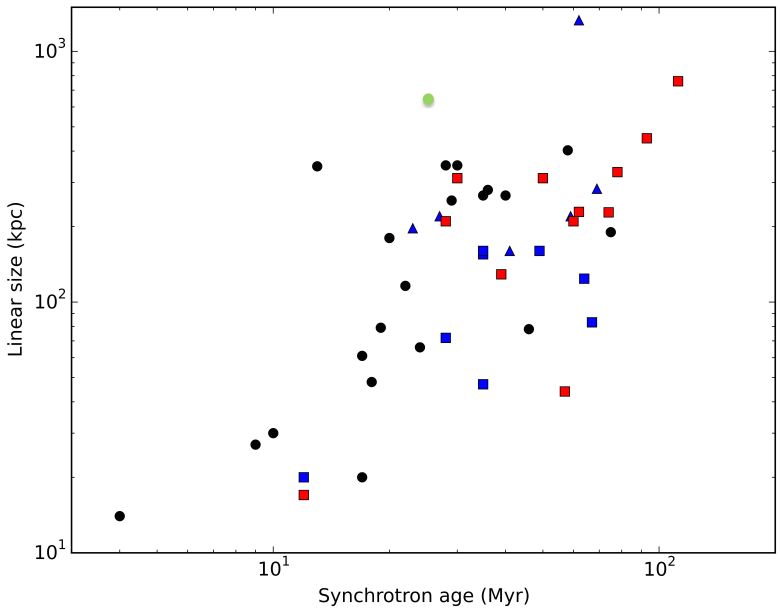

Figure 4.7: Linear size as a function of the synchrotron age for the sample of low-luminosity radio galaxies in Parma et al. [1999]. We added the values for MaxBCG J199, whose age being a lower limit is indicated by a green circle. Squares represent FRI sources, triangles FRII sources, and circles sources whose classification is not clear. The color represents the spectral type: red for type 1, blue for type 2, black for sources whose spectral classification is not clear.

The core prominence of our source is $R = P_{\mathrm{core},1.4}/P_{\mathrm{tot},1.4} \sim 6 \times 10^{-2}$, which does not place the source in the remnant range.

MaxBCG J199 is an evolved source: material was transported up to hundreds of kpc and then travelled back toward the inner regions. The youngest plasma is located at the outer lobe edges and regions closer to the host galaxy become progressively older with the oldest material is found close to the core region. However, the compact core of radio galaxies has usually a flat spectrum, on the contrary of what happens in MaxBCG J199 where it shows a steep spectral index. Therefore, we consider two possible scenarios:

- the source is still active and the core region has a spectrum steeper than standard active radio galaxies; this could be explained assuming that the steep-spectrum emission from the lobes is preventing us from resolving the core; the active core could be flat ($\alpha \sim 0$) or steep ($\alpha \sim -0.7$; e.g. [Laing & Bridle, 2014]). Assuming the lower limit $\alpha \sim -0.7$ and extrapolating from the 1.4 GHz FIRST flux density ($S_{\mathrm{core},1.4}$), we derived the upper limit on the core emission at 144 MHz to be 6.4 mJy. As expected, the result is lower than the measured value $S_{\mathrm{core},144} = 8.9 \pm 1.3$ mJy.

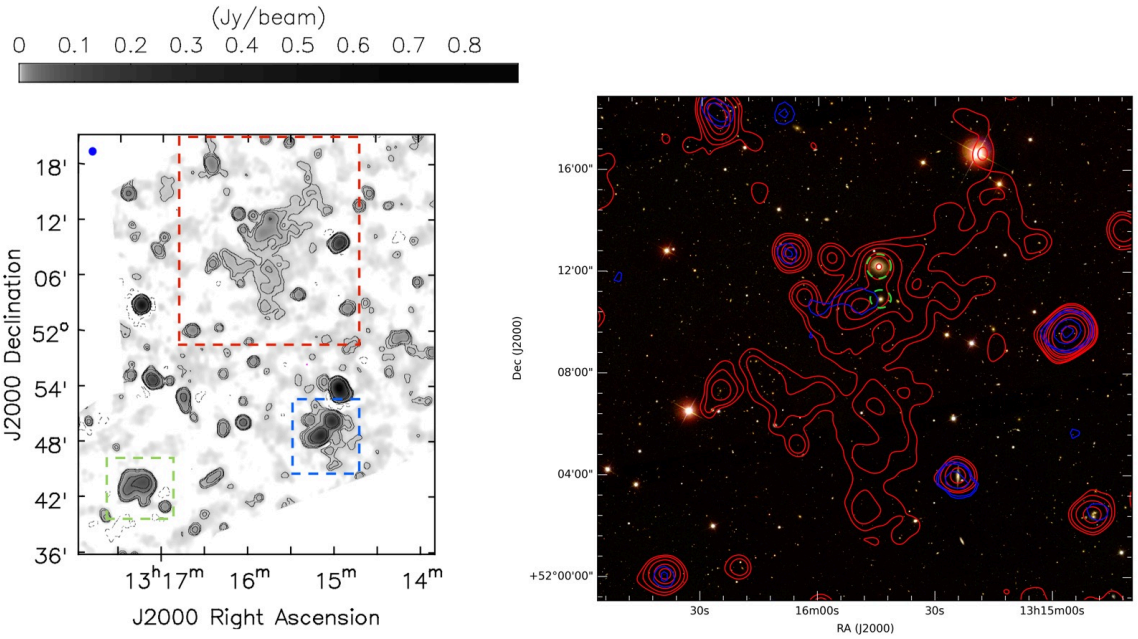

Figure 4.8: **Left panel:** Target facet image at the central frequency 144 MHz obtained with the Briggs scheme [Briggs, 1995], robust=0.2, and 30″ taper. The contour levels are at $(-3, 3, 5, 10, 50, 100) \times \sigma$ where $\sigma = 450$ μJy/beam. The beam shown in blue at the top left is 50″×47″. MaxBCG J199 (green square) is at the south-east, A1703 (blue square) at the south west and the new diffuse source (red square) extends to the north side of the facet. **Right panel:** SDSS g, r, i mosaic image of the diffuse source with radio contours from NVSS in blue and LOFAR in red. NVSS contour levels are at $(3, 5, 20, 40) \times \sigma$ where $\sigma = 440$ μJy/beam. LOFAR contour levels are at $(3, 5, 10, 20, 30, 50, 100, 300) \times \sigma$ where $\sigma = 450$ μJy/beam. The two galaxies at a redshift of $z = 0.0587 \pm 2 \times 10^{-4}$ that might be associated with this radio emission are indicated with green dashed circles.

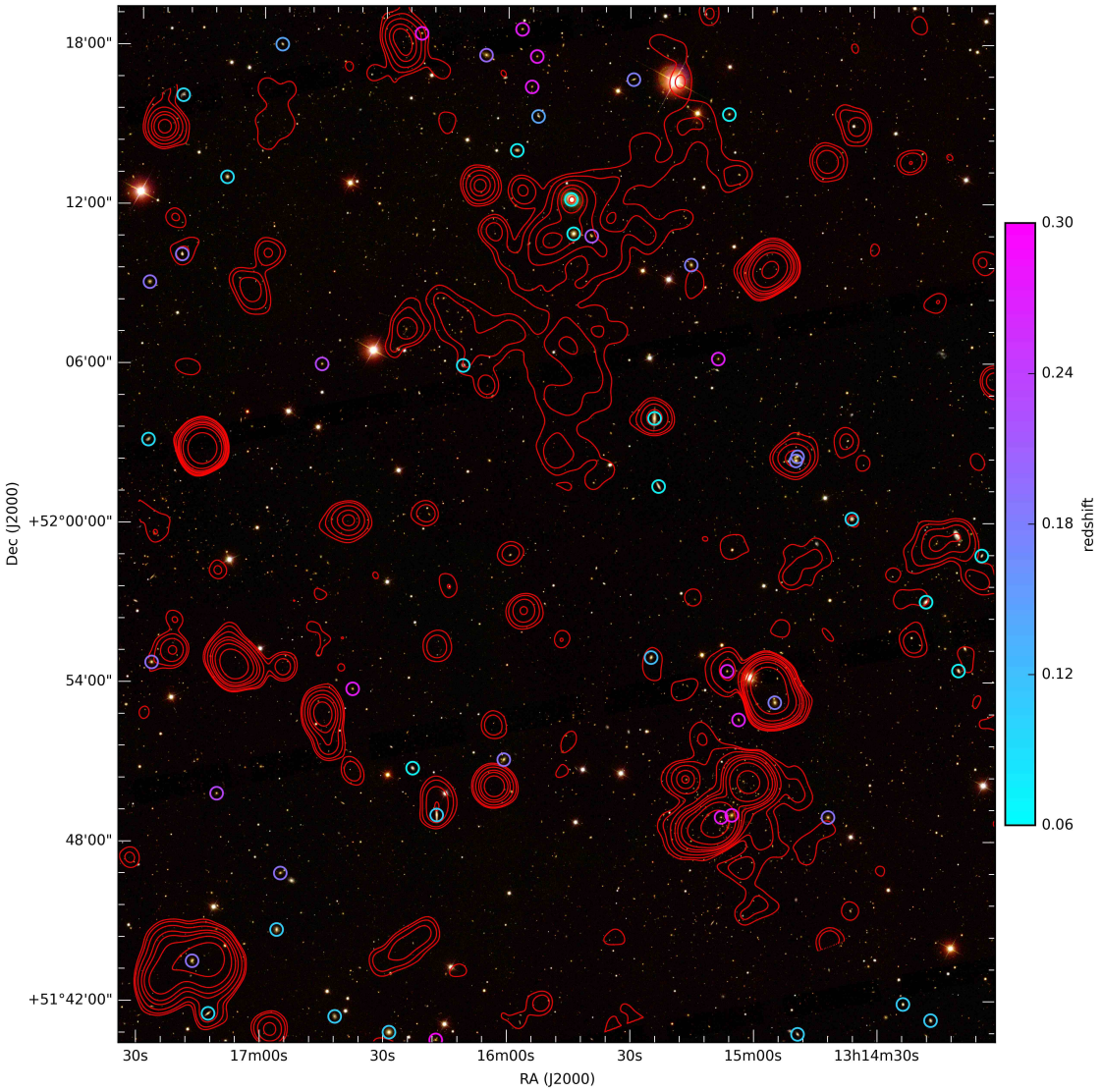

Figure 4.9: SDSS g, r, i mosaic image of the target facet. LOFAR contour levels are at $(-3, 3, 5, 10, 50, 100) \times \sigma$ where $\sigma = 450$ μJy/beam. Galaxies with known spectroscopic redshift are marked with circles colored by their corresponding redshift.

- the source could be a dying AGN with the radio emission at the position of the host galaxy being the oldest; the jets and the core are still detectable, but the synchrotron spectrum is steepening towards the inner region that has recently stopped supplying fresh particles through the nuclear activity. Moreover, the core region that includes the base of the NW jet is likely to be beamed.

  The spectral trend of the core region supports the dying-scenario, as well as the overall steep spectral value ($\alpha \sim -1.1$). Harwood [2017] shows that there is a significant difference in the spectrum of active and remnant sources and the models used to fit the spectrum can be a good indicator of a source's current state. The model fitting of the spectrum of MaxBCG J199 gives a significantly smaller chi-square value for the $CI_{\rm off}$ model. However, the dying-scenario is not fully convincing since the core region can be seen up to 1.4 GHz, even though showing a low level emission. A more detailed study of the spectrum that would allow for instance a resolved fitting (see Harwood [2017]) is needed to better understand the origin of the source and its diffuse emission.

Under simple assumptions, we derived the total radiative ages of the source despite of the problems with CI models applied to radio galaxies. The age estimated through the $\rm CI_{off}$ model is comparable with the ages of known dying radio sources ($10^7 - 10^8$ Myr, [Giacintucci et al., 2007], [Parma et al., 2007], [Murgia et al., 2011], [Brienza et al., 2016c]). We note that the dying radio sources presented in Parma et al. [2007], [Murgia et al., 2011], and[Giacintucci et al., 2007] have been studied at higher radio frequencies than LOFAR and they all have linear sizes < 230 kpc, which is much smaller than the size of the radio source in MaxBCG J199. In Brienza et al. [2016c] the discovery of a 700-kpc remnant radio galaxy is reported. The oldest and diffuse emission can be only seen up to 1.4 GHz.

With the present observations, we can not exclude other scenarios. A possibility is that we might also be observing a second episode of activity. Identifying restarting/intermitting AGN is usually related to morphological features, such as multiple radio lobes, the motion of the core or hints of a jet precession. The AGN dormant phase, i.e. the period of inactivity between two episodes, could last from several Myr to tens of Myr. In our case, the source might have switched on after a rotation of the jet axis, leaving a wing in the south-west lobe as a result of the first active phase. In this scenario, the old plasma seen in projection is the aged large-scale structure with an embedded restarted radio source. Distinct episodes of AGN activity in a radio galaxy have already been observed with LOFAR, such as recurrent AGN activity in Shulevski et al. [2015] or an AGN relic with a restarted core in Brienza et al. [2016b]. Moreover, the multiple core system might contain more than one AGN, each one of them with a different duty cycle.

4.5 A suspected remnant source

Two further interesting sources can be found close to MaxBCG J199: the lensing, X-ray luminous galaxy cluster A1703 (13:15:06.6, +51:49:29; z = 0.281), which will be treated in a separate paper (Savini et al., in prep), and a new radio source (13:15:44.0, +52:10:55.7),

which has previously never been detected. This source is clearly visible only in the LOFAR low-resolution images that are more sensitive to diffuse emission than higher-resolution (non-tapered) images. The source is shown in Fig. 4.8 and has an integrated flux density of $S_{144} \sim 600$ mJy.
NVSS, WENSS, and other radio surveys do not show any extended diffuse emission in that region of the sky. The extent of the source is $\sim 1200''$ ($20'$). We note that the largest angular scales that NVSS (VLA in D configuration, 1.4 GHz; overlay in right panel in Fig. 4.8) is $970''$, therefore this source may be partially or completely resolved out in those surveys. The largest angular scale that FIRST and VLSSr (VLA in B configuration, snapshots at 1.4 GHz and 74 MHz, respectively) can observe is $60'' \sim 1100''$. Only the latter is comparable to the extent of the source. However, no diffuse emission is present, probably due to the very low sensitivity of these snapshots surveys. The GMRT minimum baseline is 150λ, which corresponds to a maximum detectable scale of $1375''$ ($23'$), which is comparable to the extent of the source (with the caveat that the inner uv coverage could be not sufficient). However, we do not detect any emission in our GMRT observation centered on MaxBCG J199.
Hence, no upper limits on the spectrum can be computed. Observations, such as a LOFAR LBA pointing will help to determine the nature and morphology of this peculiar emission.

We searched in the NASA/IPAC Extragalactic Database (NED)[11] for possible counterparts to this diffuse emission. In Fig. 4.9, the position of close-by galaxy clusters and galaxies with known redshift is shown. We found no massive galaxy clusters in the region of the source within an angular radius of 0.5°. The two galaxies SDSS J131544.56+521213.2 and SDSS J131543.99+521055.7 at the spectroscopic redshift of $z = 0.0587 \pm 2 \times 10^{-4}$ [Adelman-McCarthy et al., 2007] might be associated with the radio emission. The emission detected by LOFAR above 10σ seems to be centered on these two galaxies, which are indicated with dashed circles in the right panel in Fig. 4.8. Therefore, we speculate that the faint diffuse radio emission in its entire extent is connected to the two galaxies with a projected separation of $\sim 79''$ that corresponds to ~ 90 kpc. They are classified as an AGN pair by Liu et al. [2011], where interacting AGN pairs with separations from kpc to tens of kpc are optically selected from SDSS (Data Release 7; [Abazajian et al., 2009]). This implies that the supermassive black holes (SMBH) in their nuclei are active during the same stage of a galaxy-galaxy merger, and accretion onto the SMBH and host-galaxy star formation is enhanced by the galaxy tidal interactions [Liu et al., 2012]. At the spectroscopic redshift of this AGN pair, the extension of the source would be ~ 1 Mpc. The northern member of the AGN pair is located at the peak of the radio emission, while the second member is offset from the second peak of the radio emission. One possible scenario is that the optical galaxies are actually dying radio galaxies which interacted as an AGN pair in the past, and whose radio emission might be old and steep. The lobes are fading away, and the emission can be interpreted as a radio remnant source.
We note that the shape of this source is comparable with the dying radio galaxy WNB 1851+5707a seen at 1.4 GHz, although the latter extends on a much smaller scale (Fig. 6 in Murgia et al. [2011]).

[11] https://ned.ipac.caltech.edu

4.6 Summary

We present the discovery of extended radio emission at LOFAR frequencies at the coordinates of the galaxy group MaxBCG J199 (RA = 13:17:16.4, DEC = +51:43:30.0, J2000). SDSS photometric data reveal a total of 13 galaxies within this group and a multiple core system composed of three galaxies. We performed the reduction of the LOFAR data using the Facet Calibration method to reach a rms noise of 135 μJy/beam and resolution of $10.6'' \times 6.0''$ at HBA frequencies (120 - 168 MHz). LOFAR observations show that the radio diffuse emission is connected to a central radio galaxy whose powerful radio jets and lobes extend on angular scales of $3.4'$, corresponding to a linear size of 650 kpc at the spectroscopic redshift of the source. The core of the radio galaxy is coincident with the brightest galaxy of the group at $z = 0.18793 \pm 5 \times 10^{-5}$.

We obtained a GMRT follow-up observation at 607 MHz to study the spectral properties of the sources. GMRT images reach a rms noise of 60 μJy/beam at $6.0'' \times 4.8''$ resolution. LOFAR images show a greater extent than GMRT emission: only the brightest and more compact emission is visible in the GMRT image, which can be used to obtain a low-frequency spectral index map. The spectral index values range from -1.3 to -1.1 in the core region and inner edges, and from -0.7 to -0.5 at the outer edges, therefore it steepens going towards the inner regions. The global spectral index value of the source calculated using the integrated flux densities above 3σ from GMRT and LOFAR is relatively steep, around -1.1. The diffuse emission detected at 120 - 168 MHz that can not be seen at 591 - 623 MHz must be steeper, and we place an upper limit of -1.8 ± 0.2. We interpret this emission as old lobe emission seen in projection. The extension of the source suggests a strong nuclear activity of the central engine. The low-frequency spectral index map obtained between LOFAR and GMRT images reveals a steepening of the spectrum from the lobe outer edge inward and a steep core, which is in disagreement with the usual spectrum of active nuclei. Moreover, the spectral index map indicates activity only at the edge of the lobes. Therefore, we considered two possible interpretations: the source is active, but we observe a mix of core and steep spectrum emission that causes the spectral index of the core to appear steeper than it really is; or the source is dying, i.e. the AGN has recently entered a phase of quiescence, where the nucleus stopped supplying fresh electrons to the lobes.

We conclude that the radio source found in MaxBCG J199 is an evolved radio-loud AGN surrounded by diffuse emission that can be best studied with LOFAR and is likely related to old plasma left behind by the jets forming the lobes or a continuation of the lobes that experienced a backflow at the edges. The two jets are interacting with the intragroup medium that shows asymmetrical features in the lobe regions.

These observations probe the great potential of LOFAR to detect old plasma, and demonstrate that low-energy electrons are present in the intragroup medium, and could furnish a seed population for particle re-acceleration mechanisms. The source that we have presented in this paper is an example of steep-spectrum radio source that low-frequency surveys, such as LoTSS, can discover.

Acknowledgments

LOFAR, the Low Frequency Array designed and constructed by ASTRON, has facilities owned by various parties (each with their own funding sources), and that are collectively operated by the International LOFAR Telescope (ILT) foundation under a joint scientific policy.
We would like to thank the staff of the GMRT that made the observation possible. GMRT is run by the National center for Radio Tata Institute of Fundamental Research.
The research leading to these results has received funding from the European Research Council under the European Union's Seventh Framework Programme (FP/2007-2013) / ERC Advanced Grant RADIOLIFE-320745. M. J. Hardcastle acknowledges support from the UK Science and Technology Facilities Council [ST/M001008/1]. P. N. Best is grateful for support from the UK STFC via grant ST/M001229/1. A. O. Clarke gratefully acknowledge support from the European Research Council under grant ERC-2012-StG-307215 LODESTONE.
This research made use of the NASA/IPAC Extragalactic Database (NED), which is operated by the Jet Propulsion Laboratory, California Institute of Technology, under contract with the National Aeronautics and Space Administration.
This research made use of APLpy, an open-source plotting package for Python hosted at http://aplpy.github.com.
F. Savini thanks Steven N. Shore (University of Pisa) for his helpful comments.

Chapter 5

Conclusions

5.1 Context

In the past decades, many efforts have been made to understand the origin of radio emission in galaxy clusters. The radio facilities have significantly improved in resolution and sensitivity, challenging astronomers to work with increasingly large samples, surveys, and datasets. In particular, new generations of radio telescopes and advances in computing are making radio astronomy at frequencies below 1 GHz an accessible and rich field. Low-frequency observations are ideal for discovering emission from low-energy cosmic ray electrons, which are invisible at higher frequencies. In the last years, such observations have shown that the zoo of radio sources in galaxy clusters is more complex than previously thought. With interferometers, such as the Low Frequency ARray (LOFAR), we have the unique possibility of exploring the sky in the frequency band 120 - 168 MHz and obtain very high-quality images of low surface brightness, extended, steep-spectrum radio emission from clusters. The study of these sources provides crucial information on the microphysics of the hot plasma that pervades the volume of a cluster (i.e. the intracluster medium; ICM), including the way energy is transported at different scales.

This PhD project has been conceived with the idea of investigating the physics of the radio-emitting sources associated with the ICM in galaxy clusters, in particular non-merging clusters. Radio emission requires the presence of magnetic fields and relativistic particles that emit synchrotron radiation. Non-thermal radio sources in clusters are characterized by low surface brightness and steep radio spectrum, and are connected to the thermal properties of the gas. Centrally-located diffuse radio sources are classified as mini halos or giant halos, depending on their morphology and size, hundreds of kpc up to a Mpc, respectively. Halos indicate the presence of cluster-wide particle acceleration mechanisms: the particle radiative lifetime ($\sim 10^8$ yr) is too short to allow the diffusion through the cluster volume on Mpc scales, thus the radio-emitting particles must undergo in situ energization (turbulence re-acceleration model) that can be provided by a merger event. Giant halos have preferentially been found in clusters that typically do not have a cool core, and display significant evidence for an ongoing major merger. Mini halos are instead found exclusively in cool-core clusters, and are confined within the cluster inner regions. In cool-core clusters, minor mergers can generate turbulence through gas sloshing.

The idea of observing non-merging clusters at low frequency is motivated by recent observations carried out with the Giant Metrewave Radio Telescope (GMRT) and the Very Large Array (VLA). Although the merger scenario does not predict halo emission in dynamically-relaxed systems, radio halos have recently been found in a few clusters that are not undergoing major mergers, and that - in some cases - host a cool core (i.e. CL1821+643, [Bonafede et al., 2014]; A2261, A2390, [Sommer et al., 2017]; A2142, [Venturi et al., 2017]). Through X-ray observations, it is possible to gather information on the dynamical state of the cluster and search for correlations with the radio properties. It has been proposed that these sources might be connected to the occurrence of minor or off-axis mergers, although it remains unclear how minor mergers could initiate continuum emission on such large scales. To assess whether the emission discovered in these few cases is common in galaxy clusters or not if looking at low radio frequencies, and to investigate how it is connected to the cluster dynamics, I focused my work on non-merging galaxy clusters, including cool-core clusters. Signatures of minor-merging activities and gas-sloshing mechanisms have been detected in cool-core clusters containing mini halos (e.g. [Gitti et al., 2007], [Giacintucci et al., 2014b], [Savini et al., 2018b]). This scenario is particularly interesting when observed at low radio frequencies, as any connection may emerge that can not be seen at higher frequencies, e.g. new insights on the connections between mini halos, giant radio halos, and the cluster dynamics.

5.2 Summary of published work

The recent advent of cluster surveys via the Sunyaev-Zel'dovich (SZ) effect measured by the Planck satellite has opened the possibility to build cluster samples that are as close as possible to be mass-selected. Moreover, only a small number of clusters has been observed with LOFAR so far. For my PhD project I studied the first SZ-sample of non-merging massive clusters at low frequencies, and reduced with a direction-dependent calibration. The aim was (i) to determine which clusters in the sample contain large-scale radio emission indicative of a transitional phase between mini halos and giant radio halos; (ii) to study how cluster-wide radio emission correlates with X-ray emission; (iii) to provide spectral analysis for the targets hosting a mini halo, making use of the already available higher frequency observations. Moreover, LOFAR observations allowed us to detect ultra-steep-spectrum emission ($\alpha < -1.5$) that could not be seen at higher frequencies. In detail, on the basis of their mass, X-ray morphology and a lack of evidence of a recent major merger, I selected a sample of nine clusters with mass $\geq 6 \times 10^{14}$ $M_{\odot}$. Five of the targets were observed as part of the LOFAR Two-metre Sky Survey (LoTSS; [Shimwell et al., 2017]). The remaining four were observed as part of dedicated proposals where I was the Principal Investigator. In Savini et al. [2018a] I have presented the results of the largest campaign of LOFAR observations targeting galaxy clusters so far. Every dataset has been calibrated following the recently-developed Facet Calibration scheme [van Weeren et al., 2016a]. Interestingly, I discovered that two clusters with a cool core and some level of dynamical disturbances, namely RXJ1720.1+2638 and PSZ1G139.6+24, show ultra-steep-spectrum emission extending well beyond the core that resembles radio halo emission. These two

clusters also host mini halos in their cores. I proposed that the sloshing of the dense core after a minor merger that powers electron re-acceleration without disrupting the core can be responsible for the formation, not only of a central mini halo, but also of larger-scale emission that is visible at low radio frequencies. In addition, I confirmed the presence of a mini halo in A1413, which is the only mini halo in a non-cool-core cluster found so far. No giant radio halos in the cool-core clusters of this sample are found since A2261 does not host a cool core. The central radio galaxy I discovered in the massive cool-core cluster A2390 might account for most or even all the radio flux that was previously attributed to the presence of a giant radio halo [Sommer et al., 2017]. Furthermore, I found a new radio halo in the cluster RXCJ0142.0+2131 that is a candidate ultra-steep-spectrum radio halo. Such sources are predicted in the framework of the turbulent re-acceleration model, in presence of minor mergers. Finally, a number of clusters, namely A478, A1576, and A1423, do not show any hint of cluster-scale diffuse emission at the sensitivity of the LOFAR observations. I used the derived limit on the radio power of A1423 to constrain the energy budget of cosmic ray protons in the ICM, and compare the result with the constraints derived from the lack of hadronic-ray emission reported by the *Fermi* satellite. The ratio of the spatial distribution of the cosmic ray energy density over the gas energy density profile derived from the LOFAR observations is $\sim 3\%$. This result is competitive with the deepest *Fermi* limits for the Coma cluster.

As a side project, I aimed to study the diffuse emission associated with a low-mass system, such as a galaxy group, since halos and mini halos have rarely been observed in such environments. However, this could be due to a lack of sensitivity of previous observations. I found radio diffuse emission extending for hundreds of kpc from the galaxy group MaxBCGJ199.31832+51.72503. After calibration, it was possible to resolve the inner structure of this emission that was found to be connected with the central radio galaxy rather than with the intragroup medium. Thus, I studied this new source, obtaining a follow-up observation at 610 MHz at the GMRT. I derived the spectral index of the different components of the source (core, jets, and lobes). A spectral steepening toward the inner regions and a steep-spectrum core region was found. I modeled the integrated radio spectrum, analyzing the energy distribution evolution with time (spectral aging models). The results suggested two possible interpretations: the radio galaxy is evolved but still active, or it is just at the end of its active phase. In the first scenario, the source is active with the core region being steeper than what is seen for standard active radio galaxies. In the second case, the source could be a dying AGN with the radio emission at the position of the host galaxy being the oldest; the jets and the core are still detectable, but the synchrotron spectrum is steepening towards the inner region that has recently stopped supplying fresh particles through the nuclear activity.

5.3 Outlook and suggestions for future work

The study of cluster-scale radio sources is a central topic in the key science programs of the new generation of radio and X-ray facilities, including LOFAR, and the up-coming *Athena* and SKA. The observations presented in this thesis show the great potential of LOFAR in detecting new diffuse sources and revealing new details on sources studied at

higher radio frequencies.

The discovery of radio sources, such as that found in the cool-core cluster PSZ1G139.61+24, suggests that, under particular circumstances, both a mini and giant halo could co-exist in a single cluster, opening new perspectives for particle acceleration mechanisms in galaxy clusters. The presence of a cool core might be significant for the formation of radio diffuse emission on scales larger than the cluster core that hosts a mini halo. The further discovery of a similar source in the cool-core cluster RXJ1720.1+2638 indicate the sloshing of the core could be responsible for particle acceleration outside the core. If other such systems will be found, we might conclude that radio emission on cluster-scale (radio halo) is common in clusters with a dense core and signs of minor-merger activities, when observed at low frequencies. In that case, the spectrum of the large-scale emission must be measured to verify its possible consistency with turbulent re-acceleration that imply a steep spectrum. To explore these new scenarios I have co-authored a successful LOFAR proposal to observe a sample of clusters with a cool core and signs of dynamical activity. The selected clusters also have good quality data at higher frequencies (i.e. GMRT and/or VLA) to determine the spectrum of the sources.

The results and conclusions drawn in this thesis open up avenues for further research with larger samples of non-merging clusters. For instance, the release of the LOFAR survey data and the research made for automatizing data calibration will help to make progress. With new low-frequency surveys covering a significant fraction of the sky, many new radio sources are expected to be discovered. Thus, with the improved statistics offered by larger samples, the role of minor mergers, and the properties and occurrence rates of halos and mini halos as a function of cluster mass, dynamical state, and other global cluster properties can be investigated in detail. Furthermore, large cluster samples will shed more light on the possible connection between halos and mini halos and their evolution over cosmic time, from $z \sim 1$ to the present epoch.

Bibliography

Abazajian K. N., et al., 2009, ApJs, 182, 543

Ackermann M., et al., 2010, ApJ, 717, L71

Ackermann M., et al., 2014, ApJ, 787, 18

Adelman-McCarthy J. K., et al., 2007, ApJs, 172, 634

Aleksić J., et al., 2012, A& A, 541, A99

Allen S. W., Rapetti D. A., Schmidt R. W., Ebeling H., Morris R. G., Fabian A. C., 2008, MNRAS, 383, 879

Augusto P., Edge A. C., Chandler C. J., 2006, MNRAS, 367, 366

Baars J. W. M., Genzel R., Pauliny-Toth I. I. K., Witzel A., 1977, A & A, 61, 99

Bacchi M., Feretti L., Giovannini G., Govoni F., 2003, AAp, 400, 465

Barr J., Jørgensen I., Chiboucas K., Davies R., Bergmann M., 2006, ApJ, 649, L1

Bartalucci I., Mazzotta P., Bourdin H., Vikhlinin A., 2014, A & A, 566, A25

Beck R., Krause M., 2005, Astronomische Nachrichten, 326, 414

Becker R. H., White R. L., Helfand D. J., 1995a, ApJ, 450, 559

Becker R. H., White R. L., Helfand D. J., 1995b, ApJ, 450, 559

Berezinsky V. S., Blasi P., Ptuskin V. S., 1997, ApJ, 487, 529

Blanton E. L., Randall S. W., Clarke T. E., Sarazin C. L., McNamara B. R., Douglass E. M., McDonald M., 2011, ApJ, 737, 99

Blasi P., Colafrancesco S., 1999, Astropart. Phys., 122, 169

Blasi P., Gabici S., Brunetti G., 2007, International Journal of Modern Physics A, 22, 681

Böhringer H., et al., 2010, AAp, 514, A32

Bonafede A., Feretti L., Murgia M., Govoni F., Giovannini G., Dallacasa D., Dolag K., Taylor G. B., 2010, AAp, 513, A30

Bonafede A., et al., 2014, MNRAS, 444, L44

Bonafede A., et al., 2017, MNRAS, 470, 3465

Borgani S., Kravtsov A., 2011, Advanced Science Letters, 4, 204

Boschin W., Girardi M., 2018, MNRAS, 480, 1187

Botteon A., Gastaldello F., Brunetti G., 2017, preprint, (arXiv:1707.07038)

Botteon A., Gastaldello F., Brunetti G., 2018, MNRAS, 476, 5591

Bower R. G., Lucey J. R., Ellis R. S., 1992, MNRAS, 254, 601

Brienza M., Godfrey L., Morganti R., 2016a, in Active Galactic Nuclei: What's in a Name?. p. 102 (arXiv:1603.01837), doi:10.5281/zenodo.60638

Brienza M., Morganti R., Shulevski A., Godfrey L., Vilchez N., 2016b, Astronomische Nachrichten, 337, 31

Brienza M., et al., 2016c, A & A, 585, A29

Briggs D. S., 1995, New Mexico Institute of Mining Technology, Socorro, New Mexico, USA,

Brüggen M., Bykov A., Ryu D., Röttgering H., 2012, SSr, 166, 187

Brunetti G., Jones T. W., 2014, International Journal of Modern Physics D, 23, 1430007

Brunetti G., Lazarian A., 2011, MNRAS, 410, 127

Brunetti G., Setti G., Feretti L., Giovannini G., 2001, MNRAS, 320, 365

Brunetti G., Venturi T., Dallacasa D., Cassano R., Dolag K., Giacintucci S., Setti G., 2007, ApJl, 670, L5

Brunetti G., et al., 2008, Nat, 455, 944

Brunetti G., Blasi P., Reimer O., Rudnick L., Bonafede A., Brown S., 2012, MNRAS, 426, 956

Buote D. A., 2001, ApJl, 553, L15

Burns J. O., Hallman E. J., Gantner B., Motl P. M., Norman M. L., 2008, ApJ, 675, 1125

Cassano R., Brunetti G., Setti G., 2006, MNRAS, 369, 1577

Cassano R., Brunetti G., Setti G., Govoni F., Dolag K., 2007, MNRAS, 378, 1565

Cassano R., Brunetti G., Venturi T., Setti G., Dallacasa D., Giacintucci S., Bardelli S., 2008a, AAp, 480, 687

Cassano R., Gitti M., Brunetti G., 2008b, AAp, 486, L31

Cassano R., Ettori S., Giacintucci S., Brunetti G., Markevitch M., Venturi T., Gitti M., 2010, ApJl, 721, L82

Cassano R., et al., 2013, ApJ, 777, 141

Cassano R., Brunetti G., Giocoli C., Ettori S., 2016, AAp, 593, A81

Cavagnolo K. W., Donahue M., Voit G. M., Sun M., 2009, ApJs, 182, 12

Cavaliere A., Fusco-Femiano R., 1976, A & A, 49, 137

Chambers K. C., et al., 2016, preprint, (arXiv:1612.05560)

Chandra P., Ray A., Bhatnagar S., 2004, ApJ, 612, 974

Clarke T. E., 2004, Journal of Korean Astronomical Society, 37, 337

Clarke A. O., et al., 2017, A & A, 601, A25

Condon J. J., Cotton W. D., Greisen E. W., Yin Q. F., Perley R. A., Taylor G. B., Broderick J. J., 1998, AJ, 115, 1693

Cornwell T. J., 2008, IEEE Journal of Selected Topics in Signal Processing, 2, 793

Croston J. H., Hardcastle M. J., 2014, MNRAS, 438, 3310

Croston J. H., Hardcastle M. J., Birkinshaw M., 2005, MNRAS, 357, 279

Cuciti V., Cassano R., Brunetti G., Dallacasa D., Kale R., Ettori S., Venturi T., 2015, AAp, 580, A97

Dahle H., Kaiser N., Irgens R. J., Lilje P. B., Maddox S. J., 2002, ApJs, 139, 313

De Grandi S., Molendi S., 2001, ApJ, 551, 153

De Young D. S., 1972, ApJ, 173, L7

Dennison B., 1980, ApJl, 239, L93

Dolag K., Enßlin T. A., 2000, AAp, 362, 151

Donnert J., Dolag K., Brunetti G., Cassano R., Bonafede A., 2010, MNRAS, 401, 47

Eckert D., Molendi S., Paltani S., 2011, AAp, 526, A79

Fabian A. C., Nulsen P. E. J., Canizares C. R., 1991, A & Ar, 2, 191

Feretti L., Giovannini G., Govoni F., Murgia M., 2012, A & Ar, 20, 54

Forman W., Kellogg E., Gursky H., Tananbaum H., Giacconi R., 1972, ApJ, 178, 309

Ghirardini V., et al., 2018, preprint, (arXiv:1805.00042)

Giacintucci S., Venturi T., Murgia M., Dallacasa D., Athreya R., Bardelli S., Mazzotta P., Saikia D. J., 2007, A & A, 476, 99

Giacintucci S., et al., 2011, ApJ, 732, 95

Giacintucci S., Markevitch M., Venturi T., Clarke T. E., Cassano R., Mazzotta P., 2014a, ApJ, 781, 9

Giacintucci S., Markevitch M., Brunetti G., ZuHone J. A., Venturi T., Mazzotta P., Bourdin H., 2014b, ApJ, 795, 73

Giacintucci S., Markevitch M., Cassano R., Venturi T., Clarke T. E., Brunetti G., 2017, ApJ, 841, 71

Gitti M., Brunetti G., Setti G., 2002, AAp, 386, 456

Gitti M., Ferrari C., Domainko W., Feretti L., Schindler S., 2007, AAp, 470, L25

Govoni F., Feretti L., 2004, International Journal of Modern Physics D, 13, 1549

Govoni F., Murgia M., Markevitch M., Feretti L., Giovannini G., Taylor G. B., Carretti E., 2009, AAp, 499, 371

Gregory P. C., Scott W. K., Douglas K., Condon J. J., 1996, ApJs, 103, 427

Hansen S. M., McKay T. A., Wechsler R. H., Annis J., Sheldon E. S., Kimball A., 2005, ApJ, 633, 122

Hardcastle M. J., et al., 2016, MNRAS, 462, 1910

Harwood J. J., 2017, MNRAS, 466, 2888

Harwood J. J., Hardcastle M. J., Croston J. H., Goodger J. L., 2013, MNRAS, 435, 3353

Harwood J. J., Hardcastle M. J., Croston J. H., 2015, MNRAS, 454, 3403

Harwood J. J., et al., 2016, MNRAS, 458, 4443

Haslam C. G. T., Salter C. J., Stoffel H., Wilson W. E., 1995, Astronomy Data Image Library,

Heald G. H., et al., 2015, A & A, 582, A123

Helmboldt J. F., Kassim N. E., Cohen A. S., Lane W. M., Lazio T. J., 2008, ApJs, 174, 313

Henriksen M. J., Mushotzky R. F., 1986, ApJ, 302, 287

Hoegbom J. A., 1974, A & A, 15, 417

Hoekstra H., Bartelmann M., Dahle H., Israel H., Limousin M., Meneghetti M., 2013, SSr, 177, 75

Intema H. T., Jagannathan P., Mooley K. P., Frail D. A., 2017, AAp, 598, A78

Jaffe W. J., 1977, ApJ, 212, 1

Jaffe W. J., Perola G. C., 1973, A & A, 26, 423

Jones C., Forman W., 1984, ApJ, 276, 38

Kaiser C. R., Alexander P., 1999, MNRAS, 305, 707

Kalberla P. M. W., Burton W. B., Hartmann D., Arnal E. M., Bajaja E., Morras R., Pöppel W. G. L., 2005, AAp, 440, 775

Kale R., Venturi T., Giacintucci S., Dallacasa D., Cassano R., Brunetti G., Macario G., Athreya R., 2013, AAp, 557, A99

Kale R., et al., 2015, AAp, 579, A92

Kardashev N. S., 1962, sovast, 6, 317

Koester B. P., et al., 2007, ApJ, 660, 239

Komissarov S. S., Gubanov A. G., 1994, A & A, 285, 27

Kravtsov A. V., Borgani S., 2012, Annual review of astronomy and astrophysics, 50, 353

Laing R. A., Bridle A. H., 2014, MNRAS, 437, 3405

Lane W. M., Cotton W. D., Helmboldt J. F., Kassim N. E., 2012, Radio Science, 47, RS0K04

Large M. I., Mathewson D. S., Haslam C. G. T., 1959, Nature, 183, 1663

Lau E. T.-H., 2010, PhD thesis, The University of Chicago

Liang H., Hunstead R. W., Birkinshaw M., Andreani P., 2000, ApJ, 544, 686

Liu X., Shen Y., Strauss M. A., Hao L., 2011, The Astrophysical Journal, 737, 101

Liu X., Shen Y., Strauss M. A., 2012, ApJ, 745, 94

Longair M. S., 2011, High Energy Astrophysics

Lovisari L., et al., 2017, ApJ, 846, 51

Macario G., Venturi T., Brunetti G., Dallacasa D., Giacintucci S., Cassano R., Bardelli S., Athreya R., 2010, AAp, 517, A43

Marin F., 2016, MNRAS, 460, 3679

Markevitch M., Vikhlinin A., 2007, Physics Reports, 443, 1

Markevitch M., et al., 2000, ApJ, 541, 542

Markevitch M., Vikhlinin A., Forman W. R., 2003, in Bowyer S., Hwang C.-Y., eds, Astronomical Society of the Pacific Conference Series Vol. 301, Matter and Energy in Clusters of Galaxies. p. 37 (arXiv:astro-ph/0208208)

Martinez Aviles G., et al., 2016, AAp, 595, A116

Mazzotta P., Giacintucci S., 2008, ApJl, 675, L9

McMullin J. P., Waters B., Schiebel D., Young W., Golap K., 2007, in Shaw R. A., Hill F., Bell D. J., eds, Astronomical Society of the Pacific Conference Series Vol. 376, Astronomical Data Analysis Software and Systems XVI. p. 127

Miley G., 1980, Annual review of astronomy and astrophysics, 18, 165

Motl P. M., Hallman E. J., Burns J. O., Norman M. L., 2005, ApJ, 623, L63

Murgia M., Fanti C., Fanti R., Gregorini L., Klein U., Mack K.-H., Vigotti M., 1999, A & A, 345, 769

Murgia M., Govoni F., Markevitch M., Feretti L., Giovannini G., Taylor G. B., Carretti E., 2009, AAp, 499, 679

Murgia M., et al., 2011, A & A, 526, A148

O'Sullivan E., Worrall D. M., Birkinshaw M., Trinchieri G., Wolter A., Zezas A., Giacintucci S., 2011, MNRAS, 416, 2916

Offringa A. R., van de Gronde J. J., Roerdink J. B. T. M., 2012, A & A, 539, A95

Offringa A. R., et al., 2014, MNRAS, 444, 606

Okabe A., ed. 2000, Spatial tessellations : concepts and applications of voronoi diagrams

Pacholczyk A. G., 1970, Radio astrophysics. Nonthermal processes in galactic and extragalactic sources

Parma P., Murgia M., Morganti R., Capetti A., de Ruiter H. R., Fanti R., 1999, A & A, 344, 7

Parma P., Murgia M., de Ruiter H. R., Fanti R., Mack K.-H., Govoni F., 2007, A & A, 470, 875

Pearce C. J. J., et al., 2017, ApJ, 845, 81

Peebles P. J. E., Yu J. T., 1970, ApJ, 162, 815

Perley R. A., Butler B. J., 2013, ApJs, 204, 19

Petrosian V., 2001, ApJ, 557, 560

Petrosian V., East W. E., 2008, ApJ, 682, 175

Pfrommer C., Enßlin T. A., 2004, AAp, 413, 17

Pinzke A., Oh S. P., Pfrommer C., 2017, MNRAS, 465, 4800

Planck Collaboration et al., 2014, AAp, 571, A29

Planck Collaboration et al., 2016, A & A, 594, A13

Rasia E., Meneghetti M., Ettori S., 2013, The Astronomical Review, 8, 40

Rau U., Cornwell T. J., 2011, A & A, 532, A71

Reimer O., Pohl M., Sreekumar P., Mattox J. R., 2003, ApJ, 588, 155

Rengelink R. B., Tang Y., de Bruyn A. G., Miley G. K., Bremer M. N., Roettgering H. J. A., Bremer M. A. R., 1997, A & As, 124

Rephaeli Y., Sadeh S., Shimon M., 2005, in Melchiorri F., Rephaeli Y., eds, Vol. 2005937974, Background Microwave Radiation and Intracluster Cosmology. p. 57

Roland J., 1981, A&A, 93, 407

Röttgering H. J. A., et al., 2006, ArXiv Astrophysics e-prints,

Rozo E., et al., 2009, The Astrophysical Journal, 699, 768

Rybicki G. B., Lightman A. P., 1979, Radiative processes in astrophysics

Rykoff E. S., et al., 2012, ApJ, 746, 178

SDSS Collaboration et al., 2016, preprint, (arXiv:1608.02013)

Sadat R., 1997, in Valls-Gabaud D., Hendry M. A., Molaro P., Chamcham K., eds, Astronomical Society of the Pacific Conference Series Vol. 126, From Quantum Fluctuations to Cosmological Structures. p. 349 (arXiv:astro-ph/9702050)

Sanders J. S., 2006, MNRAS, 371, 829

Sanderson A. J. R., O'Sullivan E., Ponman T. J., 2009, MNRAS, 395, 764

Santos J. S., Rosati P., Tozzi P., Böhringer H., Ettori S., Bignamini A., 2008, AAp, 483, 35

Sarazin C. L., 1999, ApJ, 520, 529

Savini F., Bonafede A., Brüggen M., et al. 2018a, A LOFAR study of non-merging massive galaxy clusters, Manuscript accepted to A&A for publication

Savini F., et al., 2018b, preprint, (arXiv:1805.01900)

Savini F., et al., 2018c, MNRAS, 474, 5023

Scaife A. M. M., Heald G. H., 2012, MNRAS, 423, L30

Shimwell T. W., et al., 2016, MNRAS, 459, 277

Shimwell T. W., et al., 2017, A & A, 598, A104

Shimwell T. W., Tasse C., Hardcastle M. J., et al. 2018, The LOFAR Two-metre Sky Survey - II. First Data Release, Manuscript accepted to A&A for publication

Shulevski A., et al., 2015, A & A, 579, A27

Shulevski A., et al., 2017, A & A, 600, A65

Sommer M. W., Basu K., Intema H., Pacaud F., Bonafede A., Babul A., Bertoldi F., 2017, MNRAS, 466, 996

Sonkamble S. S., Vagshette N. D., Pawar P. K., Patil M. K., 2015, Apss, 359, 21

Springel V., et al., 2005, Nature, 435, 629

Sun M., Jones C., Murray S. S., Allen S. W., Fabian A. C., Edge A. C., 2003, ApJ, 587, 619

Sunyaev R. A., Zeldovich I. B., 1980, Annual review of astronomy and astrophysics, 18, 537

Taylor G. B., Carilli C. L., Perley R. A., eds, 1999, Synthesis Imaging in Radio Astronomy II Astronomical Society of the Pacific Conference Series Vol. 180

Vazza F., Gheller C., Brüggen M., 2014, MNRAS, 439, 2662

Venturi T., Giacintucci S., Dallacasa D., Cassano R., Brunetti G., Bardelli S., Setti G., 2008, AAp, 484, 327

Venturi T., et al., 2017, AAp, 603, A125

Vikhlinin A., Markevitch M., Murray S. S., 2001, ApJ, 551, 160

Vikhlinin A., et al., 2009, ApJ, 692, 1060

Voges W., et al., 1999, A & A, 349, 389

Wik D. R., Sarazin C., Zhang Y., Baumgartner W., Mushotzky R., Tueller J., Clarke T., 2012, in American Astronomical Society Meeting Abstracts #219. p. 207.02

Wilber A., et al., 2018, MNRAS, 476, 3415

York D. G., et al., 2000, AJ, 120, 1579

ZuHone J. A., Markevitch M., Brunetti G., Giacintucci S., 2013, ApJ, 762, 78

de Gasperin F., et al., 2017, preprint, (arXiv:1710.06796)

van Haarlem M. P., et al., 2013a, A&A, 556, A2

van Haarlem M. P., et al., 2013b, AAp, 556, A2

van Haarlem M. P., et al., 2013c, A & A, 556, A2

van Weeren R. J., et al., 2014, ApJl, 786, L17

van Weeren R. J., et al., 2016a, ApJs, 223, 2

van Weeren R. J., et al., 2016b, ApJ, 818, 204

van Weeren R. J., et al., 2017, Nature Astronomy, 1, 0005

von der Linden A., et al., 2014, MNRAS, 443, 1973

Appendix A

Appendix

A.1 Bremsstrahlung emission

Bremsstrahlung is a German word that means "braking radiation", and refers to the thermal radiation that a charged particle emits when accelerated by an electric field of another charged particle (e.g. ions). Since the particle remains free before and after the interaction, the Bremsstrahlung radiation is also called free-free emission. As the particle energy changes due to the collision are continuous, this emission is characterized by a continuous spectrum over a wide range. Considering that the rate of of collisions per volume is proportional to the number of ions and electrons in this volume, $n_{\rm i}$ and $n_{\rm e}$, the emissivity of a bremsstrahlung-emitting plasma is known to be:

$$\epsilon_\nu \propto n_{\rm e}\, n_{\rm i}\, T^{-1/2}\, e^{-h\nu/kT}\, g(\nu, T)$$

where ν is the frequency, T is the temperature of the gas, and $g(\nu, T)$ is the Gaunt factor, which accounts for quantum mechanical effects. An example of spectrum is shown in Fig. A.1. The X-ray luminosity of the intracluster gas is obtained by integrating the emissivity over all the frequencies and the cluster volume, and results in:

$$L_X \propto n_{\rm e}\, n_{\rm i}\, T^{1/2}\, g(\nu, T)$$

hence, it depends strongly on the density and more weakly on the temperature.

Bremsstrahlung is important for several environments, such as HII regions around young stars and supernovae remnants. Bremsstrahlung is the main cooling process for plasmas with temperature above 1 keV ($\sim 10^7$ K), such as the ICM. In the case of galaxy clusters, at the temperature of the ICM, H and He are fully ionized. Thus, free electrons are interacting with ions in the hot intracluster gas emitting photons in the X-ray band. Due to this mechanism, clusters are the most luminous and extended X-ray sources in the universe, with typical luminosities of $L_X \sim 10^{43} - 10^{45}$ erg s^{-1}. Line emission due to highly ionized iron is also observed as a strong feature in the cluster X-ray spectrum, e.g. iron ions (mainly Fe^{+24} and Fe^{+25}). These lines are mainly at photon energies between 6 and 7 keV.

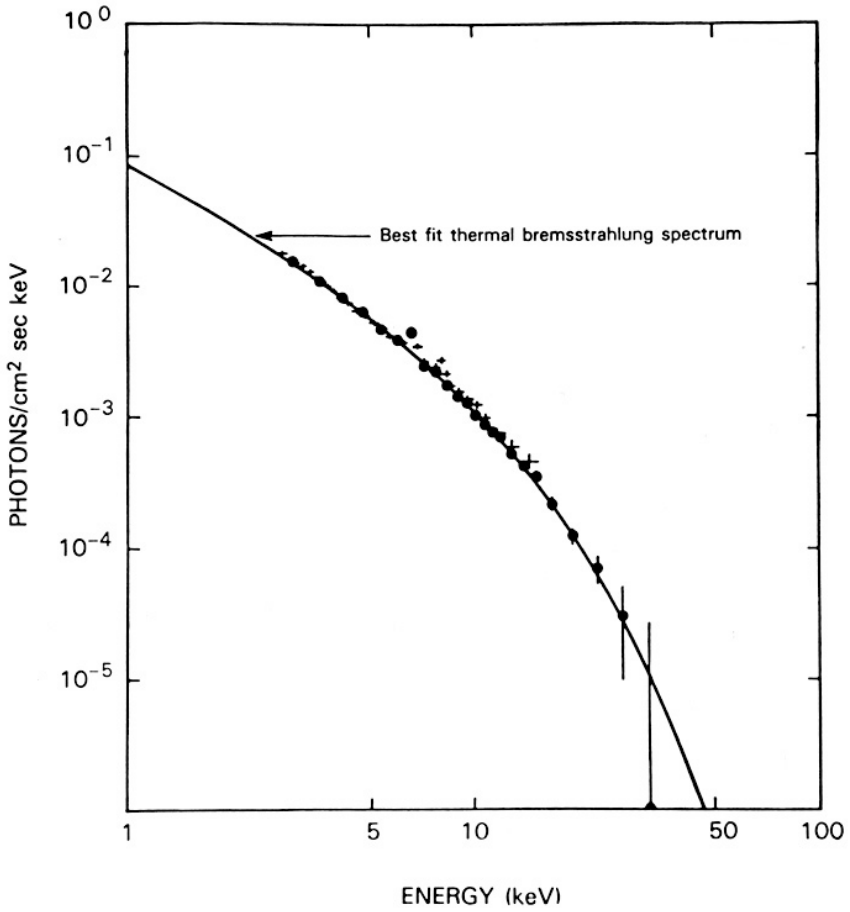

Figure A.1: X-ray spectrum of the ICM of the Coma cluster. The number flux of X-ray photons/(cm^2 s keV) is plotted against the photon energy in keV with the best-fitting isothermal bremsstrahlung continuum [Henriksen & Mushotzky, 1986].

X-rays are absorbed by the Earth's atmosphere. Therefore, X-ray observatories are placed on satellites, such as *XMM-Newton* and *Chandra*. These telescopes measure the position and energy of each individual incoming photon and can be pointed to single X-ray sources. *XMM-Newton* and *Chandra* have a higher sensitivity and spatial resolution than, for instance, the *ROSAT* satellite that was used for imaging surveys. More sensitive all-sky surveys in the X-ray band will be possible with the launch of *eROSITA* planned in 2019.

A.2 Synchrotron emission

Synchrotron radiation is non-thermal linearly-polarized emission from highly relativistic particles spiraling in a magnetic field. To stay on their path, electrons experience a constant acceleration that causes the emission of electromagnetic radiation. The emission spectrum is smooth over a large range of wavelengths without emission lines, and it can

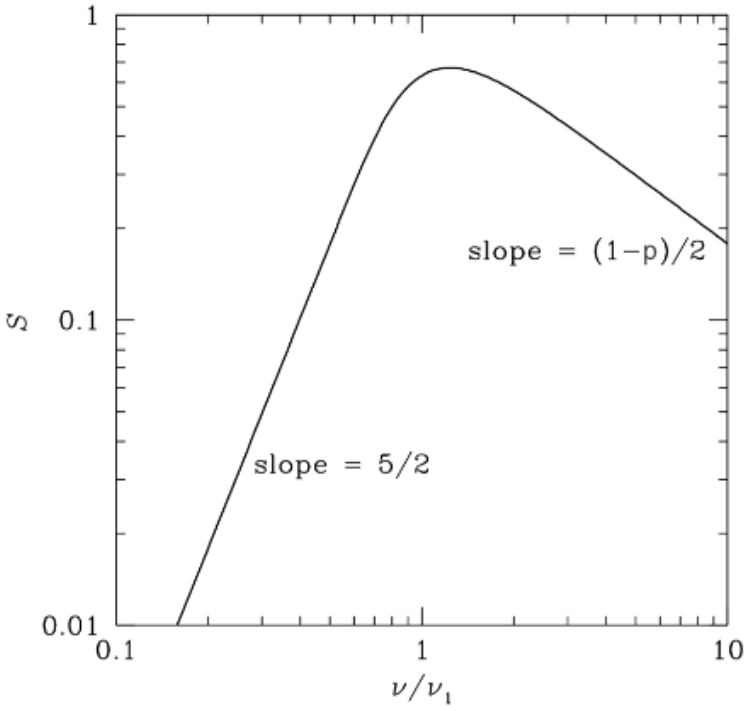

Figure A.2: Synchrotron spectrum of a power-law distribution of electrons with index p. The optically-thick, self-absorbed regime is proportional to $\nu^{5/2}$ and is independent of p, while the optically-thin part of the spectrum is proportional to ν^{α} where $\alpha = (1-p)/2$. Credit: Essential radio astronomy lectures, J. Condon and S. Ransom's website.

be approximated with power laws. The emitted power is given by:

$$\frac{\mathrm{dE}}{\mathrm{dt}} \propto m^{-2}\,\gamma^2 B^2$$

where m the particle rest mass, γ is the Lorentz factor, and B is the magnetic field strength. Note that this mechanism, because of its mass dependence, is much more efficient for electrons and positrons than for protons [Longair, 2011].

The total synchrotron emissivity derives from the integral of the power and distribution of the relativistic electron population, which is described by a power law $N(E) = N_0 \cdot E^{-p}$ where p is a constant index, and results in:

$$\epsilon_\nu \propto B^{1-\alpha}\,\nu^{\alpha},$$

where $\alpha = (1-p)/2$ is the spectral index. Therefore, a power law energy distribution of non-thermal particles radiates a power law emission spectrum, and their spectral indices are directly connected. The radio spectrum can then be described by:

$$S_\nu \propto \nu^{\alpha},$$

where S_ν is the flux density at a certain frequency. At low frequencies, however, synchrotron radiation is subject to self-absorption. Some fraction of the emitted photons can be reabsorbed by the electron population, causing the electrons to become optically thick to their own radiation. In this regime, the intensity is independent of the electron power law index, and is demonstrated to be proportional to $\nu^{5/2}$, as shown in Fig. A.2.

A.3 Inverse Compton scattering

Inverse Compton scattering is an elastic collision between a low-energy photon and a highly relativistic electron. The process is called inverse because the electrons lose energy and the photons are up-scattered to higher energy, on contrary of what happens in a standard Compton scattering. The frequency of the scattered wave $\nu_{\rm out}$ is related to that of the incident wave $\nu_{\rm in}$ as:

$$\nu_{\rm out} = \frac{4}{3}\,\gamma^2\,\nu_{\rm in}.$$

The IC plays an important role in clusters since the relativistic electron population responsible for synchrotron emission scatters the ubiquitous CMB photons whose Planck function peaks near $\sim 10^{11}$ Hz. For instance, relativistic electrons with $\gamma \sim 10^3$ are responsible for IC emission in the X-ray domain around 1 keV [Govoni & Feretti, 2004].

A.4 Synchrotron and Inverse Compton losses

The rate of energy loss by a single electron due to synchrotron and Inverse Compton is:

$$\frac{\mathrm{dE}}{\mathrm{dt}} = \frac{4}{3}\,\sigma_{\rm T}\,c\,\beta^2\,\gamma^2\,u$$

where $\sigma_{\rm T}$ is the Thomson cross section, and u is given by the magnetic energy density ($u_{\rm mag}$) in case of synchrotron or by the radiation energy density ($u_{\rm rad}$) in case of Inverse Compton. It is possible to define a cooling time:

$$\tau \equiv \frac{E}{\frac{\mathrm{dE}}{\mathrm{dt}}} = \frac{\gamma\,m\,c^2}{\frac{\mathrm{dE}}{\mathrm{dt}}} \propto \beta^{-2}\,\gamma^{-1}$$

Hence, in an ensemble of particles with a wide range of initial energies, the higher-energy particles radiate faster. The energy losses of the synchrotron-emitting electrons cause a change in the electron energy distribution, which reflects into a change of the radio spectrum. Hence, with passing time, the spectrum shows a cutoff at frequencies higher than a certain frequency related to the electron lifetime. After a time t, all electrons with $t_e < t$ would no longer be radiating, causing a break in the power law of the observed synchrotron spectrum at a critical frequency $\nu_{\rm b} \propto B^{-3}t^{-2}$, known as break frequency [Murgia et al., 2011]. This break will displaces to lower frequencies over time and its value, in addition to the magnetic field strength, is crucial in estimating the age of a synchrotron-emitting source, which is:

$$t_{\rm age} \propto \frac{B^{1/2}}{B^2 + B^2_{\rm CMB}} [(1+z)\,\nu_{\rm b}]^{-1/2}$$

where z is the source redshift, ν the observing frequency, and $B_{\rm CMB}$ is the equivalent magnetic field strength of the CMB that is proportional to $(1+z)^2$. This can be derived assuming a synchrotron source immersed in the CMB, which has $T_0 = 2.728$ K. The CMB temperature depends on redshift, i.e. $T_{\rm CMB} = T_0\,(1+z)$. Since

$$\frac{u_{\rm mag}}{u_{\rm rad}} = \frac{B^2}{8\,\pi}\,\frac{c}{4\,\sigma}\,T^{-4}_{\rm CMB}, \tag{A.1}$$

ascribing the CMB temperature an equivalent magnetic field $B_{\rm CMB}$, the formula can be rewritten as:

$$\frac{B^2_{\rm CMB}}{8\,\pi} = \frac{4\,\sigma}{c}\,T^4_{\rm CMB} = \frac{4\,\sigma}{c}\,T^4_0\,(1+z)^4, \tag{A.2}$$

so that for $T_0 = 2.728$ K, $B_{\rm CMB} = 3.25(1+z)^2$ μG.

Synchrotron emission can be seen in a large variety of environments, such as HII regions around young stars, supernovae remnants, the intergalactic medium, neutron stars, and AGN. In the case of galaxy clusters, relativistic electrons in the lobes of radio galaxies or in the intracluster gas give origin to the synchrotron emission in the radio band we observe.

A.5 Magnetic field measurements

The reference method to measure magnetic field strengths in clusters is the Faraday Rotation Measure (RM). When an electromagnetic wave, e.g. synchrotron radiation from radio galaxies located inside or behind the cluster, propagates through a magnetized plasma, such as the ICM, its polarization properties are affected by the Faraday rotation effect. Linearly-polarized radiation can be decomposed into left- and right- handed circularly-polarized components that propagate with different phase velocities [Clarke, 2004]. The intrinsic polarization angle $\chi_{\rm int}$ will be rotated by an angle $\Delta\chi$ and the observed position angle at wavelength λ is: $\chi_{\rm obs} = \chi_{\rm int} + \Delta\chi = \chi_{\rm int} + \lambda^2\,RM$ where:

$$RM = \frac{e^3}{2\pi m_{\rm e}^2 c^4} \int_{\rm source}^{\rm observer} n_{\rm e}(l)\,B_{II}(l)\,{\rm d}l.$$

where l is the path length between the source and the observer. Deriving the RM by measuring the position angle of the polarized radiation at different frequencies, and assuming that the electron density n_e is known, it is possible to estimate the component of the magnetic field along the line of sight B_{II}. The available studies of RM in galaxy clusters report values for the central magnetic field of few μG and radio observations indicate that the magnetic field strength in clusters declines from the core to the outskirts (e.g. see Bonafede et al. [2010] for the Coma cluster).

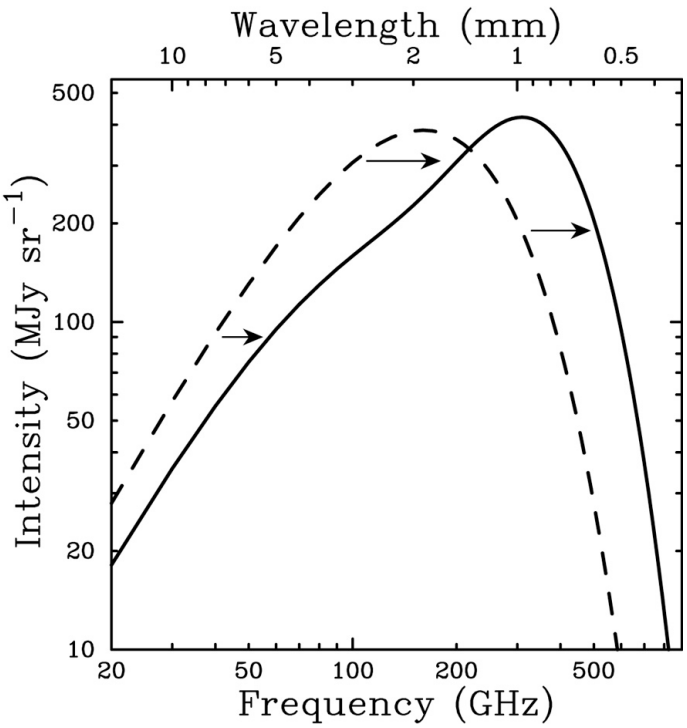

Figure A.3: The SZ spectral distortion of the CMB spectrum: a decrease in the CMB intensity at frequencies < 218 GHz and as an increase at higher frequencies. The source is a fictional cluster that is over 1000 times more massive than a typical cluster to illustrate the small effect [Sunyaev & Zeldovich, 1980].

An alternative method to estimate the magnetic field strength is measuring the hard X-ray emission, if interpreted as the result of IC scattering between CMB photons and ICM electrons. The difficulties related to this method are essentially due to the limitations of present X-ray observations in the hard X-ray domain and to the problem of distinguishing between the non-thermal and the thermal X-ray emission. When the IC X-ray emission is not detected from a radio emitting region, only lower limits to the magnetic fields can be derived [Wik et al., 2012].

Another method that is frequently used in literature is the equipartition argument, where the contributions to the total energy of the magnetic field and the relativistic particles are approximately equal [Govoni & Feretti, 2004]. However, it is not clear whether this condition holds in radio sources, and the assumptions for its derivation are based on many unknown parameters, such as the extent of the source along the line of sight, the ratio of the energy in relativistic protons to that in electrons, and the filling factor (i.e. fraction of the source volume occupied by the magnetic field).

A.6 Sunyaev Zel'dovich effect

The Sunyaev-Zel'dovich (SZ) effect is the process by which the blackbody spectrum of the Cosmic Microwave Background (CMB) is distorted by the presence of reservoir of hot plasma, such as the intracluster gas. Photons from the CMB are up-scattered to higher energies by the gas through the Inverse Compton (IC) mechanism [Sunyaev & Zeldovich, 1980]. This causes a change in the apparent brightness of the CMB radiation as a decrement (increment) at low (high) radio frequencies (see Fig. A.3). Measurements of this effect provide information on the cluster properties. Being a scattering process, the SZ effect is redshift-independent, providing a unique probe of the structure of the universe on the largest scales.

Given the combination of the photon cross section and the electron column density of the ICM, CMB photons passing through the center of a massive cluster have only $\sim 1\%$ probability of interacting with an energetic electron [Rephaeli et al., 2005]. The resulting IC scattering preferentially boosts the energy of the CMB photon by $\sim \frac{kBT}{m_e c^2}$ causing a small (~ 1 mK) distortion in the CMB spectrum.

The SZ effect can be written as: $\Delta I_{SZ} \propto I_0\, y$, where I_0 is the CMB intensity unaffected by IC scattering, and y is a parameter proportional to: $\int n_e T dl$. Thus, the SZ signal integrated over the solid angle of the cluster provides the sum of the electrons weighted by temperature, which is a measure of the total thermal energy of the cluster. Hence, the SZ signal is correlated with the cluster mass, and is a more robust indicator with respect to the X-ray luminosity [Motl et al., 2005]. For instance, to build a sample of galaxy clusters that is as close as possible to be mass-selected is using SZ surveys, such as the one carried out with the *Planck* satellite [Planck Collaboration et al., 2014] [Planck Collaboration et al., 2016].